High Velocity Oxy-Fuel (HVOF) Thermal Spray Deposition of Functionally Graded Coatings

A Thesis Submitted to the
Faculty of Engineering and Computing,
School of Mechanical and Manufacturing Engineering,
Dublin City University
For the Degree of Doctor of Philosophy

By

Mahbub Hasan, B.Sc. Eng.

Materials Processing Research Centre and
National Centre for Plasma Science and Technology
Dublin City University

DCU

Research Supervisors
Dr. Joseph Stokes (BA, BAI, Ph.D., MIEI)
Dr. Lisa Looney (BA, BAI, Ph.D., CEng., MIEI)
Professor M. S. J. Hashmi (Ph.D., D.Sc., CEng., FIMechE., FIEI, MASME)

January 2005

DECLARATION

I hereby certify that this material, which I now submit for assessment on the programme of study leading to the award of Doctor of Philosophy, is entirely my own work and has not been taken from the work of others save and to the extent that such work has not been cited and acknowledged within the text of my work.

Signed: M.HASAN   Date: 25/01/05

(Mahbub Hasan)

Student I.D. No.: 99146215

ACKNOWLEDGEMENT

I wish to thank all of my fellow postgraduate students for their support and friendship during my study in DCU. My thanks also go to the Bangladeshi Community (specially Julfikar Haider, my housemate for over four years) in Ireland who provided me a lot of support and fun during my life in Dublin.

DEDICATION

DEDICATED TO

MY PARENTS

(LATE DR. AHMAD HUSAIN & MAHBUBA HUSAIN)

AND

ELDER BROTHER

(LATE COLONEL MUHAMMAD HUSSAIN)

ABSTRACT

High Velocity Oxy-Fuel (HVOF) Thermal Spray Deposition of Functionally Graded Coatings

Mahbub Hasan

The present study investigates an innovative modification of a HVOF (High Velocity Oxy-Fuel) thermal spray process to produce functionally graded thick coatings. In order to deposit thick coatings, certain problems have to be overcome. More specifically these problems include minimizing residual stresses, which cause shape distortion in as-sprayed components. Residual stresses in coatings also lead to adhesion loss, interlaminar debonding, cracking or buckling and are particularly high where there is a large property difference between the coating and the substrate. Graded coatings enable gradual variation of the coating composition and/or microstructure, which offers the possibility of reducing residual stress build-up in coatings.

In order to spray such a coating, modification to a commercial powder feed hopper was required to enable it to deposit two powders simultaneously. This allows deposition of different layers of coating with changing chemical compositions, without interrupting the spraying process. Various concepts for this modification were identified and one design was selected, having been validated through use of a process model, which was developed using ANSYS Finite Element Analysis. The model simulates the flow of nitrogen gas and powder through the system, and verified the supply of mixed composition powders. Based on this information a multi-powder feed unit was manufactured, commissioned and calibrated. Multi-layer coatings of aluminium and tool-steel were sprayed onto aluminium substrates. The chemical composition of different layers of a five layer graded coating was determined using energy dispersive X-ray spectroscopy (EDS) to confirm functionality.

Subsequently, various controlled parameters of the HVOF spraying process were studied for this type of coating using 3^3 factorial design of experiments. Results were analysed in terms of surface stress to deposition thickness ratio. The best combination of spray parameters identified for deposition of the mixed coating resembles those recommended for aluminium powder alone. It is proposed that this arises from the thermal properties of the constituent powders.

Different types of aluminium/tool-steel functionally graded coatings were then deposited using the optimised set of spray parameters, and considered using Clyne's analytical method of stress analysis and Vickers hardness testing method. Coatings composed of thicker layers resulted in much higher residual stress, but also improved hardness compared to thinner samples. It was found that if 5 layers of graded material are sprayed, and the residual stress compared to that of a traditional single layer (of the same thickness), an approximately 48 % reduction can be achieved. However this benefit is mitigated somewhat by the fact that applying these multi-layers reduces the hardness to by approximately 16 % compared to the traditional single layered deposit. Therefore an engineer must compromise between the stress and hardness when designing a functionally graded coating-substrate system.

TABLE OF CONTENTS

PAGE

LIST OF FIGURES

LIST OF TABLES

CHAPTER 1
INTRODUCTION

1.1 INTRODUCTION

The majority of engineering components currently being utilized can potentially degrade or catastrophically fail in service due to such phenomena as wear, corrosion and fatigue. Thus serviceable engineering components not only rely on their bulk material properties, but also on the design and characteristics of their surface. Surface engineering involves the application of traditional and innovative coating technologies to engineering components and materials to improve their characteristics.

The thermal spraying process is one of the most successful of all the advanced coating techniques because of the wide range of coating materials and substrates to which it can be applied. Metals and carbides are mostly used as base materials, although spraying of polymers has also been researched [1,2]. Thermally sprayed coatings are used to protect components from different types of wear and corrosion [3-6]. Various base materials are also coated with a low thermal conductivity material to increase their heat resistance. A variety of engineering problems have been solved using the thermal spraying technique and research is ongoing to increase its application [7,8]. The current field of application of thermal spraying includes; the oil industry to protect component surface against hostile environment [7], automotive industry [8,9], and the space exploration industry [10].

The High Velocity Oxy-Fuel (HVOF) process is one of the most popular thermal spray technologies and has been used in many industries due to its flexibility and the superior quality of coatings produced compared to other thermal spray techniques. It produces a coating of higher bond strength and higher hardness together with lower porosity than other thermal spray processes such as the plasma spray [11]. Parker et al. [12] reported the growth of utilization of the HVOF process in different industries, especially in Aeronautical industry, both in the commercial and the defence airline sections [13]. Other fields of application of the HVOF process include petrolechemical [14,15], automotive [16,17], paper/pulp [18] and manufacturing industries [19].

Previous research at the Materials Processing Research Centre (MPRC) has shown that the HVOF thermal spray process has the potential to form free standing components [20-22]. However deposit thickness was quiet low, typically 0.6 mm in the case of WC-Co deposits. This is because cracking, deformation and adhesion loss of the

components/coatings results as thickness increases due to residual stress build-up. Dissimilar material properties, especially the difference of the co-efficient of thermal expansion between the substrate and coating and between different layers of the coating (if different layers consist of different materials) are the main cause of residual stress build-up. Graded deposition is one method of potentially reducing the internal stress, as it enables gradual variation of through thickness coating composition and/or properties [23,24]. This study explores the possibility of producing aluminium/tool-steel functionally graded coatings using the HVOF thermal spray process. Graded aluminium/tool-steel coated aluminium may be used in Automobile industry to replace heavy parts with lighter parts, which in turn decrease vehicle weight, increase fuel efficiency and make parts stronger by reducing residual stress build-up in them.

The remainder of the report is divided into a number of chapters. Chapter two is a review of literature relevant to the study. Initially it describes how coatings evolve and how a coating protects these surfaces. Various HVOF thermal spray processes are then examined, followed by a description of how the thermal sprayed coating is built-up. Different types of powder production techniques are then mentioned. Next functionally graded materials (FGM) are defined, and their advantages and manufacturing techniques presented, with a conclusion on the properties and field of applications for functionally graded coatings. This section also shows the effect of thermal spraying on coatings in terms of microstructure and mechanical properties.

Chapter three describes the equipment used in current work, the HVOF Diamond Jet process. Modifications including additions of some newly designed parts to the commercial powder feed hopper are described. The FLOTRAN CFD ANSYS Finite Element package is described in relation to the nitrogen gas-powder flow model, which was a feature of the design. The testing procedures that involved calibration of the newly designed parts are then described. This chapter also includes the coating deposition procedure and characterization techniques.

In chapter four, experimental and simulation results are presented. Initially the results of the simulation are detailed. Then results of calibration tests, spray parameter optimisation tests and coating characterization tests are described. The calibration tests include powder flow bench tests and in-situ flow tests. The spray parameter optimisation tests involve determination of the temperature difference between the

substrate and the coating, determination of the Young's modulus, Poisson's ratio and residual stress of different types of graded coatings. Determination of chemical composition of different layers along with microstructure and phases present in a five layer aluminium/tool-steel functionally graded coating was also carried out. The characterization tests include determination of microhardness using the Vickers hardness testing method. Chapter four also compares the simulated results with the experimental results.

Finally, chapter five summarises the major conclusions from the results of the current research, and presents recommendations for future work in this area. The future work includes further modification of the designed powder feed system to increase its efficiency.

CHAPTER 2
LITERATURE REVIEW

2.1 INTRODUCTION

The behaviour of a material is greatly dependent upon its surface, the environment and its operating conditions. Surface engineering can be defined as the branch of science that deals with methods for achieving desired surface requirements and behaviour in service for engineering components [25].

The surface of any component may be selected on the basis of texture and colour, but engineering components generally demand a lot more than this. Engineering components must perform certain functions completely and effectively under various conditions, possibly in aggressive environments. Modern process environments, which contribute to wear, can be very complex, involving a combination of chemical and physical degradation. Surface properties of the component used in a particular working environment have to be designed with that environment in mind. Surface engineering in today's production world embraces the design, evaluation and performance in service of a component including a substrate, through the interface, to the surface of a coating [26]. Coating technology can be tailored to suit certain environments. A variety of bulk materials, such as ferrous and non-ferrous metals, alloys, ceramics and cermets can be coated to achieve adequate resistance to wear, corrosion and friction. Again coating less wear resistive component materials with that of a high resistive material, offers an ideal method of surface protection.

2.2 OVERVIEW OF COATING TECHNIQUES

A coating may be defined as a near surface region, having properties different from the bulk material it is deposited on. Thus the material system (coating and substrate) forms a composite, where one set of properties is obtained from the bulk substrate and another from the coating itself. Coatings may be applied to the surface of materials in order to protect the surface from the environment that may produce corrosion or other deteriorative reactions and/or to improve the surface's appearance.

The selection of a particular deposition process depends on several factors, including:

1. Chemical, process and mechanical compatibility of the coating material with the substrate [27]
2. Rate of deposition required
3. The ability of the substrate to withstand the required processing [28]
4. Limitations imposed by the substrate (for example maximum allowable deposition temperature)
5. Adhesion of the deposited material to the substrate
6. Process energy
7. Purity of the target material (this will influence the purity content of the film)
8. Requirement and availability of the apparatus
9. Cost
10. Ecological considerations

There are many coating deposition techniques available. An overview is given in figure 2.1. These techniques are divided into two common groups, metallic and non-metallic. Metallic coating deposition has three categories, hard facing being the most important in the context of this research. Hard facing is used to deposit thick coatings of hard wear-resistant materials on either a worn component or a new component, which is subjected to wear in service. There are three techniques of hard facing available: welding, cladding and thermal spraying. Thermal spraying is of most importance in this research, hence the following section concentrates on this technique.

COATINGS

Metallic

Non-Metallic

Chemical
Conversion   Polymer   Glass Ceramic

Vapour Deposition   Hard Facing

Miscellaneous

Physical   Chemical   Physical-
Vapour   Vapour   Chemical
Deposition   Deposition   Vapour
                              Deposition

1. Atomised Liquid Spray
2. Brush, Pad and Roller
3. Electrochemical
   Deposition
4. Chemical Deposition
5. Die Process
6. Intermetallic Compound
7. Fluidized Bed
8. Spark Hardening
9. Sol Gel
10. Spin On

Welding   Thermal Spraying   Cladding

1. Deformation Cladding
2. Diffusion Cladding
3. Braze Cladding
4. Laser Cladding

1. Spray and Fuse
2. Low Pressure Plasma
3. Detonation Gun
4. Electric Arc
5. Plasma Arc
6. Flame (HVOF)

Figure 2.1: Coating Deposition Techniques [29].

6

2.3 THERMAL SPRAY TECHNIQUES

After several patents in 1882 and 1899, Dr. Max Schoop first applied tin and led coatings to metal surfaces by flame spraying [30]. Then the field of thermal spraying started to develop all over the world. Figure 2.2 gives an impression of the pace of the development of the Thermal Spray Technology. The rate of progress was slow after the inception of Schoop, then it increased at a modest rate until 1950s. At that time a variety of what then was known as modern plasmatrons appeared, which boosted the development considerably [31]. In particular, the D-gun coatings, developed by Praxair Surface Technology found a receptive market in the aerospace industry and a large proportion of subsequent technological growth was due to plasma based thermal barrier coatings [31]. The second growth occurred in the 1980s with the invention of vacuum plasma spraying, low pressure plasma spraying and the Jet Kote HVOF technique. The Jet Kote system was manufactured by Browning Engineering, in the USA [31]. In 1988 Sulzer METCO introduced the Diamond Jet HVOF system, which is the process under investigation in the current research and which is described in detail later in this report.

Thermal spraying is a process whereby a coating material is fed into a heating zone to become molten (or semi-molten), and is then propelled from there to a base material (substrate) [32]. The industrial benefit of the thermal spray coatings is the achievement of cost-effective solutions to minimize wear and corrosion, including thermal barrier coatings. The tailoring of components, or specific areas, to counteract damaging effects, prolongs new parts or provides cost-effective restoration of worn parts. Substrate materials such as low carbon steel can be thermally sprayed with thin layers of nickel alloys to provide a cost-effective product with high corrosion resistance [33]. Another advantage of thermal spraying is that it produces coatings with no dilution of the substrate, yielding a net part with little or no finishing requirements.
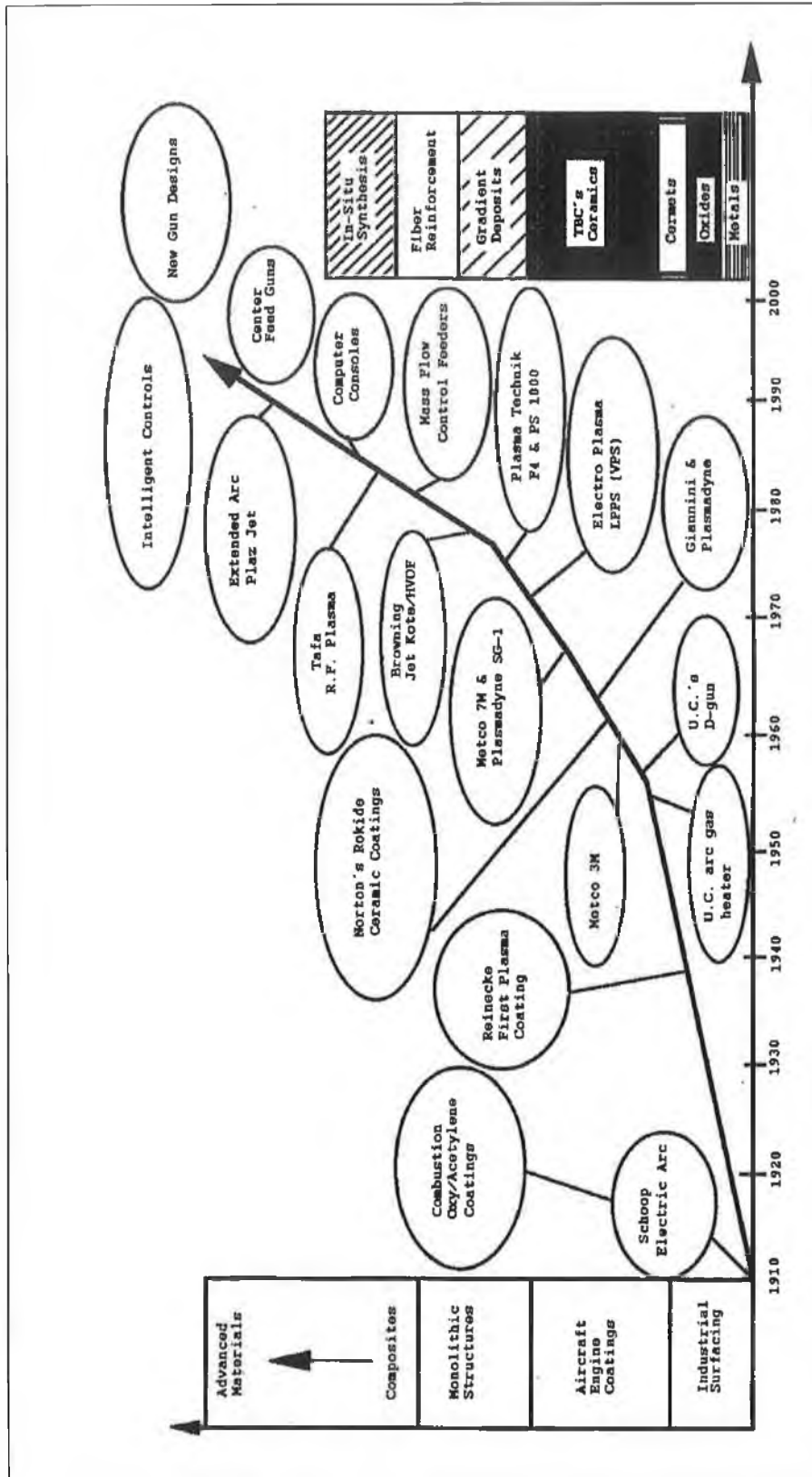
Figure 2.2: Development of the Thermal Spray Technology [31].

The thermal energy used to melt the coating material, may be divided into two categories, electrical and flame heating. There are three processes by which electrical heating is utilized to melt the coating material. They are:

(a) Electric arc process

(b) Plasma arc process

(c) Low pressure plasma spraying

Further information has been reported by Stokes [34] on those techniques, hence this is not described here. The second category is flame heating with the following three processes:

(a) Flame spraying process

(b) Spray and fuse process

(c) HVOF thermal spray process

The HVOF thermal spraying process is relevant to this study, hence this flame heating process is investigated in detail in this report.

2.3.1 HVOF Thermal Spray Process

Unlike other flame spraying processes, the HVOF (High Velocity Oxy-Fuel) thermal spray process utilizes only powder as the coating material rather than wire or rod [29]. There are two types of HVOF processes; (1) the Detonation Gun HVOF system and (2) the Continuous combustion HVOF system. The difference between each of these systems is the use of different fuel gases, cooling systems and the fact that the penultimate combustion is maintained by a timed spark, used to detonate the particle and gas mixture, but otherwise their underlying principle is same [35]. There are notable differences between the detonation gun and the Continuous combustion HVOF gun designs [34], however this report concentrates on the latter process only.

Continuous Combustion HVOF System

Within the continuous combustion HVOF process there are various types of systems namely; the Diamond Jet (DJ HVOF) and DJ Hybrid gun developed by Sulzer METCO, the Jet Kote system developed by Browning Engineering, the HV-2000 by Praxair Surface Technology, the HP/HVOF developed by TAFA and many more [36-38]. The continuous combustion Jet Kote HVOF thermal spray system was developed as an alternative to the Detonation Gun system in 1982 [39,40]. Following the Jet Kote system, the Diamond Jet (DJ) HVOF thermal spraying process was developed in 1988 by Sulzer METCO. Due to its flexibility and cost-effectiveness, it has been widely adopted in many industries [22]. This system produces dense coatings with low porosity and high bond strength due to the high kinetic energy associated with the system to propel the molten material at supersonic speeds [41-44].

In the Diamond Jet HVOF thermal spraying process, powder material is melted by the combustion of oxygen and fuel gas, and propelled at a high velocity of around 1350 m/s [45] by the use of compressed air and a nozzle assembly towards the substrate surface as shown in figure 2.3. In the combustion zone, the powder material enters the flame, where it becomes molten or semi-molten depending on the melting temperature of the powder material. The flame temperature of the HVOF process is between 2300 and 3000 ^{0}C [45]. Due to the high kinetic energy experienced by the impinging particles, the DJ HVOF system exhibits one of the highest bond strengths and lowest porosity among all thermal spraying processes [46]. Again compared to other thermal spaying process such as plasma spraying, the DJ HVOF system exhibits low thermal residual stress; therefore coatings of higher thickness may be deposited [47]. The spray gun temperature for the plasma spraying process is around 16000 ^{0}C [33], whereas that of HVOF system is between 2300 and 3000 ^{0}C [45]. Higher temperature in plasma in turn produces coatings with higher residual stress compared to HVOF thermal spray process.
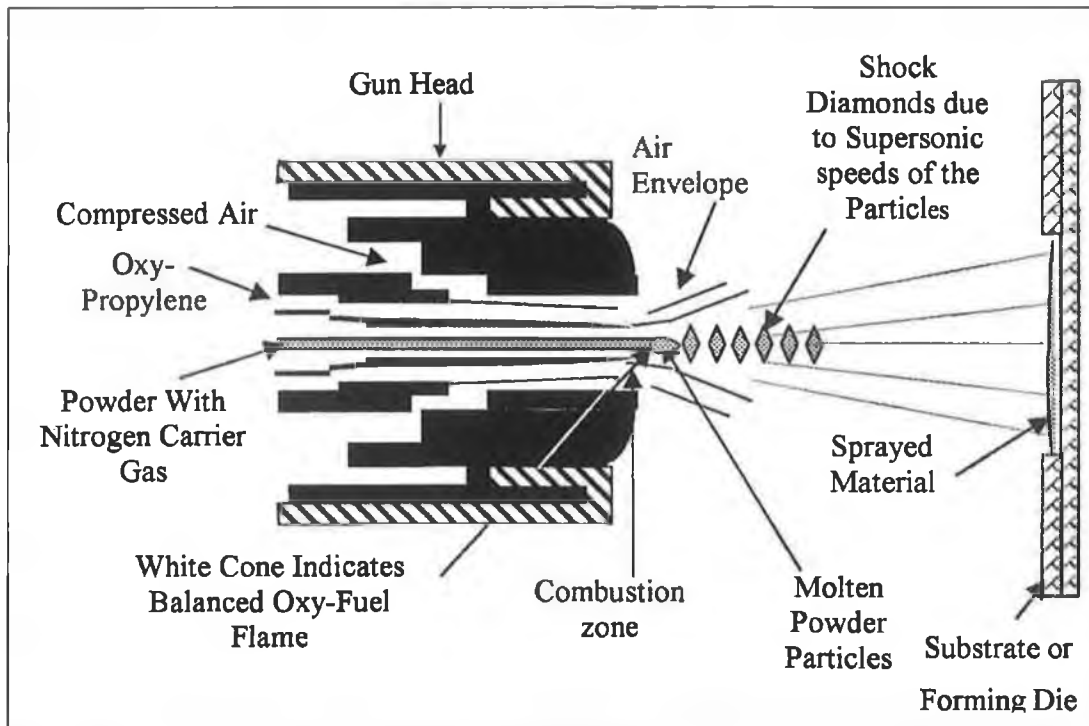
Figure 2.3: Schematic of cross-section of a Diamond Jet spray gun [22].

2.3.2 HVOF Gun Design

HVOF guns can be classified into two groups, those with (a) a throat combustion burner and (b) a chamber combustion burner. The HVOF gun used in the current research has a chamber combustion burner. The main difference between the two groups is the location of the combustion.

(a) Throat Combustion Burner

Throat combustion burners were the first type of HVOF spray guns to be developed [48]. The fuel and oxidant combust within the gun barrel, as these systems do not have separate combustion chamber as shown in figure 2.4. The powder is commonly injected axially [48]. Initially the burners were water cooled, by surrounding the gun barrel with flowing water. Then the system was modified to use air rather than water [49]. Air-cooled spray guns are simpler and have a lower weight because of the relative density between air and water. Both the air and water-cooled throat combustion burners have lower heat loss than chamber combustion burners, due to decreased surface area.

However, these systems have limited throughput because of flame stabilization requirements [48]. Due to the lower throughput, chamber pressure and, consequently, gas and powder velocities are lower [48].
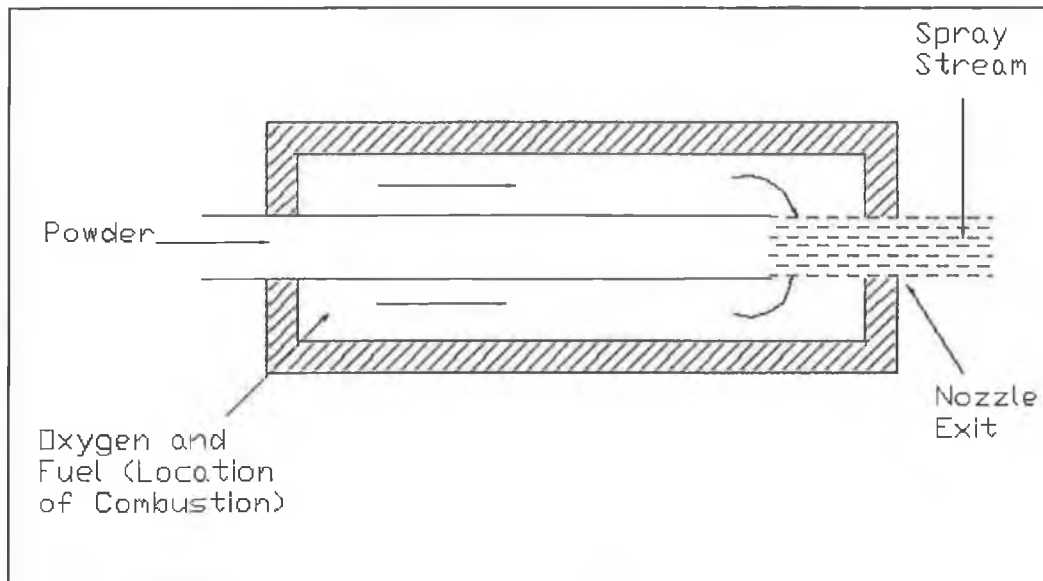
Figure 2.4: Schematic of a throat combustion burner HVOF gun.

(b) Chamber Combustion Burner

In a chamber combustion burner, the fuel gas is introduced into a combustion chamber with a larger diameter than that of the spray gun barrel. The combustion chamber is either at a right angle or a straight through orientation with the barrel as shown in figure 2.5. Powder injection may be axial, radial or central [48]. There are also some chamber combustion burners, where powder is injected beyond the flame at the beginning of the barrel [50,51].

Chamber combustion burners offer coatings with improved wear and corrosion resistance, as compared with those produced by throat combustion chambers [48]. These superior coatings are a result of large diameter combustion chambers, which results in a higher throughput and chamber pressure, leading to higher gas and powder velocities [48]. But, due to increased surface area, heat loss from the chamber combustion burner is greater, which may inhibit particle heating. Table 2.1 shows some of the important characteristics associated with the different thermal spraying processes.
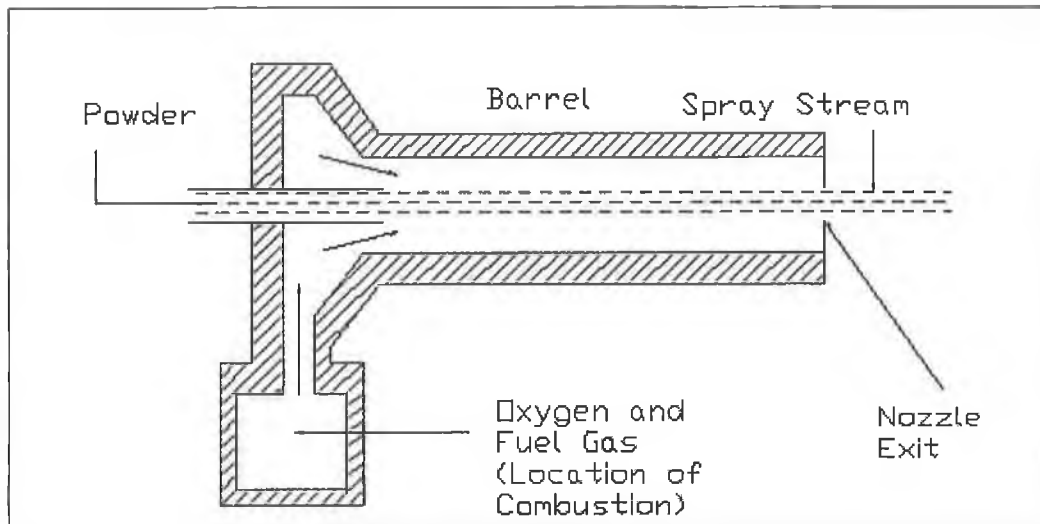
Figure 2.5: Schematic of a chamber combustion burner HVOF gun.

Table 2.1: Characteristics of different thermal spray techniques [29, 52].

Deposition Technique	Spray Gun Temp. (^{0}C)	Particle Velocity (m/s)	Coating Materials	Bond Strength (MPa)	Porosity (% volume)	Hardness*
Electric Arc	6000	240	Ductile Materials	40-60	8-15	$40R_h$-$35R_c$
Plasma Spraying	16000	120-600	Metallic, ceramic, compound	30-70	2-5	$40R_h$-$50R_c$
Low Pressure Plasma	16000	900	Metallic, ceramic, compound	>70	<5	- - -
Spray & Fuse	- - -	-- -	Fusible metals	>70	<0.5	- - -
Flame Spraying	3300	240	Metallic, ceramic	20-28	10-20	$30R_h$-$20R_c$
HVOF Detonation Gun	4500	800	Metallic, ceramic, compound	>70	0.1-1	- - -
HVOF Sulzer METCO DJ Gun	2800	1350	Metallic, ceramic	40-96	0.5-2	$100R_h$-$50R_c$

* R_c = Rockwell hardness on C scale

* R_h = Rockwell hardness on H scale

2.4 THE HVOF PROCESS

The HVOF process uses a combination of thermal and kinetic energy for melting and accelerating powder particles, in order to deposit the desired coating. Hydrocarbon gases or pure hydrogen are normally used as the fuel gas. The gun consists of three sections: a mixing zone, a combustion zone and the nozzle. Combustion and gas dynamics are important characteristics in producing coatings. They affect the coating quality in the following two ways [53]:

(1) The particles injected into the gas stream must be accelerated in order to strike the target at high velocity
(2) Heat transfer to the particles from the gas stream is required to melt them prior to impact

2.4.1 Combustion and Gas Dynamics of the HVOF System

Oxygen and fuel gas at certain pressures, are firstly mixed in the mixing zone and then directed towards the combustion zone. After ignition with an external ignitor, a chemical reaction takes place that releases heat energy. The pressure increases with an increase in temperature, and this results in the high gas velocities [54,55]. In spraying carried out using propylene and oxygen, where nitrogen is the carrier gas, the simple chemical reaction of gases is as follows [56]:

Propylene + Oxygen + Nitrogen → Water + Carbon Dioxide + Nitrogen + Heat

Equation 2.1

The Stoichiometric (theoretically required for complete combustion) oxygen to fuel ratio is 4.5 to 1. The energy released by the chemical reaction of the gases is used to heat and accelerate both the emerging gases and the spraying powder. Because of excessively high deposition temperatures, the water produced in the combustion reaction evaporates. The resulting gas velocity is a function of pressure, temperature, density, gas composition and the area through which gas travels. But the local sound velocity affects the maximum obtainable gas velocity through the minimum cross-sectional area. Substantial research [39] and information [34] has been collected on the

effects of gas dynamics on the HVOF gun and its influences on the final properties of the deposit.

Selection of fuel gas depends upon economics, coating material and desired coating properties. Hydrogen fuel gas is used when processing oxygen sensitive materials. Propylene should be used when high heat input is necessary. High melting, oxide based ceramics can only be sprayed by the HVOF process when acetylene fuel gas is used. Variation in different properties for 86WC/10Co/4Cr, produced by different fuel gases is shown in table 2.2 adopted from Sulzer METCO [57].

Table 2.2: Variation of properties of 86WC/10Co/4Cr, produced by different fuel gases [57].

Fuel Gas	Hardness (HV 0.3)	Roughness (μm)	Porosity (%)	Strength (MPa)
Hydrogen	1093	2.20	<1	>70
Propylene	1065	2.45	<1	>70
Natural Gas	1114	2.97	<1	>70
Liquid Propane	1016	2.52	<1	>70

Variation of spray parameters, such as the powder feed rate, flow rate ratio of oxygen to fuel, flow rate of the compressed air and spray distance also effects the HVOF sprayed deposition thickness and properties. With a decrease in the oxygen to fuel ratio, the deposition temperature increases (as shown in figure 2.6) [39]. This in turn increases residual build-up in the coatings, (as will be indicated by equation 2.2 later). With an increase in the spray distance, the flight time of the particles from the gun to the substrate is increased, which results in lower particle velocities and lower impact temperatures. Again lower particle velocities and temperature causes lower deposition thickness and lower residual stress in the coatings [58]. Compressed air is used in the HVOF process to accelerate powder particles onto the substrate [34]. Thus, with an increase in the flow rate of the compressed air, the particle velocities increase inside the gun, as well as from the gun to the substrate. Higher particle velocities also decrease premature solidification of coating material before impact with the substrate.
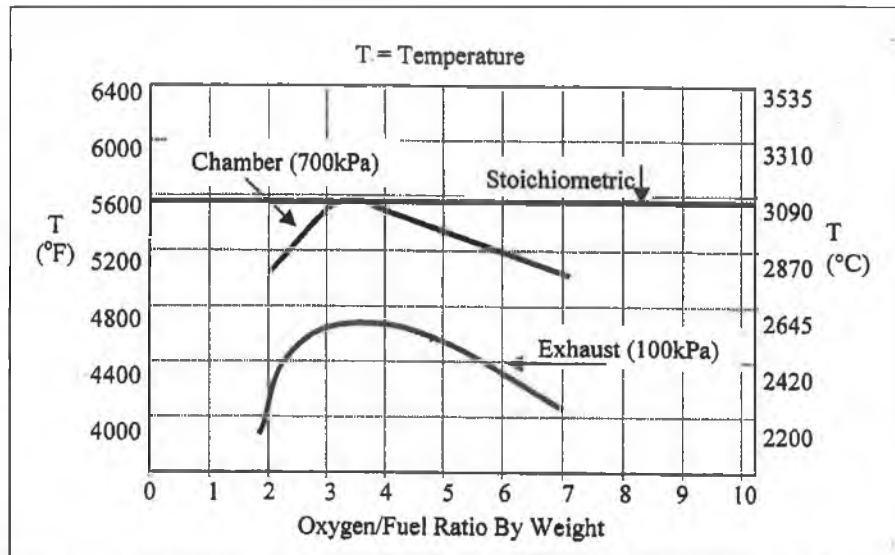
Figure 2.6: Theoretical flame temperature against oxygen/fuel ratio
adopted from [39].

2.4.2 Advantages of the HVOF Coating

Particle velocity is very important in the thermal spray process, as the higher the velocity, the higher the bond strength, and the lower the porosity [33]. This is because particles have less time to cool down at high velocities. The HVOF process is designed around producing high velocities and this confers many of the advantages that the HVOF technique has over other thermal spray techniques [33,59-61], which include:

1. More uniform and efficient particle heating, due to the high turbulence experienced by the particles
2. Much shorter exposure time in flight due to high particle velocities
3. Short particle exposure time in ambient air, once the jet and particles leave the gun, which results in lower surface oxidation of particles
4. Lower flame temperature compared with plasma spraying
5. Lower ultimate particle temperatures compared to other processes
6. Lower capital cost and ease of use compared to other processes
7. Thicker coatings than with plasma and arc spraying can be produced

Table 2.3 summarises the reasons the HVOF process produces such high quality coatings.

Table 2.3: Benefits of using the HVOF coatings [34].

Coating benefit	Main reasons for this benefit
Higher density (Lower porosity)	Higher impact energy
Improved corrosion barrier	Less porosity
Higher hardness ratings	Better bonding, less degradation, denser coatings
Improved wear resistance	Harder, tougher coating
Higher bond and cohesive strength	Improved particle bonding
Lower oxide content	Less in flight exposure time to air
Fewer unmelted particle content	Better particle heating
Greater chemistry and phase retention	Reduced time at higher temperature
Thicker coatings	Less residual stress
Smoother as sprayed surface	Higher impact energies

2.4.3 Disadvantages of the HVOF System

1. The amount of heat content in the HVOF system is very high, so over heating of the substrate is quite likely. Therefore extra cooling of the substrate is necessary, and cooling with liquid CO_2 is now a standard with the new HVOF process [58,62,63]

2. Masking of the part is still a great problem as only mechanical masking is effective. It is very difficult and time consuming to design an effective mask for a complex component with areas, which do not require deposition.

2.5 THERMALLY SPRAYED COATINGS

A thermally sprayed coating produced in air is a heterogeneous mixture of sprayed materials, oxide inclusion and porosity [11]. Each particle interacts with the surrounding environment during flight from the gun to the substrate. Sprayed coatings have distinct characteristics that distinguish them from materials manufactured by other routes such as casting or sintering. Generally any material that does not decompose, vaporize, sublimate or dissociate on heating, can be thermally sprayed.

2.5.1 Input Powder Production

Atomization is a well-known process of producing powder materials. It may be defined as the break-up of a liquid into fine droplets [64]. Both elemental and pre-alloyed powders can be formed by atomization. Types of atomization include gas atomization, water atomization, centrifugal atomization and so on, however gas and water atomization are most popular. Gas atomization uses air, nitrogen, helium or argon as a fluid for breaking up the liquid. It produces powders of more spherical and rounded shape and has lower oxygen content. On the other hand, water atomized powders are irregular in shape and have higher oxygen content. For high volume and low cost production, water atomization is preferred over gas atomization.

Thermal spraying can be used to deposit a wide range of coating materials. They can be divided into three main categories. The categories are metal/alloys, ceramics and cermets [65]. Examples of the first category are copper, tungsten, molybdenum, tin, aluminium, zinc to mention a few. The second category includes chrome oxide, aluminium oxide, alumina/titania composite, stabilized zirconia and so on. The third category, cermets consists of a ceramic and a metal or alloy. Examples are tungsten carbide in a cobalt matrix, chrome carbide in a nickel/chrome matrix and so on. In the current research the aluminium and tool-steel powders are used. Various forms of aluminium powders can be produced such as granules, regular atomized, coated atomized, spherical, high-purity powder, alloy powder, blended powder and so on [64]. While aluminium powder can be produced either by gas or water atomization, the aluminium powder used in this research is produced using the water atomization process. The tool-steel powder is produced by induction melting of raw materials or

scrap. Either gas or water atomization process mentioned earlier can be used. Gas atomized tool steel powders are spherical in shape and have high apparent densities [64]. Water atomized tool-steel powders are irregular in shape and are suitable for die compaction and sintering [64]. The tool-steel powder used in the current project is produced using the gas atomization process. The composition, particle size and some other properties of the tool-steel and aluminium powders are given in table 2.4.

Table 2.4: Detail information of the tool-steel and aluminium powder [66-68].

Code Name	Production Route	Chemical Com.	Particle Size	Colour	Hard-ness (HV)	Melting Point (^{0}C)
DIAM-ALLOY 4010 (Sulzer METCO)	Gas atomization	95.2% Fe, 3% Mo, 1.8% C	-44 +5 micron	Greyish	840	1410
AL006020 (Good-fellow)	Water atomization	99.5% Al	50 micron	Silvery white	21	660

2.5.2 Coating Deposition, Solidification and Build-Up

During the spraying process, particles become superheated and projected towards the substrate at a high velocity [69]. The common feature of thermally sprayed coatings is their lanticular or lamellar grain structure. Initially the particle is melted and propelled out from the gun in the form of a sphere, then at its first contact with the substrate the impact creates a shock wave inside the lamella and the substrate [44]. The behaviour of particle on impact has been researched intensively by various authors [70-72]. The shape and structure of the splat reveals a lot of information about the spray parameters, such as whether the correct spraying distance or spray angle have been utilized or not [73-75].

Again, the molten particles deform to lamella and solidify giving a columnar structure as shown in figure 2.7. The figure shows a cross-section of a single lamella. The approximate diameter of an alumina lamella is between 104-140 μm for starting alumina particle of diameter of 53–63 μm [76]. In most typical conditions, the solidification process starts at the interface between the particle and the substrate, this interface forms the heat sink for the liquid. Formation of solidified grains depends on a number of factors determining particle deformation (spraying technique, method of

spraying, powder grain size and sprayed material properties) and on the substrate (roughness, temperature and type of material). Substrate roughness must be adequate during spraying, otherwise adherence loss may occur [77,78]. Gawne et al. [77] reported linear increase of coating adhesion with increase in substrate roughness in the range of 4 -13 μm.
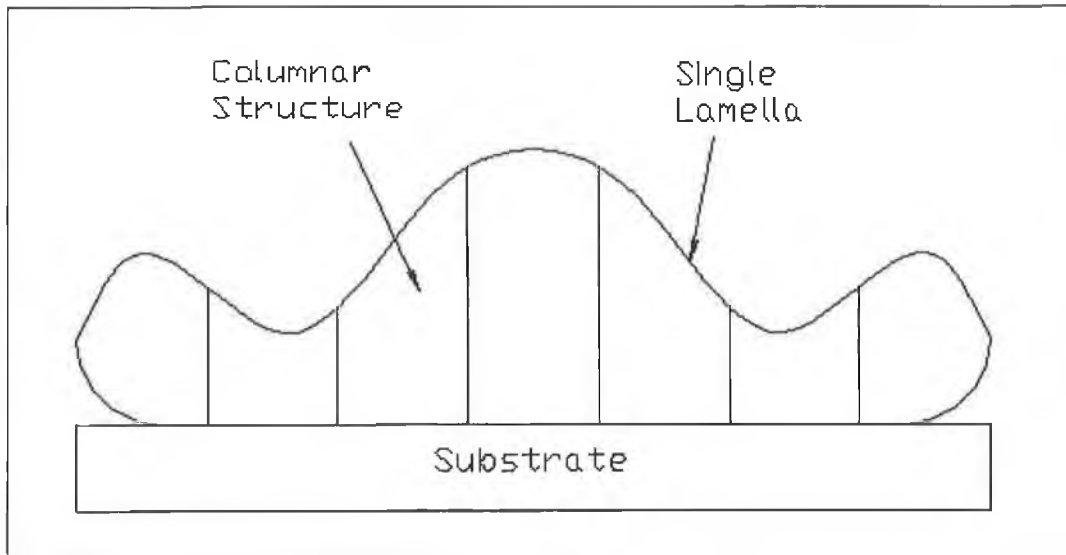
Figure 2.7: Cross-section of a columnar structure (single lamella) formed after solidification.

The coating is a build-up of individual particles that strike the substrate. Particles can be fully or partially melted at the moment of impact, depending on the relative difference between their melting temperature and the flame temperature. Rate of heat transfer from the flame to the particles also effects degree of melting of coating material. The solid particles may rebound or remain weakly connected to the rest of the coating, resulting in lower bond strength. That is why careful optimisation of the spray parameters is necessary to eliminate such problems. Generally, the spray gun is allowed to make several passes across the work piece in order to build-up a coating. The first pass of the gun deposit the first layer. It (first layer) composes usually of 5-15 lamella depending on the processing parameters [44]. This layer may be subjected to oxidation (for oxidizable material) and cooling. On the second pass, the first layer (which may be partially solidified) cools the second layer due to the temperature difference between the two layers. The final coating may comprise of a number of passes of the deposited material. Afterwards, the coating is allowed to cool down to the room temperature.

2.5.3 Residual Stress

One of the most important problems in the build-up of thermally sprayed coatings is the formation of residual stress, especially in the development of thick coatings [79-81]. In the HVOF thermal spraying process, individual molten or semi-molten particles impinge the substrate or pre-existing molten material at high speed. Thus despite their low mass, they cause certain deformations to the pre-existing material. The impingement of each particle incurs stress fields, which depend upon the solid state of the pre-existing material. In addition to the mechanical effects of impact, the temperature effects are also relevant to stress development. In the combustion chamber of the HVOF gun, each particle is heated and then projected towards the substrate. On impacting the substrate, the particles deform into lamella and cool down to their melting temperature and solidify. The temperature decrease experienced by the particles is immense. This leads to the formation of stress in each lamella. Phase transformation stresses can also develop in thermally sprayed coatings if phase transformation occurs during processing [44]. There are mainly two mechanisms of residual stress development in thermally sprayed coatings, quenching and cooling.

Quenching Stress

According to Pawlowski [44], as many as 5 to 15 lamellae exist in a single pass of spray. As the lamellae solidify they contract, but are constrained by each other, and by the substrate, thus generating high tensile stresses in the individual lamellae as shown in figure 2.8. Tensile quenching stress is unavoidable and may be estimated by the following:

$$\sigma_q = \alpha_c \, (T_m - T_s) \, E_c \qquad \qquad \text{Equation 2.2}$$

Where

$\sigma_q =$ quenching stress (Pa)

$E_c =$ elastic modulus of the coating (Pa)

$\alpha_c =$ coefficient of thermal expansion of the coating ($/^0C$)

$T_m =$ melting temperature of individual lamella (^0C)

$T_s =$ temperature of the substrate (^0C)
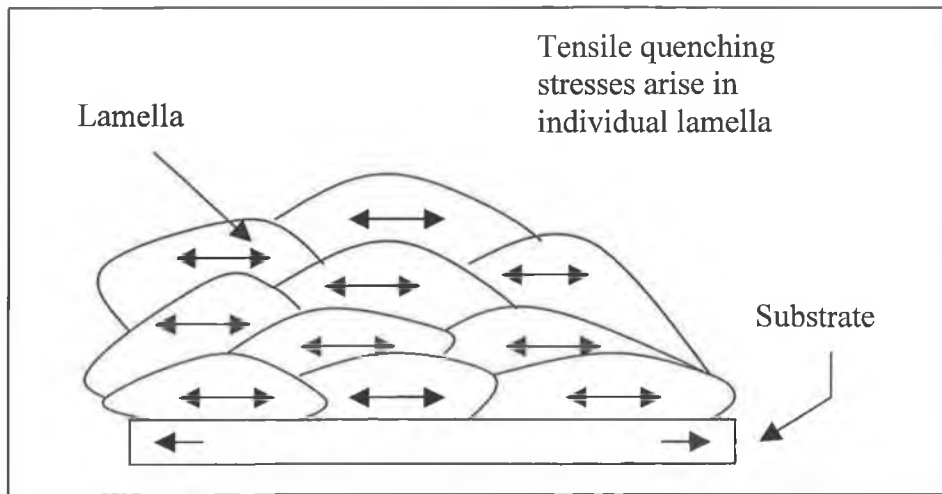
Figure 2.8: Schematic of quenching stresses adopted from [22].

For the deposition of aluminium/tool-steel functionally graded coatings, the substrate is initially preheated to 50 ^{0}C. But due to the effect of flame just before the deposition of first lamella, temperature of the substrate increases up to 500 ^{0}C, as shown in figure 2.9. At this temperature the substrate expands. The temperature of the particle is around 3000 ^{0}C when it exists the gun.
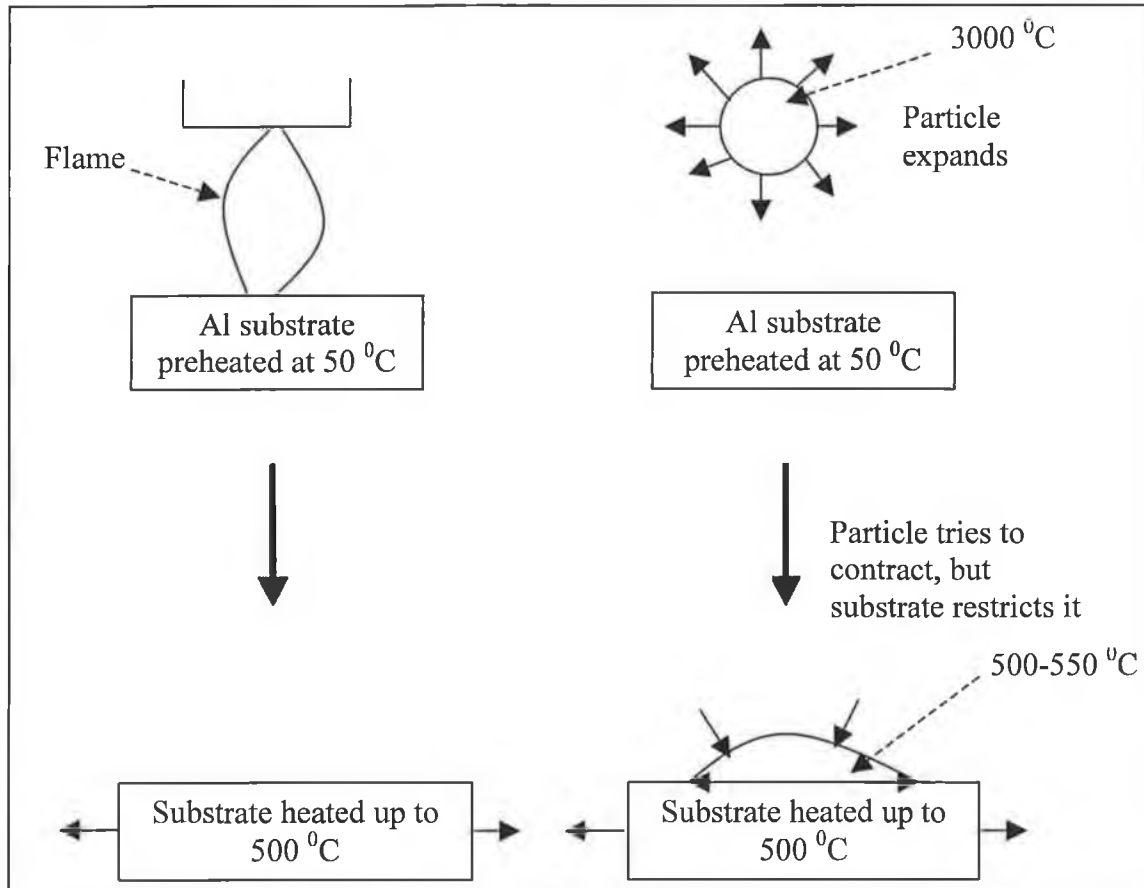
Figure 2.9: Change of state of substrate and particle during coating deposition.

But at the impact with the substrate, it is quenched to 500 ^{0}C due to the temperature difference between the particle and the substrate. Here it tries to contract, but is constrained by the substrate. The other particles are then deposited and are constrained by each particle and go through the same quenching cycle like the first particle. The final coating is built-up of individual particles that strike the substrate or pre-existing lamella as shown in figure 2.8.

Development of quenching stress through different layers of a five layer aluminium/tool-steel graded coating (explained later) is predicted by adopting a mechanistic model of stress development described by Stokes [22]. The Young's modulus and co-efficient of thermal expansion of the aluminium and tool-steel are adopted from [82-84] as shown in table 2.5. Those values for the interlayers were calculated using the "Rule of Mixture", as used by some other researchers including [23,85]. Quenching stress may be estimated by the following equation [86]:

$$\sigma_q \cong \alpha_c \Delta T E_c \qquad \qquad \text{Equation 2.3}$$

Where, σ_q is the quenching stress. Temperature difference (ΔT) between the lamella melting temperature and the substrate is approximately the same throughout the quenching cycle, hence equation 2.3 can be written as,

$$\sigma_q \propto \alpha_c E_c \qquad \qquad \text{Equation 2.4}$$

Using equation 2.4, the qualitative quenching stresses for the different layers are predicted and are shown in figure 2.10. Figure 2.10 shows that the quenching stress increases from layer 1 to layer 4 and then it decreases in layer 5 for aluminium/tool-steel functionally graded system. This is because from layer 1 to 5, the stiffness of the deposit increases, while the co-efficient of thermal expansion decreases. Hence at some point a maximum quenching stress is reached and this occurs in layer 4.

Table 2.5: Young's modulus and co-efficient of thermal expansion of different layers of a five layer aluminium/tool-steel graded coating [82-84].

Layer No	Young's Modulus, E (GPa)	Co-Efficient of Thermal Expansion, α (/^{0}C)
1	69	23.60×10^{-6}
2	101.25	20.55×10^{-6}
3	134.5	17.20×10^{-6}
4	167.25	14.45×10^{-6}
5	200	11.40×10^{-6}
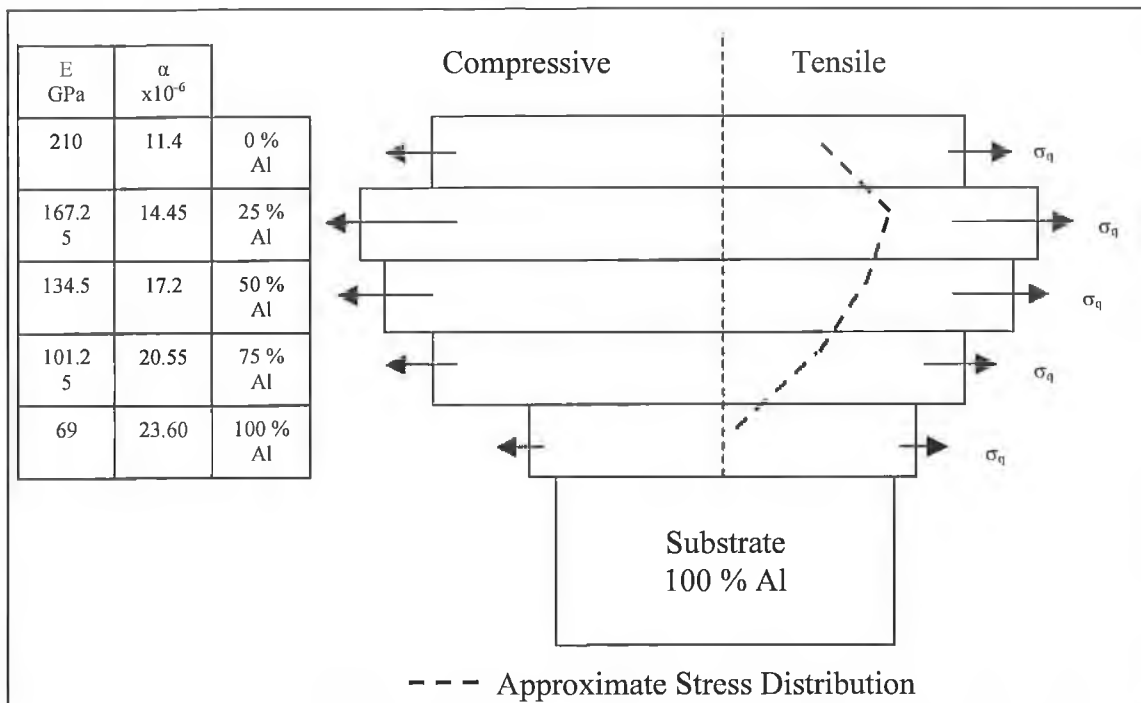
Figure 2.10: Qualitative quenching stress development in aluminium/tool-steel functionally graded coating.

Cooling Stress

When deposition is ceased or interrupted, cooling stresses generate, mainly due to the thermal expansion co-efficient mismatch between the substrate and the coating material. If the coating contracts to a greater extent than the substrate ($\alpha_c > \alpha_s$), a tensile stress generated in the coating [44]. This may lead to adhesion loss and cracking of the coating [87]. If the co-efficients are equal, then no cooling stress will develop. If the coating contracts by a smaller amount than the substrate ($\alpha_c < \alpha_s$), the resulting cooling stress will be compressive as shown in figure 2.11 [44]. The cooling stress can be estimated using the following equation [86,88-90]:

$$\sigma_c = \left[\frac{E_c \left(T_f - T_R \right) \left(\alpha_c - \alpha_s \right)}{1 + 2 \dfrac{E_c t_c}{E_s t_s}} \right]$$

Equation 2.5

Where

σ_c = cooling stress (Pa)

E_c = Young's modulus of the coating (Pa)

E_s = Young's modulus of the substrate (Pa)

α_c = coefficient of thermal expansion of the coating ($/^0C$)

α_s = coefficient of thermal expansion of the substrate ($/^0C$)

t_c = thickness of the coating (m)

t_s = thickness of the substrate (m)

T_f = deposition temperature (^0C)

T_R = room temperature (^0C)
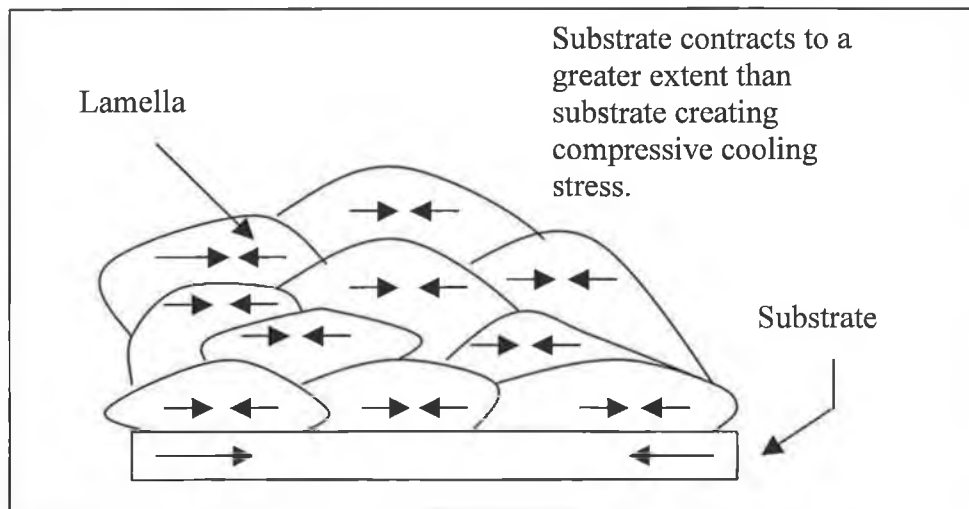
Figure 2.11: Schematic of cooling stresses adopted from [22].

Like quenching stress, development of cooling stress through different layers of a five layer aluminium/tool-steel graded coating is predicted by adopting the mechanistic development described by Stokes [22]. Cooling stress is predicted using equation 2.5. For a particular coating-substrate system, the coating thickness (t_c), substrate thickness (t_s), deposition temperature (T_f) and room temperature (T_R) are constant. Then equation 2.5 can be written as:

$$\sigma_c \propto \frac{E_c(\alpha_c - \alpha_s)}{1 + 2\frac{E_c}{E_s}}$$

<div align="right">Equation 2.6</div>

Using equation 2.6, the qualitative cooling stresses for the different layers are predicted and shown in figure 2.12. There is no cooling stress in layer 1 as this layer contracts by the same amount as that of the substrate (both have same E and α), while the cooling stress increases compressively from layer 2 to layer 5.
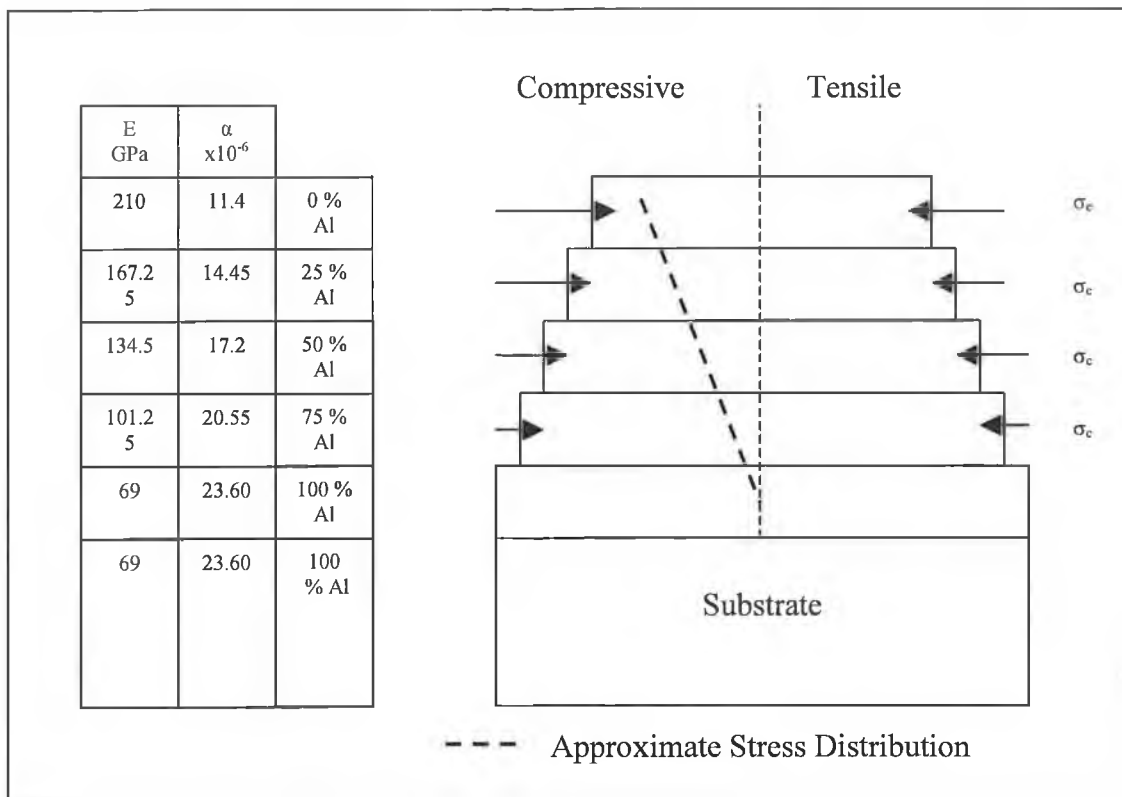
Figure 2.12: Qualitative cooling stress development in aluminium/tool-steel functionally graded coating.

Both the quenching and cooling stresses may be different to that predicted, as the Young's modulus and co-efficient of thermal expansion values for each layer may be different realistically from the values used here (derived from the Rule of mixture).

The nature of the overall residual stress may be determined by the following criteria [44]:

a) $\alpha_c < \alpha_s$ stresses in the coating may be either tensile or compressive,

b) $\alpha_c = \alpha_s$ stresses in the coating are tensile,

c) $\alpha_c > \alpha_s$ stresses in the coating are tensile.

The combination (summation) of the quenching + cooling stress produces what known as the residual stress. The possibility of either tensile or compressive residual stress when $\alpha_c < \alpha_s$ arises if the compressive cooling stress is less or greater than that of the tensile quenching stress [44]. If cooling stress is greater, then the resultant stress is compressive, and if it is less then the residual stress is tensile. Through appropriate selection of the coating and substrate material, high tensile quenching stress can be negated by the compressive cooling stress. Generation of residual stress increases with an increase in coating thickness thus results in lower bong strength of the coating [91].

2.5.4 Coating Structure and Properties

The deposit surface profile development depends on the coating structure and adhesion of the coating material to the base material [92]. A typical traverse section of a single-pass spray deposit has a conical profile, with the majority of the spray deposit concentrated around the central section [52]. Figure 2.13 shows a schematic section of a deposit in sequence A-B, B-C, C-D, where A is the periphery of the deposit, while D is the centre. The particles in the outer periphery tend to be widely spaced and poorly adhered to the substrate, while the most dense and thickest coating is deposited between C and C. The section B-C, is the transition from a dense coating to a porous coating structure. The edge sections (A-B) are extremely porous.

27
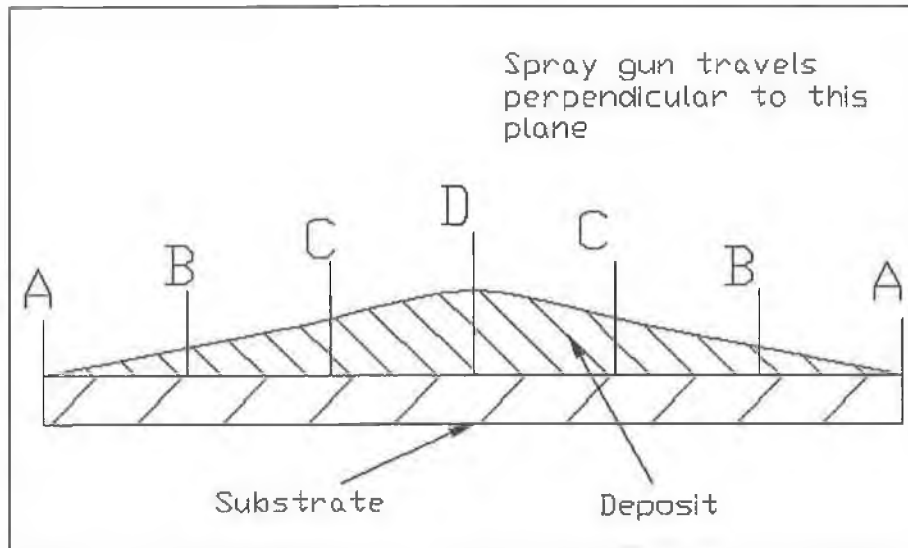
Figure 2.13: Schematic section of a spray deposit [22].

Thermal spraying has the ability to produce coating properties to suit the application required. Materials may be sprayed to create a hard or soft, dense or porous coating, thus it is difficult to report the typical coating properties. This report concentrates on functionally graded deposits; hence the properties of the coating will be discussed in section 2.7.2.

2.6 FUNCTIONALLY GRADED MATERIALS (FGM)

Functionally graded materials are those materials used to produce components featuring engineered gradual transitions in microstructure and/or composition, the presence of which is motivated by functional performance requirements that vary with location within a part. With functionally graded materials, these requirements are met in a manner that optimises the overall performance of the component.

Functionally graded materials have the potential to improve the thermomechanical characteristics of a component in several ways [93]:

1. The magnitude of the thermal stresses (residual stresses) can be minimised
2. The onset of plastic yielding and failure can be delayed for a given thermomechanical loading by decreasing the magnitude of thermal stress below the yield stress of the material
3. Severe stress concentrations at intersections between free edges and interfaces can be suppressed
4. The strength of interfacial bond between dissimilar solids, such as a metal and a ceramic, can be increased by introduction of continuous or stepwise gradations in composition as compared to a sharp interface
5. The driving force for crack growth along an interface can be reduced by tailoring the interface with gradients in mechanical properties
6. Gradients in the composition of the surface layers can be tailored to suppress the singular fields, which arise at the root of sharp indentations on the surface, or to alter the plastic deformation characteristics around the indentation

Functionally graded materials can be manufactured in two main ways [93]. Their names and classifications are shown in table 2.6 and described in the following sections.

Table 2.6: Names and classifications of different types of FGM
manufacturing processes.

(a) Constructive Processes	(b) Transport-Based Processes

1. Powder densification processes
2. Coating processes
3. Lamination processes
4. Deformation/martensitic
   transformation
	1. Mass transport processes
	2. Thermal processes
	3. Setting and centrifugal separation
	4. Macrosegragation and segragative
	   darcian flow processes

2.6.1 Constructive Processes

(1) Powder Densification Processes

Conventional solid-state powder consolidation, liquid phase sintering, infiltration and reactive powder processes are the different methods of producing FGM using powder densification process. In the solid-state powder consolidation process a preform body of powder (volume of powder) containing the desired volume fraction gradient (layers of graded amount of powders) is first produced. The powder preform is then densified following conventional solid-state procedures, by cold pressing and pressureless sintering, by hot isostatic pressing or by hot pressing in a cold die as shown in figure 2.14 [93].
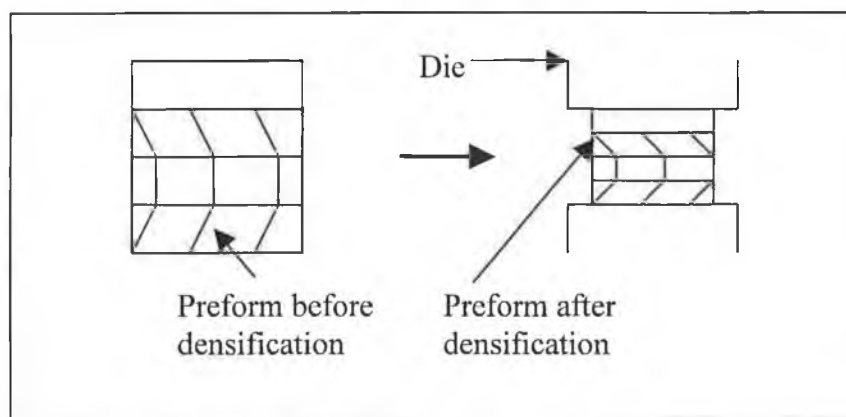
Figure 2.14: Schematic of the solid-state powder consolidation process.

In liquid phase sintering, powder compacts are heated to a temperature that is sufficiently high for a liquid phase to appear in the preform. It is an attractive process owing to the much more rapid densification, than that can be achieved in solid phase

sintering. The main drawback of the liquid phase sintering is that, the presence of a liquid phase permits motion of the liquid and solid phases relative to one another at fairly high rates [94].

Infiltration is a different liquid/solid FGM processing route that involves producing a preform of a more refractory phase, with a porosity gradient. This preform must then be infiltrated with the less refractory phase in its molten state to convert it to a FGM. The more refractory phase must not be soluble in the liquid and it must be sufficiently percolating to stand on its own weight before infiltration. The refractory phase must also resist compression by the metal during the pressure-assisted infiltration. There is no tendency towards homogenisation of the refractory phase by diffusion or motion within the liquid. This is a significant advantage over liquid phase sintering. Infiltration of graded preforms has been explored towards the production of automotive components, featuring graded transitions from aluminium to a certain reinforced aluminium at surfaces forming the combustion chamber [93].

In the reactive powder process, two or more phases are caused to react exothermally, sustaining the reaction with the heat that is released. Since these processes are based on powder preforms, combustion processes can produce functionally graded materials by spatial variation of the initial reactant distribution. Combustion synthesis has been explored for over thirty years and its utility has been demonstrated with a wide range of refractory materials and composites [95-97]. A common problem of this route is the presence of porosity in the resulting material due to gas evolution and also to incomplete sintering when product phases are not liquefied by the heat that is evolved.

(2) Coating Processes

Coating processes, in which the graded and outer layers are deposited onto a pre-fabricated bulk component, are very attractive in a large class of application of FGM. Functionally graded layers can serve as an optimal transition between a bulk component and an outer layer that protects the remainder of the component from harsh conditions of temperature, corrosion, or erosion in the external service environment of the component. Different coating techniques producing FGM are described in section 2.7.

(3) Lamination Processes

Lamination process is a constructive process of producing FGM, whereby dense layers are stacked and bonded to form a graded structure. Some researchers produced graded cutting tools by brazing together individual layers of TiC/Ni-Mo cermets with TiC percentage varying from 95 to 86 percent [98]. In another study, lamination processes developed for the production of superfine metal/metal composite structures were modified for the production of graded structures [99]. The process involved the stacking of a large number of foils, followed by diffusion bonding and cold rolling. By varying the relative thickness of the foils used across the structure, variation in phase volume fraction and layer widths, and hence in local properties, were produced across the rolled material.

(4) Deformation/Martensitic Transformation

A martensitic transformation can provide, by the strain changes that accompany it, an additional deformation mechanism, called transformation plasticity. The amount of martensite formed at constant temperature by this mechanism increases with stress, and with the amount of strain in the material. As a consequence, imposing strain gradient in materials within the proper temperature range can produce gradients of stress induced martensite volume fraction. Watanabe et al. [100] produced continuous variations in the volume fraction of ferromagnetic α martensite within specimens of paramagnetic austenitic and 18-8 stainless steel. This process is a simple method for one step production of materials containing variation in saturation magnetism, which is of potential use for the fabrication of position measuring devices [100].

2.6.2 Transport-Based Processes

(1) Mass Transport Processes

Diffusion from the surface and interdiffusion are variations of mass transport based processes producing functionally graded materials. The first method includes surface hardening of steel by carburisation or nitriding that involves transport of carbon and

nitrogen atoms at the outer surface of a component to create a hard peripheral case, gradually transitioning to a tougher and softer core [93]. Thus most transport based surface hardening processes in steel are based on diffusion of interstitial carbon and nitrogen atoms. The diffusion constants are sufficiently high for these atoms to enable creation of macroscopic layers enriched with these species after exposure for practical times to an environment, which contains carbon and/or nitrogen with a chemical activity higher than that in the bulk of the component. Nitrogen can also be introduced into the steel by ion implantation, whereby ions of high energy are driven into a substrate material under high vacuum.

Interdiffusion is the second type of mass transport based process of producing graded materials in which appropriate range of intermediate solubilities or phases are obtained between the junctions between two phases. This process has been used for centuries in steel, for example in creating gradients in swords, such as the famous Japanese Samurai swords [101].

(2) Thermal Processes

In the thermal processes, heat is conducted at sufficient speed into the materials so that it can be used to create gradients in the materials properties. Variations in thermal treatment cause variations in microstructure and local properties. Again hardenable steel is a prime example of thermally processed FGM because of its strong dependence of its properties on the thermal history. In fact it can be said that any hardenable steel component, which is quenched from a uniform elevated temperature in the austenitic range, contains a graded transition from a hard outer layer to a softer core. The location of this transition, and its extent, can be controlled to a significant degree by alloy control (by referring to a database of steels with varying properties as a result of various heat treatment) [93].

(3) Setting and Centrifugal Separation

Setting and centrifugal separation is another type of transport-based process of producing FGM. It involves production of a suspension of particles of one phase in a liquid matrix of the other, followed by separation of solid and liquid, by holding the slurry in gravity, or using applied centrifugal force. A well-explored application of this

processing route is with metal matrix composite slurries produced by stir-casting technique, typically of SiC particles in molten aluminium [93]. Fishing boat cable pulleys have been produced at near-commercial scale by centrifugal casting of such components, to demonstrate their excellent performance. With similar slurrys, gravity has also been used to produce property gradients in various experimental components [93].

(4) Macrosegregation and Segregative Darcian Flow Processes

Macrosegregation and segregative flow process is the last method of producing FGM using transport-based process. When an alloy is solidified such that the solid grows along a well defined, essentially planar surface, alloying elements partitioning along the solid/liquid interface causes the formation of macroscopic gradients within the solid phase. When the phase diagram is such that the solid contains less solute than the liquid, solute is rejected from the liquid/solid interface towards the liquid because solute diffusion through the solid is very slow. Conversely, if the solidus composition is higher than the liquidus composition, solute diffusion takes place through the liquid towards the solidification front as the solid grows [93]. This solute migration process causes gradual alteration in the composition of the liquid bath as the solidification front advances. In turn this alterations in liquid composition causes changes in solidification time in the composition of the solid that is grown, such that the material that is finally formed contains a solute gradient that extends along its length in the solidification direction.

2.7 FUNCTIONALLY GRADED COATINGS

A functionally graded coatings is one in which the composition, microstructure and properties vary gradually from the bond coat to the top coat [102]. An example of a graded coating of material A and B is shown in figure 2.15.
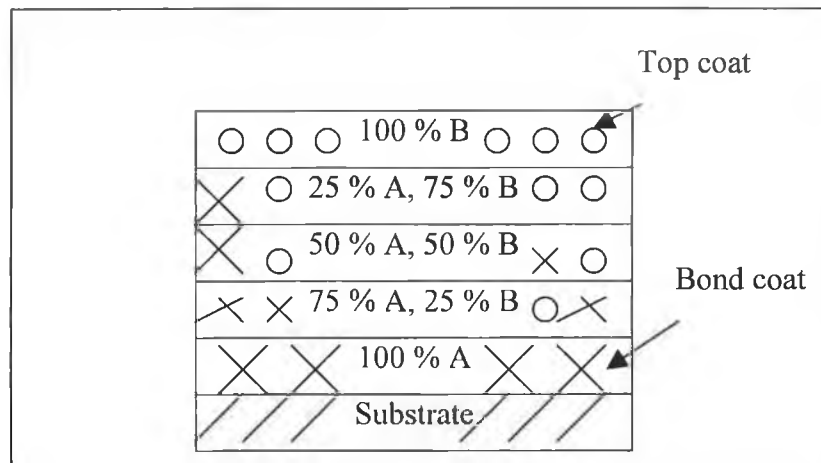
Figure 2.15: Functionally graded coating of material A and B.

The bond coat is 100 % A and the top coat is 100 % B. The percentage of material A is decreased from the bond coat to the top coat, while the percentage of material B is increased from the bond coat to the top coat. Gradual changes in the composition and microstructure result in gradual changes in the elastic modulus and thermal expansion coefficient [24]. This in turn reduces coating residual stresses and stresses induced during heating and cooling as shown in equations 2.2. Residual stresses also decrease with an increase in number of graded layers [91,103]. So a duplex coating (two layers) has a higher residual stress than a layered coating (more than two layers) of same thickness.

2.7.1 Different Techniques Producing Functionally Graded Coatings

The first development of functionally graded coatings was carried out in Japan in 1987 using the CVD (Chemical Vapour Deposition), PVD (Physical Vapour Deposition) and Plasma thermal spraying processes [104]. Since then some other techniques are used to manufacture graded coatings. Some of them are described in the following sections.

(a) Plasma Spraying Process

So far the Plasma spraying is mostly used both in industry and in research for the production of FGM [105, 106]. Three processing methods exist for plasma spray processing of graded coatings [105]:

1. Single torch system, utilizing multiple feeders
2. Multiple torch system, employing independent feeding system for each torch
3. Single torch and single feeder system with process combinations or using pre-mixed powders

Single torch system with dual feeders was used by several researchers in producing functionally graded coatings [23,107-111] as shown in figure 2.16. Deposition rates of Mo-Mo_2C and stainless steel powders were measured prior to the deposition of graded coating by Sampath et al. [109]. Based on those measurements, the powder feed rate and number of passes were adjusted to obtain the required phase content and thickness of each layer. Kesler et al. [23] produced two types of graded coatings on steel substrate. The first type consisted of Ni and Al_2O_3, while the second one was a graded coating of NiCrAlY and YSZ (Yttria-Stabilized Zirconia). In the first system the bond coat was 100 % Ni and the top coat was 100 % Al_2O_3, with the interlayers containing different proportions of those two powders. In the second system, the bond coat was NiCrAlY and the top coat was YSZ with the interlayers containing different proportions of NiCrAlY and YSZ. The composition of the different layers of graded coatings was varied by adjusting the feed rates of the two different powders contained in two different feeders. Kim et al. [110] manufactured graded coatings of W (Tungsten) and Hf (Hafnium) on W substrate with W and Hf forming alternate layers. The powders were fed to the plasma gun alternately from two different feeders. W/Hf graded coatings gave better compressive strength than tungsten/steel (non-graded) samples. Mateus et al. [111] manufactured Al_2O_3-TiO_2/Perfluorinated Vinylether (PFA) composite coatings on aluminium-based alloy using the plasma spraying process. Due to the differences between the thermal characteristics of ceramic Al_2O_3-TiO_2 and organic PFA powders, the two powders were injected separately into the plasma jet. The ceramic powder was injected into the hottest part of the flame, while the organic powder was injected into the colder area of the jet in order to favour the melting of ceramic powder without degrading the organic one (figure 2.17).
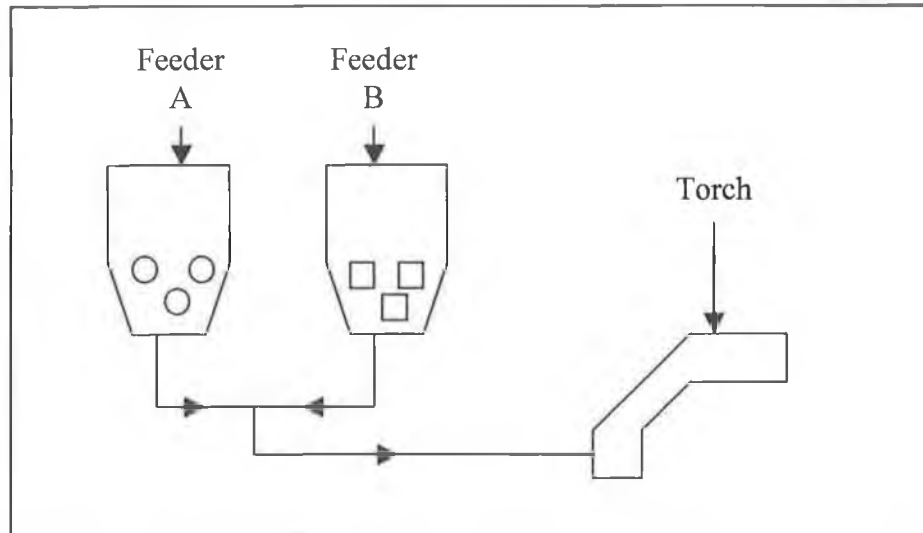
Figure 2.16: Schematic of a single torch and dual feeder system for the production of functionally graded coatings.
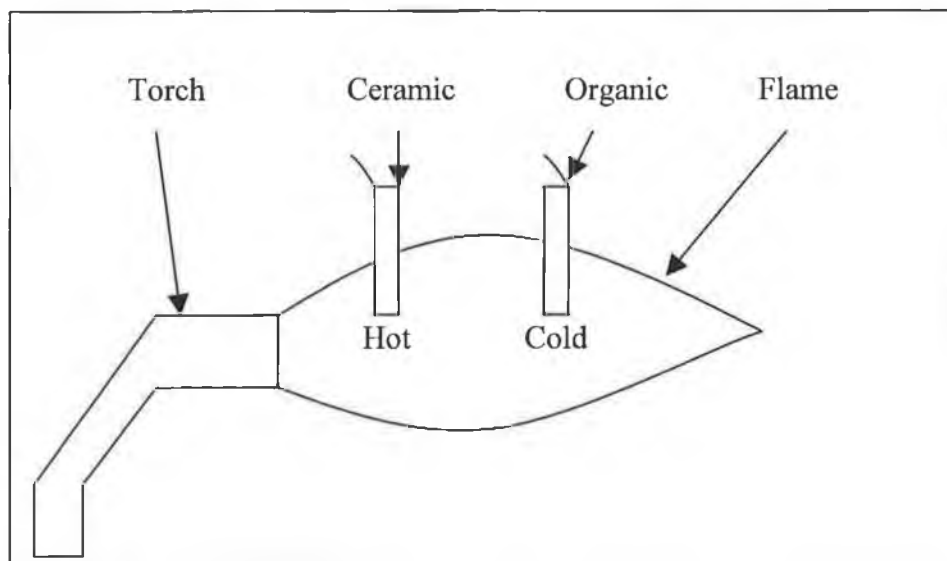
Figure 2.17: Injection of the ceramic and organic powders in the hottest and colder part of the flame respectively.

Using pre-mixed powders and a single torch is another way of producing graded coatings, used by [112-118] as shown in figure 2.18. Initially powder mixture 1 was put into the feeder and sprayed onto the substrate to produce the first layer. Subsequently the rest of the mixtures were put into the feeder one after another and deposited onto the substrate separately to deposit the rest of the layers of graded coatings. Figure 2.18 shows only the deposition of the first two layers. Khor et al. [113,114] used planetary ball mills to mill blended powders mixtures of different proportions of NiCoCrAlY and

YSZ powders. The powder mixtures were then dried in a furnace and agglomerated and spheroidized in distilled water. Finally they were put into the plasma gun to produce different layers of graded coating on Ni substrate. The bond coat was 100 % NiCoCrAlY and the top coat was 100 % YSZ with three different interlayers. Hu et al. [115] used high pressure hydrogen reduction process to produce pre-mixed powders of Ni and Y_2O_3 stabilized ZrO_2 of different composition. Those powders were then plasma sprayed to produce graded coatings on Ni substrate. Ni was used as the bond coat and ZrO_2 was used as the top coat. The interlayers consisted of different proportions of Ni and ZrO_2. Cetinel et al. [117] manufactured $NiCrAl/MgZrO_3$ functionally graded coatings on AISI 304L Stainless Steel substrate using the plasma spraying process. Premixed powders of different proportions of NiCrAl and $MgZrO_3$ were used to produce the interlayers of graded coatings. The bond coat was 100 % NiCrAl and the top coat was 100 % $MgZrO_3$. Yin et al. [118] produced Fe_3Al/Al_2O_3 functionally graded coatings using the plasma spraying technique. Fe_3Al powder was initially ball-milled and sieved. It was then blended with different proportions of Al_2O_3 powder to manufacture the interlayers of graded coatings. The bond coat was 100 % Fe_3Al, while the top coat was 100 % Al_2O_3. All of the above authors recognised the advantages of producing functionally graded coatings, in the resulting properties of the deposits.
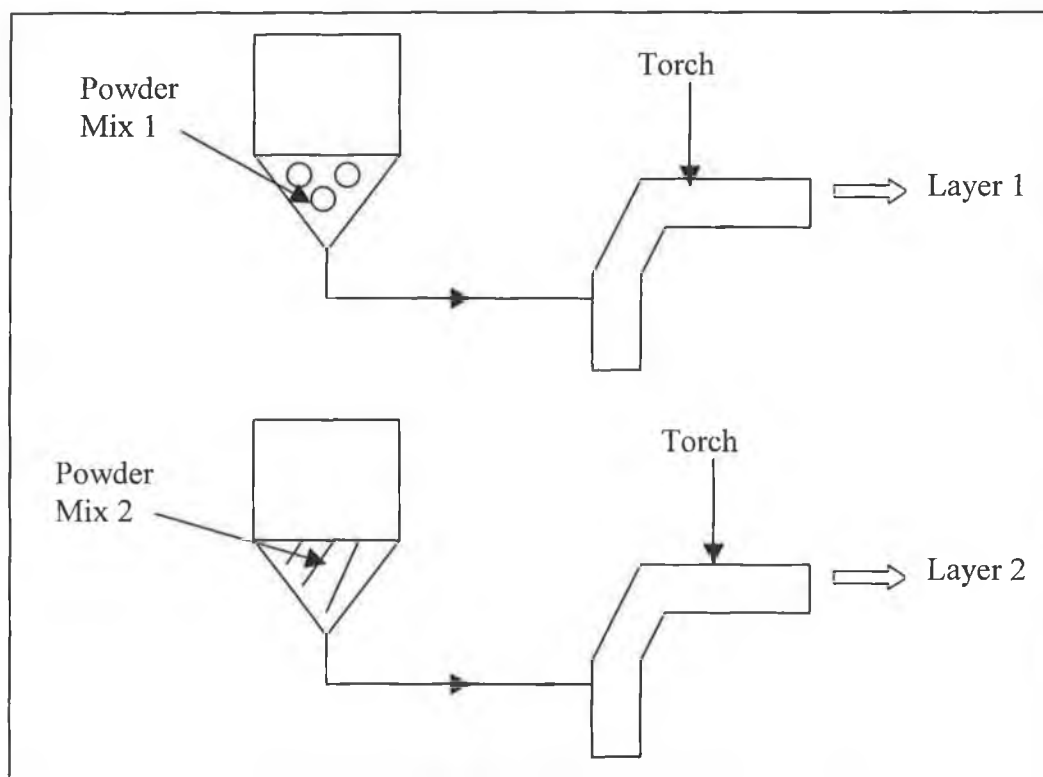
Figure 2.18: Schematic of the production of graded coatings using pre-mixed powders and a single torch.

Low pressure plasma spraying (LPPS) is another variation of the original plasma spraying technique that was used in producing graded coatings. Hamatani et al., [119] manufactured NiCr/YSZ graded coatings using the LPPS. The composition of the different interlayers was varied by using different flow rates of the two powders. The bond coat was 100 % NiCr and the top coat was 100 % YSZ. The plasma gas used was a mixture of hydrogen and argon. Hydrogen was added to argon in order to increase the overall plasma enthalpy at a fixed discharge current and to increase the plasma thermal conductivity.

(b) Physical Vapour Deposition (PVD) and Chemical Vapour Deposition (CVD)

In Physical Vapour Deposition (PVD) and Chemical Vapour Deposition (CVD) process, the coating material is deposited onto the substrate in the form of ions. Only thin coatings (μm range) can be deposited using these processes. This is the main limitation of CVD and PVD compared to thermal spray processes. However metals, alloys as well as refractory compounds can be deposited using CVD and PVD processes [120]. Several researchers used these processes to manufacture functionally graded coatings, including [121-125]. Koch et al. [121] used hollow cathode arc discharge plasma to produce graded coating of C-H and aluminium on aluminium and steel substrates. Hydrocarbon precursor gas (CH_4 or C_2H_2) was introduced into the plasma to deposit C-H layers. Pinkas et al. [122] used reactive magnetron sputtering to produce TiAl-N graded coatings. The graded composition was achieved by varying the power supplied to the aluminium targets. W-C graded coatings on steel substrates were manufactured by Harry et al. [123]. Different interlayers of those coatings consisted of different proportions of carbon. He et al. [124] produced graded coatings of aluminium and stainless steel on stainless steel substrate using the co-sputtering and magnetron sputtering techniques. The whole deposition process was divided into three stages. In the first stage, radio frequency power was applied to stainless steel target to deposit a thin layer of stainless steel on stainless steel substrate. In the second stage, a smaller proportion of RF power of 7 % total output energy was introduced into aluminium target, while in the last stage the power on aluminium target was increased to 14 % of total output. The thickness of the total coating deposited was in the range of 2.5-3.0 μm. Choy [125] used close field unbalanced magnetron sputtering to produce functionally

graded protective C/TiC/Ti coatings on SiC fibres. The graded intermediate layer was deposited using an additional Ti target in parallel with C targets in a C_4H_{10} atmosphere.

EB PVD (Electron Beam Physical Vapour Deposition) is a variation of the simple PVD producing graded coatings. Several researchers used this technique to produce graded coatings including [126-131]. Movchan [126] and Hongbo et al. [127] initially made a composite ingot. Different portions of that ingot contained composites of different compositions. The electron beam is focused onto those composites to evaporate and deposit them (composites) onto the substrate. Marinski et al. [128] and Gong et al. [129] produced different ingots of different compositions. The gradation was obtained by selective evaporation from those ingots. Gust et al. [130] produced Ti-Ni graded coatings onto silica glass. Their procedure involved the making of Ni and Ti cathodes. Graded coatings were obtained by changing the discharge power, thus changing the discharge current to those cathodes. Guo et al. [131] manufactured NiCoCrAlY/Al_2O_3-YSZ graded coatings using three different ingots of NiCoCrAlY, Al_2O_3 and YSZ. The bond coat was 100 % NiCoCrAlY, which was deposited initially by evaporation from the relative ingot. Different interlayers were then deposited from Al_2O_3 and YSZ ingots by controlling the feed rate and the evaporating electron beam current to those ingots. The top coat was 100 % YSZ, which was obtained by evaporation of the YSZ ingot only.

There are also hybrid processes of the PVD known as the Plasma Enhanced Chemical Vapour Deposition (PECVD) process. Initially metal and/or ceramic atoms were evaporated and ionized into a dense plasma. That plasma was subsequently deposited onto a substrate. In order to manufacture graded coatings, different gasses (for example C_2H_2) were introduced into the plasma during deposition process [132,133].

(c) Laser Cladding

Functionally graded coatings are being manufactured using the laser cladding by many researchers [134-136]. West et al. [134] produced graded coatings of Ni-Al and Fe-Al on nickel base and low carbon steel using a laser. Separate feeders were used to feed different proportions of Al and Ni in the case of Al-Ni and Al and Fe in the case of Fe-Al to form layers of the graded coatings. A 2 kW CO_2 laser operating at 1.8 kW laser power, was used during deposition. Levin et al. [135] used a continuous CO_2 laser with

a maximum power of 10 kW to manufacture graded coatings of WC. A M2 high speed tool steel was used as substrate. Different proportions of W and carbon were premixed. A common feeder was used to feed the premixed mixtures onto the laser. Pei et al. [136] produced graded coatings of AlSi40 via laser cladding. They used aluminium based alloys as their substrates.

(d) Other Techniques

Reaction diffusion [137], powder metallurgy [138], wet chemical method [139], electroforming process [140] and slurry dipping are some other techniques used in producing functionally graded coatings. Tomota et al. [137] manufactured $FeAl_3$ graded coatings on pure Fe and carbon steel using the reaction diffusion process. The surface of the substrate was pasted with $FeAl_3$ along with a solvent. The substrate was then heated and then furnace cooled and quenched in water. Graded FGM of PSZ (partially-Stabilized Zirconia) and stainless steel was manufactured by Watanabe et al. [138] using the powder metallurgy process. The technique involved pressureless sintering and hot pressing methods in their research. Kumar et al. [139] manufactured graded coatings of HA-G-Ti composites on Ti substrate using the wet chemical method. Jun et al. [140] produced Ni-PSZ graded coatings using the sediment electrodeposition (SED) technique. Different layers of the graded coating were obtained by varying the quiescent period and weight percentage of PSZ in the bath. Slurry dipping is another method of producing functionally graded coatings [141]. Metal and/or ceramic powders were suspended in ethanol and milled by ball mill to get a slurry having an appropriate viscosity for dipping according to [141]. The substrate was dipped into the slurry, then withdrawn and dried. This process was repeated with slurries of different compositions to get graded layers (figure 2.19). The formed compacts were finally densified by hot isostatic pressing (HIP).
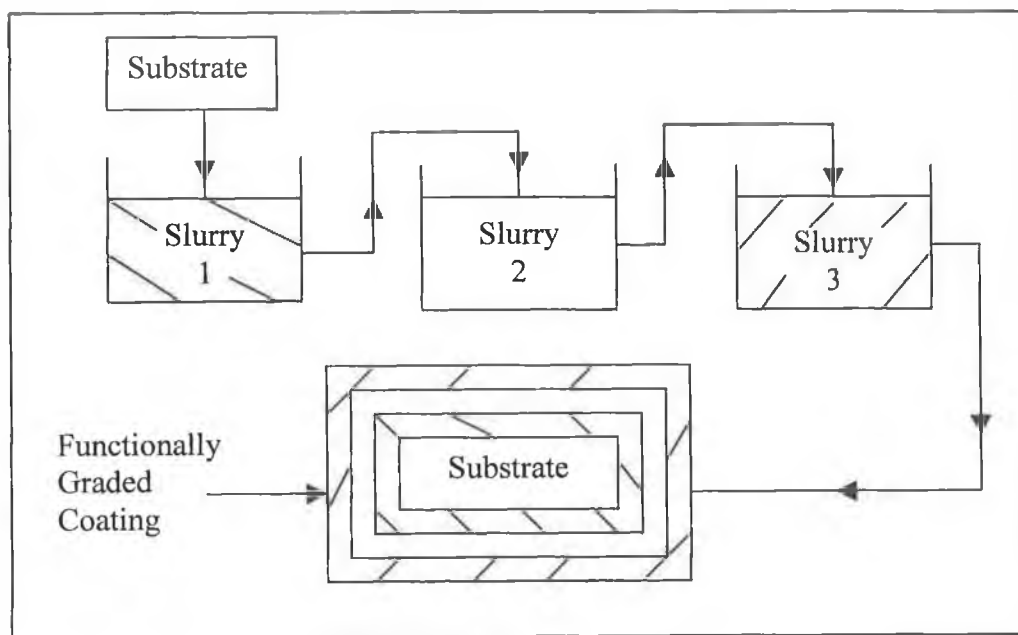
Figure 2.19: Schematic of the production of FGC using the slurry dipping process.

(e) HVOF Thermal Spraying Process

Production of graded coating using the HVOF spraying process is a recent idea. Sampath et al. [109] used HV 2000 HVOF system to manufacture graded coatings of WC-Co and stainless steel on a steel substrate. In this research two powder feeders were used for two different powders with a single gun. The feed rates of two powder feeders were changed to vary the proportion of the two powders to form different interlayers. The top coat was 100 % steel and the bond coat was 100 % WC-Co. HVOF sprayed coatings had denser microstructure, uniform phase distribution within the layers and lower wear rates than graded coatings produced by plasma spraying. Peters et al. [142] manufactured MCrAlY/Al_2O_3-YSZ functionally graded coatings using the oxy-acetylene HVOF (OSU) thermal spraying process. The bond coat was 100 % MCrAlY, interlayers consisted of different proportions of Al_2O_3 and YSZ with increased amount of Al_2O_3 from the second layer to the top layer, while the top coat consisted of 75 % YSZ and 25 % Al_2O_3. HVOF sprayed graded coatings had dense net-like structure, while plasma sprayed coatings had porous structure. As a result HVOF sprayed graded coatings yielded better wear and erosion resistance than the graded coatings produced by air plasma spraying (APS). Kim et al. [143] manufactured NiCrAlY/YSZ functionally graded coatings using the Detonation Gun HVOF thermal spraying process. An alternate spraying method of ceramic YSZ and metallic NiCrAlY was used in their project. Two powder feeders were utilised to carry two different powders. The bond

coat was 100 % NiCrAlY, while the top coat was 100 % YSZ. The interlayers consisted of different proportions of NiCrAlY and YSZ. The percentage of ceramic and metallic powders in the interlayers was varied by using different shot ratios of those powders. As an example, spraying with a shot ratio of 1:3 meant that spraying sequence consisted of three shots of metal powders followed by one shot of ceramic powder, resulted in a mixture of ceramics and metals with ceramic to metal volume ratio of 1:3. In the area overlapped by successive shots, an excellent mixture of ceramic and metal was produced. Functionally graded NiCrAlY/YSZ coatings gave better thermal shock resistance than duplex NiCrAlY/YSZ coatings.

Compare to other thermal spraying processes, the HVOF process is relatively new in producing functionally graded coatings. Previous research [109,142,143] showed that the HVOF process has the potential to produce graded coatings. They have reported better coating properties than the graded coatings produced by other techniques. But the range of materials used in the research to date has been limited to WC-Co, stainless steel (SS) and MCrAlY/Al_2O_3-YSZ. However, there is a large range of materials, which have potential to benefit from graded structure yet to be researched. The current study aims to contribute new knowledge in these areas by depositing aluminium/tool-steel functionally graded coatings on aluminium substrates using the HVOF process. Aluminium/tool-steel graded coatings could be used in the automotive and aerospace industry not only to decrease the weight of the automobiles and aeroplanes, but also to increase strength of the coated system, as is described in section 7.3. Also previous researchers used commercial separate powder feeders to deposit two different coating materials in producing graded coatings, which was costly. The current study aims to deposit graded coatings in a more cost effective way.

Thermal spraying can be used to produce inter layers of FGM coating in two methods:

a) Using premixed powder to produce each different layer or,
b) Co-injecting two different powders and varying their relative proportions during deposition.

Almost all the researchers, such as [112-116], used the former method while producing functionally graded coatings. However the latter method was used in this project.

2.7.2 Characteristics and Properties of Functionally Graded Coatings

The main characteristics of functionally graded coatings is the gradual change in coating structure, which results in gradual change in coating properties. Some of those properties, such as microstructure, hardness, corrosion resistance, porosity and residual stress are described below.

(a) Microstructure

Several researchers [108,115,144-150] have reported the gradual changes in microstructure of graded coatings. Hu et al. [115] reported gradual changes of structure from the Ni bond coat to the ZrO_2 top coat. Khor et al. [144-146] manufactured ZrO_2-NiCrAlY graded coatings by plasma spraying using premixed powders. From the NiCrAlY base layer to the ZrO_2 top layer, NiCrAlY changed its morphology from lamellar to a dispersed pattern, while the morphology of ZrO_2 was changed from a dispersed to a porous pattern. No clear interface between the two adjacent different layers was found. Sampath et al. [109] produced graded coatings of NiCrAlY/ZrO_2-Y_2O_3 by plasma spraying using a single torch and a two feeder system. It was also reported that there was a gradual change of coating structure from the NiCrAlY bond coat to the ZrO_2-Y_2O_3 top coat. Avci et al. [148] manufactured graded coatings of NiCrAl-MgZrO$_3$ from premixed powders using the plasma spraying. Again gradual changes in microstructure from the NiCrAl base layer to the MgZrO$_3$ top layer were observed. No distinct interfaces between the layers were found. Voevodin et al. [150] produced Ti-TiC-TiC/DLC (Diamond Like Carbon) functionally graded coating on steel substrate using the magnetron assisted pulsed laser deposition technique, and also reported gradual metal-carbide-DLC transition across the coating thickness.

(b) Hardness

Thermal spray coatings generally include voids and oxides within the coating, thus macro-hardness levels are less than those of the equivalent material in wrought or cast form. There are two ways to measure hardness, macro hardness test and micro hardness test. To determine the resistance of the total coating deposit to point penetration, macro hardness tests are carried out using either the Brinell or Rockwell hardness test. While micro-hardness tests are carried out at low loads on individual particles using, what is

known as the Knoop or Vickers hardness test [151]. Functionally graded coatings produce gradual variation of hardness throughout the coating thickness. Several researchers [103,108,109,115,137,144] have measured the hardness value of graded coating using different types of hardness tests. In each case hardness changed gradually from the base layer to the top layer of the coatings. Khor et al. [103,144] measured hardness values of a five layer graded coating and a duplex coating of same materials and reported almost same surface hardness values for the two types of coatings. But deposition thickness was different for the two cases. Thus it was not clear whether deposition thickness or number of layers had any effect on hardness values of graded coatings. In the current research, effect of deposition thickness and number of layers on hardness values of aluminium/tool-steel graded coatings is investigated.

(c) Corrosion Resistance

One of the applications of thermal spraying is to increase corrosion resistance to such materials as iron and steel [152]. Steel valves used in the marine industry are subjected to corrosion from salt water; hence failure of such component is inevitable over time. Tungsten carbide-cobalt coatings offer high corrosion resistance, therefore allowing a more serviceable substrate material.

FGM deposition is one way of increasing corrosion resistance of a substrate material. Evans et al. [153] reported increased corrosion resistance of overlay MCrAlY/Al graded coatings. The bond coat was NiCrAlY or CoCrAlY, the interlayers were heat-treated NiCrAlY or CoCrAlY and the top coat was an Al enriched β-NiAl. At high temperature, the top coat gave the component its corrosion resistance, while at low temperature the interlayer and bond coat provided corrosion resistance for the substrate.

(d) Porosity

Porosity or voids in the coating structure is an important issue in thermal spraying as it affects many other mechanical properties, such as bond strength [45]. Depending on the thermal spraying process utilized, porosity may vary from 0.1 to 15 of the volume percent. The HVOF process exhibits the lowest porosity among all of the thermal spraying processes due to its high particle impact velocity that compresses most air

pockets out of the microstructure [29]. Table 2.7 shows porosity results for various Diamond Jet HVOF coatings.

Table 2.7: Coating porosity in various Diamond Jet HVOF coatings [67,152].

Coating material	Porosity (%)
Nickel/Chromium Molybdenum Base Superalloy	1
Tungsten Carbide-Cobalt	<0.5
Cobalt Base Alloy	1.5
Chromium Carbide/ Nickel Chromium	1
Tool Steel	<1
Al_2O_3–$13TiO_2$	1.2

Because of the gradual structural changes from the bond top layer to the top layer, porosity in functionally graded coatings changes gradually through coating thickness as reported by Khor et al. [146,149]. The author [146] reported a gradual increase of porosity from the NiCoCrAlY base layer to the YSZ top layer. The same author [154] again reported gradual change of porosity from the Ti-6Al-4V base layer to the HA (Hydroxyapatite) top layer. In each case, the plasma spraying was used to deposit graded coatings.

(e) Residual Stress

Cooling residual stress, mentioned earlier occurs due to mismatch of properties between the substrate and coating and also between different layers of the coating. Co-efficient of thermal expansion (CTE) and elastic modulus are the two main properties causing cooling stress build-up in the coating. Graded coating is one way of reducing cooling stress as it reduces the difference of the CTE and elastic modulus between the substrate and coating and also between different layers of the coating. Several researchers reported gradual change in the CTE and elastic modulus including [24,109,113,155-157], which results in a reduced residual stress in coatings. Residual stress increases with an increase in coating thickness, while an increase in number of graded layers maintaining same thickness decrease residual stress [91,103].

2.7.3 Applications of Functionally Graded Coatings

Since its invention in 1987, functionally graded coatings have been applied to various fields and sectors to improve the performance of components. The most common application of functionally graded coatings is as thermal barrier coatings (TBC). Duplex thermal barrier coatings, consisting of a metallic bond coat and a ceramic top coat, are applied in diesel engines, gas turbines and aircraft engines to increase the service life of the component [158-161]. The metallic bond coat increases adhesion with the substrate, while the ceramic top coat reduces the temperature of the bond coat and substrate. But mismatch of properties between the bond coat and top coat induces cooling residual stress, which in turn causes delamination and spalling of duplex coatings [162,163]. Functionally graded coatings, consisting of a metallic bond coat, ceramic top coat and intermediate layers consisting of different compositions of ceramic and metallic materials, is one way of reducing delamination and spalling of thermal barrier coatings [103,113,115,144,164,165]. The bond coat increases adhesion with the substrate, the top coat reduces temperature of the interlayers and substrate, while the intermediate layers decrease residual stress.

Another important application of graded coatings is in the biomedical field. Several researchers report the use of functionally graded coatings in engineering [166-174]. Kon et al. [166] and Wang et al. [168] manufactured functionally graded coatings of calcium phosphate/titanium. The calcium phosphate top coat gave excellent biocompatibility, the titanium bond coat gave mechanical adhesion strength with the substrate, while the gradient interlayers decreased residual stress build-up and increased coating adhesion. Remer et al. [169] reported an improved bond strength of titanium/hydroxyapatite (HA) coatings, while Liu et al. [170] reported improved bond strength of Ni-P-PTFE coating by obtaining composition gradation in their coatings. Verne et al. [171] deposited bioactive glasses and particle reinforced composites on alumina substrate in order to combine mechanical properties of high strength alumina with the bioactivity of the coating. Graded structure in the coating was used to minimise the stress build-up. Khor et al. [154] manufactured hydroxyapatite/Ti-6Al-4V functionally graded coatings using the plasma spraying process. Hydroxyapatite (HA), which is widely preferred as the bioactive material in both dentistry and orthopaedics gave favourable osteoconductive and bioactive properties, titanium bond coat gave excellent strength to the coatings, while the interlayers decreased stress. Multilayered non-graded HA coatings have

already been manufactured using the HV 2000 HVOF process [175], so this process may be the next technique in producing functionally graded hydroxyapatite coatings, not only to reduce residual stress, but also to produce coatings suitable for biomedical applications.

The Automotive industry may be a potential field for the application of graded coatings. Weight reduction in automobiles is particularly important. The average vehicle weight is expected to increase, as the automobile industry continues to market new models with luxury, convenience, performance and safe cars as demanded by their customers [176]. According to the "European Transport Policy for 2010: time to decide", by 2010, the demand for mobility will increase in the EU by 24 % in the passenger domain [177]. Replacing the steel or iron parts by lightweight materials is a useful way of reducing vehicle weight. Several researchers [178-184] mentioned the importance of lightweight materials like aluminium, magnesium and titanium in the automotive industry. Reduction in vehicle weight, in turn increases fuel efficiency. As an example, 10 % of vehicle weight reduction results in a 8 to10 % fuel economy improvement [176].

Aluminium (Al) metal matrix composites (MMC's) are used in engine connecting rods, propeller shafts, rocker arm, braking system to replace steel parts to reduce the vehicles weight [185-187]. Al MMC's provide adequate strength and high temperature properties needed in those parts. Aluminium sheets are used to manufacture cylindrical bores, but need wear resistance coats. Currently they are coated with ferrous materials [188]. Hence aluminium/tool-steel graded coatings could be used to coat cylinder bores instead of only ferrous materials. Top tool-steel layer can provide wear resistance, while the rest of the layers can make the cylinder bore stronger than single layer ferrous coat. Aluminium is also used in the building of car bodies using the space frame techniques [189-191]. Examples of cars using the space frame is Audi A8, Ford AIV, Honda NSX to mention a few [176]. However theses cars need thicker aluminium frames and corrosion and wear resistant paints. Again aluminium/tool-steel coated aluminium may be an alternative way of building the car bodies. The top tool-steel layer could give wear resistance, the FeAl or FeAl$_3$ formed in the interlayers could give enhanced corrosion resistance [192], and again the graded layers can provide adequate strength to the frame.

Lightweight materials are also used in the Aerospace industry to decrease weight and increase fuel efficiency [193,194]. At the moment laser joined aluminium and iron

sheets are used to build parts of an aircrafts body [193]. But brittle intermetallic phases pose problems during the manufacturing of those parts. Graded aluminium/tool-steel coated aluminium may be a useful solution to this problem.

Functionally graded coatings have other potential application areas including improved machine tools with high fracture toughness, lightweight armour materials with high ballistic efficiency [155], optical components [195] to mention a few. Thin film optical coatings play an important role for the design of optical components used in the laser field. Optical components with graded coatings allow the improvement of the quality of the laser beam without introducing additional optical elements inside the cavity.

HVOF thermal sprayed coatings offer higher density, better wear and corrosion resistance, higher bond strength, lower oxide content, less unmelted particle content, better chemistry and smoother as-sprayed surfaces compared to other thermal spraying processes due to the high particles velocities associated with the system to propel molten material at supersonic speed towards the substrate [46]. But deposition of thick coatings is still a problem due to the build-up of residual stress [79-81]. Functionally graded coatings in which the CTE and elastic modulus vary gradually from the substrate to the coating [24,109,113,155-157] is one method of reducing residual stress. The current research investigates an innovative modification of a commercial HVOF thermal spraying process to produce aluminium/tool-steel functionally graded coatings. Two powder co-injection method is chosen here to deposit graded coatings. The current HVOF thermal sprayed facility, along with the design of a dual powder feed system needed to deposit graded coatings is described in the following chapter.

CHAPTER 3
EXPERIMENTAL WORK & DESIGN

3.1 INTRODUCTION

The present study investigates an innovative modification of the HVOF thermal spray process to produce functionally graded thick coatings. This required development of the current HVOF facility to spray gradually changing powder composition to get graded coatings, carrying out a series of spray tests at range of parameters and characterize resulting coatings in regard to chemical composition, mechanical properties and residual stress. In this chapter, the HVOF thermal sprayed facility used in the research is described, along with the design of a dual powder feed system needed to deposit graded coatings. Calibration tests of the new system are then detailed. In addition to the process equipment used, equipment employed to measure various characteristics of the coatings, along with the procedure used to conduct these measurements is also presented.

The HVOF thermal sprayed facility used in the current project is a manually controlled continuous combustion Sulzer METCO Diamond Jet thermal spray system. It consists of two units: the spraying system and the support system. Both the systems are integrated together, so that the spraying system should not be used alone. Figure 3.1 shows the whole HVOF thermal spray system available in Materials Processing Research Centre (MPRC). The HVOF system shown in figure 3.1 is modified in the current project in order to spray two powders simultaneously. Modification to the system is described later in this chapter.

3.2 HVOF THERMAL SPRAYING SYSTEM

The HVOF thermal spraying system consists of the followings:

1. Gas supply and flow meter unit
2. Powder feed unit
3. Diamond Jet (DJ) gun
4. Support system
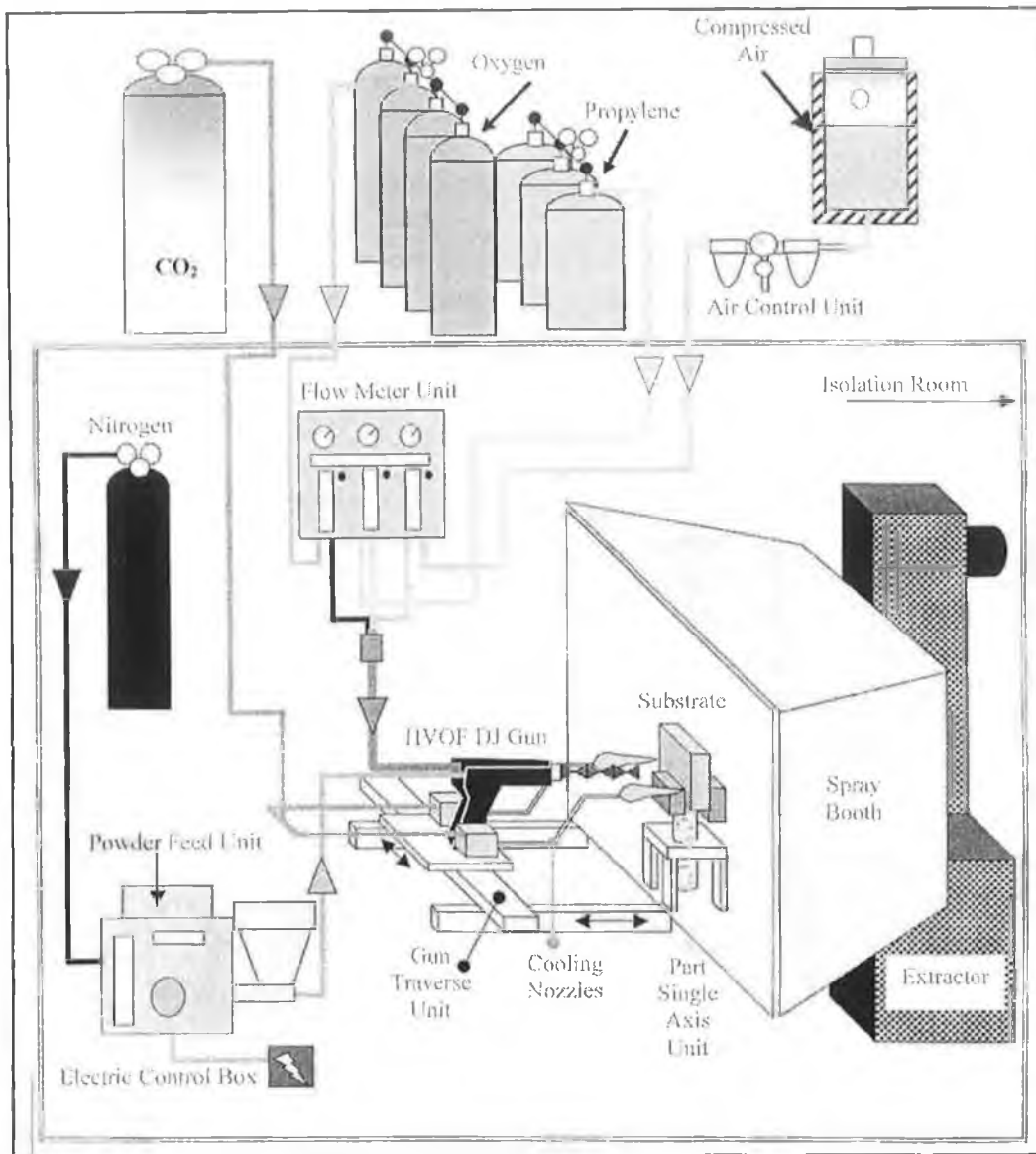
Figure 3.1: The HVOF thermal spray system [22].

3.2.1 Gas Supply and Flow Meter Unit

The gas supply unit controls the pressure and flow of oxygen, propylene, compressed air and nitrogen gasses used by the HVOF thermal spraying system. Oxygen is used as an oxidant during combustion and requires high flow rates, while propylene is used as the combustion gas. The pressures of both of those gases may be adjusted at the manifolds of each set of fuel tanks. Compressed air is used by the system for two reasons, to cool the combustion chamber and to accelerate molten and semi-molten particles to the substrate. An air control unit regulates compressed air. It consists of a pressure regulator and two filters. The regulator provides a means for adjusting air

pressure to the gun. It maintains the required pressure constant regardless of fluctuation in line pressure. The filters are mounted in front of the regulator. They remove water from air as a result of pressure drop through the regulator. The oxygen, propylene and compressed air facilities are located outside the spraying housing area for safety reasons. Nitrogen gas is used as the powder carrier gas in the system. The cylinder carrying nitrogen gas is located inside the spraying area as it is an inert gas.

Compressed air, oxygen and propylene gasses are sent from the gas supply unit to a flow meter unit to control the flow rates. A type DJF gas flow meter unit as shown in figure 3.2 is used for this purpose. It comprises of three gas tube flow meters, pressure gauges and accurate flow adjustment valves. Different rates of those gases are required depending on the spraying condition and the coating material been utilized. There is a float located within each graduated glass tube, free to travel up and down depending on the flow rate. Gas flowing through the flow meter causes the float to rise to a point of dynamic balance. As the flow area increases the float rises, while it descends when the flow area decreases. The flow rate of each individual gas can be changed by twisting the adjustment valve. Flashback arrestors and check valves are installed in both oxygen and propylene line to guard against any danger of backfire. The pressures and flow rates may be adjusted within ± 0.1 Bar and ± 1 Flowmeter Reading (FMR), within a range from 0 to 11 Bar and 0 to 100 FMR respectively.
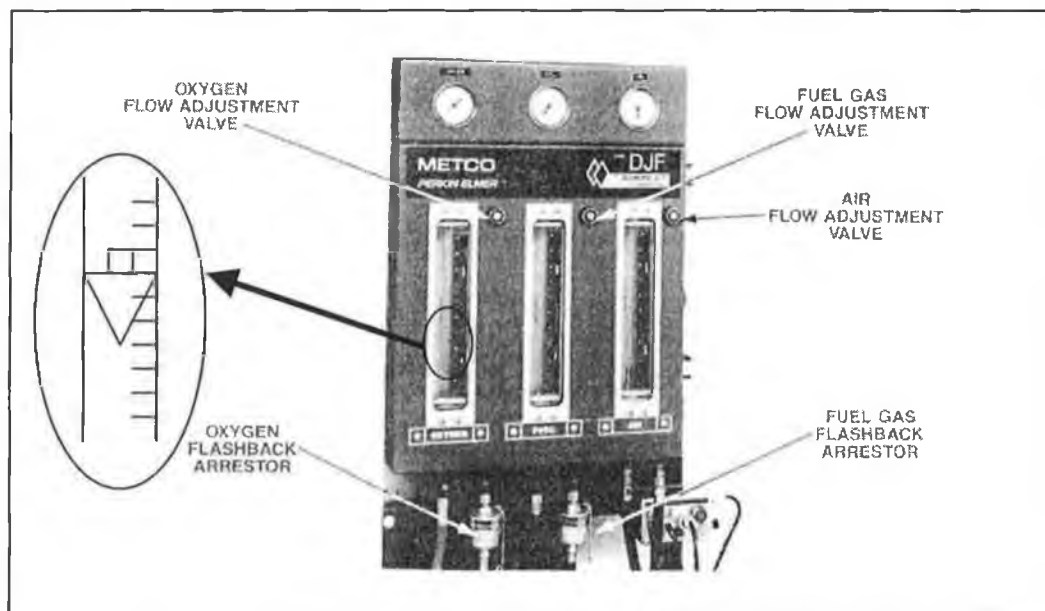
Figure 3.2: The gas flow meter unit [196].

3.2.2 Powder Feed Unit

The powder feed unit is a completely self-contained unit, designed to deliver powder to the DJ gun at a precise flow rate [196]. It comprises of a hopper assembly, air vibrator, load cell, powder feed rate meter and control cabinet as shown in figure 3.3. A carrier gas, typically nitrogen, is used to carry powder from the powder feed unit to the combustion zone of the gun. The powder material is placed inside the hopper assembly. Gravity, vibration of the air vibrator and nitrogen differential pressure between the top of the hopper to the pick-up shaft drop the powder into the hole of the pick-up shaft. The nitrogen carrier gas that flows through the pick-up shaft (figure 3.4), carries the powder on its way to the combustion zone. Adjusting the carrier gas flow meter knob located on the control cabinet regulates the flow rate of nitrogen gas. The feed rate meter controls the amount of powder fed to the gun. Powder delivery from the hopper is determined by the rate at which the hopper loses its weight. A load cell, used for this purpose, continuously weighs the hopper and from this determines the powder delivery rate. The result is calculated against a certain period of time and the flow rate of powder in pounds per hour or grams per minute is displayed. The feed rate meter has an accuracy of ± 0.1 g/min and a range of 0 to 100 g/min. A switch on the gun activates the powder flowing to the gun.
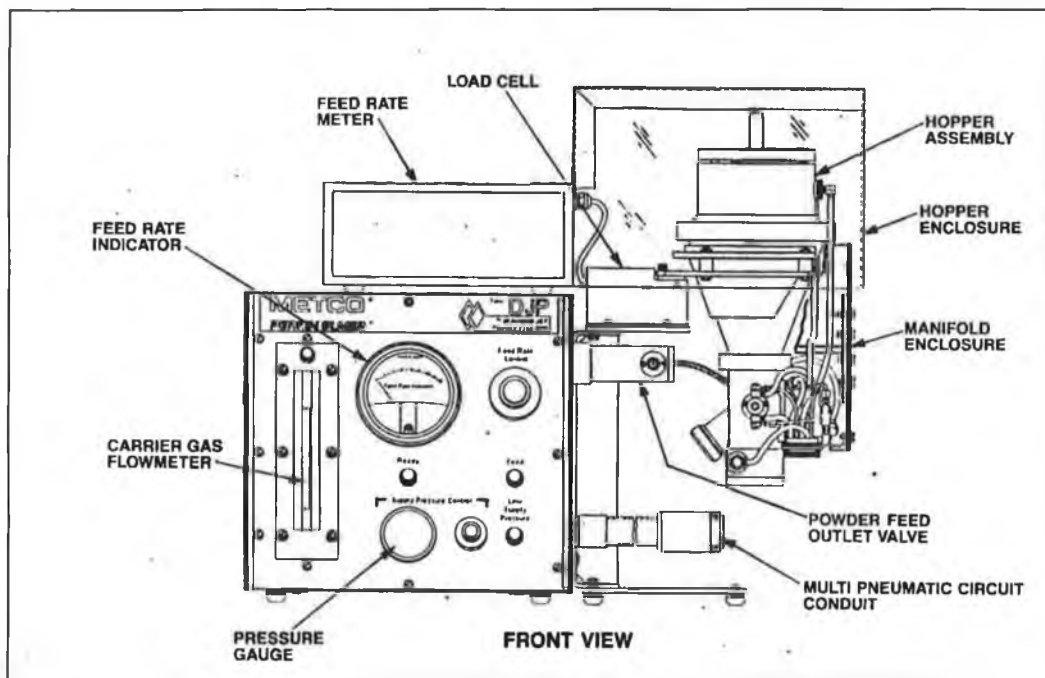
Figure 3.3: The powder feed unit [196].
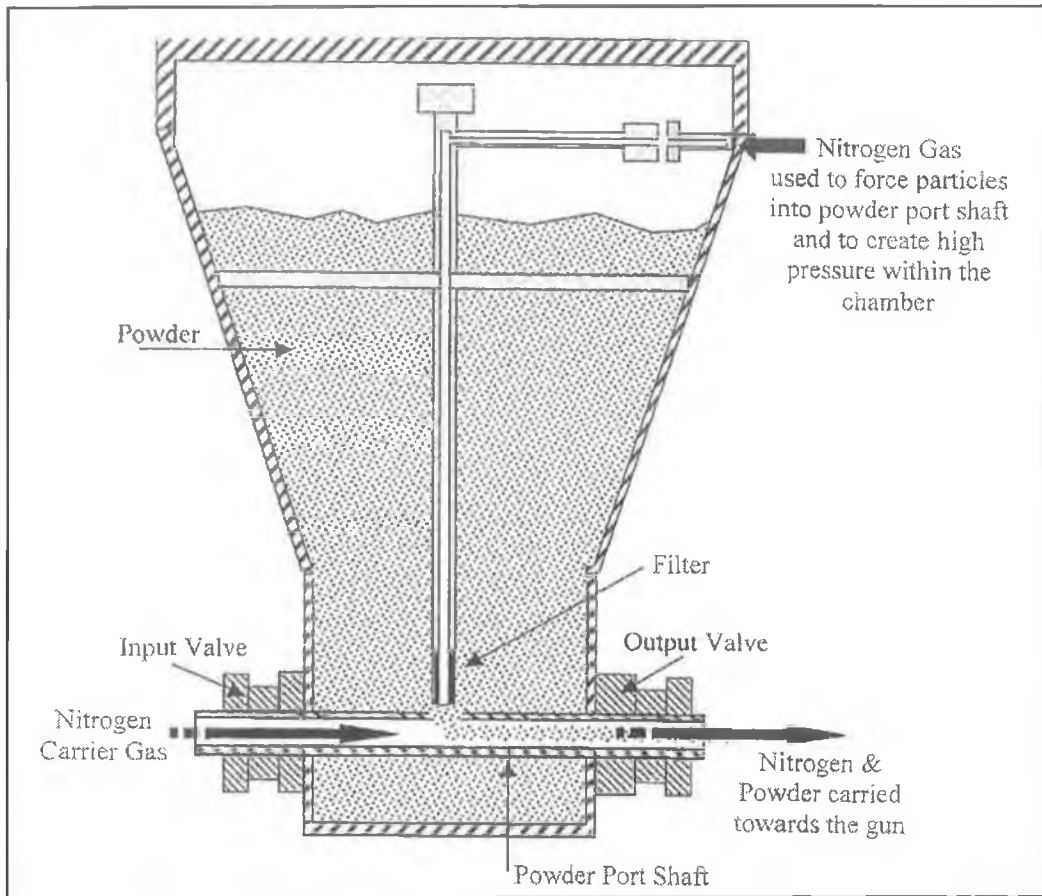
Figure 3.4: Schematic cross-section of the hopper assembly on the DJ powder feed unit [34].

3.2.3 Diamond Jet (DJ) Gun

The METCO Diamond Jet (DJ) gun is the central component of the HVOF system. The gun weighs about 2.27 kg and may be hand held. A schematic of the Diamond Jet gun is shown in figure 3.5. The system gases and powder material enter the back-end of the gun and pass through the combustion zone at the front end. The gun consists of four parts; hose connection block, valve core, control handle and the front end.

The hose connection block consists of the air, fuel and oxygen hose connections and gas tight plungers, which allow the gases to be transferred into the valve core as shown in figure 3.5.
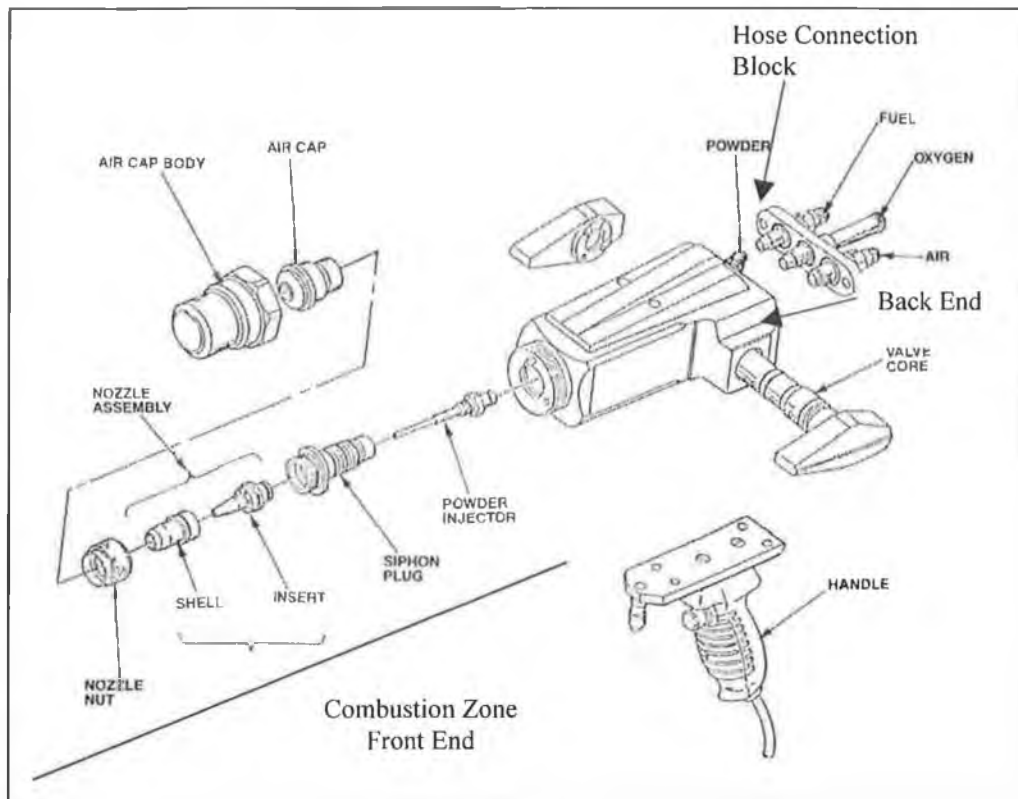
Figure 3.5: Different parts of the Diamond Jet gun [45].

The valve core contains a series of passages (pipelines), grooves and O-rings (to prevent leakage). They are housed within the gun body. With the help of the lever-type valve handle attached to the end of valve core, rotational movement of the valve core permits the flow of gases and powder (or powders) through the gun. To turn off the flame at the gun, the valve handle must be rotated (through $90°$) to the full up position.

The control handle assembly contains the spray powder ON/OFF pushbutton switch. This switch controls the powder flow from the powder feed unit to the gun. It does not turn off the flame.

The front end of the gun is made up of the powder injector, siphon plug, nozzle assembly and air cap assembly as shown in figure 3.5. These nozzles and inserts control the pressure of the gases (when the gases are on) and in doing so the coating particle velocities. Depending on the powder being used, the inserts and nozzles are inter changed. The function of powder injector is to limit the feed rate of powder particles and direct those particles from region 1 axially into the combustion zone (region 4) as shown in figure 3.6. After leaving the powder injector at a set feed rate, particles enter the combustion zone, where they are melted and propelled by the combustion gases at

high velocities. The central zone (region 2 and 3 in figure 3.6) is occupied by siphon plug. The propylene and air gases run parallel to the gun body via drilled out pathways in region 2, while the oxygen travels obliquely. The three gases are passed onto the nozzle assembly after being mixed in region 3. The nozzle assembly comprises of three components; a shell, insert and nozzle nut. The nozzle nut locks the nozzle assembly to the siphon plug. It accelerates the entering gases so as to give the powder particles higher velocities on impact. The air cap and the air cap body combine to form the air cap assembly. Combustion of the powder particles occurs in region 4 within the air cap. The molten material is then propelled at high velocity towards the substrate. The air cap body locks all the assemblies mentioned, to the gun body. Compressed air cools the assembly during combustion as it circulates within the air cap body (region 5). Combustion temperatures approaches 2760 ^{0}C and combustion product are propelled at speeds of up to 1350 m/s [45].
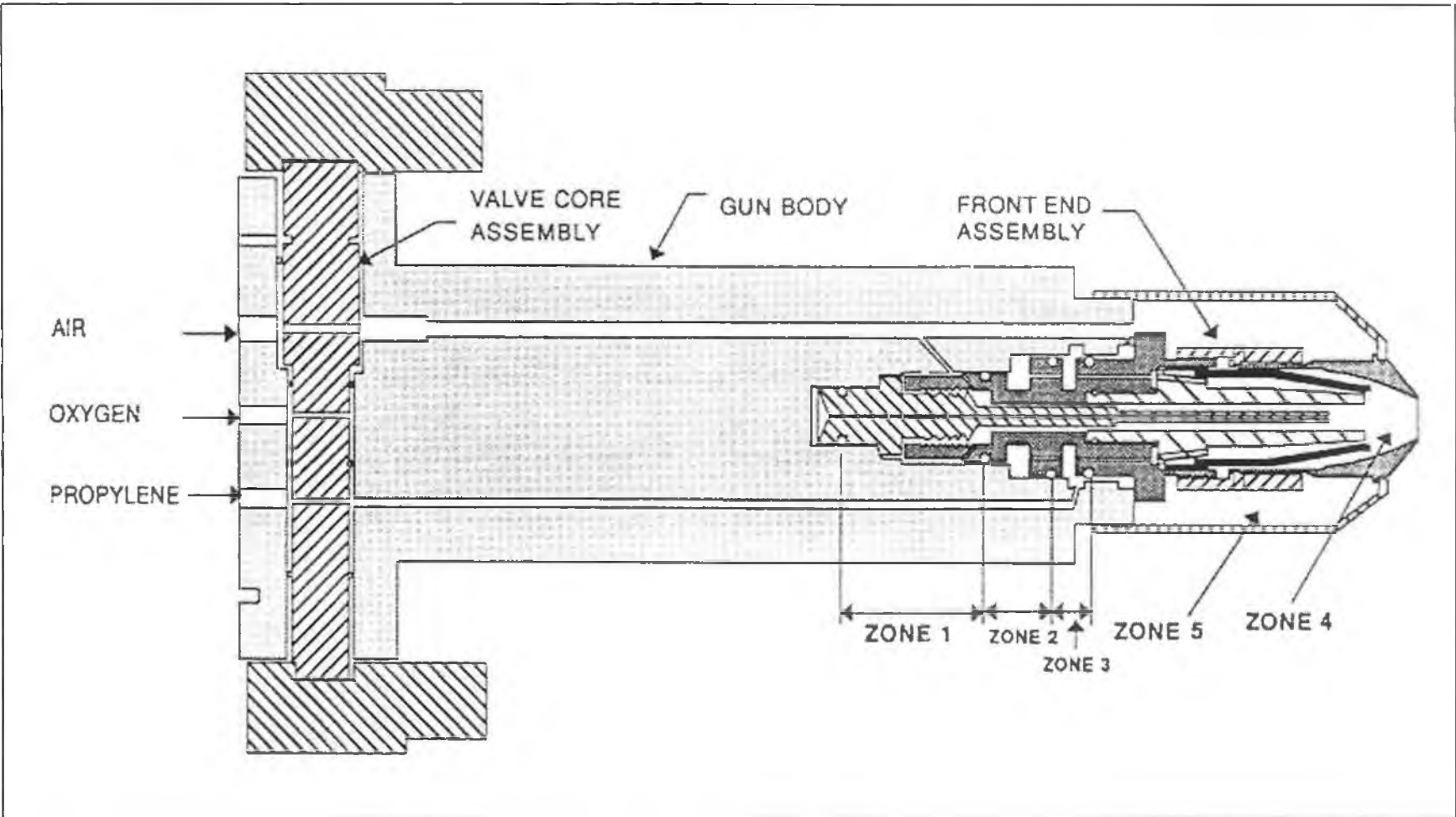
Figure 3.6: Cross-section of assembled Diamond Jet gun [20].

VALVE CORE ASSEMBLY

GUN BODY

FRONT END ASSEMBLY

AIR

OXYGEN

PROPYLENE

ZONE 1

ZONE 2

ZONE 3

ZONE 5

ZONE 4

3.2.4 Support System

The thermal spraying system requires some support facilities to make the process safe and workable. Safety for the operator is very important; therefore proper functioning facilities must be installed before spraying. Spray powders are often hazardous. Therefore personal safety equipments must be worn. Some of the supporting facilities and additional equipments are discussed below.

(a) Exhaust System

To minimize the danger of dust explosion and prevention of fumes and dust accumulation, adequate ventilation must be provided for spray booth and other confined spaces. A wet collector extractor is installed in MPRC to extract away all those fumes. It works on the principle of sucking air from the working area through a water reservoir, where the waste products submerge. It is to be ensured that the water level is topped up and the contents within the reservoir are regularly discarded appropriately.

(b) Facility Isolation

The potential hazards associated with the thermal spraying are toxic materials generated during spraying, airborne metal dust, fumes and the high sound level (130 dB [22]). Therefore it is necessary not only to isolate the spraying equipments into a confined room, but also to insulate the room with a sound proof material. A cavity wall of peg-board sheets is built in. The structure is supported by a steel bar frame. The central portion of the peg-board is filled with fibreglass. To support the structure and to protect the surrounding room in case of fire, the outside room structure is covered with aluminium sheets.

(c) Traverse Unit

In order to control the spraying distance and reduce the residual stress, a semi-automated process for traversing the spray gun was developed for the HVOF process [22]. To traverse the spray gun back and forth, a LX-L20 Series Linear Stepper Motor (LX means Linear X-direction), developed by the Compumotor Division, is utilised. It

has two components: a platen and a forcer. The stationary element is called the platen, while the moving element on which gun is mounted is called a forcer. The traverse unit and the cooling system described later are shown in figure 3.7. A specially written computational programme is used to control the traverse distance, speed and accelerations. This in turn accomplishes an ideal path of motion of the gun during preheating and spraying.
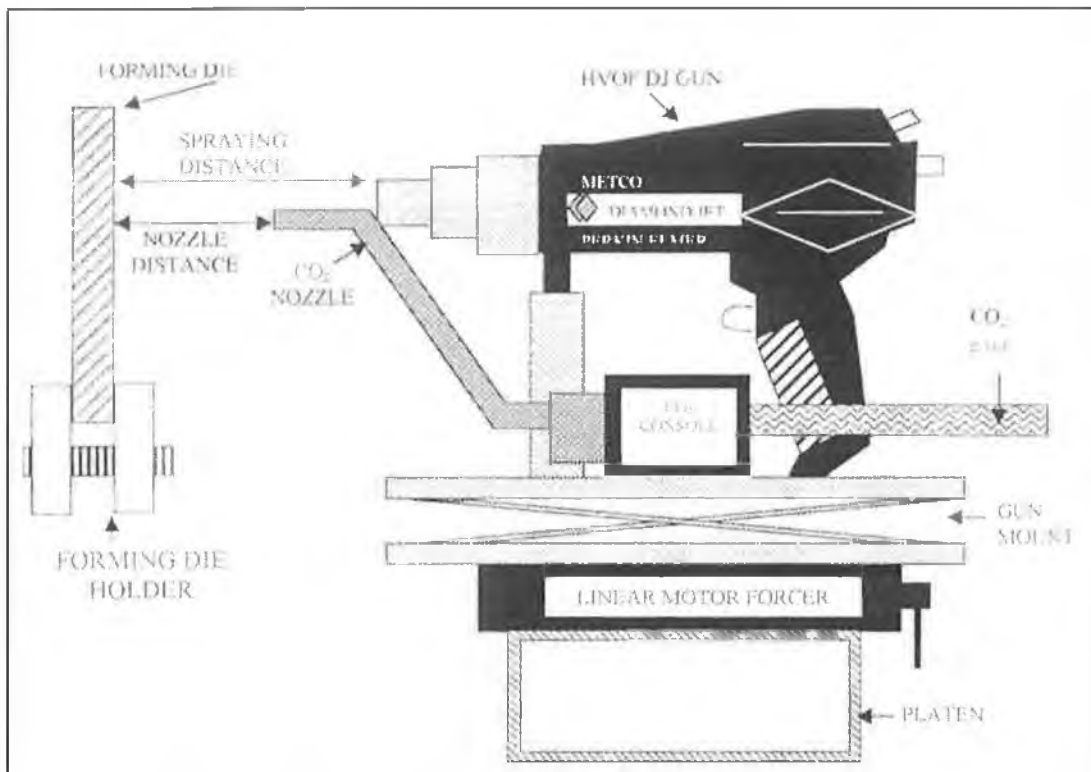
Figure 3.7: Schematic of the traverse unit and carbon dioxide cooling system [22].

(d) Cooling System

In order to carry out continuous spraying, while limiting the rise in spraying temperature, a carbon dioxide cooling system designed by BOC Gasses was adopted here. Two carbon dioxide cooling solenoid consoles and nozzles are attached to the gun mount as shown in figure 3.7. Pressure from the gas cylinder feeds the liquid carbon dioxide through the nozzle onto the die, controlled by a switch connected to the carbon dioxide consoles. Carbon dioxide cools the sprayed region, thus reducing and controlling the spraying temperature as found by Stokes [22].

(e) Grit Blasting Unit

A clean substrate surface is of prime importance for good quality coating, as the adhesion of a coating is directly related to the cleanliness of the substrate surface and total surface area of the substrate [197]. Grit blasting a substrate with a hard media such as silicon carbide is one known process of increasing the subsequent adhesion between the deposit and substrate. A grit blasting unit supplied by Sulzer Metco, known as the Ventublast Mammouth, has been used to prepare the substrate surface during the current research in DCU. The grit blasting unit has an internal area of 0.87 square meters, a hand held blasting gun and a grit collector. An eye visor enables visibility over the entire work. The grit is collected into a compressed air stream and then propelled to the substrate. The impinging grit falls down through grit into the grit collector for recycling. The roughness of the substrate can be controlled between the ranges of 6 to 15 μm. A mount was designed to carry out the erosion of samples [198]. The mounting system allows blasting distance and impact angle to be measured accurately.

(f) Furnace

A furnace made by Lenton Thermal Designs (type EF 10/8) is used for heat-treatment (post spraying) in DCU's Materials Processing Research Centre. The furnace is equipped with an analogue temperature controller. Temperature can be controlled within $\pm$ 3 ^{0}C. The furnace operates at a temperature range between (0-1000) ^{0}C.

(g) Safety Equipment

The operator of thermal spray equipment in industry remains outside the spraying area controlling the system from a monitor or through an eyeglass. But in the current facility the operators needs to stay within the housing area due to the current set up of the system. Thus the operators must wear adequate protective clothing.

Spray operators need to wear earmuffs and earplugs due to the excessive high level of noise (125-130 dB) developed in the HVOF booth [22]. Fire resistant clothing is also essential. The operator must use eye protective glasses or shields of shade #5 or greater

to guard against brilliant white flame that gives off ultra-violet light. Besides those, heat resistant gloves are also necessary as the operating temperature rises well above $100\,^0C$.

A respiratory mask must be worn while operating the HVOF thermal spray equipment. Two filter types must be used, one for particle protection and the other for gas fumes. Even during changing the powder material in the hopper of the powder feed unit or when cleaning, the mask must be worn as powder particles become airborne easily. Clear eye protection and rubber gloves are also essential as most powder materials cause skin and eye irritation. Skin must be washed thoroughly with soap and water to avoid ingestion of powder material. The powder itself should be kept away from food or protective clothing, in a well-ventilated room, as it is often cryogenic.

3.3 DESIGN OF A DUAL POWDER FEED SYSTEM

As mentioned earlier, thermal spraying can be used to produce interlayers of functionally graded coatings in two ways:

1. Using pre-mixed powders to produce different discrete layers or
2. Co-injecting two different powders and varying their composition during spraying

The spraying process is interrupted when the former method is used. The process is interrupted, so as to change over to various composition mixtures of the powders. Interruption to the spraying results in the final coating consisting of a series of layers rather than heterogeneous graded material [199] as shown in figure 3.8 and the individual particles experience a greater cooling rate compared to the co-injection method. This in turn produces higher residual stress in the coating. Residual stress can cause interlaminar debonding and adhesion loss between the coating and substrate [200]. When the latter method of co-injection of two or more powders is used, the spraying process is not interrupted; hence this method was chosen in current research to produce functionally graded coatings. However using the existing HVOF facility, only one powder or a single powder mixture can be sprayed at a time. Therefore some significant developments of the existing system were needed to deposit two powders simultaneously. Various concepts were examined for potential feasibility. Those concepts along with the current system are described in the following sections. Advantages and disadvantages of each concept along with a rating chart are also mentioned. Finally description of the chosen concept (based on the chart and the advantages and disadvantages) is also given at the end of this section.
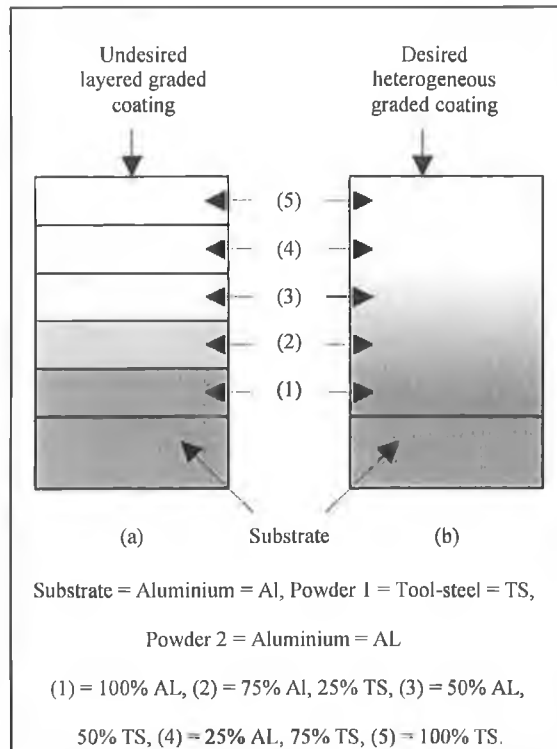
Figure 3.8: Schematic of graded coatings; (a) undesired layered, (b) desired heterogeneous.

3.3.1 Design Concept

(a) Current System

The schematic cross-section of the existing hopper assembly is shown in figure 3.4, while the schematic picture of the control system and powder feed hopper is shown in figure 3.9.

In figure 3.9, all of the items on the left hand side of the dotted line, consist the control system, while the things on the right hand side of that line consist the feeding system. There are four different flow lines for the nitrogen carrier gas and a flow line for the air, as shown in figure 3.9. The pressure of the nitrogen gas is set using the pressure regulator in lines (1) and (2) before putting the flow into the four nitrogen lines mentioned earlier. Through the lines (13) and (15), the nitrogen gas flows from an initial pressure regulator to an inlet pinch valve, then through the pick-up shaft, up to the output pinch valve, then finally to the gun. The flow of the nitrogen gas is controlled

by the flow control flow meter at the start of this line. Line (3), (9) and (12) are the flow lines for the nitrogen gas from an initial pressure regulator to the top of powder feed hopper. Nitrogen gas flowing through this line provides the adequate differential pressure between the top of the hopper to the pick-up shaft to force the powder through the pick-up shaft hole into the pick-up shaft nitrogen gas flow. Lines (3) and (18) are there to supply nitrogen gas if there is a shortage of nitrogen gas flow in the inlet and outlet pinch valves, while lines (3), (6) and (11) provide nitrogen gas flow to pinch valve 3 and pinch valve 4 when only the gun is lit without any powder flow. Lines (4) and (5) are the flow lines for the compressed air to supply adequate air pressure to the air vibrator (which when activated vibrates the powder feed hopper to cause continuous powder flow).

(b) Concept 1

Sulzer METCO supply dual feeders such as the type 4MP powder feeder, the Twin 120A powder feeder and the Twin 10C powder feeder [201]. The Type 4MP powder feeder can be used simultaneously for high spray rates of two powders or separately for convenient operation when a bond coat and top coat are required for the coating system. The Twin 20A also has a dual feeder to feed powders continuously or separately, while the Twin 10C powder feeders provide precise, volumetric feeding of powdered materials. Each hopper can be used independently or simultaneously. The initial concept was to buy either of those dual feeders from Sulzer METCO and integrate up with the existing control system.

(c) Concept 2

The second concept was to install the same control and the powder feed system, as the existing one, as shown in figure 3.8 and integrate it into the existing system using a "T" fitting. The flow diagram of the second concept is shown in figure 3.10, while the schematic drawing of the same concept is shown in figure 3.11.
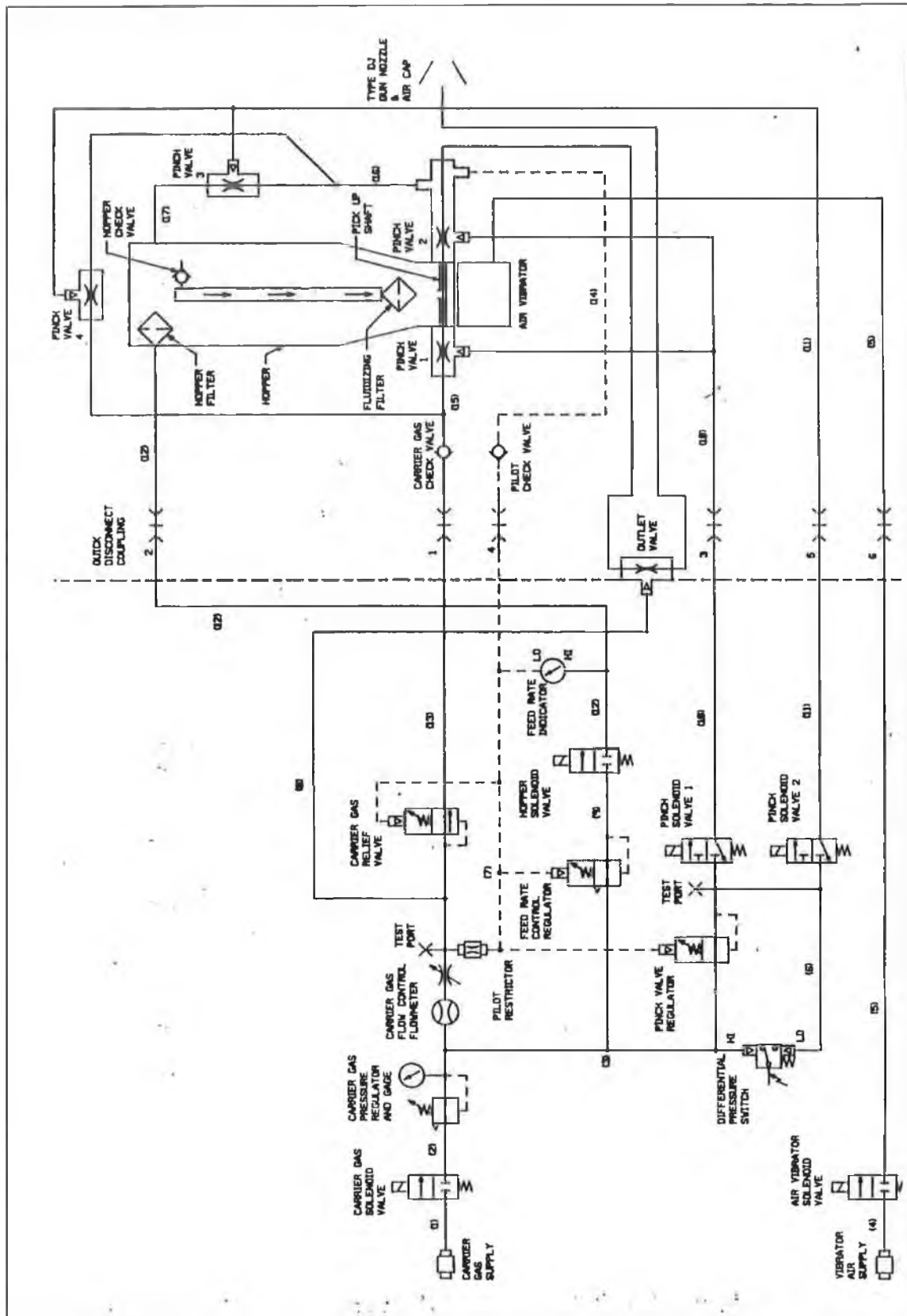
Figure 3.9: Schematic of the control system and powder feed hopper [196].
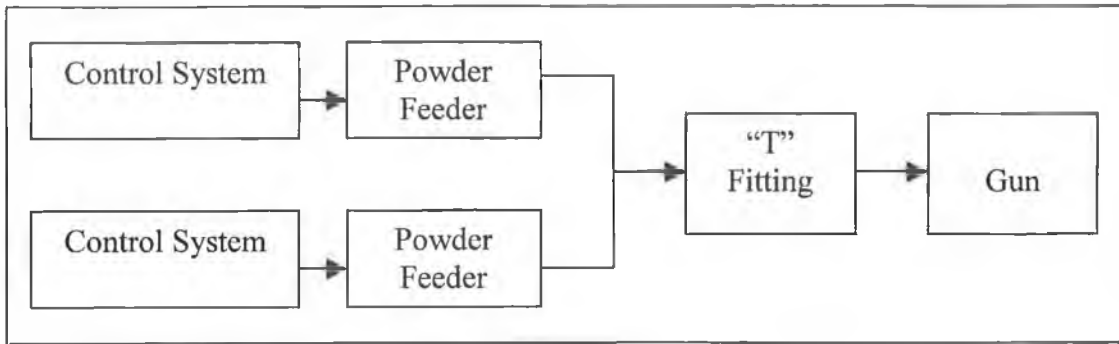
Figure 3.10: Flow diagram of the second proposed system.
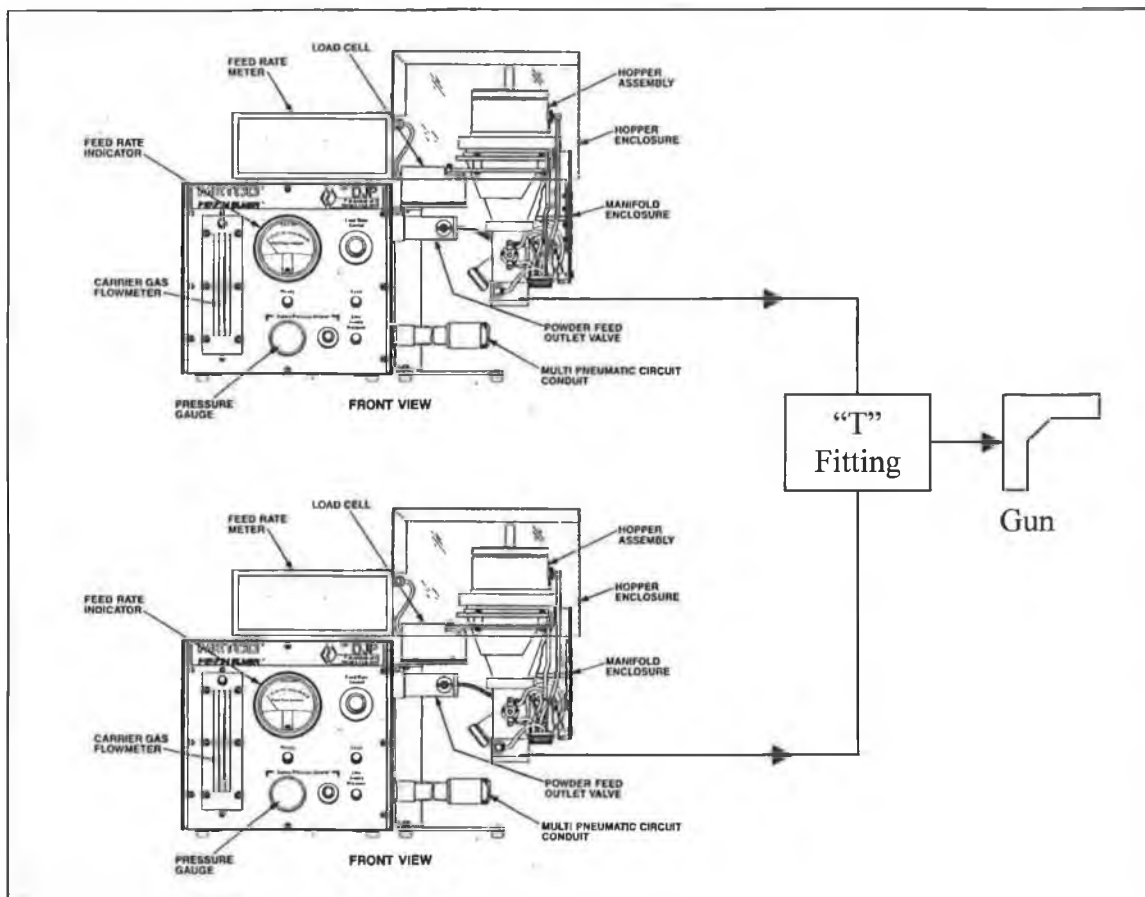
Figure 3.11: Schematic diagram of concept two.

(d) Concept 3

Another concept was to replace the current cylindrical powder feed hopper with a divided hopper with two different flow paths for two different powders. The flow diagram of the third concept is shown in figure 3.12.
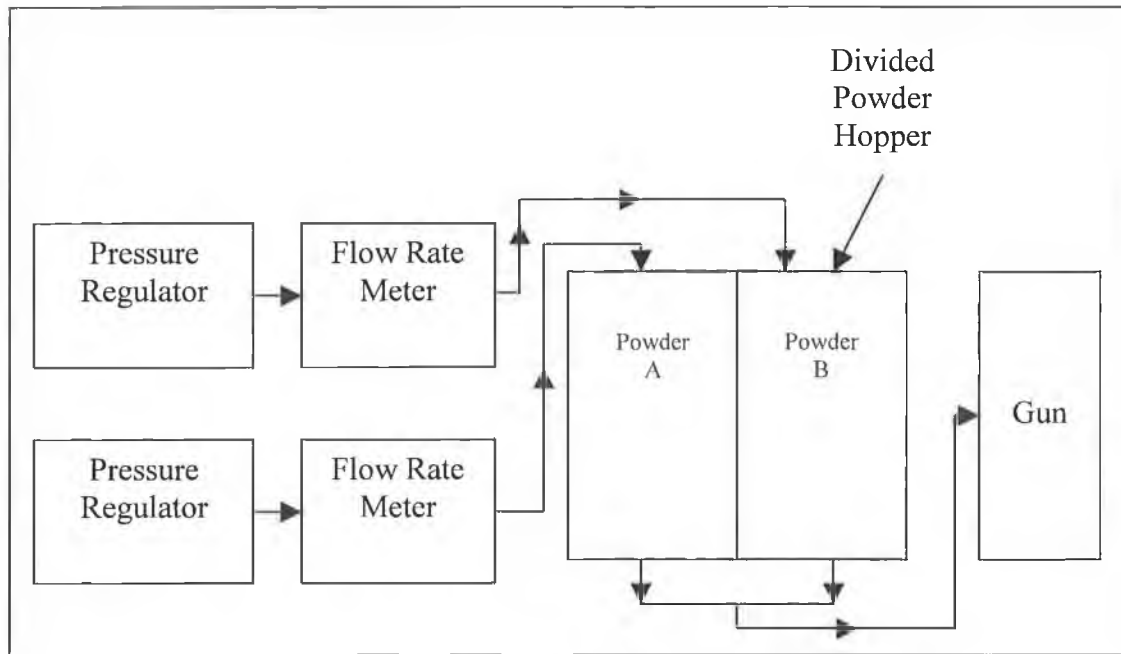
Figure 3.12: Flow diagram of the third proposed system.

(e) Concept 4

Concept 4 was to carry out some innovative modifications on the pre-existing cylindrical powder feed hopper. Modifications include addition of some parts inside the powder feed hopper. Various dimensions of the modified parts chosen were constrained by the previous hopper, as the new parts had to fit inside that hopper. Sectional assembly drawing of the proposed designed parts is shown in figure 3.13, while the sectional assembly drawing of the designed parts along with the previous hopper is shown in figure 3.14. There are two separate holders for two different powders. Powders would be mixed inside the hopper, and then the mixture flow through to the nitrogen gas flow inside the pick-up shaft, and up to the combustion zone of the gun. Although the new modifications have two powder holders inside the powder feed hopper, the difference between these and the dual hoppers mentioned earlier is that dual hoppers use two different hoppers for different powders, while this system uses only one feed hopper (with two powder chambers inside it) for two dissimilar powders.
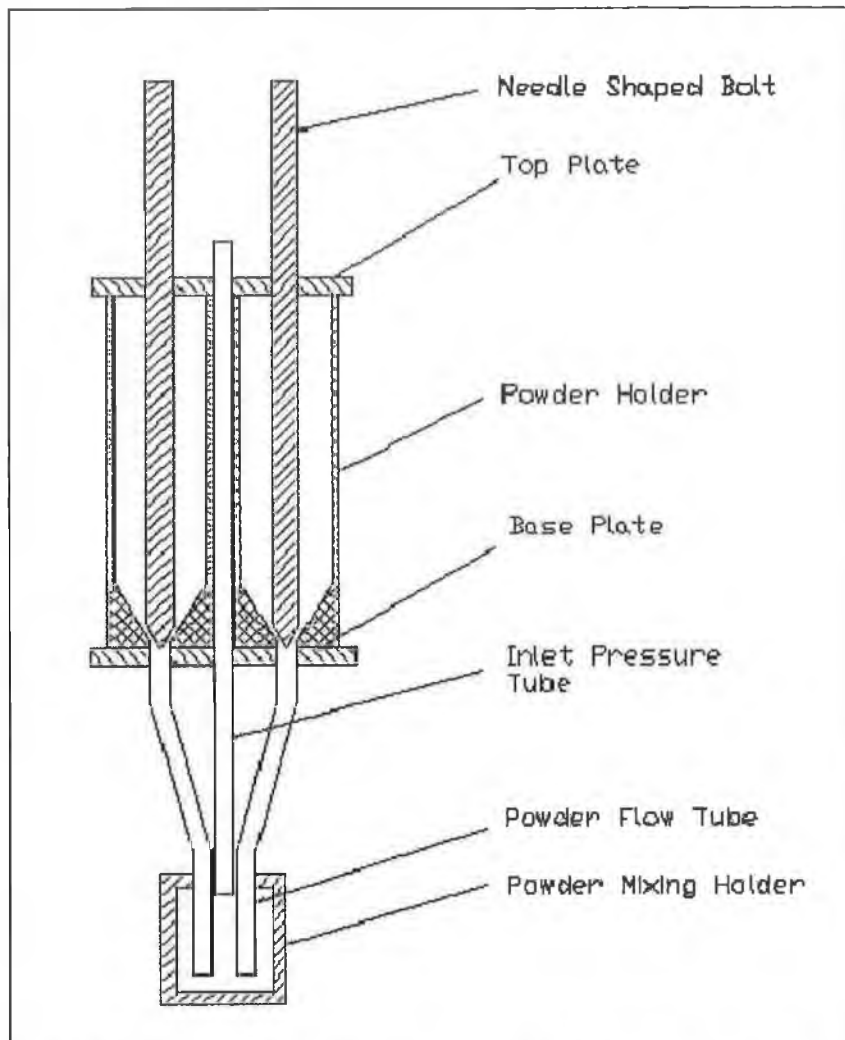
Figure 3.13: Sectional assembly drawing of the proposed designed parts.
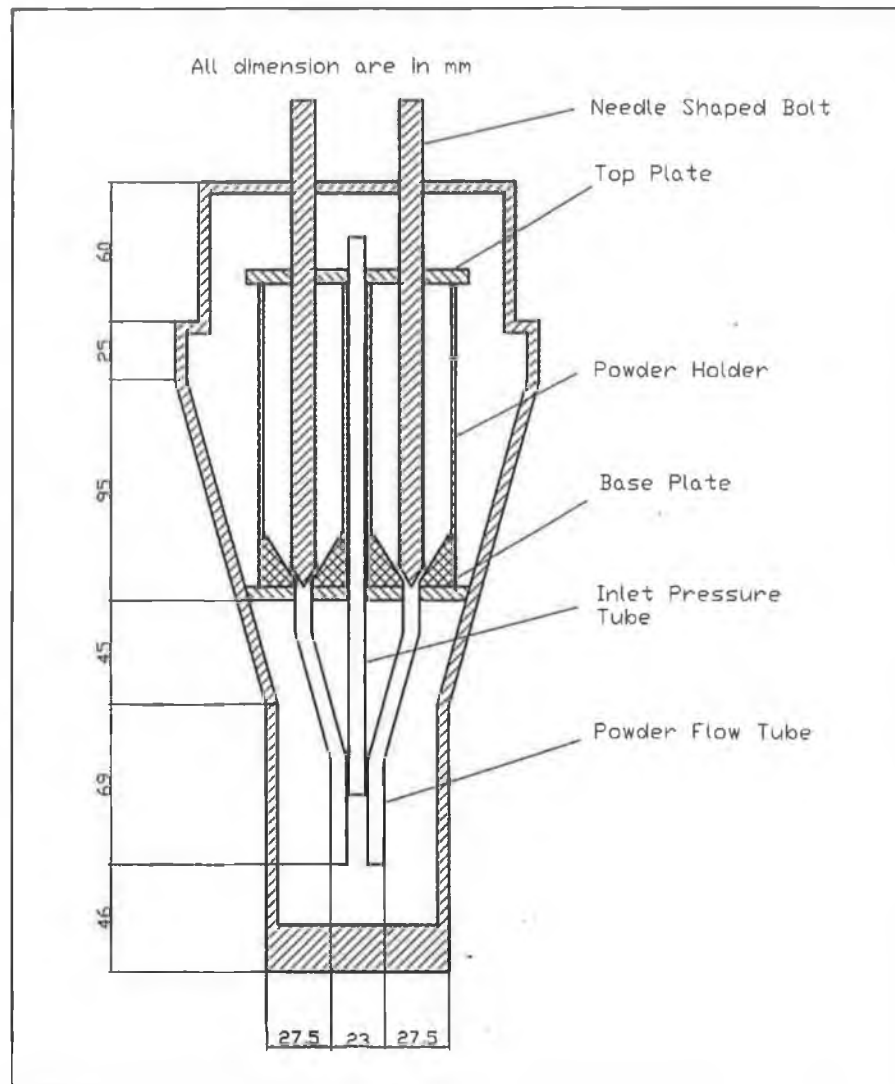
Figure 3.14: Sectional assembly drawing of the designed parts along with the previous hopper.

3.3.2 Rating Chart

A rating chart was used to determine which of the 4 concepts was the best for the current project. Confidence in functionality, cost, ease of manufacturing and setting up in the lab are the different categories, with which each concept was examined under. A value was then given, on a scale from one to three to each category. Higher value means higher ability of the concept to comply with the categories chosen. All the values given to each concept were added and the concept with the highest total value was chosen. The rating chart is shown in table 3.1.

Table 3.1: Rating chart for concept designs.

	Concept 1	Concept 2	Concept 3	Concept 4
Confidence in functionality	3	3	1	3
Cost	1	1	3	3
Ease of manufacturing	3	3	1	3
Setting up in the lab	3	2	2	3
Total	10	9	7	12

1 = Low   2 = Average   3 = High

3.3.3 Advantages and Disadvantages

(a) Concept 1

Main advantage of the first concept was that it could be bought straight away off the self, and it could be set up in the lab easily. There was no doubt about the functionality of the first concept. However it was costly to buy.

(b) Concept 2

Concept two could be bought off the self like the first concept. But it was costly as the HVOF process facility has three main components; the gas supply unit, the Diamond Jet gun and the powder feed unit. The gas supply unit is relatively cheap compared to the powder feed unit along with the control system. Buying a new powder feed unit for concept two would cost around 35,000 – 40,000 Euro. Secondly, it would not have been too easy to set it up in the lab. Thus, in spite of confidence in functionality, it would not have been a good idea to adopt concept two.

(c) Concept 3

Concept three would be cheap to manufacture. However the manufacturing of this chamber would not be easy and certain problems were identified. This would require two flow paths for two different powders, thus two input pinch valves would have to be used and the nitrogen gas flow (point 15 in figure 3.9) would have to be divided into two sections using a "T" junction. There was doubt whether enough nitrogen gas

pressure could have been maintained in both flow lines, thus reducing the efficiency of the powder flow.

(d) Concept 4

There was no doubt about the functionality of concept four in depositing functionally graded coating. It would be cheap and easy to manufacture. Again it could be set up in the lab easily.

Table 3.1 shows that concept 4 had the highest total rating value. Again considering the advantages and disadvantages of the 4 different concepts, concept four was chosen to be used in the current project in depositing functionally graded coatings. A full description of concept four is given in the following section.

3.3.4 Description of Chosen Design Concept

The sectional assembly drawing of the parts involving concept four is already shown in figure 3.13. Figure 3.15 shows a photograph of those parts, while the separate parts are shown in Appendix A (figures A1 through to A11). All dimensions were informed by modelling described latter.

Figure A1 shows the 200 mm long needle shaped bolt. Two bolts of same dimension were used to vary the composition of each powder. The bolts could be moved upwards and downwards by rotation. Their movement had to be calibrated in order to control the amount of the powder flow, using permanent indicators on the top plate to measure angle of rotation of the bolts. The bolts were placed just on top of the base plate.

Figure A2 shows the plan view of the 95 mm diameter, 6 mm thick top plate. It contains eight 8 mm diameter holes, two 10 mm diameter holes and a single 7 mm diameter hole. The 8 mm diameter holes were used to feed (pour in) the powders initially. The 10 mm diameter holes (M10) had internal threads to hold the needle shaped bolts, thus controlling their movement, while 7 the mm diameter hole was used to put through the inlet pressure tube. Inlet pressure tube was there to maintain enough differential

pressure to put the powder mixture through the pick-up shaft hole into the nitrogen gas flow inside the pick-up shaft.
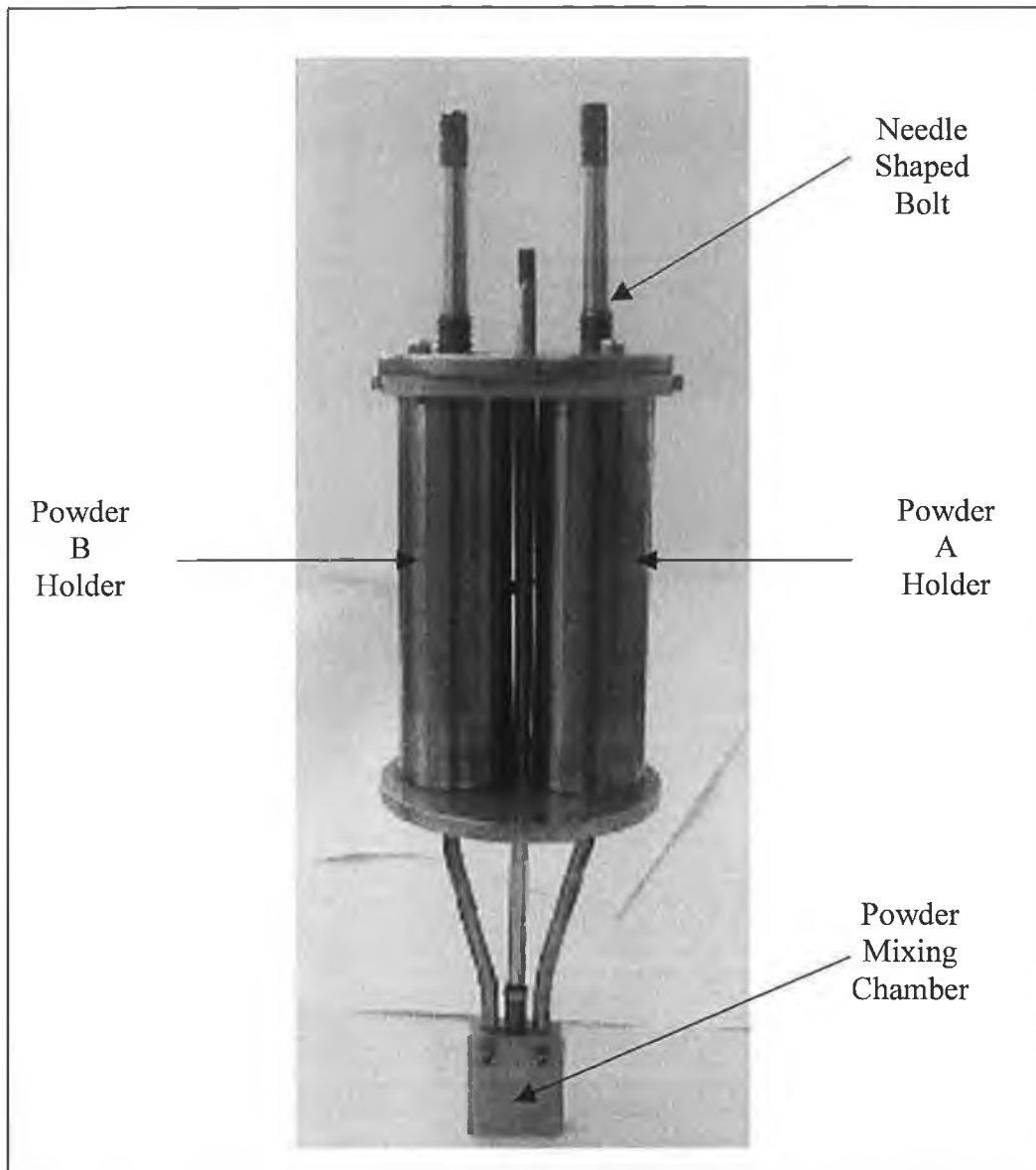
Figure 3.15: Photograph of dual powder feed unit.

Figure A3 shows the cylindrical shaped powder holder (38 mm outside diameter, 34 mm inside diameter). Two holders of same dimensions were used to contain the two different powders. The needle shaped bolts remained in the middle of these two powder holders, moving upwards and downwards, allowing powder to flow out through the hole at the end of the cylinder.

Figure A4 shows the 95 mm diameter, 6 mm thick base plate. It contains three 7 mm diameter holes. The central hole was to accommodate the inlet pressure tube, while the

other two holes were there for attaching the two powder flow tubes (which were attached to the two powder holders).

Figure A5 shows the sectional assembled drawing of the top plate, the powder holders and the base plate. It shows where these were all attached to each other.

Figure A6 shows the 7 mm outside diameter, 122 mm long powder flow tube. Two tubes of same dimension were used. These were placed at the bottom of the base plate to carry the powders from the powder holders to just above the pick up shaft where the powders mixed. In order to increase the degree of powder mixing, each powder flow tube had two bend sections and they had to be positioned very close inside the mixing zone (figure A9). The mixing zone is shown in chapter three (figure 3.16).

Figure A7 shows the combined drawing of the base plate, the inlet pressure tube and the two powder flow tubes. It shows where each part was attached to each other.

Figure A8 shows the powder mixing holder. The pick-up shaft went through this powder holder. The powder flow tubes ended inside this holder, just above the pick-up shaft.

Figures A9 and A10 are the two assembled cross-sectional drawings. They show how the designed parts fit into the powder feed hopper. Figure A9 is the assembled sectional drawing of the powder feed hopper, the needle shaped bolts, the top plate, the base plate, the individual powder holders, the inlet pressure tube and the powder flow tubes explained already.

Figure A10 shows the assembled cross-sectional drawings of the lower portion of the powder feed hopper, the inlet pressure tube, the powder flow tubes, the powder mixing holder and the pick-up shaft.

Figure A11 shows the schematic drawing of the rectangular hopper cover. It was placed on top of the hopper instead of the current circular hopper cover. The four φ 8 mm C'BORE φ13 mm holes were there to attach the cover to hopper top, while the two 10 mm diameter (M10) holes were used to put through the two needle shaped bolts.

3.3.5 Nitrogen Gas-Powder Flow Model

Concept four, mentioned in the previous section was chosen in the current work to accommodate spraying of two powders simultaneously. In order to check the effectiveness of that concept before manufacturing, a nitrogen gas-powder flow model was developed in this project using the FLOTRAN CFD ANSYS Finite Element package. Finite Element Analysis is a unique method of predicting results from engineering solutions before producing a component. Hence verification that the design would work was first tested on model of the design. Various information regarding the building of the model in ANSYS is described in the following sections.

(a) Selection of Element

FLUID and FLOTRAN CFD (Computational Fluid Dynamics) are the two branches of the ANSYS that deal with fluid flow simulation problems. FLUID provides some elements are mainly used for sound wave propagation and submerged structure dynamics problems. Some of the FLUID elements are used for the fluids that have no net flow. Another FLUID element deals with the heat flow problems. So none of them is suitable to simulate nitrogen-powder flow. FLUID 141 (element of FLOTRAN CFD) is capable of achieve solutions for lift and drag on an airfoil, the flow in supersonic nozzles and complex two dimensional flow patterns in bend pipes [202]. Thus it was chosen here to simulate the two-dimensional nitrogen-powder flow through the designed dual powder feed system. The nitrogen gas-powder flow system was assumed as steady, incompressible and laminar during the simulation.

(b) Selection of Solver

There are mainly three types of solver available for FLUID 141. They are; Tri-Diagonal Matrix Algorithm (TDMA) solver, Exact solver and Sparse Direct solver. The Conjugate Residual Exact solver was found to be the best in solving both the velocity and pressure Degree of Freedom (DOF). The TDMA solver is not recommended for pressure DOF, while the Sparse direct solver is not suitable for velocity Degree of

Freedom [202]. As both the velocity and pressure Degree of Freedom was necessary for the current research, The Conjugate Residual Exact solver was selected to simulate the nitrogen gas-powder flow.

(c) Selection of Type of Analysis

The multiple species transport analysis was chosen to simulate the gas-powder flow in the current work. It enables tracking of several different fluids at a time. Single momentum equation is solved using properties of a main fluid or combination of fluids. There are three types of multiple transport analysis available. They are; dilute mixture analysis, composite mixture analysis and composite gas analysis. In a dilute mixture analysis, small mass fractions of species fluids are tracked in a flow field and the species properties do not significantly influence the flow field. It was not suitable for current work. The composite gas analysis is suitable when two or more gases have to be analysed. The composite mixture analysis calculates the properties used in the solution from a linear combination of the species, weighted by mass fractions as a function of space. The solution of the momentum equation depends on the species distribution, so the momentum and transport equations are strongly coupled [202]. Hence composite mixture analysis was chosen to simulate the nitrogen gas-powder flow here.

(d) Material Property

Material properties input include the density and viscosity of the tool-steel and aluminium powder, as well as the nitrogen gas. Those are given below:

(1) Density

Tool-steel powder-   6.10 g/cm^3 [64]
Aluminium powder-   2.70 g/cm^3 [64]
Nitrogen gas-   0.00125 g/cm^3 [203]

(2) Viscosity

Tool steel powder-   350.031 g/cm.s [204]

Aluminium powder-   619.671 g/cm.s [64]

Nitrogen gas-   0.000173 g/cm.s [203]

(e) Geometry of the Model

Figure 3.16 shows the geometry of the powder and nitrogen gas flow tubes. The geometry of the model is dictated by size constraints of the pre-existing powder feed hopper. The central tube was the tube to carry nitrogen. Other two vertical tubes were there to carry two dissimilar powders up to where they were supposed to mix. The pick-up shaft at the bottom was also carrying nitrogen gas. The nitrogen gas in the pick-up shaft was there to carry the powder mixture to the combustion zone of the HVOF gun.
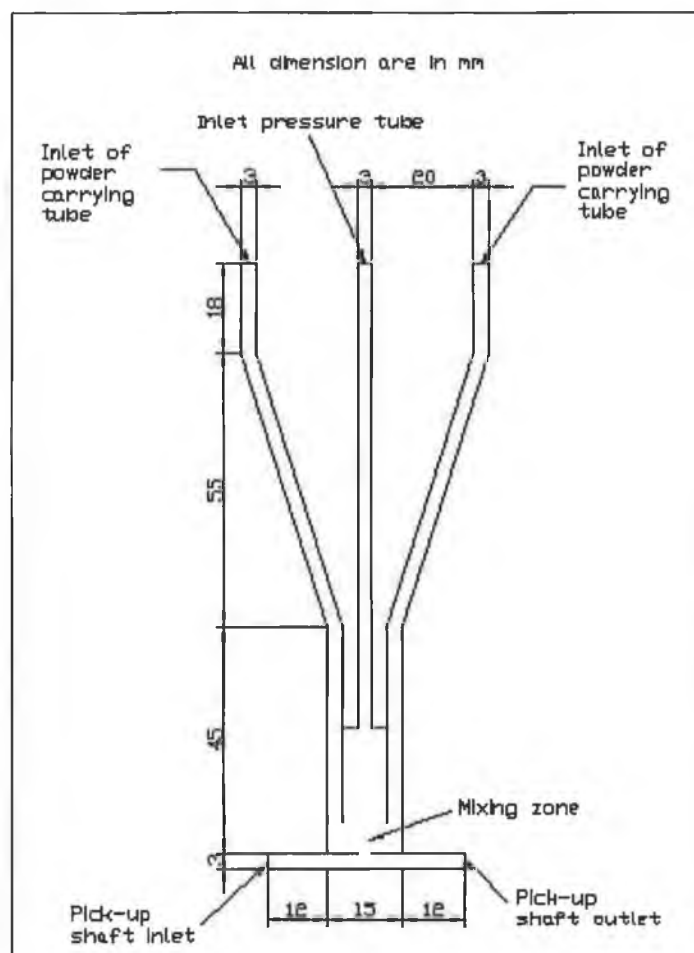
Figure 3.16: Geometry of the powder and nitrogen gas flow tubes.

76

(f) Boundary Conditions

Figure 3.17 shows all the boundary conditions applied. Two types of conditions were applied; velocity and pressure. The velocities of the aluminium and tool steel powders were used as input velocities on the powder carrying tube inlet on top of the model. The velocities of the nitrogen were used as the velocity input on the central tube inlet on top and also on the pick up shaft inlet at the bottom of the model. Zero velocity was applied to some other boundaries as shown in the figure. Zero pressure was applied at the outlet of the pick up shaft (figure 3.17).
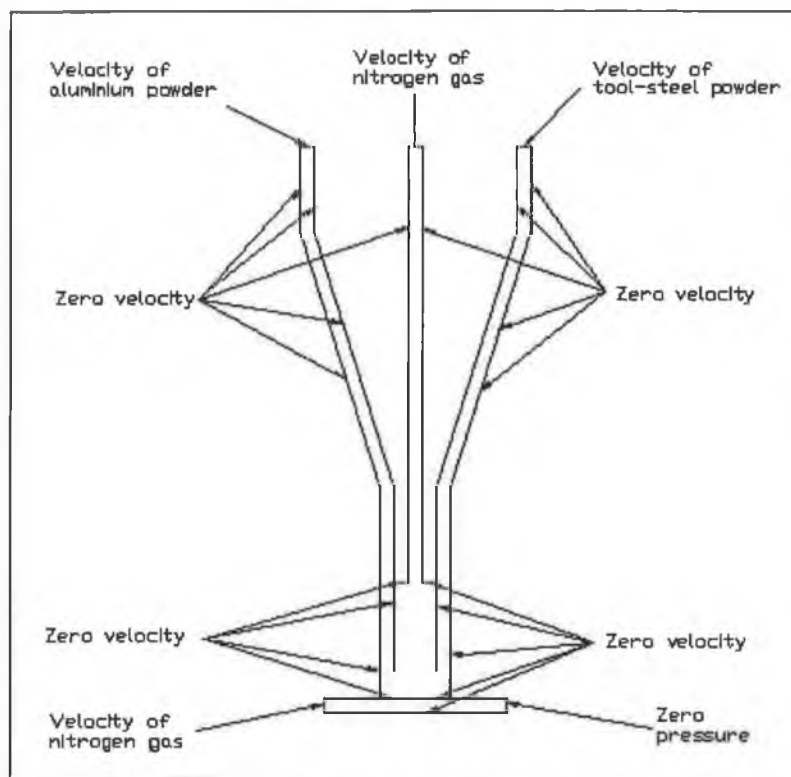
Figure 3.17: Schematic of applied boundary conditions.

(g) Governing Equations

The physical aspect of any fluid flow are governed by three fundamental principles:

(a) Conservation of mass

(b) Newton's second law

(c) Conservation of energy

These fundamental physical principles can be expressed in terms of basic mathematical equations, which in their most general form are either integral equations or partial differential equations [205]. The conservation of energy principle is used to obtain temperature. The first two equations along with the transport equation were used to simulate the nitrogen gas-powder flow during the current research. Those equations are described below.

(1) Continuity Equation

The equation of continuity is really a mathematical statement of the principle of conservation of mass, which states that [206],

"In the absence of nuclear reaction, the rate at which mass enters a particular region = rate at which mass leaves that region + rate of accumulation of mass in that region".

Equation 3.1

If the flow is steady, then the rate at which mass is accumulated within the region is zero. Then the continuity equation becomes [206],

"Rate at which mass enters a region = rate at which mass leaves that region".

Equation 3.2

In differential form continuity equation can be written as;

$$\frac{\partial \rho}{\partial t} + \frac{\partial(\rho u)}{\partial x} + \frac{\partial(\rho v)}{\partial y} = 0 \qquad \text{Equation 3.3}$$

Where

u = velocity of fluid in x direction (cm/s)

v = velocity of fluid in y direction (cm/s)

ρ = density of fluid (g/cm^3)

As the powder was assumed to be incompressible, the first term can be neglected. Then the equation becomes,

$$\frac{\partial(\rho u)}{\partial_x} + \frac{\partial(\rho v)}{\partial_y} = 0 \qquad \text{Equation 3.4}$$

78

Now for incompressible fluid flow through a pipe, there is a relation between the flow rate and pressure [207]:

$$Q = \frac{\pi D^4}{128\mu} \frac{\Delta P}{L}$$

Equation 3.5

Where

Q = flow rate of the fluid (cm^3/s)

μ = viscosity of the fluid (gm/cm.s)

D = diameter of the pipe (cm)

L = length of the pipe (cm)

ΔP = pressure drop in the pipe (dynes/cm^2)

The FLOTRAN CFD uses this equation to calculate the pressure results from the flow rate values.

(2) Transport Equation

The FLOTRAN uses transport equation when multiple species transport option is chosen. It is the mass balance or continuity equation for each of the species. The differential form of transport equation is [208],

$$\frac{\partial(\rho Y_i)}{\partial t} + \frac{\partial(\rho Y_i u)}{\partial x} + \frac{\partial(\rho Y_i v)}{\partial y} = 0$$

Equation 3.6

Where

Y_i = mass fraction of the i_{th} species

ρ = bulk density (g/cm^3)

u = velocity of fluid in x direction (cm/s)

v = velocity of fluid in y direction (cm/s)

For incompressible analysis the first term can be neglected. Then the equation becomes,

$$\frac{\partial(\rho Y_i u)}{\partial x} + \frac{\partial(\rho Y_i v)}{\partial y} = 0$$

Equation 3.7

(3) Momentum Equation

The momentum equation states that [206]:

"For a fluid, which is a continuum of particles, the net force acting on that fluid in any fixed direction equal to the total rate of increase of momentum in that direction"

Equation 3.8

The differential forms of momentum equations in x and y directions are for incompressible flow,

$$-\frac{\delta P}{\delta x} + \frac{\partial}{\partial x}\left(\mu \frac{\partial u}{\partial x}\right) + \frac{\partial}{\partial y}\left(\mu \frac{\partial u}{\partial y}\right) + \rho g_x = \frac{\partial(\rho uu)}{\partial x} + \frac{\partial(\rho uv)}{\partial y}$$

Equation 3.9

$$-\frac{\delta P}{\delta y} + \frac{\partial}{\partial x}\left(\mu \frac{\partial v}{\partial x}\right) + \frac{\partial}{\partial y}\left(\mu \frac{\partial v}{\partial y}\right) + \rho g_y = \frac{\partial(\rho uv)}{\partial x} + \frac{\partial(\rho vv)}{\partial y}$$

Equation 3.10

Where

u =   velocity component in the x direction (cm/s)

y =   velocity component in the y direction (cm/s)

g_x =   component of acceleration due to gravity in the x direction (cm/s^2)

g_y =   component of acceleration due to gravity in the y direction (cm/s^2)

P =   pressure force acting on the fluid (dynes/cm^2)

ρ =   density of the fluid (g/cm^3)

μ =   viscosity of the fluid (g/cm.s)

3.3.6 Design Calibration and Test

This section describes the procedures of different types of calibration tests on the design eventually chosen. Initially the powder flow bench tests were carried out in order to calibration powder flow. This is governed by a needle shaped bolt (figure 3.13). Then the in-situ flow tests were carried out to check functionality of the design.

(a) Powder Flow Bench Tests

The bench tests were carried out to calibrate the movements of the bolts inside the powder holders, named chamber A and B. These tests were carried out without using the previous powder feeder, so no nitrogen gas was involved. The bolts inside chambers were moved upwards and downwards by giving it different number of turns. When the bolts were in full closed position, no powder could flow. With an increase in number of turns, more powder was able to flow through to powder flow tubes and vice versa. Initially chamber A was filled with the aluminium powder. The bolt inside that chamber was turned by specific amounts (for example 1080^0, 1440^0, 1800^0 and so on) to vary the amount of powder flowing through the hole at the end of the chamber. A container of known weight was used to collect the outputted powder over a given length of time (20 seconds). The container was placed at the end of powder flow tubes. The post flow weight of the powder plus container was measured and then the amount of powder flow at a particular bolt rotation was deduced. For each number of turns five readings were taken.

Next the chamber B was filled with the tool-steel powder and the procedure was repeated. To verify the results, chamber A was then filled with the tool-steel powder and chamber B was filled with the aluminium powder, to clarify if there was any discrepancy between the two chambers. Results of all of the above calibration tests are given in chapter four.

(b) In-Situ Flow Tests

The in-situ flow tests were carried out to check the functionality of the designed assembly in terms of mixing the two powders and then carrying them to the combustion chamber. To accommodate the bolts, the newly designed rectangular hopper cover was used, to maintain the internal pressure of the chamber. The rectangular hoper cover is shown in Appendix A (figure A11). Two bolts were put inside the powder holders before filling them with the powders. One powder holder was filled with the aluminium powder and the other was filled with the tool-steel powder. Using the data in table 4.3 (derived from the bench results), the bolts were given different numbers of turns to allow the aluminium and tool-steel powder to flow at ratios' of 1:3, 1:1 and 3:1 into the mixing zone (figure 3.16). The nitrogen gas was passed through the pick-up shaft. A container of known weight was used to collect the resulting powder mixture from the tube connected to the pick-up shaft. The total weight of the mixed powders was measured. The tool-steel powder used in the current research was grey in colour while the aluminium powder was silvery white. Visual inspections were carried out to ensure whether the grey and white powders were properly mixed or not. A magnetic separation technique was then used to calculate the quantity of the aluminium and tool-steel powder in the powder mixture. The technique involved using a magnet to attract the grey tool-steel powder away from powder mixture. The remaining white powder was aluminium. This remaining powder was weighed and the weight of the tool-steel powder was calculated. The experimental time was 6 minutes and powder feed rate used was 38 g/min for all the tests.

3.4 HVOF SPRAYING PROCEDURE

The HVOF process can be used to produce good quality coatings if correct optimisation of its parameters is utilized. The total thermal spray process can be divided into two main steps: surface preparation and spraying process.

3.4.1 Surface Preparation

In most coating processes the integrity of the deposit is critically dependent on the substrate surface condition. The HVOF thermal spraying is no exception, but unlike other methods, it is often applied on site in ambient atmosphere. Thus surface cleanliness in the true scientific sense is never achieved. Cleaning is generally carried out by eroding the substrate surface by a harder material (that is by grit blasting as stated earlier). Heavy-duty applications require the use of large metallic grits which, because of their momentum, can remove surface scale as well as providing a course texture to support the thick coating. But for thinner coatings, grit blasting is usually carried out with finer ceramic (Al_2O_3, SiC and so on) materials. Grit blasting has some disadvantages too. Some substrate materials may be too hard to roughen, while others can become work hardened and thin sections may become distorted. A freshly prepared surface is very reactive (with the oxygen in air) and therefore the thermal spraying operation must be carried out as soon as possible after blasting. Areas not requiring a coated surface are usually masked during grit blasting and spraying, to prevent the build-up of the sprayed material.

3.4.2 Spraying Process

Immediately prior to the deposition of the powder, the substrate needs to be preheated to remove moisture and condensation from the substrate. Preheating will also help in reducing the thermal stress that may arise due to the difference in the co-efficient of thermal expansion between the substrate material and the coating material [44]. Preheating can also improve coating adhesion by encouraging more diffusion between the substrate and the coating [44]. Preheat temperature for aluminium substrate is 50 ^{0}C according to METCO [209], which was obtained by a single pass of the spray gun.

Thermocouple was fixed to the surface of the substrate during calibration of the preheating temperature.

The spray process parameters for the HVOF system depend on the type of application, coating material and substrate. Sulzer METCO has outlined recommended spraying parameters for deposition of the tool-steel and aluminium powder and they are given in table 3.2. Table 3.3 shows the spraying parameters used for lighting the gun. All the safety clothing and corrective ventilation must be in place before spraying start. Both of the powders were then poured into the powder feed hopper. The oxygen bottle was opened and set to the pressure as shown in table 3.3, then its flow rate was adjusted. The compressed air was then turned on and set to pressure and flow rate as shown in table 3.3. The propylene gas was finally set to its parameters. The gun was then lit. Next the flow rates of the oxygen, propylene and compressed air were changed to match the values recommended for spraying. The nitrogen was allowed to flow through the powder feed unit and was adjusted to its parameters. The powders were fed to the gun by switching on the feed button on the gun. The percentages of two powders used were varied by giving the bolts different number of turns. The spraying distance was controlled by the use of the linear motor that also controls the traverse speed of the deposit.

In the current work, the spray parameters had to be optimised in order to deposit the aluminium and tool-steel powder simultaneously. Spray parameters used during optimisation tests are between the range recommended for the tool-steel and aluminium powder as mentioned in table 3.2. The optimisation tests are described in the following section.

The as-sprayed coatings are seldom ready for use. In most practical applications they have to be ground and polished to get required surface roughness. Heat treatment of the sample may be necessary to change coating phase composition, to decrease porosity and residual stress or to improve other coating properties. Among the heat treatment processes, furnace treatment seems to be the most usually applied, especially in research laboratories [44]. The HVOF thermally sprayed coatings can also be machined by different machining processes such as grinding.

Table 3.2: Spray parameters for the tool-steel and aluminium coating material [67,152].

Gun Setting and Spraying Parameters	Powder Material	
	Tool-Steel	Aluminium
Siphon Plug	2	2
Shell	A	A
Insert	2	2
Injector	2	2
Air Cap	3	3
Oxygen Pressure (Bar)	10.3	10.3
Oxygen Flow (SLPM)	278.1	196
Propylene Pressure (Bar)	6.9	6.9
Propylene Flow (SLPM)	74.9	44
Air Pressure (Bar)	5.2	5.2
Air Flow (SLPM)	338.6	269
Nitrogen Carrier Gas Pressure (Bar)	8.6	8.6
Nitrogen Carrier Gas Flow (SLPM)	60	60
Spraying Distance (mm)	220-275	200-300
Spray Rate (g/min)	38	- - -

Table 3.3: Spray parameters for lighting the gun [45].

Name of the Gas	Pressure (psi)	Flow Rate (SLPM)
Oxygen	150	40-44
Propylene	100	35-40
Air	75	60-65
Nitrogen Carrier Gas	125	55

3.5 OPTIMISATION OF SPRAY PARAMETERS

In a functionally graded coating, chemical composition of different layers changes gradually from the bond coat to the top coat. In order to get best quality coatings, control parameters has to changed gradually from recommended values for one coating material to recommended values for other coating material simultaneously with change in composition. But it was not possible in the current research to change the spray parameters during coating deposition. Thus compromised parameters were required to get best possible coating quality. The Design of experiments technique was used in the current project to optimise the spray parameters in depositing aluminium/tool-steel functionally graded coatings. Design of experiments refers to the process of planning the experiment so that it is done in a systematic way and significant data are collected at the end of the experiment. The Taguchi design of experiments method and Factorial design of experiments method are the two Design of experiments methods widely used by researchers all over the world.

The Taguchi method is used where the number of variables is high. It divides all the variables into two types: control variable and noise variable. Control variables are those, whose values can be controlled during operation, while the values of the noise variables can't be controlled during experiment. The Taguchi method does not consider all the interactions involving noise variables. The Factorial design of experiment is used in experiments where it is necessary to study the joint effect of variables. The number of variables in experiment must be low in order to use this type of design of experiment. Number of experiments is not reduced when Factorial method is used.

The flow rate ratio of oxygen to fuel, flow rate of the compressed air, powder feed rate and spray distance are the spray parameters (variables) that affect the quality of the HVOF thermal sprayed coatings. If the value of one of these factors is changed keeping the others constant, coating quality will change. The joint effect of those parameters therefore must be studied to figure out the effect of the spray parameters on coating quality. In the current work a special powder feed system was developed to deliver two powder materials at desired ratio to produce different layers of aluminium/tool-steel graded coatings. Powder feed rate could not be controlled directly during coating deposition due to the use of the modified powder feed system. That is why it was not considered while setting the spray parameter calibration matrix. 3^3 Factorial design of

experiments was employed to establish the effects of the spray parameters on residual stress build-up in aluminium/tool-steel functionally graded coatings. The independent variables were set to three levels, which imply that 27 experiments were necessary to explore the variation of all variables at the chosen levels. Higher value of the oxygen to fuel ratio is the recommended value for the aluminium powder [152], while a lower ratio is recommended for the tool-steel powder [67], however a middle value was chosen between the two recommended values. With a decrease in oxygen to fuel ratio, the flame temperature increases [39]. Melting point of the tool-steel powder is greatly higher than the aluminium powder. Thus, the tool-steel powder requires higher temperature of the flame than the aluminium powder, which is provided by decreasing the oxygen to fuel ratio for the tool-steel powder. Higher value of the compressed air flow rate is recommended for the tool-steel powder [67] and lower one for the aluminium powder [152], however again a middle value was chosen (that was the average of two established values). With an increase in the flow rate of compressed air, particle velocities inside the gun and from the gun to the substrate increase. May be the tool-steel powder requires higher particle velocities than the aluminium powder, which is provided by increasing the flow rate of the compressed air. The range of spray distance used was recommended for both powders [67,152]. Factorial design of experiments matrix is shown in table 3.4.

Table 3.4: Level of 3^3 Factorial design of experiments.

Variables	Levels			Number of	Coating
	0	1	2	Layers	Thickness (mm)
Oxygen to Fuel Ratio	3.75	4.00	4.50		
Flow Rate of the Compressed Air (SLPM)	270	305	340	5	varying
Spray Distance (mm)	225	250	275		

Using table 3.3, twenty seven (3x3 matrix) different types of functionally graded coatings were deposited on aluminium substrates. Residual stress was then measured using the Clyne's analytical method. The Clyne's analytical method of stress measurement is described later. Finally a set of values of spray parameters giving best compromise between low surface residual stress and high deposited coating thickness was identified. The economy of the system was also considered during identification. This set of values of spray parameters was used subsequently in the project to deposit different types of aluminium/tool-steel functionally graded coatings.

3.6 COATING CHARACTERIZATION TECHNIQUES

Coatings deposited by any type of coating technique must be scientifically characterized before they go into service. Visual inspection (either macro or microscopic) is the primary characterization technique used to gain coating microstructural information such as chemical composition, grain morphology and orientation, defects and so on. Mechanical properties such as coating adhesion can also be measured using the optical techniques [210]. There are numerous optical techniques available such as the optical microscope and scanning electron microscope. In most cases the coating surface is grinded and polished properly before optical examination. Blemishes, such as scratches, deformation, pull-out, cracks, contamination and so on can result from poor surface preparation according to Glancy [211]. Electrical properties, thermal properties, mechanical properties (hardness, adhesion, fracture, toughness, elastic modulus, wear resistance) and residual stress should also be evaluated.

3.6.1 Microscopy

(a) Metallographic Preparation

Metallographic specimen preparation is a valuable tool for characterization of thermally sprayed coatings. Metallographical process can be divided into four different areas; sectioning, mounting, grinding and polishing.

(1) Sectioning

Sectioning is necessary when component under investigation is too large to handle effectively. Sectioning control is essential as inaccurate operation of sectioning equipment causes debonding and over-heating of the sectioned surface [212]. The Buehler Abrasimet 2 Abrasive Cutter is used in the Materials Processing Research Centre (MPRC), which relies on manually applied force to section the specimen, hence the rate at which sectioning proceeds, is determined by the operator. Along with the operating parameter, selection of the cut-off wheel is also crucial, this is generally depends on the material to be sectioned. Generally ceramic materials are sectioned with

a diamond cut-off wheel [213], ferrous materials are sectioned with a Al_2O_3 abrasive wheel, while SiC wheel is used to section non-ferrous materials [214]. In all cases the wheel and the specimen is water-cooled to prevent thermal damage. Table 3.5 shows various types of cut-off wheels available in the MPRC.

Table 3.5: Various types of cut-off wheels available in the MPRC.

Abrasive wheel type	Material to be cut
HHH	Extremely hard ferrous alloys
HH	Hard ferrous materials in large sections
H	Hard ferrous materials and general cutting under 25 mm
HHS	MMC's
NF	Non-ferrous materials
FS	Soft ferrous materials
Ultra Thin	Delicate materials

(2) Mounting

Next step in metallographic preparation is mounting. There are two techniques available; hot-compression mounting and cold-castable mounting. Hot-compression mounting involves setting the sample in thermoplastic or thermosetting resin subjected to elevated temperature (140-200) ^{0}C and high pressures (20-40 MPa) for 7-10 minutes. In cold-castable mounting, the sample is cured in epoxy at 80 ^{0}C for 60 minutes and mounted in a vacuum. The second technique should be used to determine the true structure of thermal spray coatings according to Glancy [215]. In the current research the Buehler Simplimet 2000 Mounting Press was used to mount different types of graded coatings and powder samples.

(3) Grinding

Next step of metallographic preparation is grinding. The Buehler Motopol 2000 Semi-Automatic Specimen Preparation unit is used in the MPRC. Automation of grinding and polishing stage is essential as it eliminates operational error such as applied load and rotation per minute. Abrasive machining or grinding is divided into two stages; plane grinding and fine grinding.

(a) Plane Grinding

The function of plane grinding is to remove the damage experienced during sectioning and bring all the specimens in the holder to the same plane. P60 (very coarse) silicon carbide paper is used to machine away the excess damage surface. This paper lasts a duration of around 60 seconds, after which the abrading particles are washed away.

(b) Fine Grinding

The removal of the deformation experienced during the plane grinding stage is called fine grinding. Again silicon carbide paper is used to fine grind the samples, but the procedure moves from a coarse (P200) up to a fine abradable paper (P1200). Each abrasive size is used for five minutes in turn, starting from P200 working towards P1200. In the current work, only the P240 and P600 abradable papers were used to fine grind the graded coating samples. Each paper was used for a duration of 4 minutes.

(4) Polishing

Optical microscopy requires that a specimen must be both flat and highly reflective. Thus polishing is an essential step in metallographic preparation. Polishing also removes deformation induced during fine grinding, plus removes all smears from the surface of the specimen. Again according to Whichard et al. [216], X-Ray diffraction analysis requires the specimens to be properly polished, especially to evaluate each phase in thermally sprayed coatings [217]. There are two steps involved in polishing; diamond polishing and oxide polishing.

Diamond abrasives are very effective during the polishing stage and sufficient enough to prepare a coating for general inspection. The most common diamond particle sizes are 6, 3 and 1 micron. Normally each abrasive size is used for 5 minutes in turn. Starting from 6 micron working towards 1 micron. For the aluminium/tool-steel graded coating specimens, only the 6 and 3 micron particles were used during diamond polishing stage. Each particle was used for a duration of 3 minutes. Oxide polishing is used where photographic grade polishing is required. There are many commercial final abradables available, such as aluminium oxide, silicon oxide, magnesium oxide and

cerium oxide. Normally the oxide-polishing step is completed in just one minute at a low force using a high nap polishing cloth. The nap cloth is soft and it secures the abradable during the polishing process. In the current research, an oxide polishing particle (0.05 micron) was used for a duration of 3 minutes to prepare the graded specimens.

(b) Metallographic Etching

When observed under microscope, the metallographically prepared specimens reflect incident light uniformly [218]. To observe small differences in microstructure some means of producing image contrast is required. The technique of producing the image contrast is known as "etching". There are different types of etching techniques available. Their names are given in table 3.6.

Optical etching uses special illuminating techniques to produce brightfield illumination, which is characterized by normal reflection of the incident ray from the sample surface through an objective lens. Different reflective intensities appear as different shades of dark and bright, so they can be identified.

Physical etching involves deposition of a transparent or interference layer, such as titanium oxide, using physical methods onto a sample surface. Incident light is partially absorbed by the layer and repeatedly reflected at the layer/specimen interface before it exists. The reflected rays interfere with each other and produce a contrast that appears in colour under microscope.

Electrochemical etching, often known as chemical etching, involves reduction or oxidation of metallic specimens. A wide variety of etchants are available, including acids, base alkaline solutions, neutral solutions, mixture of solutions, molten salts and gasses. The rate of etch attack is mainly determined by the degree of dissociation and electrical conductivity of the etchant. Etching time may vary from seconds to hours.

Table 3.6: Various methods of etching.

Metallographical etching					
No alteration of the surface	Alteration of the surface				
Optical etching	Physical etching			Electrochemical etching	
-	Interference layers	Ion etch.	Thermal etch.	Classical	Electrolytic
• Darkfield • Phase contrast • Polarized light • Differential-interference contrast	• Evaporation • Reactive sputtering			•Dissolution etching • Heat tinting • Precipitation etching	• Anodic etching • Anodizing

(c) Optical Microscope

The optical microscope is the first basic tool of material analysis used to examine, evaluate and quantify the microstructure of various materials. Its main advantage being relatively cheap in its simplest form compared to other microscopic observation instruments and easy to operate. Operating in its reflecting mode, it is well capable of revealing polished and etched material specimens. It comprises of an illumination system, condenser, light filters, objective lens, eyepiece, stage and stand. The optical microscope enables analysing of the [219],

1. Microstructure and constitutes of any surface including coatings
2. Fraction and size of voids in the coating
3. Fraction and size of unmelted particles in the coating
4. Deformation (mechanical or thermal) of the substrate near the coating
5. Distribution of phases in the coating if an etchant is used
6. Fabrication and heat-treatment history of the deposit if an etchant is used
7. Braze and weld joint integrity
8. Surface failure

In most cases, prior to the microscopic observation, the surface of the sample must be prepared metallographically by machining, grinding, polishing and finally etching. However there are some materials including nitrides, certain carbides and intermetallic phases, which do not need etching [220]. As the total field of microscopic observation is

no greater than a few square millimetres, it is important to select a typical part of the surface of the material to get representative information about that material.

The Reichert "MeF2" Universal Camera Optical Microscope was used in the current research to obtain microstructure of aluminium/tool-steel coated aluminium sample.

(d) Scanning Electron Microscope

The optical microscope mentioned above is used for small scale material characterization. As the sophistication of investigations increased, either the Transmission Electron Microscope (TEM) or the Scanning Electron Microscope (SEM) often replaces the optical microscope. Both of those instruments have superior resolution and depth of focus. Because of its reasonable cost and wide range of application that it provides, the SEM is the preferred instrument used in material studies. The SEM provides the investigator with a highly magnified image of the surface of a material that is very similar to what one would expect if one could actually "SEE" the surface visually. The resolution of the SEM can approach a few nm (nano-metre) and it can operate at magnifications from about 10X to 300000X. There are various applications of the SEM, such as [219]:

1. Examinations of metallographically prepared samples at magnifications well above the useful magnification of the optical microscope
2. Examination of fractured surfaces and deeply etched surfaces requiring depth of field well beyond that possible by the optical microscope
3. Evaluation of crystallographic orientation of features on a metallographically prepared surface
4. Evaluation of chemical composition gradients on the surface of bulk samples over distances approaching 1 μm

Schematic of a SEM is shown in figure 3.18. In a scanning electron microscope, a source of electron is focused in a vacuum into a fine probe that is passed over the surface of a specimen. A diffusion or turbomolecular pump creates the vacuum, while an electron gun provides the source of electrons. A series of lenses are used to demagnify the "spot" of electrons on to the specimen surface. As the electrons penetrate

the surface, a number of interactions occur that result in the emission of electrons or photons from the surface. Detectors collect the emitted (output) electrons that are used to modulate the brightness of a cathode ray tube (CRT). Every point that the electron beam strikes on the sample is mapped directly onto a corresponding point on the screen. The collective points that are displayed onto a monitor or else transmitted to a photographic plate provide an image of the sample.

Samples used in a scanning electron microscope can be of any form, as in any solid or liquid having a low vapour pressure. Electrically conductive materials can be prepared using standard metallographic polishing and etching techniques. Non-conducting materials are generally coated with a thin layer of carbon, gold or gold alloy. Samples must be free from water, organic cleaning solutions, and remnant oil-based films and must be electrically grounded to the holder. Fine samples, such as powder, are dispersed on an electrically conducting film. The scanning electron microscope used in the current study, was the "Stereoscan 440" developed by Leica Cambridge Ltd.
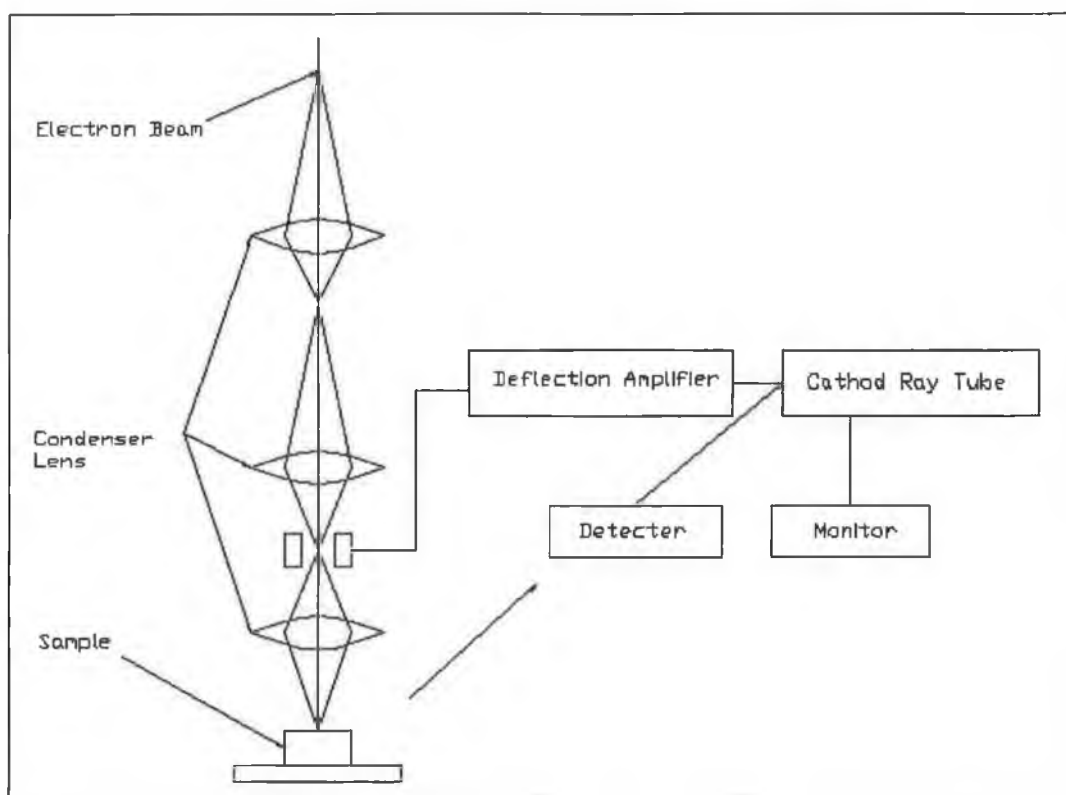
Figure 3.18: Schematic of a scanning electron microscope (SEM).

3.6.2 Energy Dispersive X-Ray Spectroscopy (EDS)

The energy dispersive spectroscopy is frequently used in electron column instruments like the scanning electron microscope (SEM), transmission electron microscope (TEM) to detect different elements on the periodic table. With modern detectors and electronics, most EDS systems can detect X rays from elements in the periodic table above beryllium. Qualitative as well as quantitative analysis can be done using the EDS. Other applications include quality control and test analysis in many industries including computer, semiconductors, metals, cements and polymers. The EDS has been used in medicine in the analysis of blood, tissues, bones and organs [219].

Schematic of an EDS is shown in figure 3.19. Primary X-ray radiation is incident the sample. The sample then omits secondary radiation. The various wavelengths in the secondary radiation emitted by the sample are separated on the basis of their energies by means of a Si(Li) counter and a multichannel analyser (MCA). This counter produces pulses proportional in height to the energies in the incident beam, the MCA then sorts out the various pulse heights. Thus various elements can be detected [221].
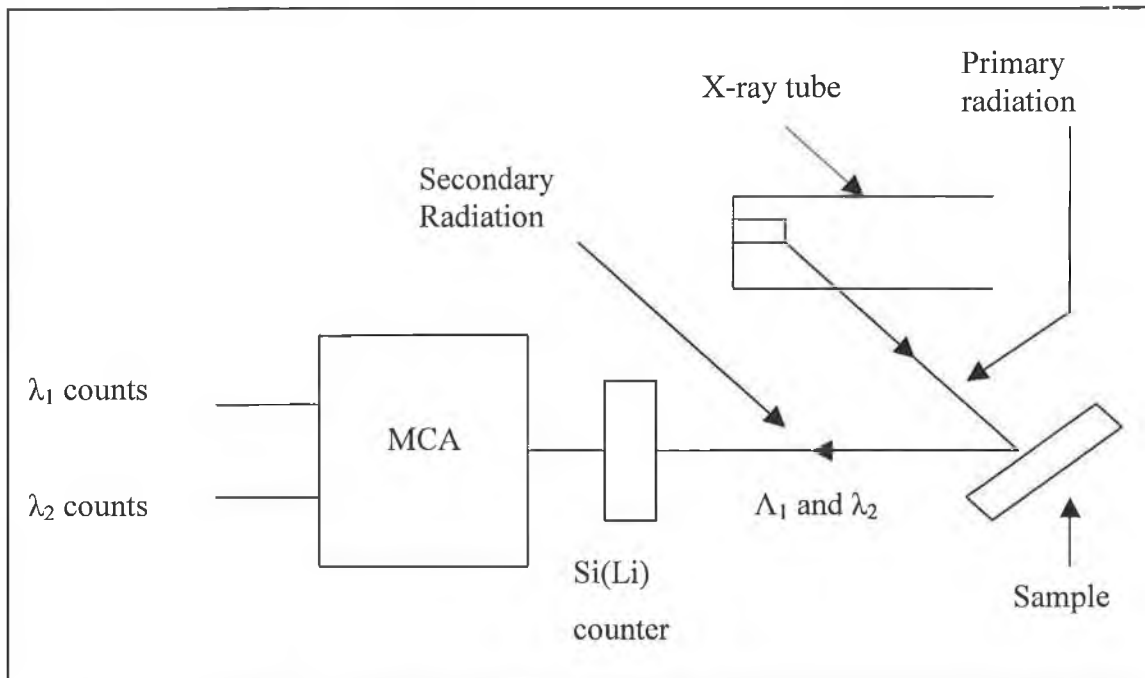
Figure 3.19: Schematic of an energy dispersive X-ray sprectroscopy (EDS).

Any type of sample can be used in the EDS analysis as long as it can be put on the specimen stage of the microscope. The choice of accelerating voltage should be

determined by the type of sample analysed, since the X-ray generation volume depends on the electron range in the material.

In the current research a scanning electron microscope with an EDS X-ray instrument, provided by Princeton Gamma-Tech company was used to investigate aluminium/tool-steel functionally graded coatings.

3.6.3 X-Ray Diffraction Phase Characterization

The X-ray diffraction technique is a powerful material characterization technique used to identify structural properties such as strain state, grain size, phase composition and orientation and so on. Polycrystalline materials are made up of individual crystal, which in turn made up of families of identical plane of atoms, with a fairly uniform interplaner spacing d. X-ray beams will be diffracted from a given family of planes at a certain angles of incident known as Braggs angle. So diffraction occurs at an angle of 2θ, defined by Bragg's law [221],

$$n\lambda = 2d \sin \theta$$
Equation 3.11

Where

n = integer

d = lattice spacing of crystal planes (mm)

θ = the angle of diffraction (^{0})

λ = wavelength of X-ray beam (mm)

For diffraction to be observed, the detector must be positioned so as to receive the diffracted ray at angle of 2θ. The crystal must be oriented so that the normal to the diffracting plane is coplanar with the incident and diffracted beam.

One of the most important uses of XRD is phase identification of materials. Identification is done by comparing the measured d spacing in the diffraction pattern and, to a lesser extent, their integrated intensities with known standards in the JCPDS (Joint Committee on Powder Diffraction Standards, 1986) Powder Diffraction software, attached to the DIFFRACT+ Measurement Part 2002 X-ray diffraction system. In the

current work, XRD was used to identify phases present in aluminium/tool-steel graded coating deposited onto an aluminium substrate.

3.6.4 Measurement of Mechanical Properties

(a) Hardness Measurement

There are usually three types of methods of measuring hardness; Static indentation tests, Dynamic hardness tests and Scratch tests. The Static indentation tests are most widely used. These tests are reproducible and can be accurately quantified. The Rockwell hardness test, Brinell hardness test, Vickers hardness test and Knoop Hardness test are all variations of the static hardness test.

The Rockwell hardness test and Brinell hardness tests are the examples of macrohardness test. The Rockwell test includes application of a minor load by using an indenter to the surface of the testing sample and establishing a zero datum position. The major load is then applied for a certain period and then removed. Difference in depth of indentation from the zero datum represents the hardness value, which is expressed as combination of a hardness number and a scale symbol. There are several scales representing the hardness. These scales depend on the types of indenter used and amount of applied load [151]. While in the Brinell hardness test, the load is applied using a 5 to 10 mm diameter steel or tungsten carbide ball on the flat surface of the test specimen. Hardness is determined by taking the mean diameter of the indentation and calculating the Brinell hardness number (HB) by dividing the applied load by the surface area of the indentation according to following formula:

$$HB = \frac{2P}{\pi D \left(D - \sqrt{D^2 - d^2} \right)}$$

Equation 3.12

Where

P = load in kg

D = ball diameter in mm

d = diameter of the indentation in mm

Microhardness test includes the Knoop and Vickers hardness tests [151]. Both of these tests involve forcing a diamond indenter of specific geometry into the surface of the test material at various loads. For the Knoop test load applied is less than 200 gm. The Knoop hardness number (HK) is the ratio of the load applied to the indenter to the uncovered projected area:

$$HK = \frac{P}{A} = \frac{P}{CL^2}$$
Equation 3.13

Where

P = applied load in kg

A = uncovered projected area of indentation in mm^2

L = measured length of long diagonal in mm

C = a constant for the indenter relating projected area of the indentation to the square of the length of the long diagonal

In the Vickers hardness test, the indenter is a highly polished, pointed, square-based pyramidal diamond with face angles of 136^0. The applied load is greater than 200 gm. With the Vickers indenter, the depth of indentation is about one-seventh of the diagonal length. The Vickers hardness number (HV) is the ratio of the load applied to the indenter to the surface area of the indentation:

$$HV = \frac{2P\sin\left(\frac{\theta}{2}\right)}{D^2}$$
Equation 3.14

Where

P = applied load in kg

D = mean diameter of the indentation in mm

θ = angle between opposite faces of the diamond (136^0)

In the current project, the Vickers hardness testing was used to measure the hardness values for different types of aluminium/tool-steel functionally graded coatings.

(b) Thickness Measurement

Thickness of thermally sprayed coatings may vary from the nm to mm range. Highly accurate measurement techniques such as the Fischerscope multi thickness measuring instrument is needed to measure the thickness of coatings in the μm range. But for thicker coatings, less expensive methods such as the dial gauge measurements may be used. Those two methods along with the microscopic method are described below.

(1) Fischerscope Multi Thickness Measuring Instrument

The Fischerscope instrument is based on eddy current and magnetic induction principles as described in ASTM E367-69 [222]. Schematic of an eddy current gauge is shown in figure 3.20. A high frequency current is passed through the sensing coil of the instrument. An eddy current is induced into the testing material when it is brought closer to the coil. The induced current experiences a loss in back emf (electromotive force) energy, through each medium (that is the coating and substrate). Impedance of the sensing coil is changed due to loss of energy. The impedance difference from the substrate and coating is converted into coating thickness values. This technique has an accuracy of 0.1 μm.
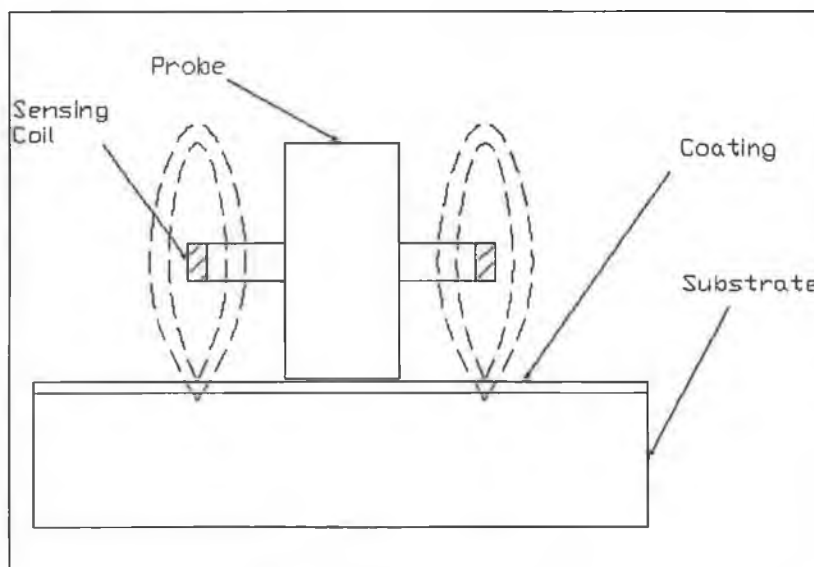
Figure 3.20: Schematic of an eddy current gauge.

(2) Dial Gauge Measurement

As mentioned earlier the dial gauge method is used to measure thickness of relatively thick coatings. The gauge is set up on a mount resting on a flat surface. First the substrate is placed on the flat surface and the dial gauge is zeroed to exclude its thickness. After coating deposition the sprayed part is again put onto the flat surface. The dial gauge then measures the displacement the gauge has moved due to its new height. It has an accuracy of $\pm 25 \mu m$. This measurement system was used in the current project to measure coating thickness and deflection of spray deposits as a result of residual stress.

(3) Microscopic Measurement

The microscopic analysis is a destructive method of coating thickness measurement that uses optical or scanning electron microscope to measure coating thickness. Specimens must be sectioned, mounted, grinded and polished before thickness measurement. In some cases etching is also necessary. Measurement error generally increases with decrease in magnification, that's why scanning electron microscope gives better result than optical microscope. According to ISO 1463, magnification chosen should be such that the field of view is between 1.5 to 3 times the coating thickness [223].

(c) Young's Modulus Measurement

The Elastic modulus (E_c) and Poisson's ratio (v_c) are two of the factors effecting the residual stress distribution in a coating-substrate system, hence determination of those properties of functionally graded aluminium/tool-steel coatings was required in the current project. Young's modulus determination of a coating is difficult, as it is attached to a substrate. In the current work, the cantilever beam method described by Rybicki et al. [224] was used to determine the Young's modulus and Poisson's ratio of graded coatings. The Laminate plate theory is used in the cantilever beam method, to relate unknown E_c and v_c to the applied loads. This theory assumes a linear strain distribution through the thickness of the coated cantilever beam and plane stress conditions.

Figure 3.21 shows the experimental set up used to determine the Young's modulus and Poisson's ratio of graded coatings. Two biaxial strain gauges were placed on the coating surface, while two more were placed directly opposite on the substrate side. A force was applied at the end of the substrate, thus the strain was measured to yield the two properties using the Laminate plate theory.
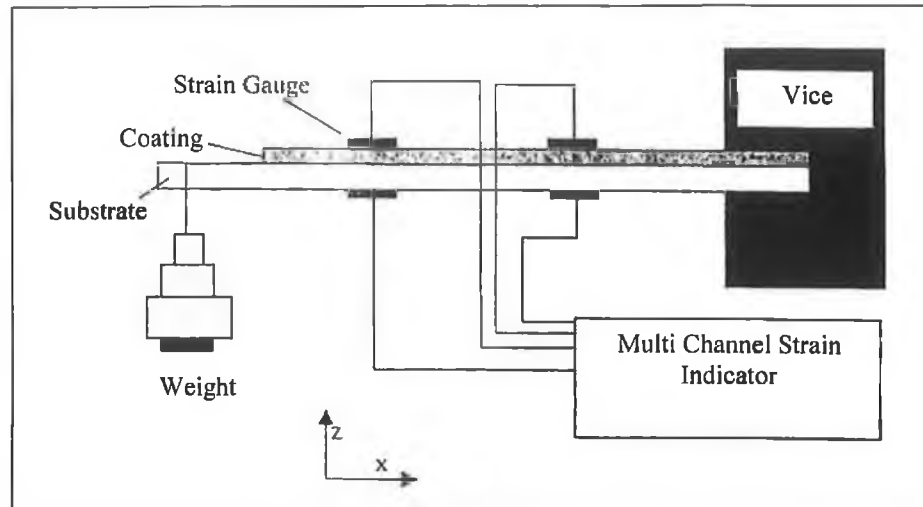
Figure 3.21: The cantilever approach for measuring the Young's modulus and Poisson's ratio adopted from [22].

Figure 3.22 shows a schematic of the strain (a) and stress (b) distribution respectively for a coated cantilever with applied load. The equilibrium equations for the coated beam are as follows [224], where the stresses are related to the forces and moments by:

$$0 = F_x = \iint \sigma_x dz dy \qquad \overline{M} = M_x = \iint \sigma_z z dz dy \qquad \text{Equation 3.15}$$

$$0 = F_y = \iint \sigma_y dz dy \qquad 0 = M_y = \iint \sigma_y z dz dy \qquad \text{Equation 3.16}$$

For the coated beam,

$$F_x = w(\sigma_{xsi} + \sigma_{xsg})\frac{t_s}{2} + w(\sigma_{xci} + \sigma_{xcg})\frac{t_c}{2} \qquad \text{Equation 3.17}$$

$$M_x = w\left[\sigma_{xsg}\frac{t_s^2}{2} + \left(\sigma_{xsi} - \sigma_{xsg}\right)\frac{t_s^2}{3}\right] + w\left[\sigma_{xci}\left(t_c\right)\left(\frac{t_s}{2} + \frac{t_c}{6}\right) + \sigma_{xcg}\left(t_c\right)\left(\frac{t_s}{2} + \frac{t_c}{3}\right)\right]$$

<div align="right">Equation 3.18</div>

$$F_y = w\left(\sigma_{ysi} + \sigma_{ysg}\right)\frac{t_s}{2} + w\left(\sigma_{yci} + \sigma_{ycg}\right)\frac{t_c}{2}$$

<div align="right">Equation 3.19</div>

$$M_y = w\left[\sigma_{ysg}\frac{t_s^2}{2} + \left(\sigma_{ysi} - \sigma_{ysg}\right)\frac{t_s^2}{3}\right] + w\left[\sigma_{yci}\left(t_c\right)\left(\frac{t_s}{2} + \frac{t_c}{6}\right) + \sigma_{ycg}\left(t_c\right)\left(\frac{t_s}{2} + \frac{t_c}{3}\right)\right]$$

<div align="right">Equation 3.20</div>

Where

w =   width of both the coating and substrate (m)

$\overline{M}$ =   applied bending moment at gauge location (N-m)

P =   applied load (N)

t_c and t_s =   thickness of the coating and substrate respectively (m)

ε_{xcg} and ε_{ycg} = longitudinal and traverse strain on the coating respectively

ε_{xsg} and ε_{ysg} = longitudinal and traverse strain on the substrate respectively

ε_{xci} and ε_{yci} = longitudinal and traverse strain at the coating interface respectively

ε_{xsi} and ε_{ysi} = longitudinal and traverse strain at the substrate interface respectively

σ_{xcg} and σ_{ycg} = longitudinal and traverse stress on the coating respectively (Pa)

σ_{xsg} and σ_{ysg} = longitudinal and traverse stress on the substrate respectively (Pa)

σ_{xci} and σ_{yci} = longitudinal and traverse stress on the coating interface respectively (Pa)

σ_{xsi} and σ_{ysi} = longitudinal and traverse stress on the substrate interface respectively (Pa)

The surface stresses, σ_{cg} and σ_{sg}, are related to the strains and mechanical properties of the coating and substrate from the following:

$$\sigma_{xcg} = \frac{E_c}{\left(1 - v_c^2\right)}\varepsilon_{xcg} + v_c\varepsilon_{ycg}$$

<div align="right">Equation 3.21</div>

$$\sigma_{xsg} = \frac{E_s}{\left(1 - v_s^2\right)}\varepsilon_{xsg} + v_s\varepsilon_{ysg}$$

<div align="right">Equation 3.22</div>

Where

E_c = Young's modulus of the coating (Pa)

E_s = Young's modulus of the substrate (Pa)

v_c = Poisson's ratio of the coating

v_s = Poisson's ratio of the substrate
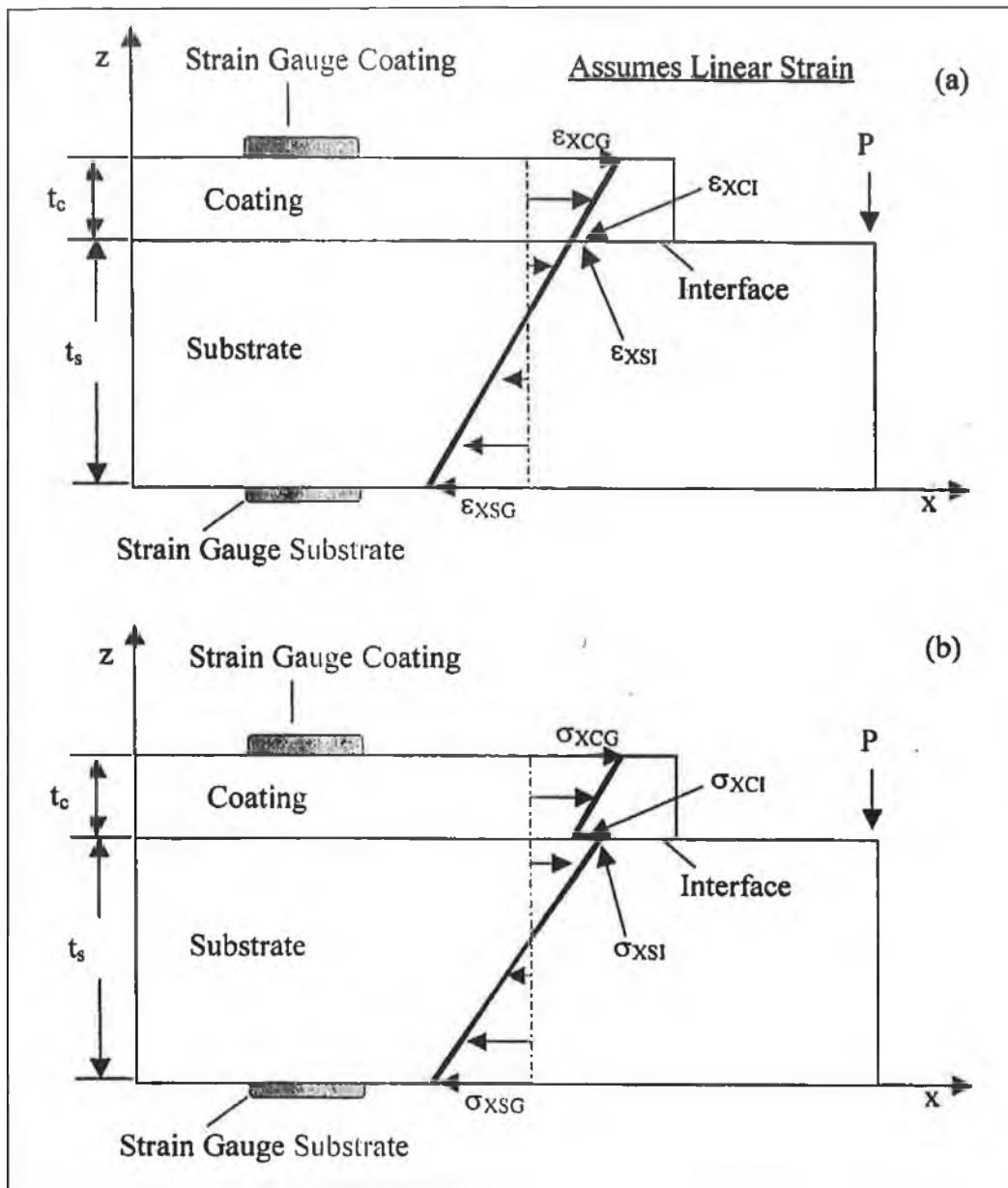
Figure 3.22: Strain and stress distribution for a coated cantilever beam with applied load P adopted from [22].

The interface stresses can be calculated from:

$$\sigma_{xci} = \frac{E_c}{\left(1 - v_c^2\right)} \varepsilon_{xci} + v_c \varepsilon_{yci} \qquad \text{Equation 3.23}$$

103

$$\sigma_{xsi} = \frac{E_s}{\left(1 - v_s^2\right)} \varepsilon_{xsi} + v_s \varepsilon_{ysi} \qquad \text{Equation 3.24}$$

The surface strains ε_{xcg}, ε_{ycg}, ε_{xsg} and ε_{ysg} are measured with strain gauges, while the interface strains ε_{xci}, ε_{yci}, ε_{xsi} and ε_{ysi} can be found from the assumption of a linear strain distribution for the surface strains.

The least squares method minimizes a function composed of four equilibrium equations. The function Φ (E_c, v_c) is based on minimizing the maximum stress difference [224]. $\overline{M}$ is the applied force times the distance between the load location and the gauge location.

$$\phi(E_c, v_c) = \frac{(t_c + t_s)^2}{36} \left[F_x^2 + F_y^2\right] + \left[M_x - \overline{M}\right]^2 + \left[M_y\right]^2 \qquad \text{Equation 3.25}$$

(c) Yield Stress Measurement

In order to find out the stiffness of aluminium/tool-steel functionally graded aluminium samples, graded specimen was tensile tested with the Hounsfield H20K-W tension/compression tester. The rate of displacement was set at 5 mm/min. The data was transferred to Excel spreadsheet to obtain stress-strain relation. From the stress-strain curve, yield stress of aluminium/tool-steel coated aluminium sample was determined.

3.6.5 Measurement of Residual Stress

Residual stress is a major problem in the production of thermally sprayed coatings especially in thick coatings. It can cause spallation and debonding of coating from the substrate. There are several methods of measuring residual stress in thermally sprayed coatings including the X-ray diffraction method [225-227], hole drilling method [228-235], micro-raman spectroscopy method [236,237], layer removal method [238-240], Almen test method [241-245] to mention a few. The X-ray diffraction and the Hole drilling method are the most used methods at the moment, while simpler method of determining residual stress are found using an analytical method derived by Clyne

[246]. Hole drilling method and Clyne's analytical method of stress determination are described below.

(a) Hole Drilling Method

The Hole drilling residual stress method is a semi-destructive method as it causes very localised damage and in many cases does not significantly affect the usefulness of the specimen. The test is carried out by applying a three rosette type strain gauge to the surface of the coating and connecting it up to a strain-recording instrument [229-232]. The strain gauge rosettes used in the current work were the CEA-06-062UM-120 precision strain gages, which are constructed of self-temperature compensated foil on a flexible polymer carrier and incorporate a centering target for use of a precision milling guide. A hole is drilled through the coating via the central region of the strain gauge to relax the residual stress in the material. For accuracy, it is important to drill the hole perpendicular to the surface exactly at the central region of the strain gauge. The combination of drilling at high cutting rate and low drilling depth per drilling step guarantees a stress free drilling process with negligible heat development [233]. Residual stress is based on Kirch's theory [234]. Kirch calculated the strain distribution around a circular hole, made upon an infinite plate, loaded with plane stress. Certain hypothesis must be launched:

1. The material itself is an isotropic and linear elastic material
2. The tension perpendicular at the surface is negligible
3. The main tension direction are constant along the depth
4. The internal tensions are not in excess of one-third of the yield strength
5. The hole is concentric with the rosette

The RS-200 milling guide is a high precision instrument used for stress analysis by the hole drilling method and was the unit used in the current research. The gauge and surface of the coating is thoroughly cleaned with alcohol before the gauge is attached. An adhesive is used to bond the gauge to the surface. The hole is drilled by a carbide precision cutter, which is powered by a high-speed air (pneumatic) unit. According to ASTM E837-95 [235], the residual stress is calculated using the following equation:

$$\sigma_{min,}\,\sigma_{max} = \frac{\varepsilon_3 + \varepsilon_1}{4A} \pm \frac{\sqrt{(\varepsilon_3 - \varepsilon_1)^2 + (\varepsilon_3 + \varepsilon_1 - 2\varepsilon_2)^2}}{4B} \qquad \text{Equation 3.26}$$

Where

$$A = -\frac{1+v}{2E}a \qquad \text{Equation 3.27 (a)}$$

$$B = -\frac{1}{2E}b \qquad \text{Equation 3.27 (b)}$$

$$\tan 2v = \frac{\varepsilon_3 + \varepsilon_1 - 2\varepsilon_2}{\varepsilon_3 - \varepsilon_1} \qquad \text{Equation 3.27 (c)}$$

E and v are the Young's modulus (Pa) and Poisson's ratio respectively for the coating material, a and b are constant for the blind holes according to the data supplied by the gauge manufacturer, σ_{min} and σ_{max} are the minimum and maximum residual stress (Pa) respectively, while ε_1, ε_2 and ε_3 are the strain values in the three axis directions.

(b) Clyne's Analytical Method

The Clyne's analytical method is a quick method of measuring residual stress compared with other methods such as the X-ray diffraction and hole drilling method. The simplest coating system consists of just two layers, the coating and the substrate. But actually it may be appropriate (particularly for thick coatings) to consider the coating being deposited as a series of layers. It is useful therefore to consider the situation in terms of misfit strains, that is, relative differences between the stress free dimensions of various layers. Tsui and Clyne [246] used an analytical method, which considers a pair of plates bonded together with a misfit strain Δε in the x-direction as shown in figure 3.23. Stress distribution through coating thickness, stress at the coating-substrate interface, as well as at the bottom of the substrate can be measure using Clyne's method. The resultant stress distribution, for thick coatings, was derived by Clyne [246], found for the simple misfit strain case using the following equations:

106

Stress at the middle of the j_{th} layer

$$\sigma_{cj} = \frac{F_j}{bw} - E_c'\left(k_j - k_{j-1}\right)\left((j-0.5)w - \delta_j\right) +$$

$$\sum_{i=j+1}^{n}\left(\frac{-E_c'F_i}{b\left(h_s E_s' + (i-1)wE_c'\right)} - E_c'\left(k_i - k_{i-1}\right)\left((j-0.5)w - \delta_i\right)\right) +$$

$$\frac{F_{CTE}}{bh_c} - E_c'\left(k_c - k_n\right)\left((j-0.5)w - \delta_n\right)$$
Equation 3.28

Stress at the top of the substrate

$$\sigma_{st} = \sum_{i=1}^{n}\left(\frac{-E_s'F}{b\left(h_s E_s' + (i-1)wE_c'\right)} + E_s'\left(k_i - k_{i-1}\right)\left(h_s + \delta_i\right)\right) -$$

$$\frac{F_{CTE}}{bh_s} + E_s'\left(k_c - k_n\right)\left(h_s + \delta_n\right)$$
Equation 3.29

Stress at the bottom of the substrate

$$\sigma_{st} = \sum_{i=1}^{n}\left(\frac{-E_s'F}{b\left(h_s E_s' + (i-1)wE_c'\right)} + E_s'\left(k_i - k_{i-1}\right)\delta_n\right) -$$

$$\frac{F_{CTE}}{bh_s} + E_s'\left(k_c - k_n\right)\delta_n$$
Equation 3.30

$\Delta\varepsilon$, E_c' and E_s' are given as,

$$\Delta\varepsilon = \left(\alpha_s - \alpha_c\right)\Delta T$$
Equation 3.31

$$E_c' = \frac{E_c}{\left(1 - v_c\right)}$$
Equation 3.32

$$E_s' = \frac{E_s}{\left(1 - v_s\right)}$$
Equation 3.33

Where

α_c = co-efficient of thermal expansions of the coating $(^0C)^{-1}$

α_s = co-efficient of thermal expansions of the substrate $(^0C)^{-1}$

v_c = Poison's ratio of the coating

v_s = Poison's ratio of the substrate

ΔT = difference between deposition and room temperature (^0C)

$F_j =$ force on the j_{th} layer (N)

$F_{CTE} =$ force on the specimen due to co-effiecient of thermal expansion mismatch (N)

$b =$ width of the specimen (m)

$w =$ thickness of each layer (m)

$k_j =$ curvature of the j_{th} layer $(m)^{-1}$

$k_c =$ curvature of the specimen after cooling $(m)^{-1}$

$k_n =$ curvature of the specimen before cooling $(m)^{-1}$

$\delta =$ distance of coating-substrate interface from neutral axis (m)

This method was found to be very effective in the study carried out by Stokes [22] to measure residual stress in WC-Co deposits; hence the method was used in the present study. In order to measure residual stress, (10mm X 80mm X 0.90mm) aluminium strips were coated with aluminium/tool-steel graded coating to desired thickness, as shown in figure 3.24. A photograph of the coated aluminium sample is shown in figure 3.25. Following deposition, the distributed stresses were deducted by measuring the resulting deflection of the samples and using equations 3.28 to 3.30.

Deposit

Substrate

w

y

z

x

$\Delta\varepsilon$

Force Balance: $w \int_{-h_s}^{h_c} \sigma(y)dy = 0$

P   P

-P   -P

ε (millistrain)

-1   0   1 $y=h_c$

$y=0$

$y=h_s$

σ (MPa))

-20   0   20

P   P

M   M

-P   -P

$\frac{1}{\kappa}$

ε (millistrain)

-1   0   1

$y_{cur}=0$

σ (MPa))

-20   0   20

$y=\delta$

Moment Balance:

$w \int_{-h_s-\delta}^{h_c-\delta} \sigma(y_{cur})y_{cur}dy_{cur} = 0$

$y_{cur} = y$ curvature
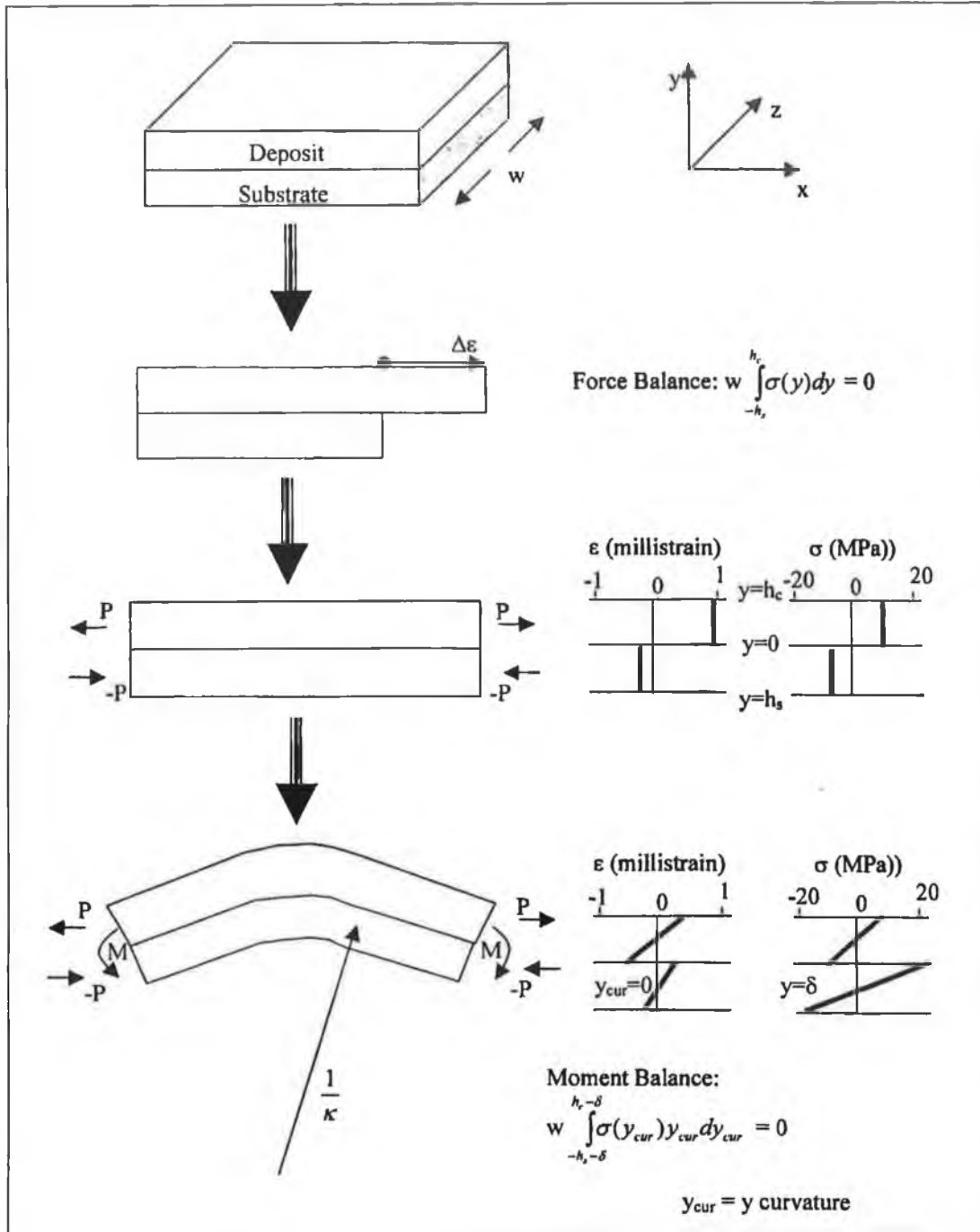
Figure 3.23: Schematic description of the generation of curvature in a bi-material
plate as a result of misfit strain adapted from [22].
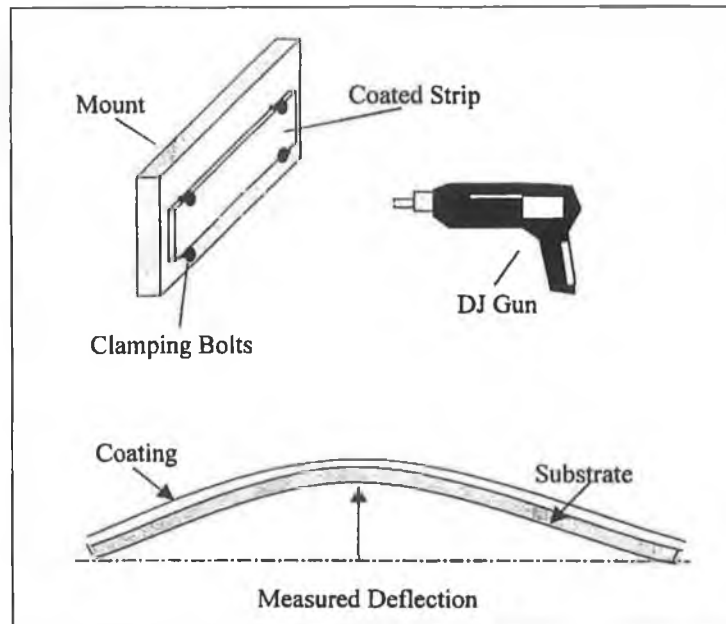
Figure 3.24: Clyne's method used to determine distributed stress in graded coatings adapted from [22].
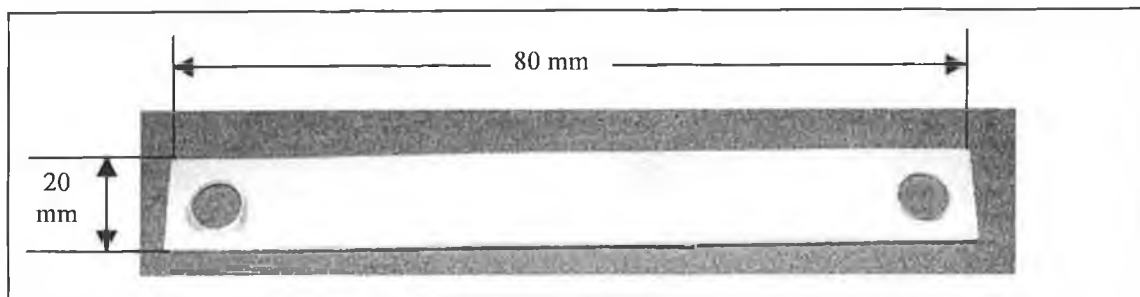
Figure 3.25: Photograph of aluminium/tool-steel graded coated aluminium sample.

Clyne's analytical method uses the temperature difference between the substrate and coating while measuring residual stress values in them (substrate and coating). Therefore it was needed in the current project to know the value of the temperature difference between the substrate and coating. The Optical pyrometer and thermocouple were previously used in MPRC to measure different temperature values. But according to Helali [20], reliability of temperature readings measured by the optical pyrometer was unsatisfactory. Hence thermocouples were used in the current project to measure the temperature difference between the substrate and coating. One thermocouple was fixed to the back of the substrate, where another one was fixed to the top of the coating to establish temperature gradient across the substrate and across the substrate and graded coatings of different thickness. The temperature gradient was found by heating the top of the coating at different temperatures with the help of heating torch and

110

measuring the temperature difference between the substrate and coatings. The temperature of the substrate and coatings was allowed to stabilise (around 10 seconds) at each individual temperature, before values were recorded. At each temperature 3 readings were taken and the average is mentioned in the result chapter.

In order to check the accuracy of temperature measurement using thermocouple, a process model of 2-dimensional steady state heat transfer across the coating-substrate system was simulated using the Thermal ANSYS Finite Element Analysis. 4-noded quad (PLANE5) was chosen as the element during simulation. Thermal conductivity of the aluminium (substrate and the base layer) was taken to be 125 W/mK [247], while thermal conductivity of the tool-steel (final layer) was taken as 25 W/mK [83]. The thermal conductivity of the other layers was calculated using the "Rule of Mixture" mentioned in chapter 2. The air film co-efficient was taken to be equal to 0.03 W/mK [248]. Temperature at the top of the coatings was set to different values similar to those used during experiment. Temperature difference between the coating and substrate was calculated from the simulation results and compared with the experimental results.

CHAPTER 4
RESULTS & DISCUSSION

4.1 INTRODUCTION

Chapter four details results, which fall under two main headings: rig design and process optimisation. Figure 4.1 shows a list of various results observed in this research.

■ **Rig Design and Verification**

- Results of Simulation
  - Initial tests
  - Final simulation
  - Effect of gravity and change of dimension of the powder flow tubes, inlet pressure tube and pick-up shaft on simulated result

- Calibration Tests
  - Powder flow bench test
  - In-situ flow test using needle shaped bolt

■ **Process Optimisation**

- Optimisation of Spray Parameters
  - Chemical composition of different layers of a five layer graded coating
  - Microstructure and phase identification
  - Measurement of Young's modulus and Poisson's ratio
  - Measurement of Residual Stress

Figure 4.1: List of various results sets achieved in this research.

4.2 RESULTS OF SIMULATION

As mentioned earlier the FLOTRAN CFD (Computational Fluid Dynamics) ANSYS Finite Element Analysis method was used in the current research to simulate the tool-steel, aluminium powder and nitrogen gas flow through the newly designed parts. Simulation was done to see whether; (1) the designed parts would be able to carry the powders up to the mixing zone (inside the parts) where they were supposed to mix, (2) whether the mixed powders would be picked up in the nitrogen gas flow inside the pick-up shaft. The approximate nitrogen gas pressure ratio on top of the new part to the pick-up shaft was also figured out to get powder mixing and putting the powder mixture into the nitrogen gas flow inside the pick-up shaft. The geometry of the nitrogen gas and powder flow tubes is shown in the previous chapter. The velocities of the tool-steel powder were used as the velocity inputs on the tool-steel flow tube, while velocities of the aluminium powder were used as the velocity inputs on the aluminium flow tube (figure 3.17, which is redrawn below). The mass fraction ratios' of the tool-steel and aluminium powders, as well as their velocity ratios' were varied at 1: 1, 1: 3 and 3:1. The velocities of the nitrogen gas were used as the velocity inputs on the inlet pressure tube and also on the left hand side of the pick-up shaft situated in the bottom part of the design. The velocities of the nitrogen gas on the inlet pressure tube and the pick up-shaft were varied to obtain different pressure ratios' of the nitrogen gas on those two parts. The FLOTRAN CFD provided the pressure distribution using the velocity inputs on different sections of the model. Two types of meshing techniques were used; (a) homogeneous mesh all through the model and (b) fine mesh in the mixing zone with a coarse mesh in the outer zones of the model. The first type of mesh was used for the initial tests, while the second type was used for the final simulation. Finally, further simulation was done (with fine mesh in the mixing zone) in order to check whether gravity and dimensions of different gas and powder flow tubes had any effects on the simulated results.
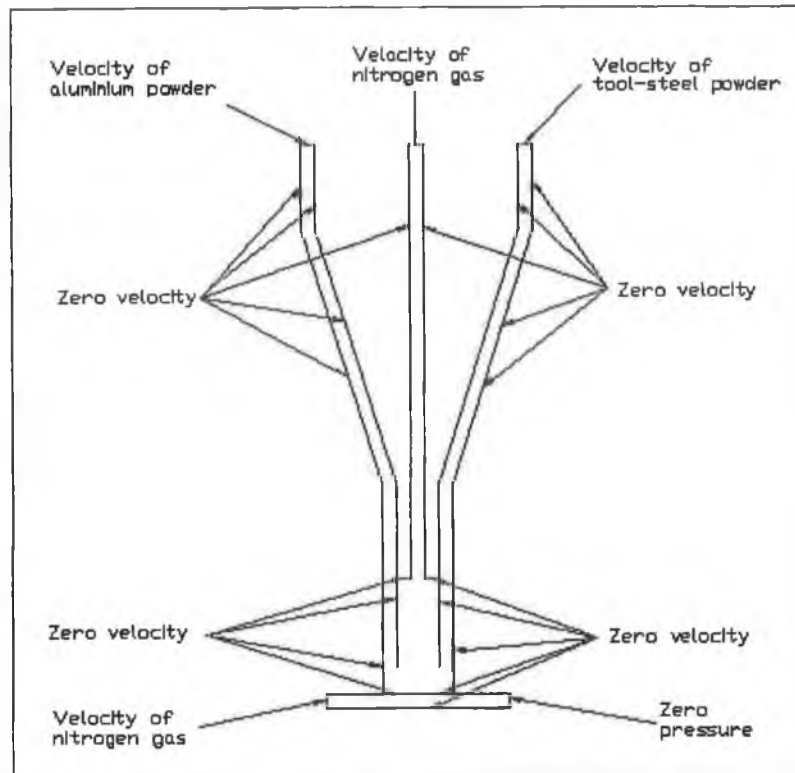
Figure 3.17: Schematic of applied boundary conditions (redrawn).

4.2.1 Initial Tests

Initial tests were run using the homogeneous mesh (1 mm wide) all through the model as shown in figure 4.2. These tests were done to calculate the velocities of the nitrogen gas at the inlet pressure tube and pick-up shaft. The information found resulted in a pressure ratio of the nitrogen gas on those two parts. Tests were carried out using trial and error method to find the best ratio, which caused mixing of the two powders. As an example, when the velocities of 3974 cm/s and 2965 cm/s of the nitrogen gas were used on the inlet pressure tube and pick-up shaft respectively, it gave a pressure ratio of 8:1 (figure 4.3). Numerical values shown in figure 4.3 represents pressure (dynes/cm^2) variation throughout the model. Some other examples are given in table 4.1.
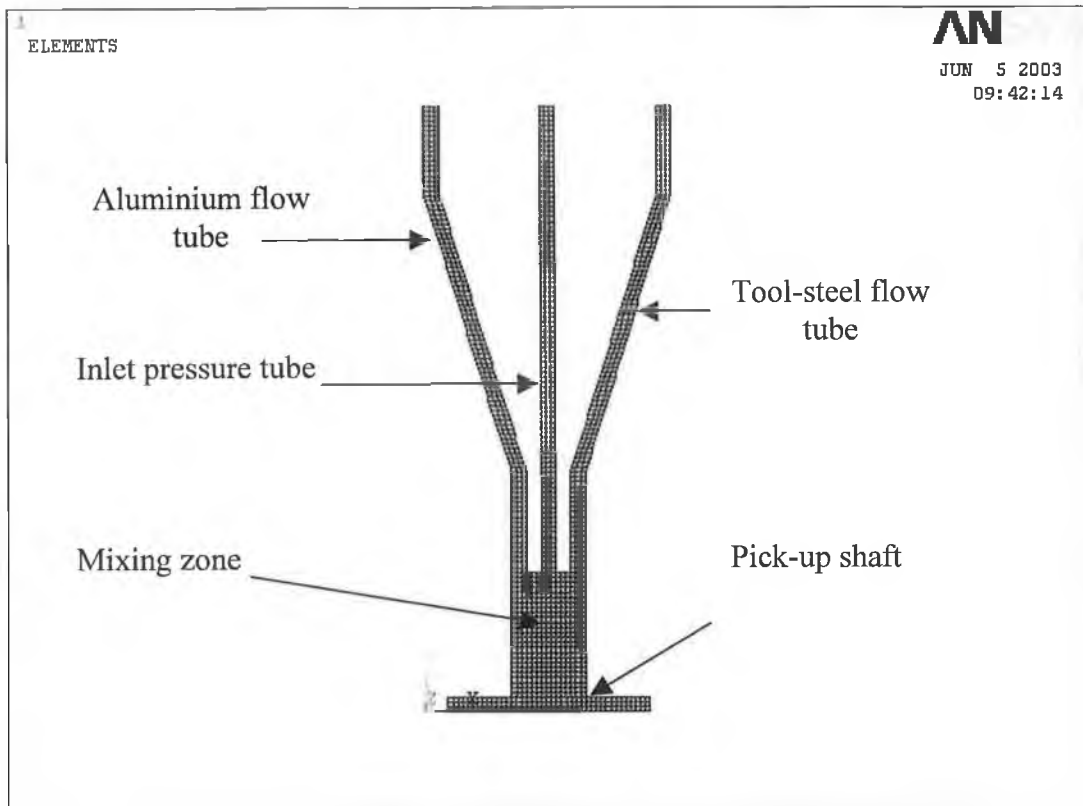
Figure 4.2: Dual powder feed unit with a homogeneous mesh all through the model.

Table 4.1: Pressure ratio for different velocity input.

Velocity of the nitrogen gas		Nitrogen gas pressure ratio on the inlet pressure tube to the pick- up shaft
Inlet pressure tube (cm/s)	Pick-up shaft (cm/s)	
3470	2965	6:1
4471	2965	9:1
4722	2965	10:1

Initial tests showed that pressure ratios' from 8:1 to 10:1 gave the best results in terms of mixing the two powders and putting the powder mixture into the nitrogen gas flow inside the pick-up shaft as indicated by the flow lines. Those ratios' were used subsequently in the final simulation to achieve more accurate results.
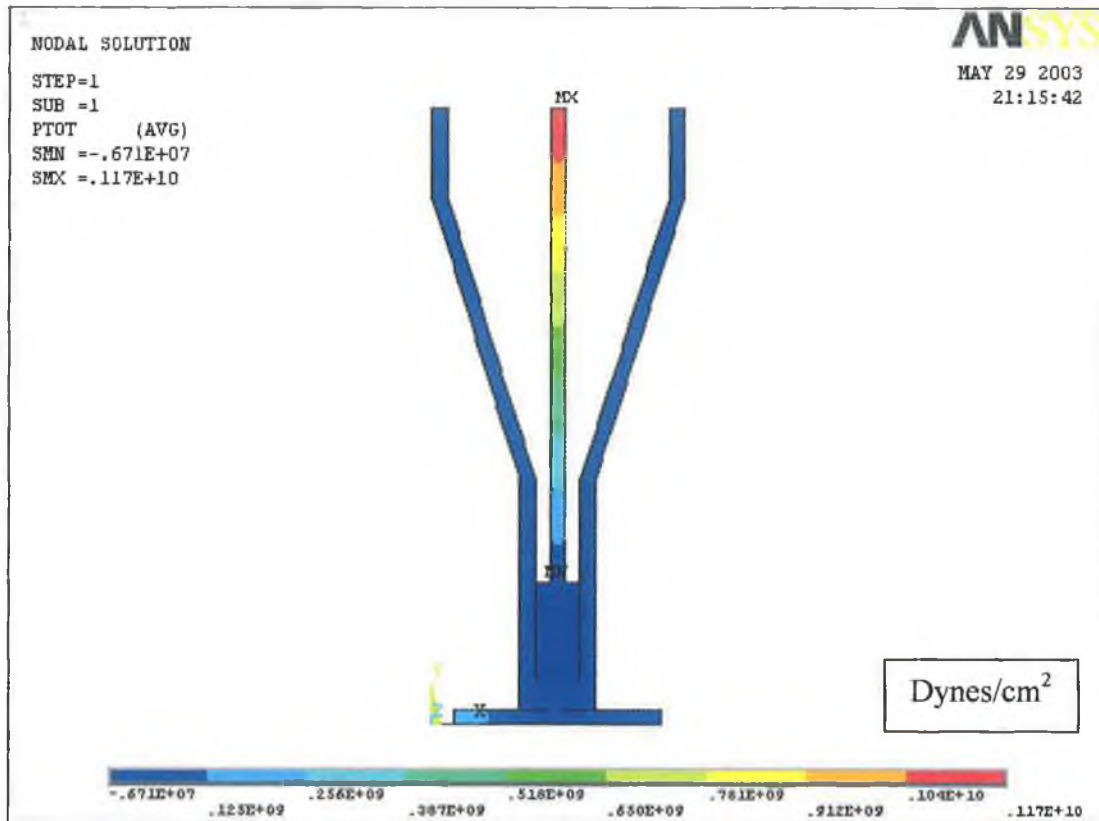
Figure 4.3: A nitrogen gas pressure ratio of 8:1 on the inlet pressure tube to the left-hand side of the pick-up shaft.

4.2.2 Final Simulation

As mentioned earlier, a fine mesh in the mixing zone (0.5 mm wide), as shown in figure 4.4, was used for the final simulation to achieve more accurate results. The mass fraction ratios' of the aluminium and tool-steel powders, as well as the velocity input ratios' of those powders were varied at 1:1, 1:3 and 3:1. The pressure ratios' of the nitrogen gas in the inlet pressure tube to the pick-up shaft were varied at 8:1, 9:1 and 10:1 for each ratio of the tool-steel and aluminium powder. The results are described in the following sections. Numerical values shown in the particle flow figures indicate the particle velocity (cm/s) at a particular point on the simulated flow.
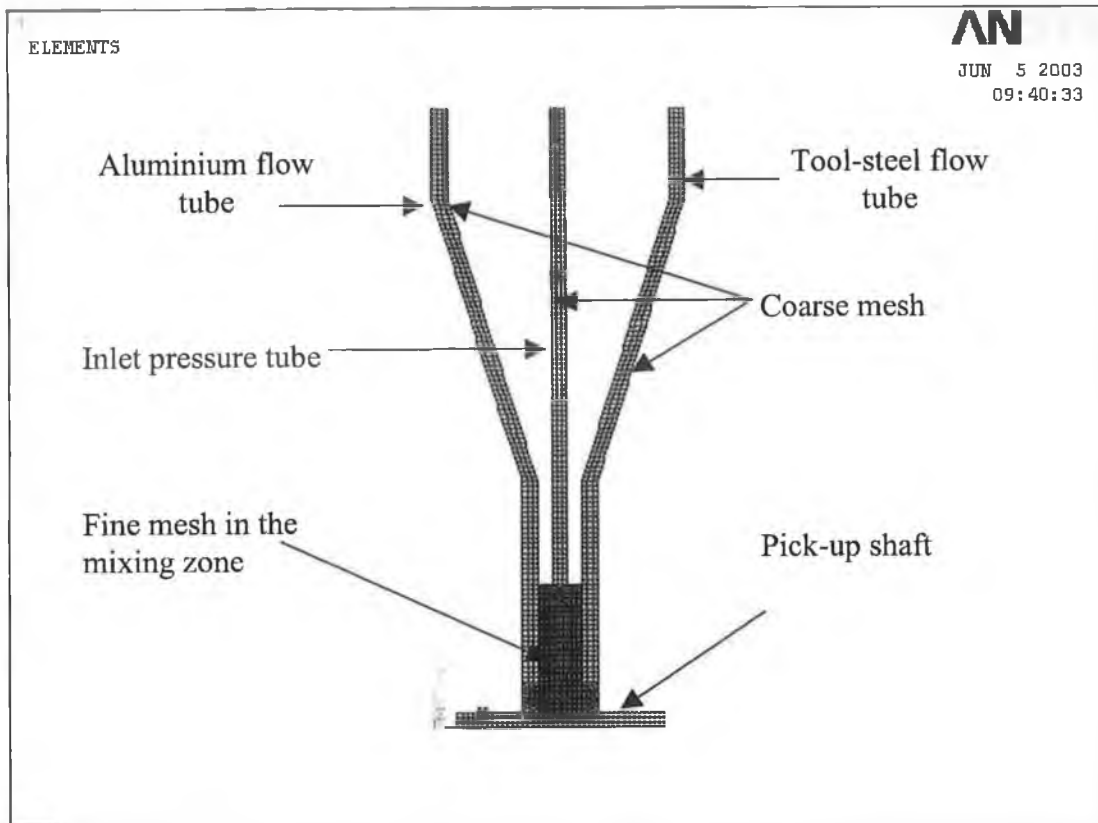
Figure 4.4: Dual powder feed unit with a fine mesh in the mixing zone.

(a) Simulation Results for the Aluminium and Tool-Steel Powder at a Ratio of 3:1

Figures 4.5 and 4.6 show the particle flow and mass fraction simulation results of the aluminium and tool-steel powders (3:1) and nitrogen gas for pressure a ratio of 8:1 respectively. In the zoomed picture Al (red line) is indicating the flow line for the aluminium powder, TS (blue line) is indicating the flow line for the tool-steel powder, NT2 (pink line) is indicating the flow line for the nitrogen gas from the inlet pressure tube, while NP2 (black line) is indicating the flow line for the nitrogen gas from the pick-up shaft. A nitrogen gas pressure ratio of 8:1 was set on the inlet pressure tube versus the pick up shaft. Both the aluminium and tool-steel were allowed to flow through to the mixing zone, but according to the simulation, the aluminium powder did not quite mix with the tool-steel powder. The powder mixture moved to the right, away from the pick-up shaft hole as clear from the magnified diagram. The first reason for this is that the nitrogen gas in the pick up shaft moved through the pick up shaft hole into the mixing zone and then to the tool-steel powder flow tube, moving the powder mixture to the right of the pick up shaft hole. Another reason may be that a greater

117

amount of the aluminium powder was flowing through from the aluminium flow tube at the same instance as that of the tool-steel powder from the tool-steel flow tube, hence it may have had an effect on the moving of the powder mixture to the right. Some portion of the nitrogen gas that flowed through from the top middle-tube to the mixing zone also flowed up through the powder flow tubes as indicated by the mass fraction results in figure 4.6.

Figure 4.5: Particle flow lines for the nitrogen gas and powders for a pressure ratio of 8:1 and powder ratio of 3:1.

Figure 4.6: Mass fraction simulation results of the (a) aluminium and (b) tool-steel
powder at a ratio of 3:1, nitrogen gas in the (c) inlet pressure tube and
(d) pick-up shaft for a pressure ratio of 8:1.

The velocity profile of the fluids through the top gas-powder flow tubes for a pressure
ratio of 8:1 is shown in figure 4.7 (b), while the velocity profile of the fluid through the
pick-up shaft is shown in figure 4.7 (c). The velocities of the fluids in the powder flow
tubes remained constant from (A) to (B). Then the velocities decreased from (B) to (C)
due to the bending of the tubes. The velocities again remained constant from (C) to (D)
and then decreased from (D) to (E), again due to a bend in the tube. The velocities then
remained constant until (F), where the velocities increased due to the effect faster fluid
(nitrogen) flowing from the mixing zone. The velocities of a fluid flowing through a
tube can be calculated using the Bernoulli's equation [206], which is defined as,

$$\frac{P_1}{\rho g} + \frac{v_1^2}{2g} + z_1 = \frac{P_2}{\rho g} + \frac{v_2^2}{2g} + z_2 + h \qquad \text{Equation 4.1}$$

119

Where, v_1 and v_2 are the velocities of the fluid, z_1 and z_2 are the vertical heights above a datum, P_1 and P_2 are the pressure values acting on the fluid at two different points in the tube, ρ is the density of the fluid, h is the head loss between them and g is acceleration of gravity. For two particular points in the tube and a particular fluid, ρ, z_1 and z_2 are constant. So equation 4.1 can be written as,

$$P_1 + v_1^2 \propto P_2 + v_2^2 + h \hspace{4cm} \text{Equation 4.2}$$

When a fluid flows through a straight tube, the velocities remain same throughout if the diameter of the tube remains same. If there is a bend section in the tube, the pressure increases in the direction of flow [206]. Also there is an extra head loss due to effect of tube bending [249]. So both P_2 and h increases after the bending. In order to keep the balance of the equation, therefore the velocity v_2 must decrease, which was found in the current work (for example from (B) to (C) in figure 4.7 (b)). The velocity of the fluid flowing through the inlet pressure tube remains constant from (A) to (E). Then the velocity decreased due to an abrupt enlargement of cross sectional area from the inlet pressure tube to the mixing zone, which is supported by Benedict [249]. At point E, the velocity was lowest due to the slow moving fluids coming from the two powder flow tubes.

The velocity of the fluid flowing through the pick-up shaft (1) remained constant until it reached near the pick-up shaft hole (2) (figure 4.7 (c)). This point acts as a "T" junction, where the flow was divides into two sections. Some portion of the fluid entered the pick-up shaft hole into the mixing zone, where as the rest of the fluid continued to flow through the pick-up shaft. Due to the effect of the "T" junction, velocities of the fluids in both sections decreased, as supported by findings by Corcoran [250] in his research for fluid flow in a "T" junction. The velocity of fluid flowing through the pick-up shaft then remained constant until it reached the pick-up shaft outlet (4).
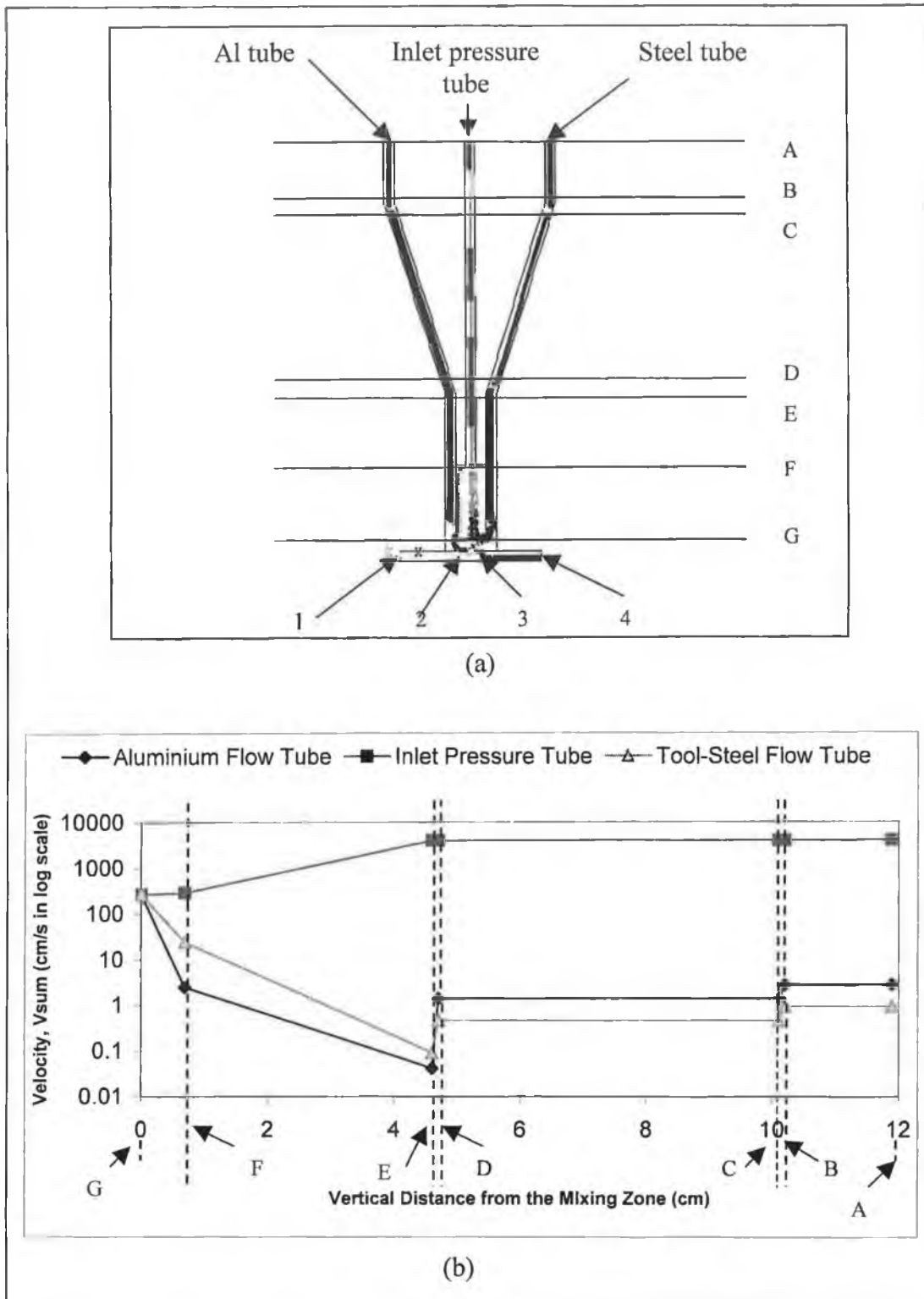
Figure 4.7: Different points on the fluid flow (a), the velocity profile of the fluid through the top gas-powder flow tubes (b) and the pick-up shaft (c) for powders at a ratio of 3:1 and a nitrogen gas pressure ratio of 8:1 (continuation on the next page).
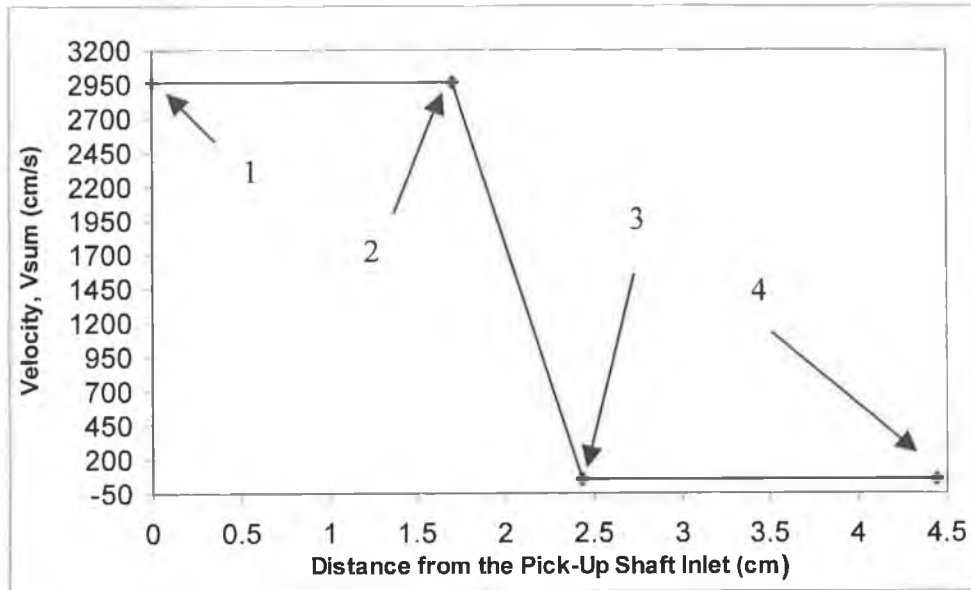
Figure 4.7: Different points on the fluid flow (a), the velocity profile of the fluid through the top gas-powder flow tubes (b) and the pick-up shaft (c) for powders at a ratio of 3:1 and a nitrogen gas pressure ratio of 8:1 (continuation on the next page).

When a pressure ratio of 9:1 was used, both the aluminium and tool-steel powder flowed through to the mixing zone and mixed with each other. The fluids flowing through the different gas-powder flow tubes and the pick-up shaft showed the same behaviour as they showed for the pressure ratio of 8:1. The powder mixture stayed close to the pick-up shaft hole but did not enter the hole as shown in figure 4.8. The reason for this is the lesser amount of the nitrogen gas flowing through the pick-up shaft, entered the mixing zone (than it did for 8:1 pressure ratio) and then onto the tool-steel carrying tube. The mass fraction simulation results for the two powders and nitrogen gas for a pressure ratio of 9:1 is shown in figure 4.9. Again some portion of the nitrogen gas flowing through the inlet pressure tube to the mixing zone entered the two powder flow tubes from the mixing zone. The velocity profile of the fluids through the top gas-powder flow tubes for pressure ratio of 9:1 is shown in figure A12 (a) (Appendix B), while figure A12 (b) (Appendix B) shows the velocity profile of the fluid through the pick-up shaft.

122

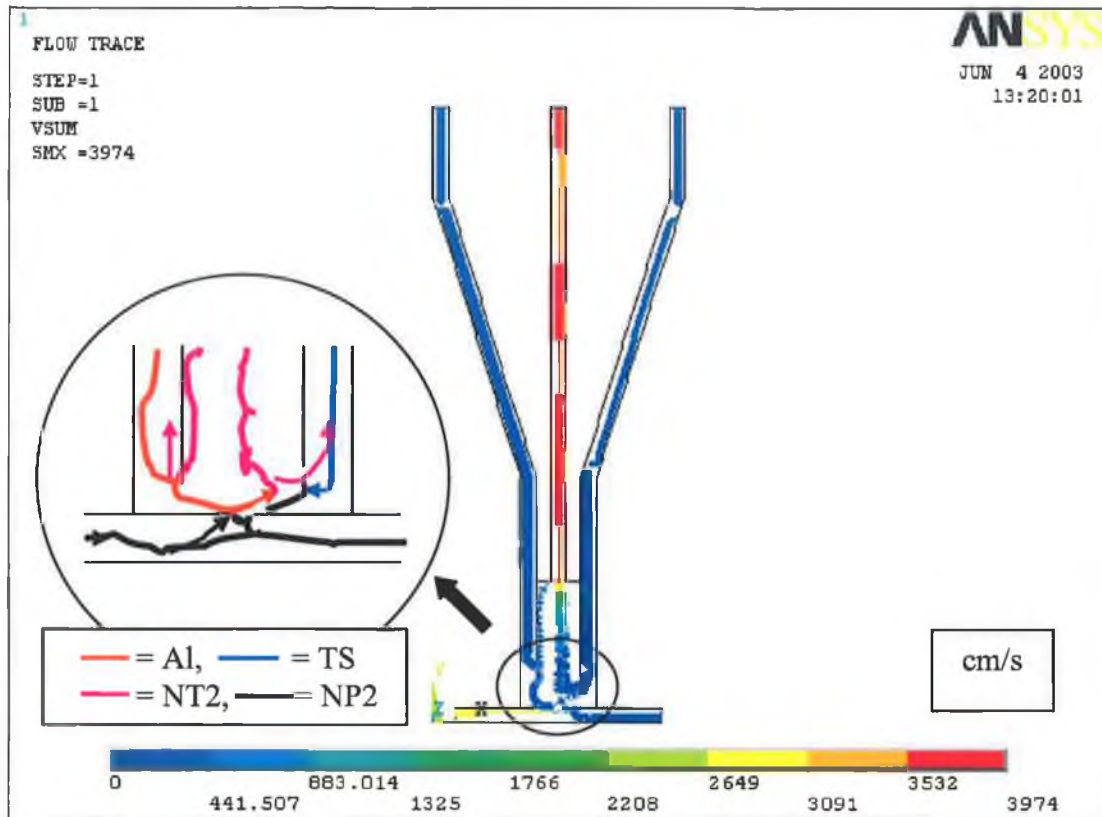Figure 4.8: Particle flow lines for the nitrogen gas and powders for a pressure ratio of 9:1 and powder ratio of 3:1.

Figure 4.9: Mass fraction simulation results of the (a) aluminium and (b) tool-steel
powder at a ratio of 3:1, nitrogen gas in the (c) inlet pressure tube and
(d) pick-up shaft for a pressure ratio of 9:1.

Figures 4.10 and 4.11 show the particle flow and mass fraction simulation results of the
aluminium and tool-steel powders (3:1) and nitrogen gas for a pressure ratio of 10:1
respectively. This time the velocity of the fluids flowing through the pick-up shaft had
the lowest velocity near the pick-up shaft hole (3) amongst the three different pressure
ratios' due to the effect of slow moving fluids coming from the mixing zone into the
pick-up shaft. At this pressure ratio, the aluminium and tool-steel powder flowed
through to the mixing zone, mixed with each other and the powder mixture entered the
pick up shaft hole where it was picked up in the nitrogen gas flowing through the pick-
up shaft (figure 4.10), suggesting that the pressure on the inlet pressure tube should be
10 times than that of the pick-up shaft to cause mixing and to force the mixture into the
nitrogen gas flow inside the pick-up shaft. MX (green line) is indicating the flow line
for the nitrogen gas-powder mixture in the zoomed picture in figure 4.10. The nitrogen

124

gas from the pick-up shaft entered the mixing zone and then onto the tool-steel powder flow tube, but at least amount amongst the three pressure ratios' as indication by figure 4.11. Again some portion of the nitrogen gas that flowed through from the inlet pressure tube to the mixing zone entered both the powder flow tubes. The velocity profile of the fluids through the top gas-powder flow tubes for pressure ratio of 10:1 is shown in figure A13 (a) (Appendix B), while the velocity profile of the fluids through the pick-up shaft is shown in figure A13 (b) (Appendix B). Again all the fluids had almost the same velocity profile as earlier.

Figure 4.10: Particle flow lines for the nitrogen gas and powders for a pressure ratio of 10:1 and powder ratio of 3:1
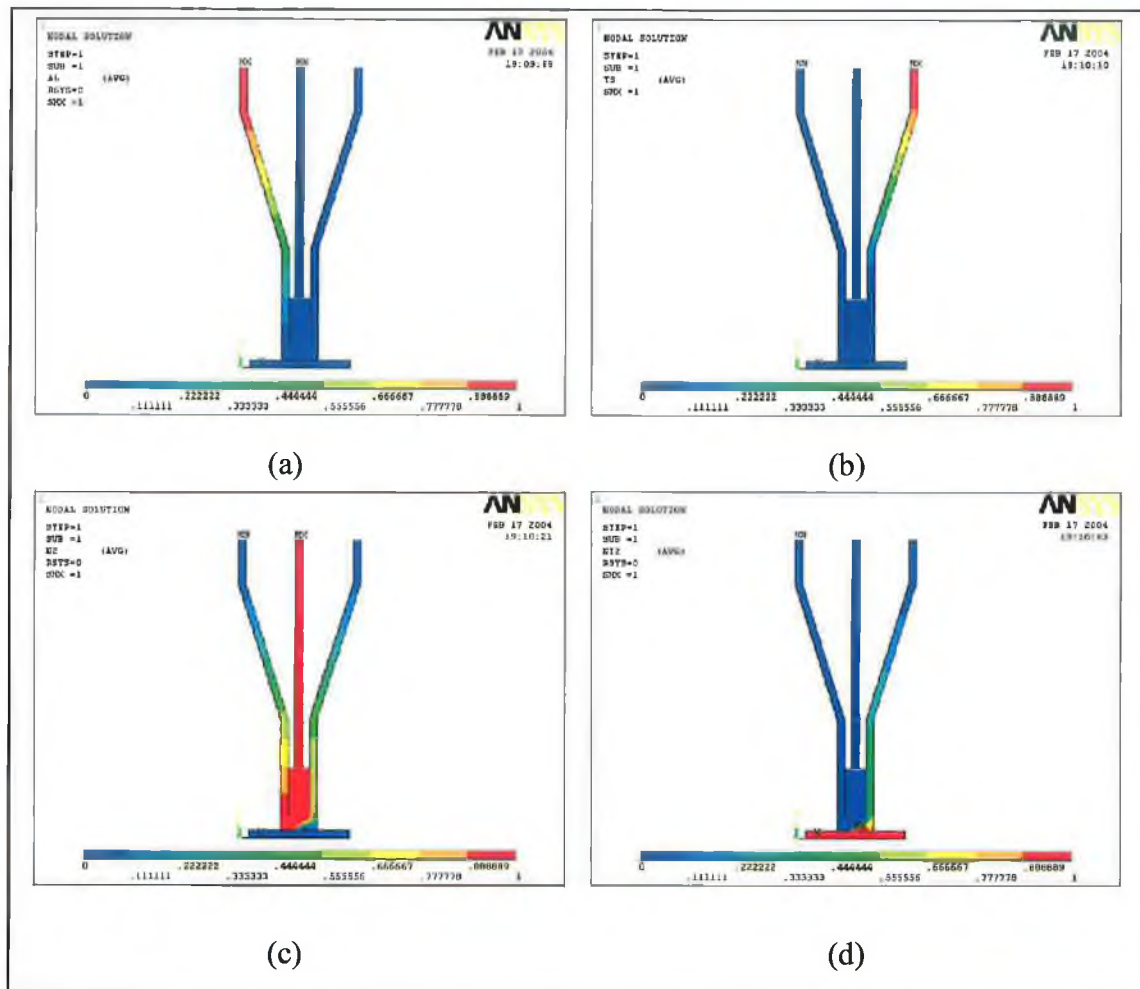
Figure 4.11: Mass fraction simulation results of the (a) aluminium and (b) tool-steel
powder at a ratio of 3:1, nitrogen gas in the (c) inlet pressure tube and
(d) pick-up shaft for a pressure ratio of 10:1.

In order to figure out the mixing of aluminium and tool-steel in the mixing zone, mass fraction plots of the two powders were rescaled and shown in figure 4.12. Figure 4.12 is showing that both powders had a mass fraction of 0.01-0.02 in the mixing zone. The rest was nitrogen gas.

(a)

(b)
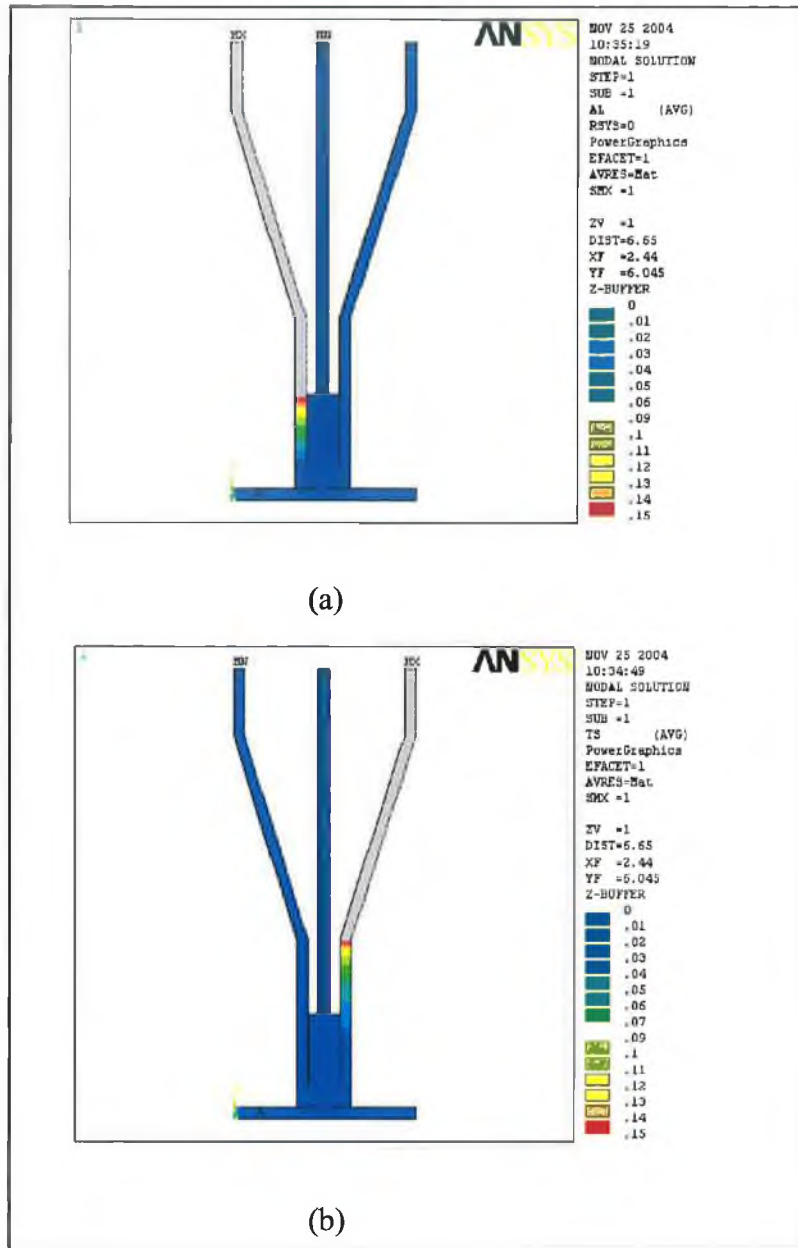
Figure 4.12: Mass fraction results of (a) aluminium and (b) tool-steel powder (rescaled).

(b) Simulation Results for the Aluminium and Tool-Steel Powder at a Ratio of 1:1

The particle flow and mass fraction simulation results of the aluminium and tool-steel powders (1:1) and nitrogen gas for a pressure ratio of 8:1 are shown in figures 4.13 and 4.14 respectively. Results showed a similar behaviour to that found for the 8:1 ratio for a ratio of 3:1 of aluminium to tool-steel powder. Both the aluminium and tool-steel powder flowed through to the mixing zone and mixed with each other. The powder

127

mixture however showed a tendency to move towards the right, but to a lesser extent to that for the 3:1 powder ratio. The reasons may be the similar flow rate of the aluminium and tool-steel powders from the two top powder flow tubes and lesser amount of flow of the nitrogen gas from the pick-up shaft into the mixing zone. The nitrogen gas flowing through the pick-up shaft entered the mixing zone but at much lesser extent than it did for 3:1 powder ratios' due to the greater amount of flow of the tool-steel powder from the tool-steel flow tube. Again some portion of the nitrogen gas from the inlet pressure tube flowed up through to the powder flow tubes from the mixing zone as indicated by figure 4.14. The velocity profile of the fluids through the top gas-powder flow tubes for a pressure ratio of 8:1 is shown in figure A14 (a) (Appendix B), while figure A14 (b) (Appendix B) shows the velocity profile of the fluid through the pick-up shaft.
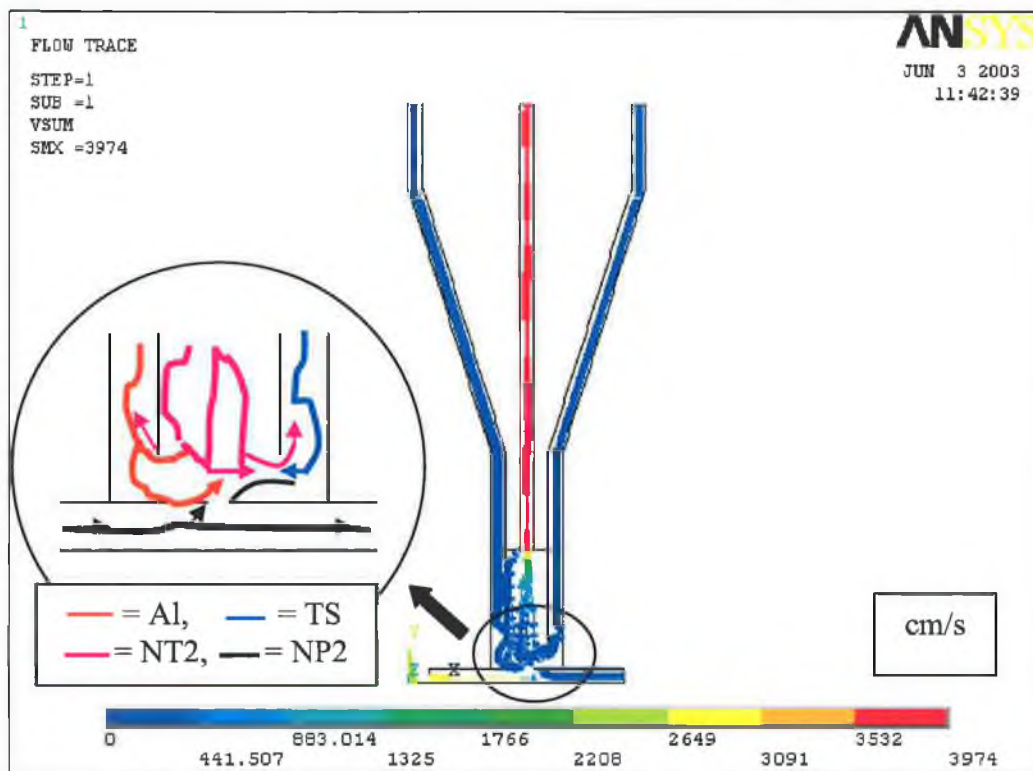
Figure 4.13: Particle flow lines for the nitrogen gas and powders for a pressure ratio of 8:1 and powder ratio of 1:1.
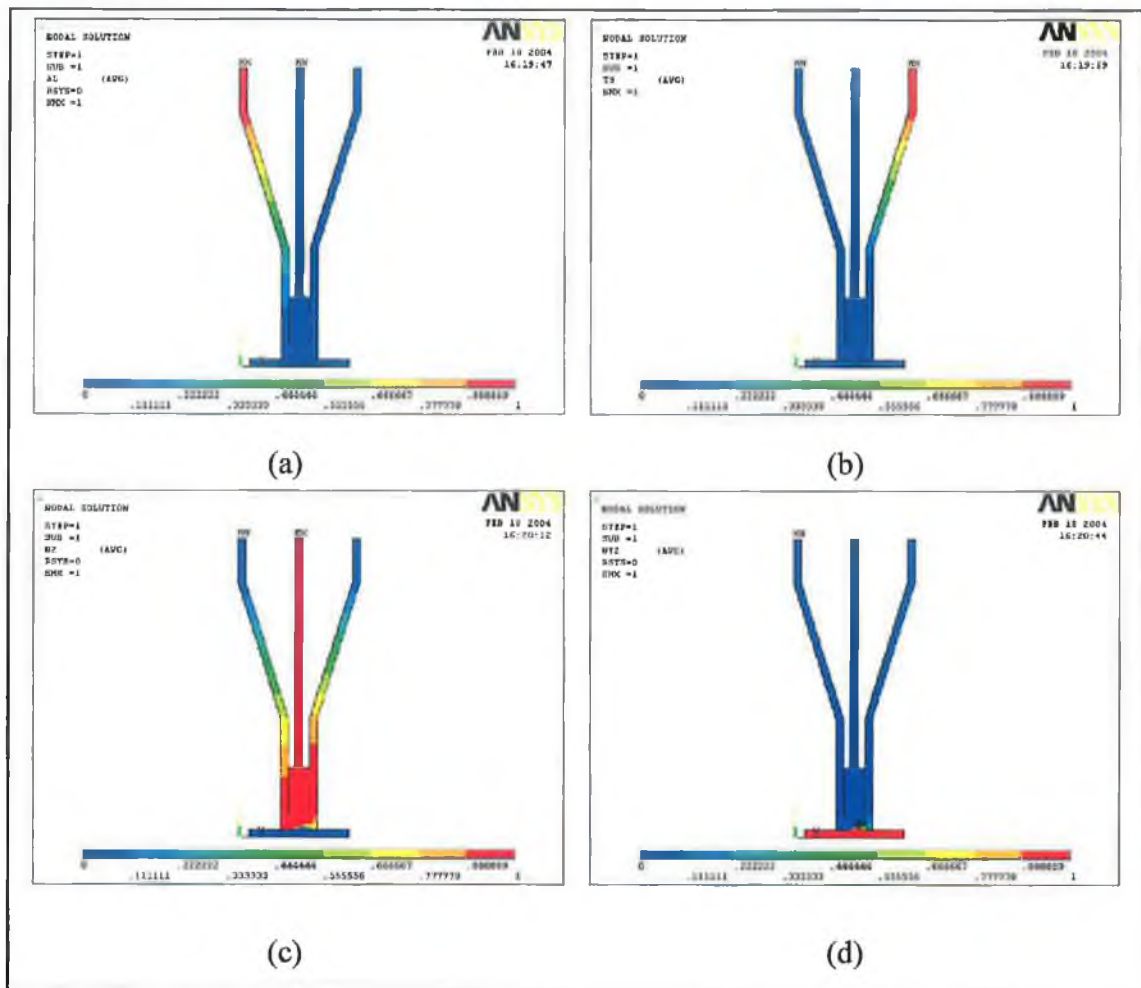
Figure 4.14: Mass fraction simulation results of the (a) aluminium and (b) tool-steel
powder at a ratio of 1:1, nitrogen gas in the (c) inlet pressure tube and
(d) pick-up shaft for a pressure ratio of 8:1.

When the pressure ratio was increased to 9:1, both the aluminium and tool-steel powder
flowed through to the mixing zone and the mixture stayed close to the pick-up shaft
hole, but not quite able to flow through it (figure 4.15). The nitrogen gas flowing from
the inlet pressure tube showed the same behaviour as it showed earlier. A little amount
of the nitrogen gas entered the mixing zone from the pick-up shaft as indicated by figure
4.16. The velocity profile of the fluids through the top gas-powder flow tubes for a
pressure ratio of 9:1 is shown in figure A15 (a) (Appendix B), while the velocity profile
of the fluid through the pick-up shaft is shown in figure A15 (b) (Appendix B). The
fluids flowing through the various gas-powder flow tubes and the pick-up shaft gave the
same velocity profile as they did for a 8:1 pressure ratio.
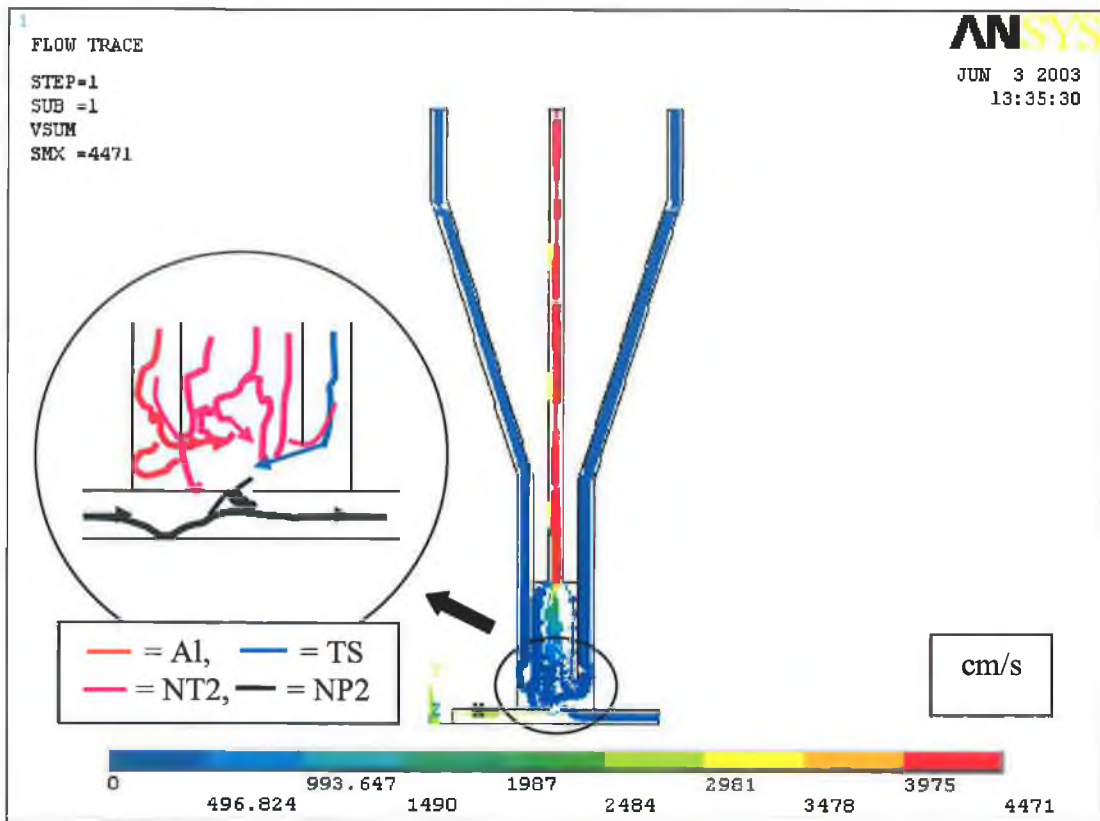
Figure 4.15: Particle flow lines for the nitrogen gas and powders for a pressure ratio of 9:1 and powder ratio of 1:1.
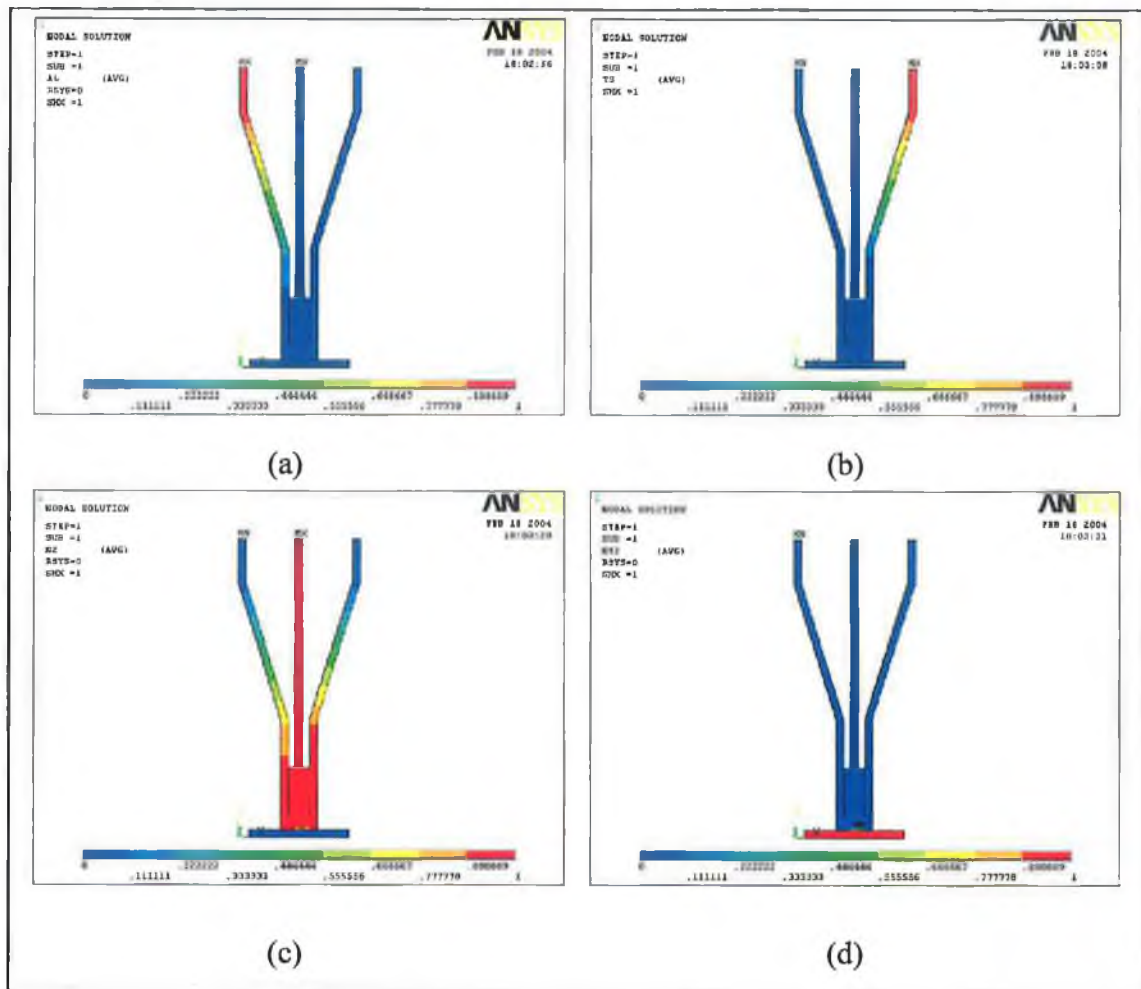
Figure 4.16: Mass fraction simulation results of the (a) aluminium and (b) tool-steel powder at a ratio of 1:1, nitrogen gas in the (c) inlet pressure tube and (d) pick-up shaft for a pressure ratio of 9:1.

Figures 4.17 and 4.18 show the particle flow and mass fraction simulation results of the aluminium and tool-steel powders (1:1) and nitrogen gas for a pressure ratio of 10:1 respectively. Both the powders flowed through to the mixing zone and the powder mixture was able to flow through the pick up shaft hole and it was picked up there by the nitrogen gas flow, again suggesting that the ratio of 10:1 to be the sufficient for powder mixing and forcing the mixture into the nitrogen gas flow through the pick-up shaft hole. Some portion of the nitrogen gas flowing through from the inlet pressure tube flowed up through to the powder flow tubes from the mixing zone. Very little amount of the nitrogen gas flowed through to the mixing zone from the pick-up shaft. The velocity profiles of the fluids can be found in Appendix B, Again all the fluids showed almost the same velocity profile as earlier. Due to the effect of the slow moving fluids coming from the mixing zone into the pick-up shaft, the velocity of the fluids

flowing through the pick-up shaft had the lowest velocity near the pick-up shaft hole (3) amongst the three different pressure ratios'.
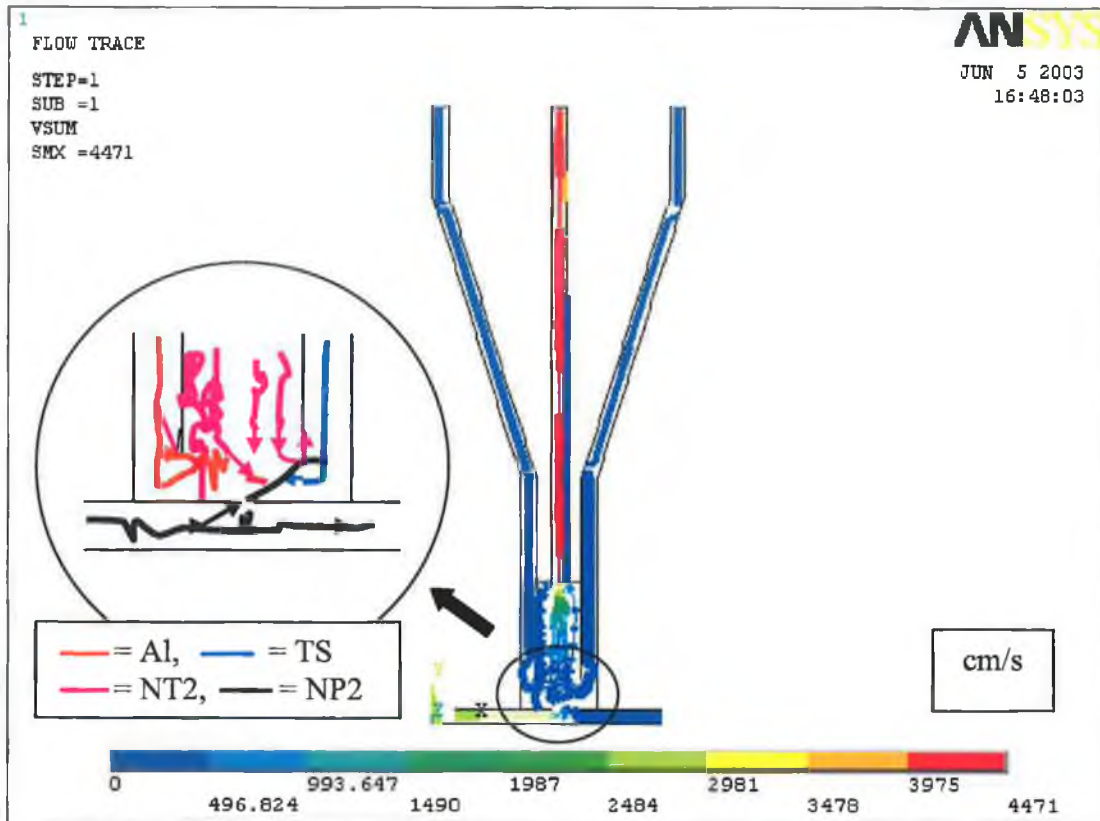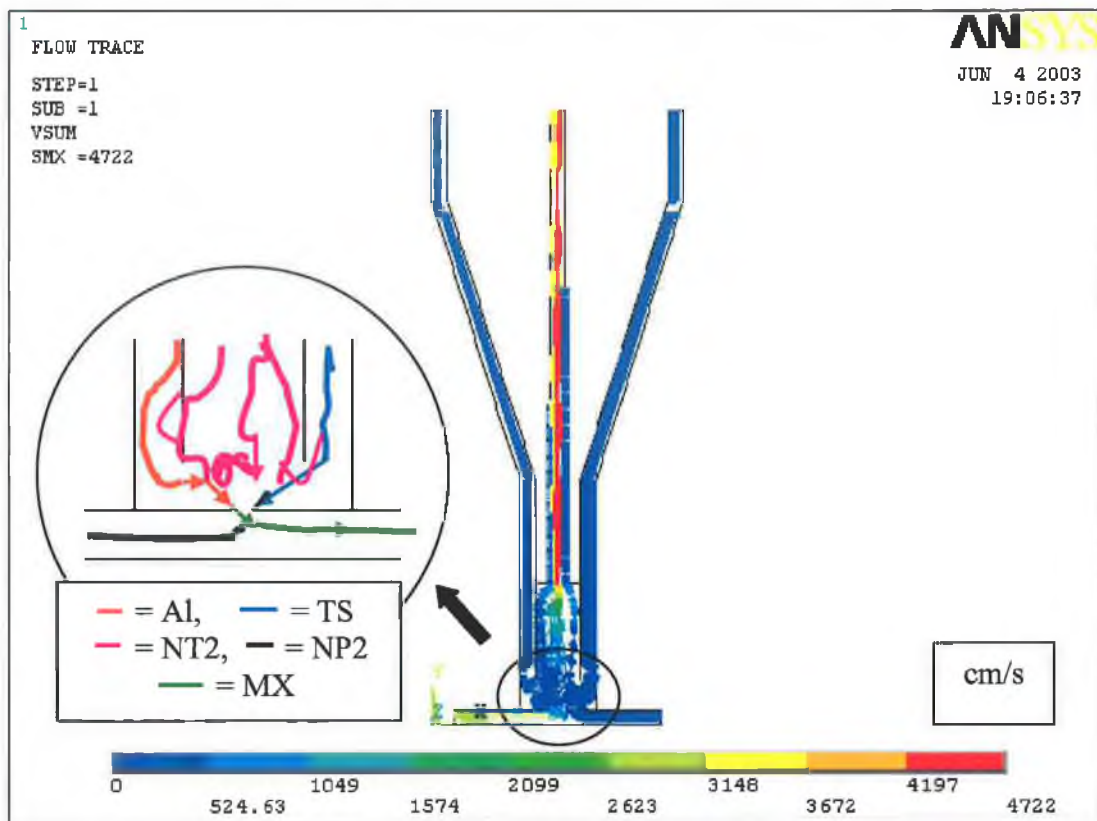

Figure 4.17: Particle flow lines for the nitrogen gas and powders for a pressure ratio of 10:1 and powder ratio of 1:1.
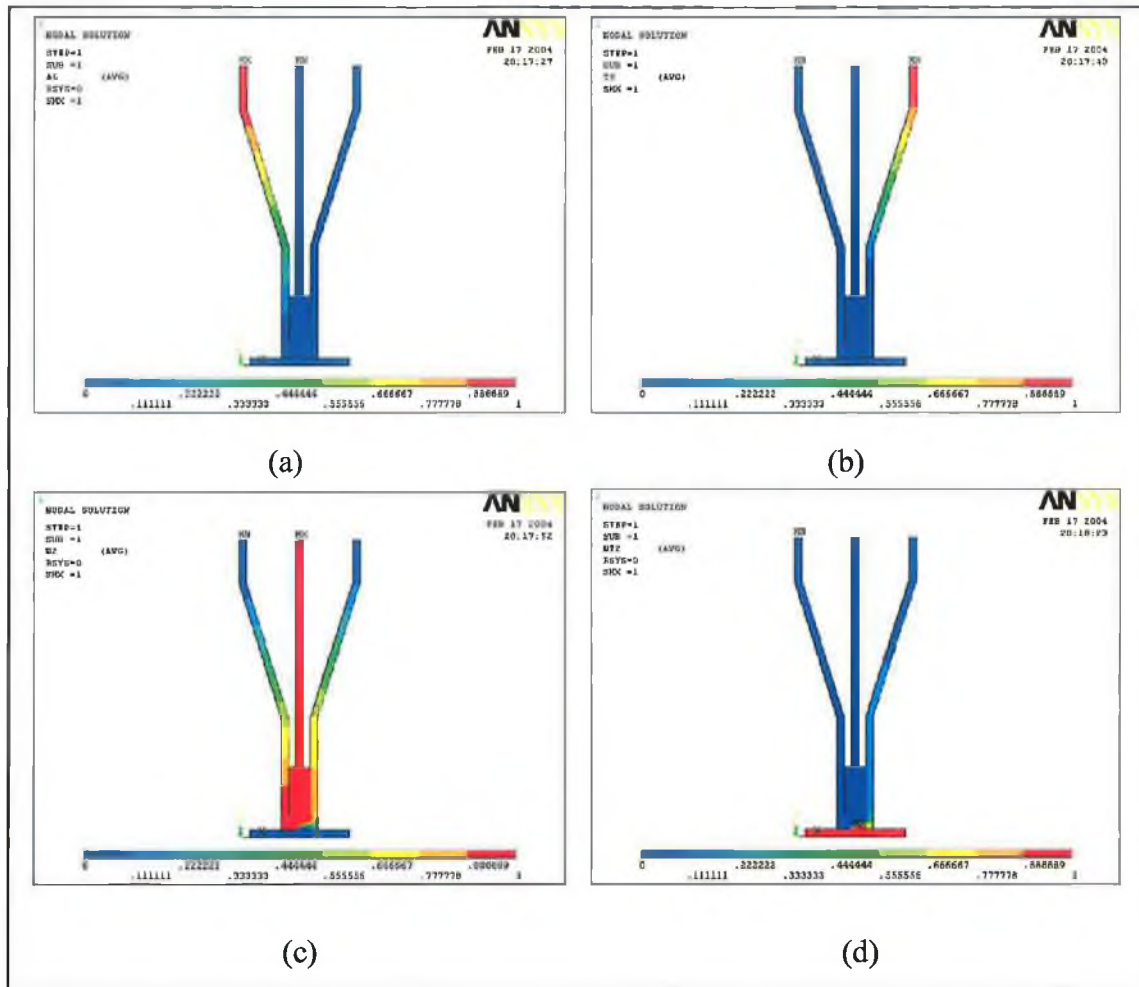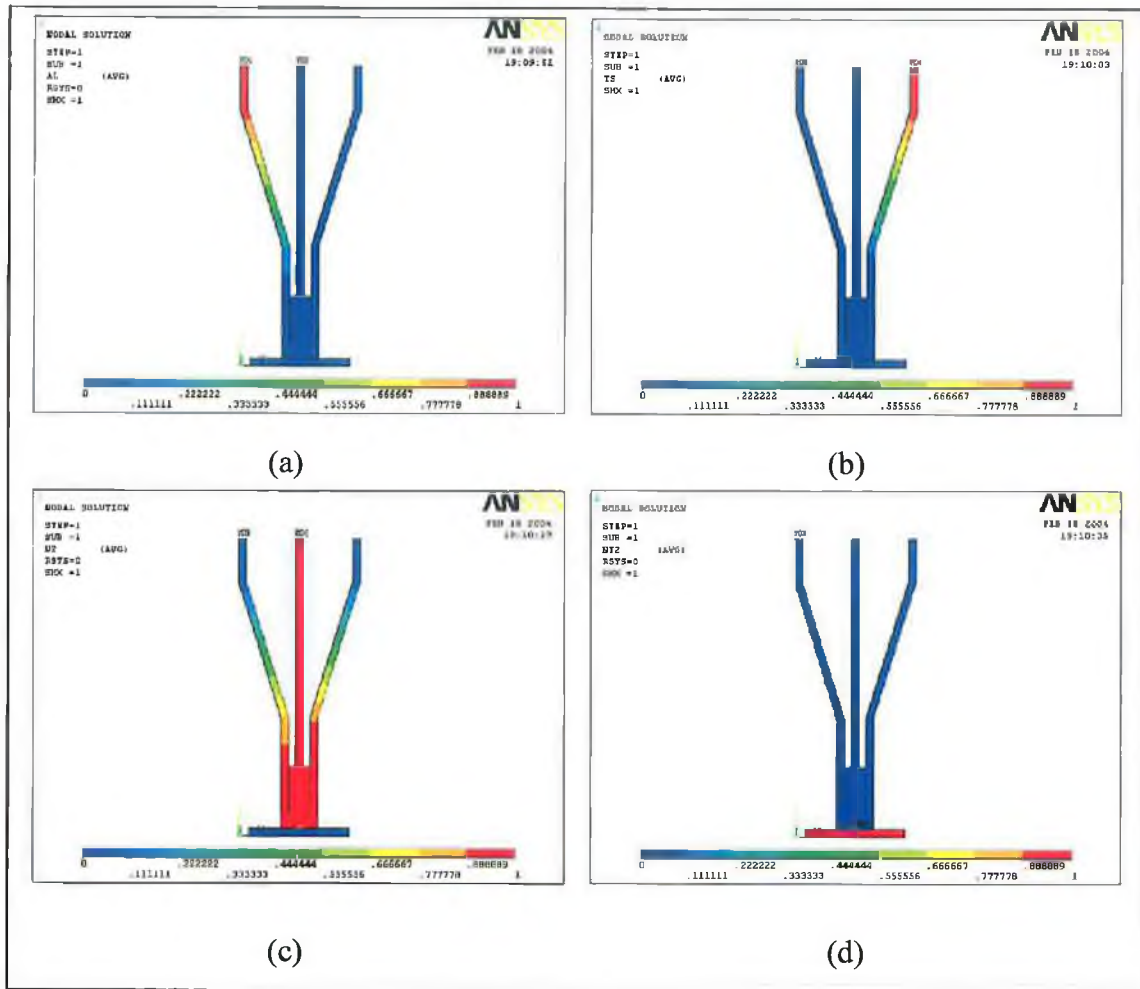
Figure 4.18: Mass fraction simulation results of the (a) aluminium and (b) tool-steel
powder at a ratio of 1:1, nitrogen gas in the (c) inlet pressure tube and
(d) pick-up shaft for a pressure ratio of 10:1.

(c) Simulation Results for the Aluminium and Tool-Steel Powder at a Ratio of 1:3

The particle flow and mass fraction simulation results of the aluminium and tool-steel powders (1:3) and nitrogen gas for a pressure ratio of 8:1 are shown in figures 4.19 and 4.20 respectively. Both the aluminium and tool-steel powders flowed through to the mixing zone where they mixed with each other. However the powder mixture did not show any tendency to move towards the right. A greater amount of the tool-steel powder from the tool-steel flow tube at the same instance as that of the aluminium powder from the tool-steel flow tube and lesser amount of the nitrogen gas from the pick-up shaft prevented the powder mixture from moving towards the right, away from the pick up-shaft hole. The nitrogen gas from the inlet pressure tube showed the same

behaviour. The velocity profiles of the fluids for a pressure ratio of 8:1 are shown in Appendix B.
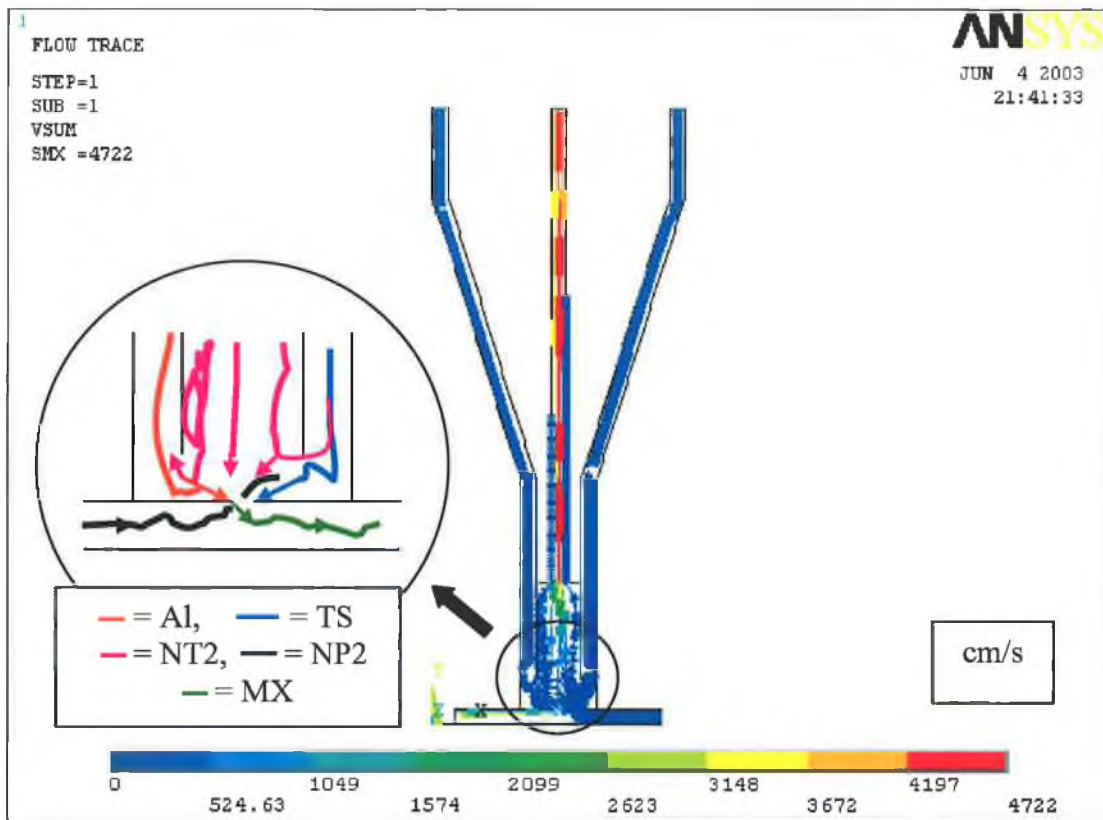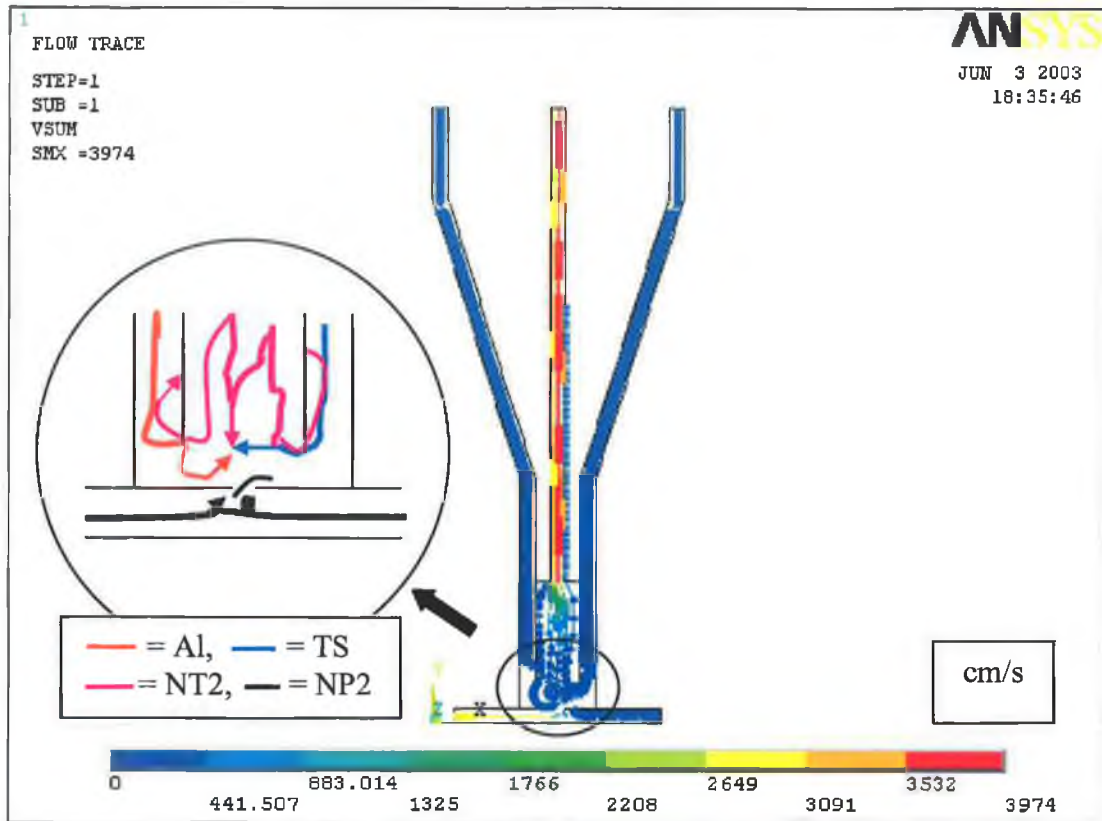

Figure 4.19: Particle flow lines for the nitrogen gas and powders for a pressure ratio of 8:1 and powder ratio of 1:3.
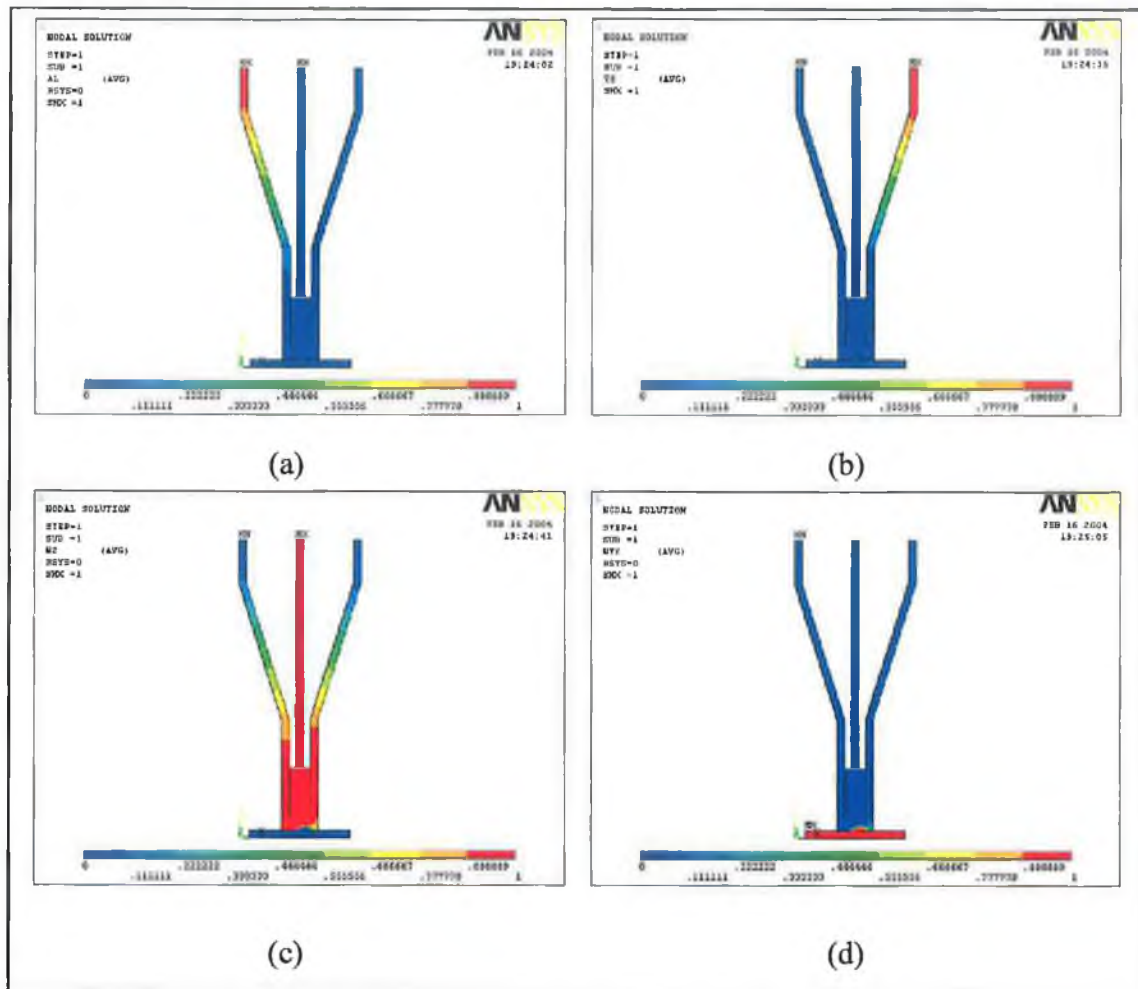
Figure 4.20: Mass fraction simulation results of the (a) aluminium and (b) tool-steel powder at a ratio of 1:3, nitrogen gas in the (c) inlet pressure tube and (d) pick-up shaft for a pressure ratio of 8:1.

When the pressure ratio was increased to 9:1, both the aluminium and tool-steel powders mixed with each other and the powder mixture moved closer to the exit hole, but still could not manage to enter it (figure 4.21). Some portion of the nitrogen gas that flowed through from the inlet pressure tube to the mixing zone entered the powder flow tubes. A small amount of the nitrogen gas flowing through the pick-up shaft entered the mixing zone (figure 4.22). The velocity profiles are shown Appendix B. The velocity profile of the fluids flowing through the different tubes and pick-up shaft were almost the same as they were for a 8:1 pressure ratio.
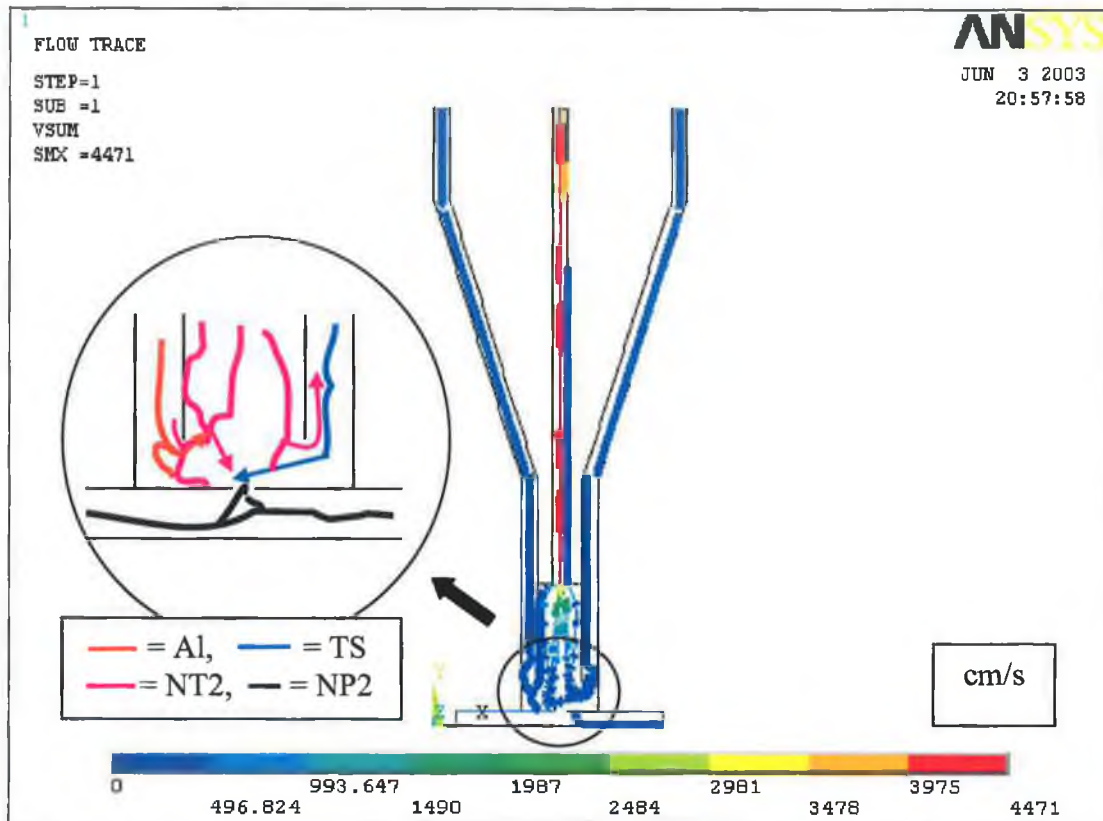
Figure 4.21: Particle flow lines for the nitrogen gas and powders for a pressure ratio of 9:1 and powder ratio of 1:3.
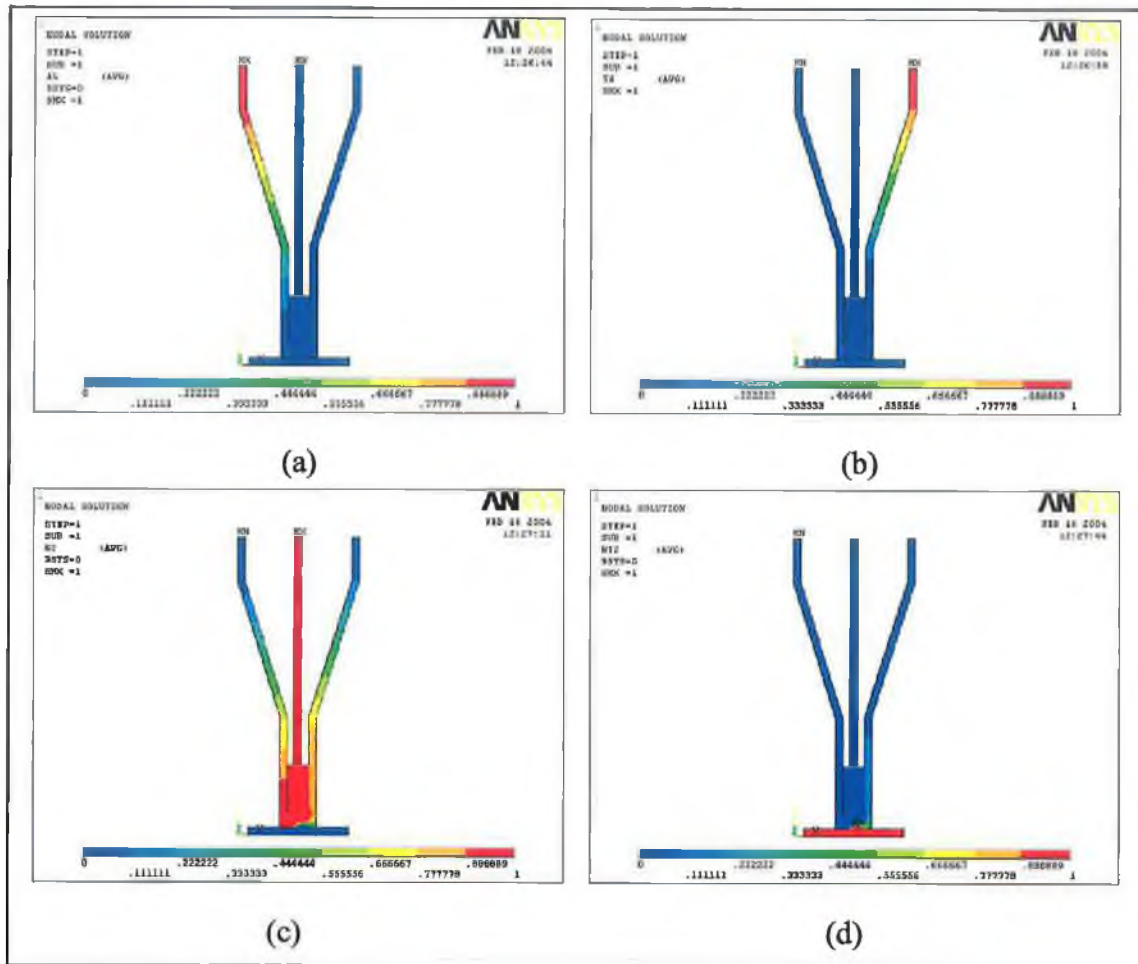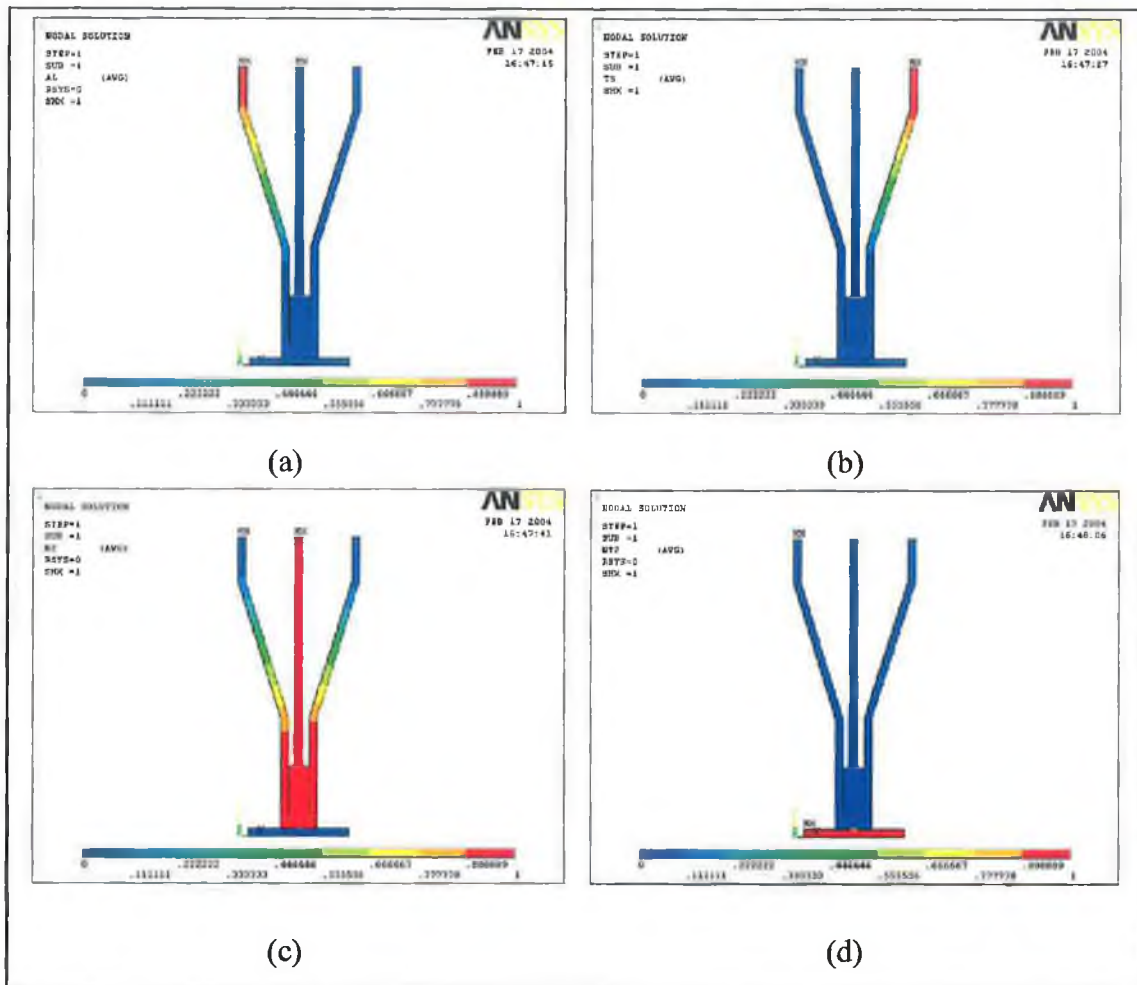
Figure 4.22: Mass fraction simulation results of the (a) aluminium and (b) tool-steel

powder at a ratio of 1:3, nitrogen gas in the (c) inlet pressure tube and

(d) pick-up shaft for a pressure ratio of 9:1.

Figures 4.23 and 4.24 show the particle flow and mass fraction simulation results of the aluminium and tool-steel powders (1:3) and nitrogen gas for a pressure ratio of 10:1 respectively. Both the aluminium and tool-steel powder mixed with each other in the mixing zone and significantly the powder mixture was able to enter through the pick up shaft hole where it was picked up by nitrogen gas flowing through pick-up shaft (figure 4.23), again suggesting that 10:1 was a sufficient ratio here. The nitrogen gas from the inlet pressure tube showed the same behaviour. The nitrogen gas from the pick-up shaft could not enter the mixing zone as indicated by figure 4.24. The velocity profiles are shown in figure Appendix B.
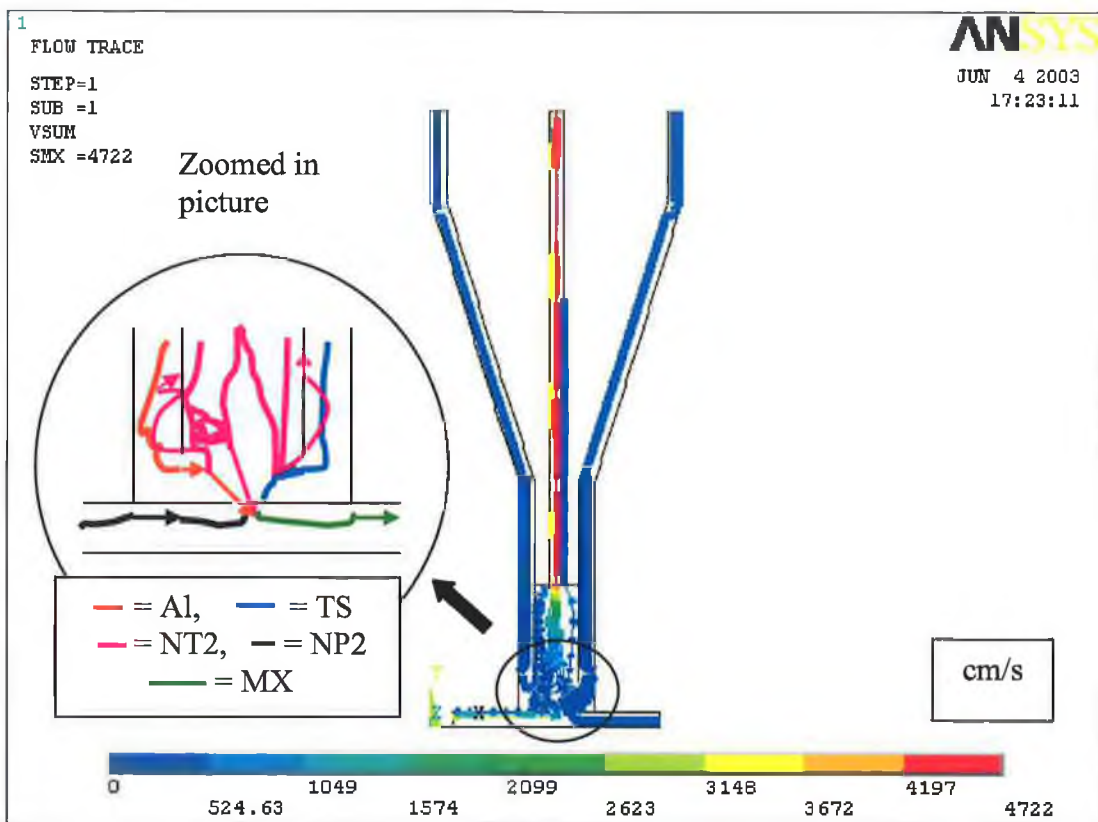
Figure 4.23: Particle flow lines for the nitrogen gas and powders for a pressure ratio of 10:1 and powder ratio of 1:3.
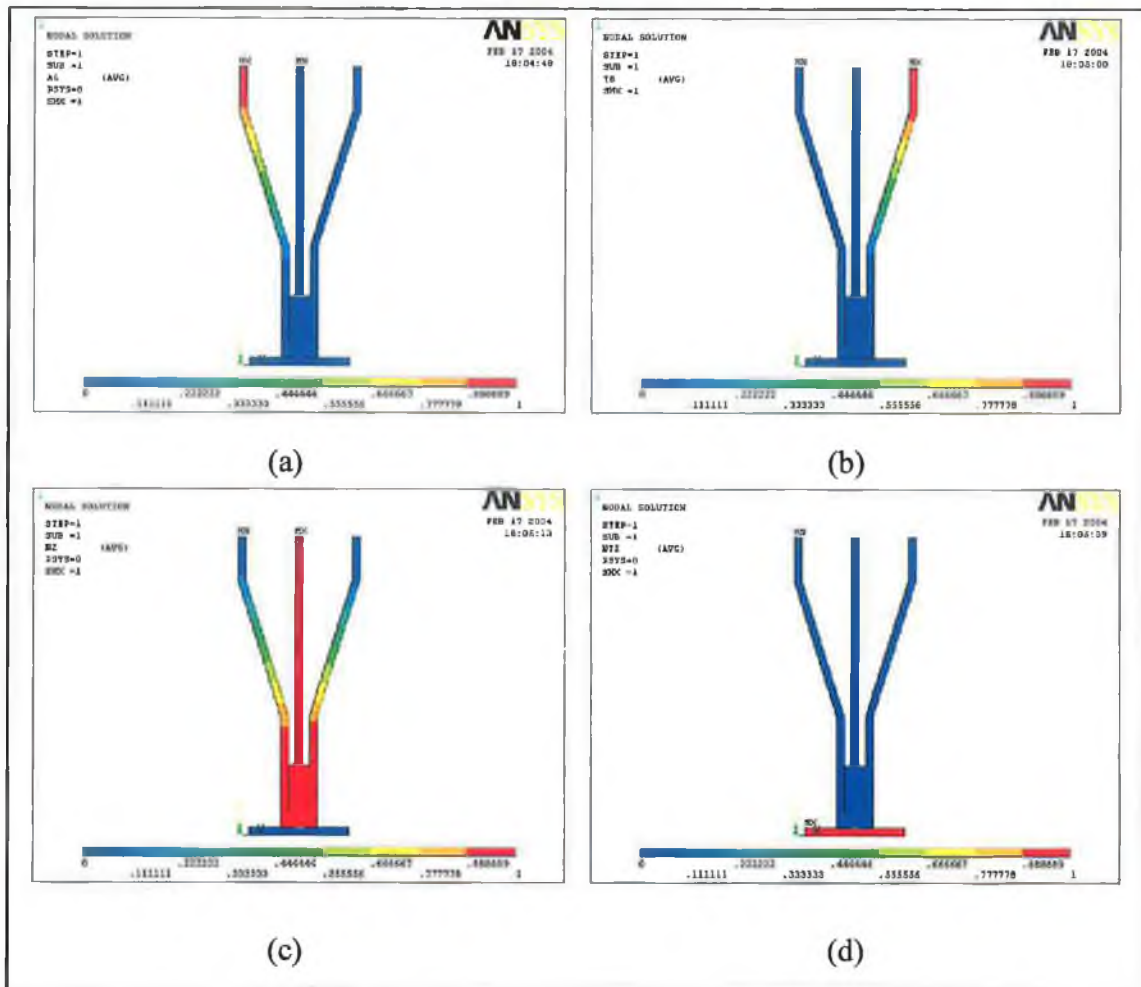
Figure 4.24: Mass fraction simulation results of the (a) aluminium and (b) tool-steel
powder at a ratio of 1:3, nitrogen gas in the (c) inlet pressure tube and
(d) pick-up shaft for a pressure ratio of 10:1.

4.2.3 Effect of Gravity and Change of Dimension of the Gas - Powder Carrying Tubes and Pick-Up Shaft

In order to check whether gravity and the geometric dimensions of the different gas and
powder flow tubes and pick-up shaft had any effect on simulated results, further
simulation were done using fine mesh in the mixing zone. The results are shown in the
following sections.

(a) Effect of Change of Diameter of the Inlet pressure tube

The diameter of the inlet pressure tube was changed from 3 mm to 6 mm to check whether the change of the diameter had any effect on the simulated results Initially the nitrogen gas velocities of 3970 cm/s and 2965 cm/s were set on the inlet pressure tube and the pick-up shaft respectively. Simulation results showed that due to increase of diameter of inlet pressure tube, the velocity of the nitrogen gas was increased from 3970 cm/s to around 4500 cm/s there. Increase of velocity with an increase in diameter is explained below. When a fluid enters a pipe, all the particles except those in contact with the wall flow with some velocity (figure 4.25). The friction at the wall slows the fluid down more and more near the wall, thus forming a boundary layer. Since the total flow rate past any section of the pipe is constant, the velocity of the fluid near the axis must increase to compensate for the retardation of fluid near the walls [249]. This process continues until the final flow pattern is obtained, where the velocity of the fluid at centre line is maximum. The entry length of the pipe up to the onset of fully developed laminar flow is defined as [251],

$$L = 0.06DRe \qquad\qquad \text{Equation 4.3}$$

Where

$L =$ entry length

$D =$ diameter of the pipe

$Re =$ Reynolds number
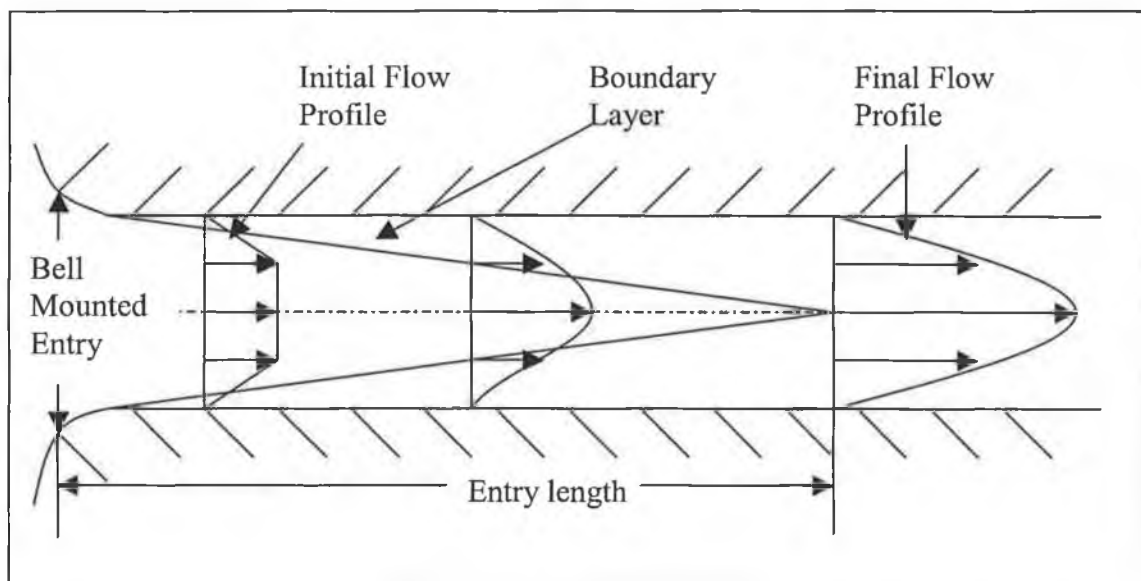
Figure 4.25: Growth of boundary layer in a pipe.

Thus, in a pipe of larger diameter, the fluid has to travel further than it has to do in a pipe of smaller diameter, to obtain the developed flow. Thus the velocity (developed) is higher for larger diameter than that for smaller diameter [249]. Compared to 6 mm diameter tube, the velocity of the fluid flowing through the 3 mm diameter tube increased less, as it had to travel a shorter distance to obtain the final flow profile. For this reason, the simulation showed a constant velocity for the fluid flowing through the 3 mm diameter inlet pressure tube. The entry length calculated for the fluid flowing through the 6 mm diameter inlet pressure tube was 0.632 cm for an initial velocity of 2000 cm/s, as compared to 0.158 cm for the 3 mm diameter tube. Simulated results showed that the velocity of the fluid did indeed increase from 2000 cm/s to a maximum of 2565 cm/s over a distance of around 0.60 cm from the inlet.

In the simulation, when the nitrogen gas reached the mixing zone, it still had a velocity of 1600 cm/s. It prevented the aluminium and tool-steel powders from mixing with each other, as shown in figure 4.26 (a) by forming a jet of high speed, which was not penetrable. Then the velocity of the nitrogen gas on the inlet pressure tube was changed to 3450 cm/s. But still the two powders could not mix. Finally when the velocity was set to 2000 cm/s on the inlet pressure tube, the aluminium and tool-steel powder mixed with each other and the powder mixture entered the nitrogen gas flow inside the pick-up shaft through the pick-up shaft hole for each ratio of the starting aluminium and tool-steel powders (figure 4.26 (b)). In this case, the velocity had reduced to around 800 cm/s (low enough to allow the powders to penetrate the jet) when it reached the mixing zone and the pressure ratio of the nitrogen gas on the inlet pressure tube to the pick-up shaft was around 1:1.
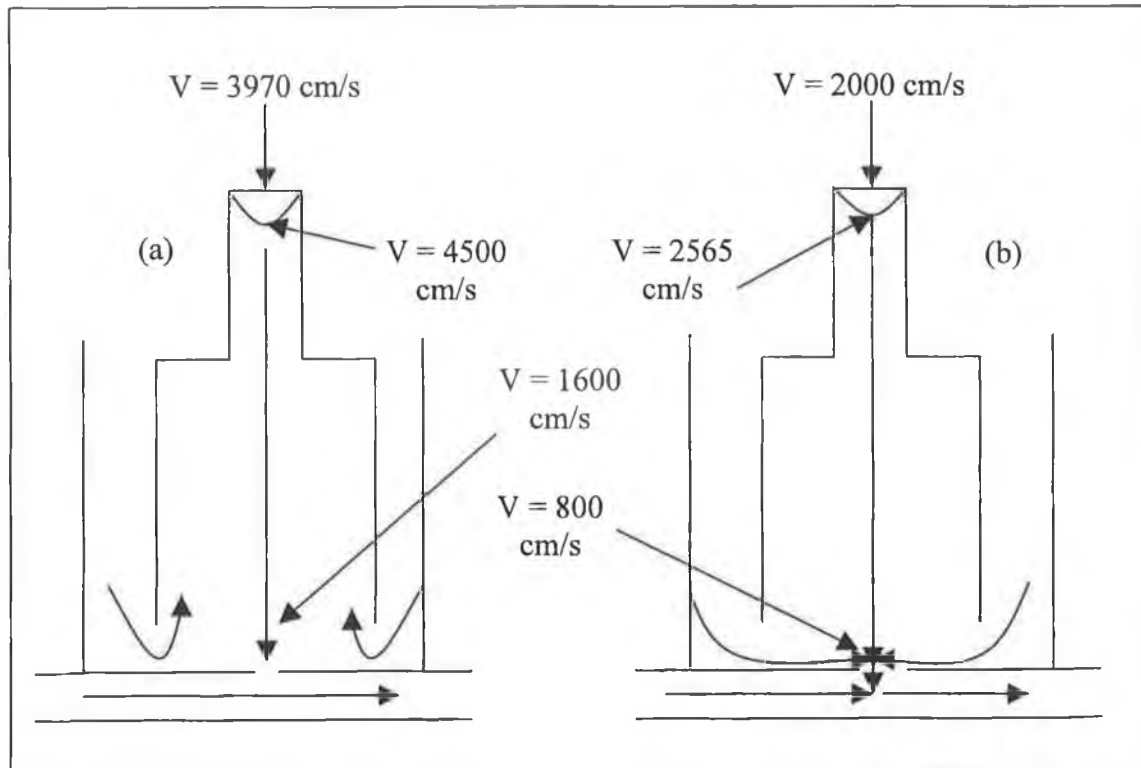
Figure 4.26: Schematic of (a) powders not mixing and (b) powders mixing for nitrogen gas velocity of 3970 cm/s and 2000 cm/s respectively on the inlet pressure tube.

Particle flow lines for the aluminium and tool-steel powder at a ratio of 1:3 with nitrogen gas velocities of 2000 cm/s and 2965 cm/s on the inlet pressure tube (of a diameter of 6 mm diameter) and the pick-up shaft respectively is shown in figure 4.27. The nitrogen gas flowing from the inlet pressure tube entered both the powder flow tubes through the mixing zone. For the aluminium and tool-steel powder ratio of 3:1, some portion of the nitrogen gas flowed from the pick-up shaft to the tool-steel powder flow tube through the mixing zone. When the ratio was 1:1, a little amount of the nitrogen gas entered the mixing zone, while it was unable to enter the mixing zone for aluminium and tool-steel powder ratio of 1:3. The mass fraction simulation results of the nitrogen gas (from the pick-up shaft) for three different ratios' of the powders with a 6 mm diameter inlet pressure tube are shown in figure 4.28.
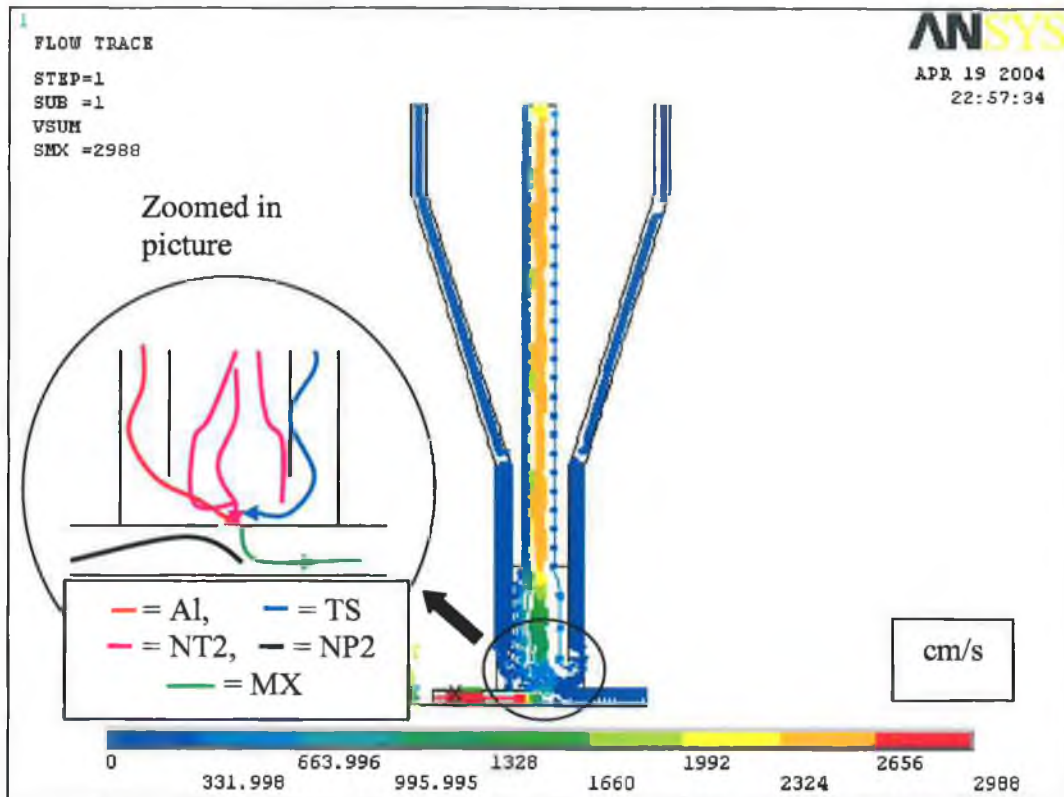
Figure 4.27: Particle flow lines for the nitrogen gas and powders (at a ratio of 1:3) with nitrogen gas velocities of 2000 cm/s and 2965 cm/s on the inlet pressure tube (of a diameter of 6 mm) and pick-up shaft respectively.

(a)

(b)

(c)
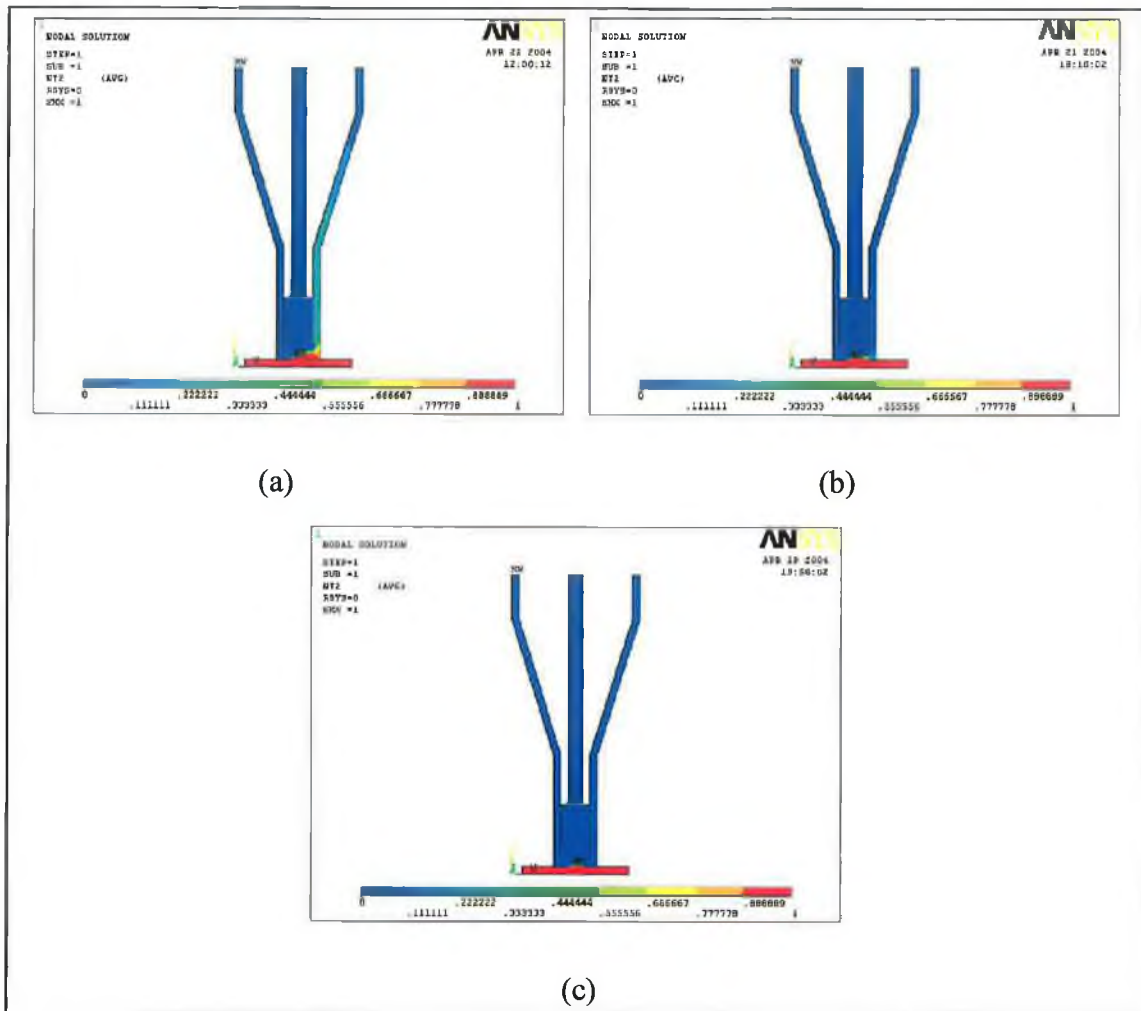
Figure 4.28: Mass fraction simulation results of the nitrogen gas (from the pick-up shaft) for the aluminium and tool-steel powder at ratios' of (a) 3:1, (b) 1:1 and (c) 1:3 with nitrogen gas velocities of 2000 cm/s and 2965 cm/s on the inlet pressure tube (of a diameter of 6 mm) and the pick-up shaft respectively.

(b) Effect of Change of Length of the Pick-Up Shaft

Next the length of the pick-up shaft was changed from 40 mm to 48.8 mm. Again, a fine type of meshing technique in the mixing zone was used. The nitrogen gas pressure ratio on the inlet pressure tube to the pick-up shaft was set to 10:1. Again for each ratio of the aluminium and tool-steel powders, the two powders mixed in the mixing zone, then the powder mixture went through pick-up shaft hole into the nitrogen gas flow inside the pick-up shaft. The nitrogen gas flowing from the pick-up shaft showed the same behaviour as it showed in did for 40 mm pick-up shaft. This is supported by theory, as once developed flow has occurred the velocity remains constant from then on as long as there are no interruptions in the pipe [249]. The velocity loss near the pick-up shaft was

144

same for both cases. A schematic of the velocity profile of the fluid through the pick-up shaft for two lengths is shown in figure 4.29, while, the particle flow lines of the aluminium and tool-steel powder at a ratio of 3:1 are shown in figure 4.30.
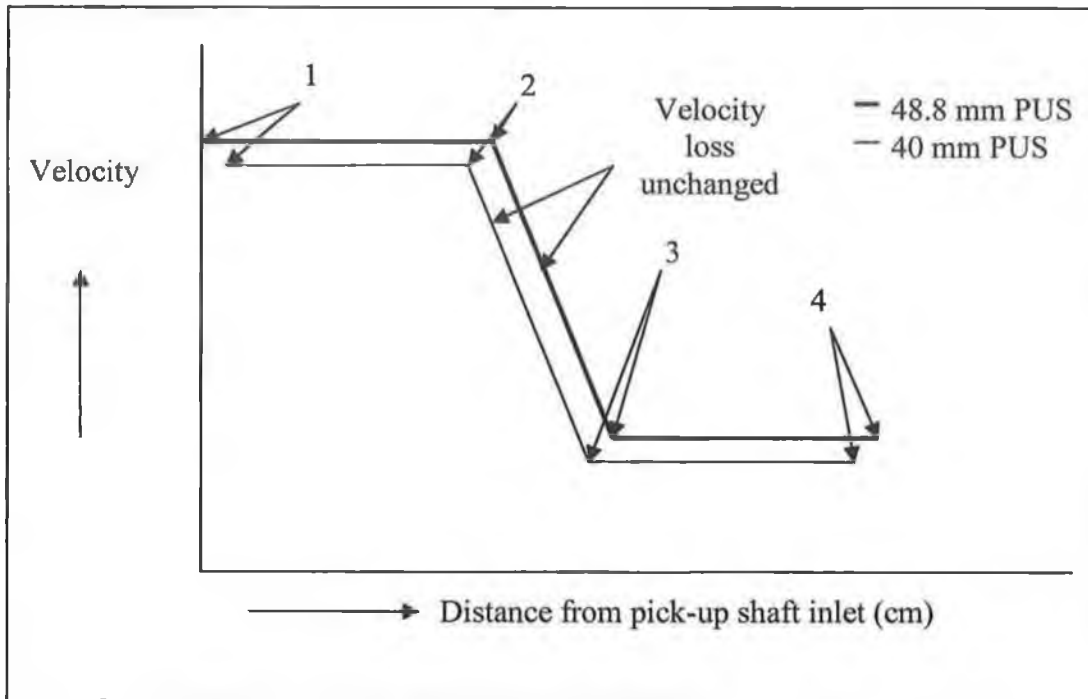
Figure 4.29: Schematic of the velocity profile of the fluid through two different pick-up shaft having different lengths.
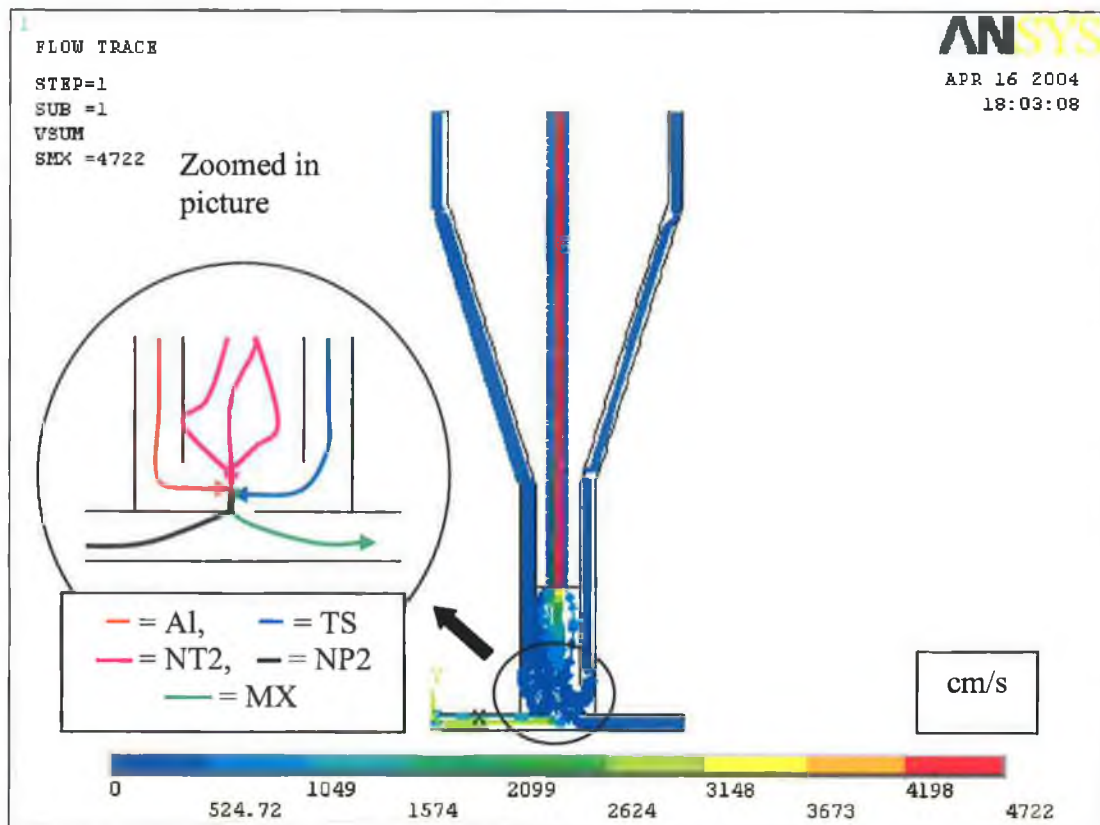
Figure 4.30: Particle flow lines of the nitrogen gas and powders (at a ratio of 3:1) for a pressure ratio of 10:1with a 48.8 mm long pick-up shaft.

(c) Effect of Change of Diameter of the Pick-Up Shaft

In order to check whether the change of diameter of the pick-up shaft had any effect on simulated results, the diameter of the pick-up shaft was changed from 3 mm to 6 mm for the next set of simulations. Initially the nitrogen gas velocities on the inlet pressure tube and the pick-up shaft were set to 4720 cm/s and 2965 cm/s respectively, which gave a pressure ratio of 10:1 on those two parts. The aluminium and tool-steel powder flowed through to the mixing zone and mixed with each other for each ratio of starting powders. Due to the increase in diameter of the pick-up shaft, the velocity of the nitrogen gas increased from a value of 2965 cm/s to around 3750 cm/s there, due to the same reason mentioned for the fluid flow through the inlet pressure tube. The velocity remained constant until it reached close to the pick-up shaft hole. As a result of the high velocity jet again the powder mixture from the mixing zone could not penetrate the nitrogen gas flow inside the pick-up shaft (figure 4.31 (a)). In order to force the powder mixture through the pick-up shaft hole, the velocity of the nitrogen gas at the inlet

pressure tube was increased to 5220 cm/s. This produced two jets perpendicular to each other combining as one output flow. Then the simulation showed that the powder mixture was able to enter through the pick-up shaft hole into the nitrogen gas flow inside the pick-up shaft in spite of increase of nitrogen gas velocity in the shaft (figure 4.31 (b)). Here the pressure ratio of the nitrogen gas on the inlet pressure tube to the pick-up shaft was around 17:1, as expected because a change in velocity means a change in pressure (equation 3.5). The particle flow lines for the aluminium and tool-steel powder at a ratio of 1:3 with nitrogen gas velocities of 5220 cm/s and 2965 cm/s on the inlet pressure tube and the pick-up shaft (of a diameter of 6 mm) respectively is shown in figure 4.32. The nitrogen gas flowing from the inlet pressure tube entered the powder flow tubes through the mixing zone. For each ratio of starting powders, the nitrogen gas flowing through the pick-up shaft could not enter the mixing zone due to increased velocity of the nitrogen gas from the inlet pressure tube.
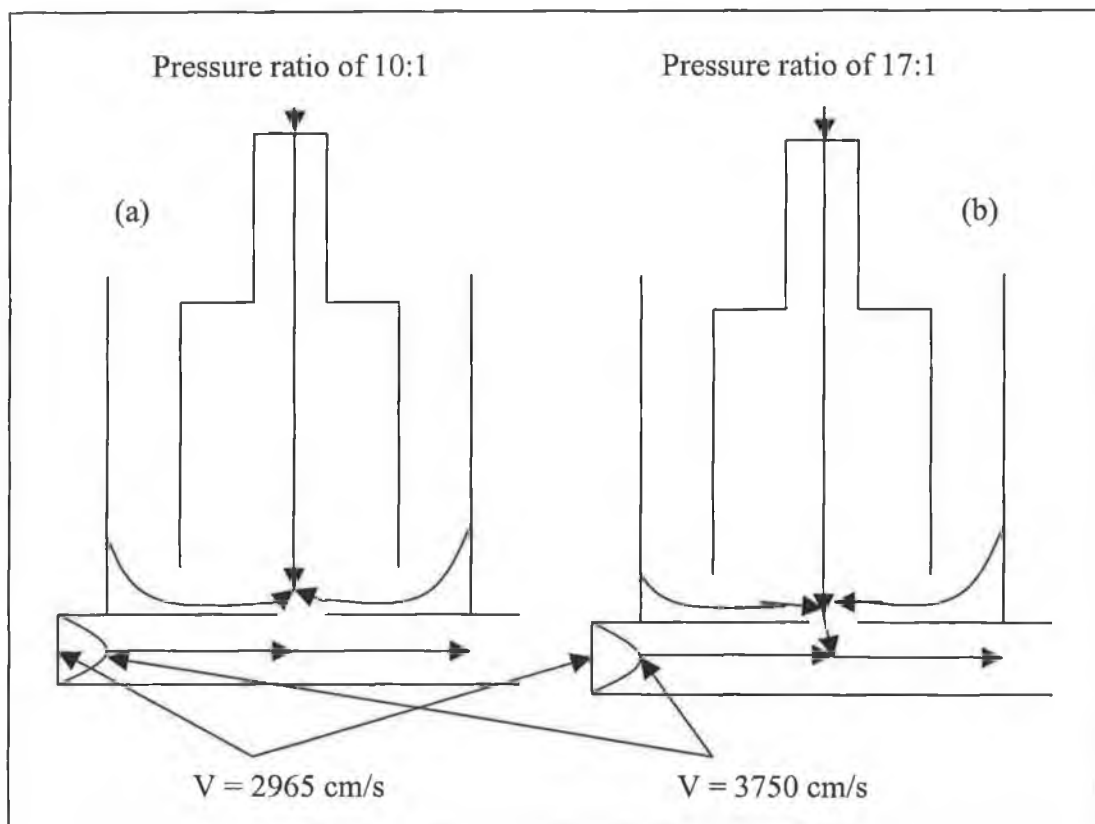
Figure 4.31: Schematic of (a) powders not entering and (b) powders mixing entering through the pick-up shaft hole for pressure ratio of 10:1 and 17:1 on the inlet pressure tube to the pick-up shaft respectively.
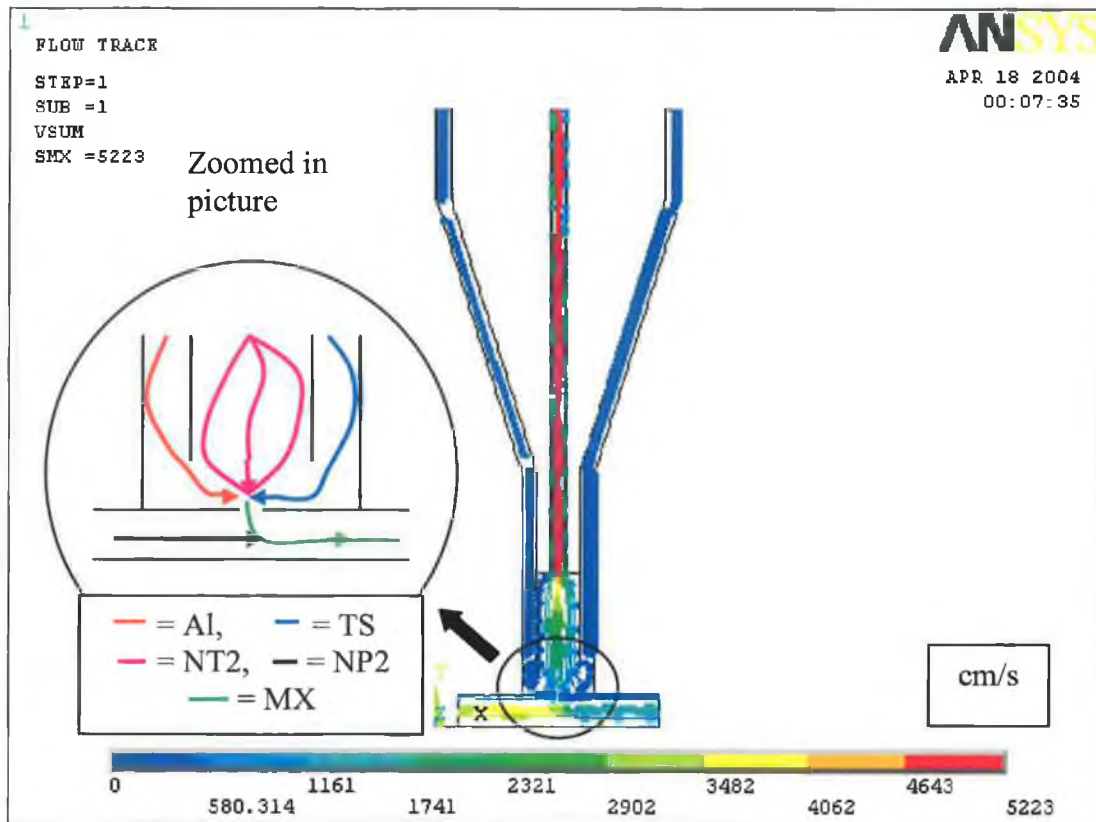
Figure 4.32: Particle flow lines for the nitrogen gas and powders (1:3) with nitrogen gas velocities of 5220 cm/s and 2965 cm/s on the inlet pressure tube and the pick-up shaft (of a diameter of 6 mm) respectively.

(d) Effect of Change of Dimension of the Powder flow Tubes

Finally, the diameter of the two powder flow tubes were changed from 3 mm to 6 mm to check whether the change of the diameter had any effect on the simulated results. The nitrogen gas velocities on the inlet pressure tube and the pick-up shaft were set such a way that it gave a pressure ratio of 10:1 on those two parts. The simulated results found were almost the same as that found for the 3 mm diameter tubes. Due to the increase of diameter of the powder flow tubes, velocity of the fluids flowing through there increased slightly as expected. However due to bend section in the tube, velocities decreased again and it did not have any further effect in changing the results. For each ratio of the aluminium and tool-steel powders, the powders mixed in the mixing zone, then the powder mixture entered the nitrogen gas flow inside the pick-up shaft through the pick- up shaft hole. Particle flow lines for the aluminium and tool-steel powder at a ratio of 1:3 are shown in figure 4.33 for an example. Some portion of the nitrogen gas

148

coming from the inlet pressure tube entered the powder flow tubes through the mixing zone. For powder ratio of 3:1, some portion of the nitrogen gas flowing from the pick-up shaft, entered the mixing zone and then onto the tool-steel powder flow tube. But for the other two ratios' it did not enter the mixing zone. The mass fraction simulation results of the nitrogen gas (from the pick-up shaft) for three different ratios' of powders with 6 mm diameter powder flow tubes are shown in figure 4.34.
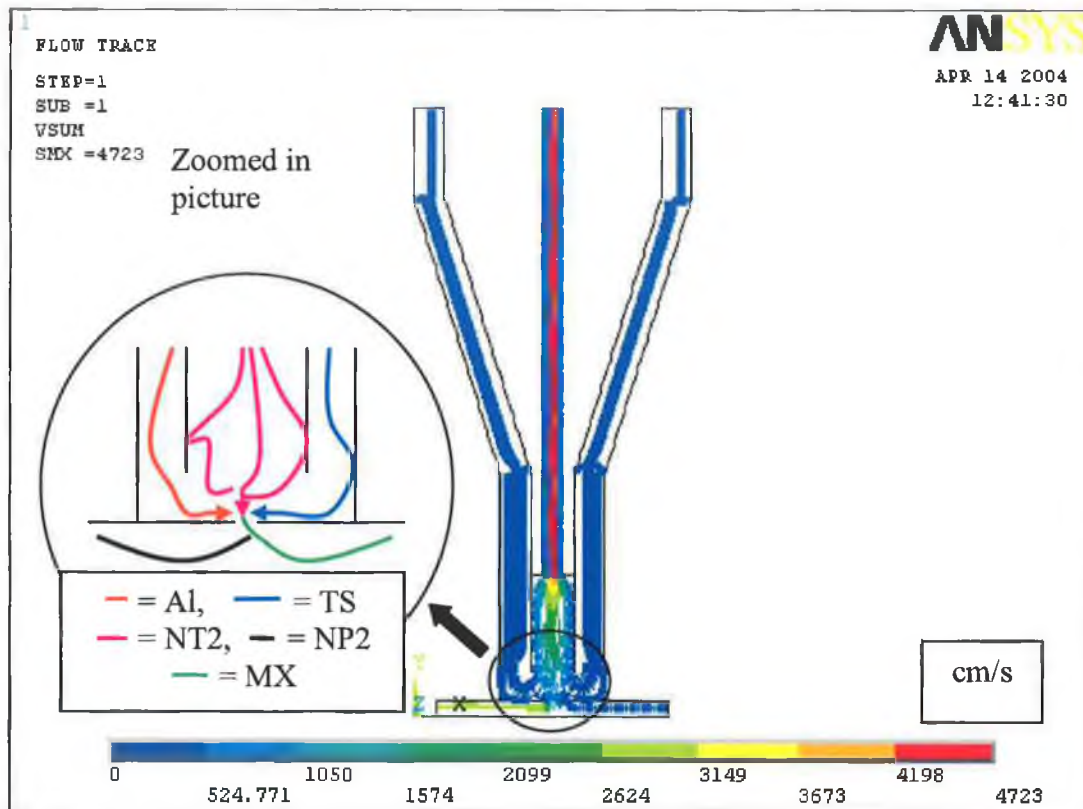
Figure 4.33: Particle flow lines for the nitrogen gas and powders (at a ratio of 1:3) for a pressure ratio of 10:1 with 6 mm diameter powder flow tubes.
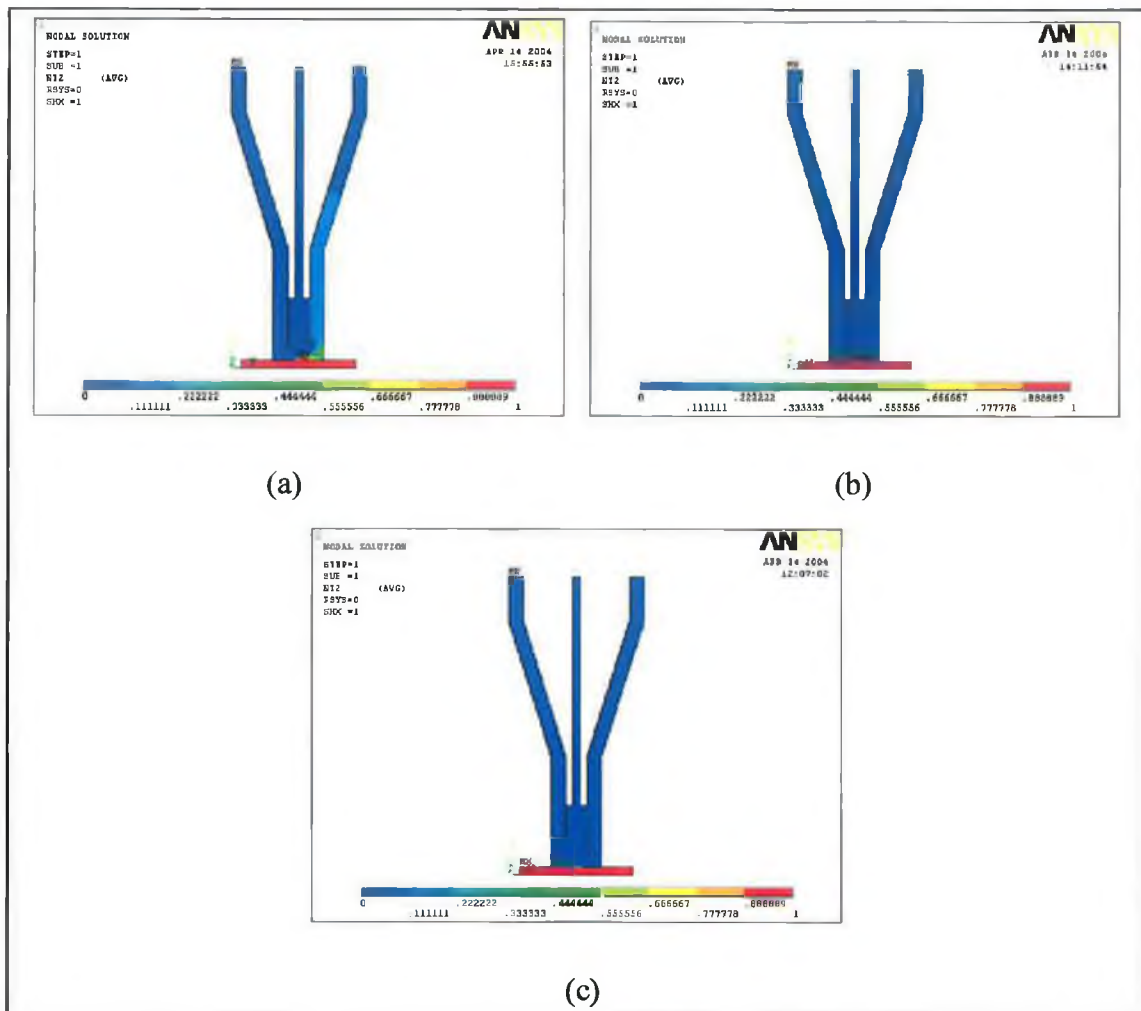
Figure 4.34: Mass fraction simulation results of the nitrogen gas (from the pick-up shaft) for the aluminium and tool-steel powder at ratios' of (a) 3:1, (b) 1:1 and (c) 1:3 with a nitrogen gas pressure ratio of 10:1 on the inlet pressure tube to the pick-up shaft and 6 mm diameter powder flow tubes.

(e) Effect of Gravity

In order to check gravity has any effect on the results, the simulation was re-run with 6 mm diameter powder inlet tubes, aluminium and tool-steel powder at a ratio of 1:3 and the nitrogen gas pressure ratio of 10:1 on the inlet pressure tube to the pick-up shaft. A value of acceleration of gravity of 981 cm/s^2 was used as an input parameter. The velocity results were found the same as that found without applying the gravity. The density of the fluids used in the simulation was very low, as a result the effect of gravity on the simulation results was very minor.

4.2.4 Conclusion of the Results

The simulation results show

1. That both the tool-steel and aluminium powder reach the mixing zone of the proposed design. Changes in the velocity and mass fraction ratios' of the two powders, as well as changes of the pressure ratio of the nitrogen gas on the inlet pressure tube to the pick-up shaft did not have a major effect on this result. The velocity and mass fraction ratio of 1:3 for the aluminium and tool-steel powder gave the best results in term of remaining closer to the pick-up shaft hole.

2. The aluminium and tool-steel powder almost completely mix with each other in the mixing zone of the designed part as shown by zoomed in pictures of particle flow lines for different powder and nitrogen gas pressure ratios'. Changes in the velocity and mass fraction ratio of the two powders, as well as changes of the pressure ratio of the nitrogen gas on the inlet pressure tube to the pick- up shaft do not affect this result at all.

3. The nitrogen gas pressure ratio of 10:1 for the inlet pressure tube to the pick-up shaft is required in terms of carrying the two powders up to the mixing zone, mixing the powders and then putting them through the pick up-shaft hole into the nitrogen gas flow inside the pick-up shaft.

4. At this 10:1 pressure ratio, the velocity profile results show that the fluid flowing through the pick-up shaft has lowest velocity near the pick-up shaft hole for all three ratios' of the aluminium and tool-steel powders. This is due to the flow of the slow moving fluid (compared to the fluid flowing through the pick- up shaft) from the mixing zone into the pick-up shaft.

5. Changing the diameter of the powder flow tubes, and changing the length of the pick-up shaft, does not have any major effect on the results. If the diameter of the pick-up shaft is increased, a higher pressure from the top nitrogen gas is required to force the powder mixture through the pick-up shaft hole. When the diameter of the inlet pressure tube is increased from 3 mm to 6 mm, a pressure

ratio of 1:1 on the inlet pressure tube to the pick-up shaft is required to force the powder mixture through the pick-up shaft hole into the nitrogen gas flow.

6. The acceleration of gravity had a very minor effect on simulated results. The density of the aluminium and tool-steel powders, as well as the nitrogen gas is very low, which resulted in a negligible effect of gravity on results.

4.3 CALIBRATION TESTS

FLOTRAN CFD simulation results showed that proposed design, having dimensions proposed in concept four would work in terms of mixing two powders and putting the powder through pick-up shaft hole inside the nitrogen gas flow there. Designed parts were then manufactured and calibrated. This section describes the results of the powder flow bench tests and in-situ flow tests outlined in chapter 3. Powder flow bench tests were carried out in order to calibrate powder flow in relation to number of turns of the needle shaped bolts, while the in-situ flow tests were carried out to check functionality of the dual powder feed system.

4.3.1 Powder Flow Bench Tests

Results of the different types of bench tests for both the aluminium and tool-steel powder mentioned in chapter three are described in the following sections. These tests did not involve the current powder feed hopper, so that tests were done outside the hopper. As a result no pressure was involved in the tests.

(a) For Aluminium Powder

The amount of flow of the aluminium powder for different number of turns of the needle shaped bolt using chamber A are given in Appendix C (tables A1 to A5), while equivalent results for the aluminium powder using chamber B are shown in Appendix C (tables A6 to A10). The flow time was 20 seconds for each of the experiments. As an example table A1 shows the results of the flow tests of the aluminium powder for 3 turns of the needle shaped bolt in chamber A. Third column in the table shows the combined weight of the container of known weight and the powder (that is collected inside the container during the test). The weight of the container is deducted from the combined weight to calculate the weight of the aluminium powder. Five tests of same procedure were done. The average weight of the aluminium powder is shown in the last column of the table. The weight of the container shown in the table is different for different tests, this is due to accumulation of some powder in the container from the previous test.

The data is represented as average mass flow rate (g/sec) against number of turns for both chamber A and B in figures 4.35. Zero number of turns was the closed position of the needle shaped bolts. It means that the flow path of powders from the powder holder was totally closed. With the increase in number of turns, the flow area opened more and as a result more powder flowed through. For a particular number of turn, mass flow rate of the aluminium powder was greater in chamber B than in chamber A. As an example, for 3 turns of the needle, the average mass flow rate in chamber B was 0.134 g/sec, which was 1.5 % higher than that of 0.132 g/sec in chamber A. The flow path of powder in chamber B might be smoother than that of chamber A. The maximum scatter of weight for a particular number of turn in chamber A was 5.4 %, while that in chamber B was 2.4 %. It was not possible to clean the container completely before starting the next bench test, which gave some scatter in results. Again it was not always possible to give the valves the exact number of turns, which might be another cause of scatter. Due to less scatter of weight in chamber B, it would be the preferable choice for the aluminium powder during spraying.
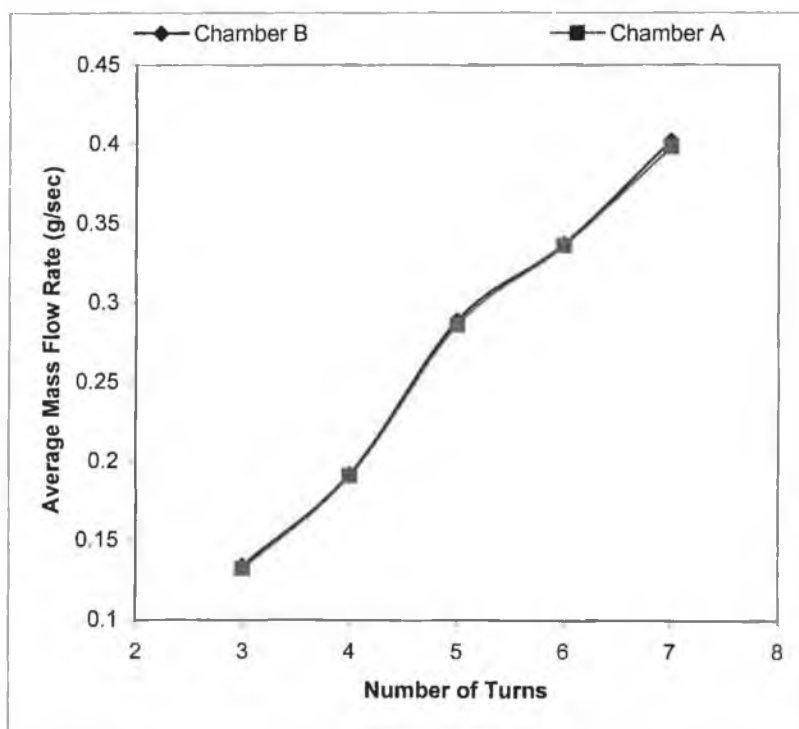
Figure 4.35: Average mass flow rate (g/sec) Vs number of turns of the needle shaped bolt for the aluminium powder in chamber A and B.

(b) For Tool-Steel Powder

Appendix D (tables A11 to A15) shows the flow results of the tool-steel powder for different number of turns of the needle shaped bolt in chamber B, while Appendix D (tables A16 to A20) has the data for the tool-steel in chamber A. The experimental time (flow time) was 20 seconds in both cases. Again the data is represented as average mass flow rate (g/sec) against number of turns for both chamber A and B in figure 4.36. Like the aluminium powder, the mass flow rate of the tool-steel powder was greater in chamber B than in chamber A for a particular number of turns. As an example, for ¼ a turn of the needle, the average mass flow rate in chamber B was 0.102 g/sec, which was 6.25 % higher than that of 0.096 g/sec in chamber A. Again the smoothness of the flow path of powder in chamber B might be the cause for the increased amount of flow in chamber B. For a particular number of turns, maximum scatter of weight in chamber A was 3.65 %, while that in chamber B was 10.8 %. As the mass flow rate of the tool-steel powder in chamber B was higher than chamber A, slight deviation in fraction number of turn of the bolt resulted in higher scatter in Chamber B compared to chamber A. Due to less scatter of weight in chamber A, it would be the preferable choice for the tool-steel powder during spraying.
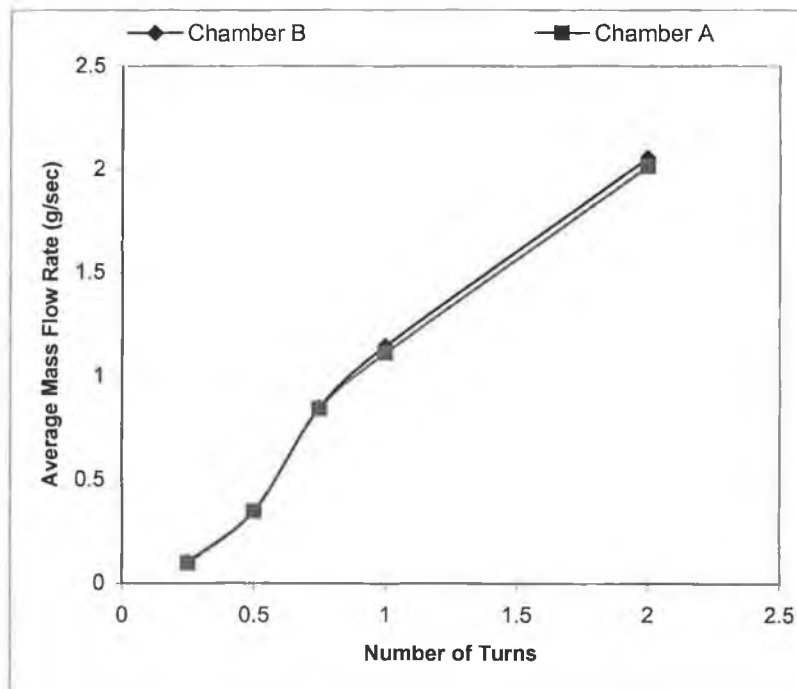
Figure 4.36: Average mass flow rate (g/sec) Vs number of turns of the needle shaped bolt for the tool-steel powder in chamber A and B.

(c) For both Aluminium and Tool-Steel Powder

As mentioned earlier, the mass flow rate of the aluminium powder showed greater scatter in chamber A than in chamber B. While the mass flow rate of the tool-steel powder showed greater scatter in chamber B than in chamber A. Thus chamber A was used for the tool-steel powder and chamber B was used for the aluminium powder subsequently. The mass flow rate of the aluminium powder in chamber B and mass flow rate of the tool-steel powder in chamber A is plotted against number of turns of the needle shaped bolt as shown in figure 4.37.

The mass flow rate of the tool-steel powder per turn of the needle bolt valve was much higher than that of the aluminium powder as shown in figure 4.37. The mass flow rate of the aluminium powder was 0.407 g/sec for 7 turns, while that of the tool-steel powder was 0.407 g/sec only for ½ a turn. The volumetric flow rate of the aluminium powder was 0.075 cm^3/sec for 4 turns, while that of the tool-steel powder was 0.075 cm^3/sec for only ½ a turn. The volumetric flow rate was obtained by dividing the mass flow rate by density using the following equations:

$$\rho = \frac{m}{Q}$$
Equation 4.4 (a)

$$\Rightarrow Q = \frac{m}{\rho}$$
Equation 4.4 (b)

Where

ρ = density (g/cm^3)

m = mass flow rate (g/sec)

Q = volumetric flow rate (cm^3/sec)

For an example, the mass flow rate of the tool-steel powder for 2 turns was 2.0858 g/sec. Dividing it by 6.10 g/cm^3 (the density of the tool-steel powder [64]), the volumetric flow rate (0.342 cm^3/s) was obtained. It is assumed that the relatively high flow rate of the tool-steel powder was associated to its high density. The tool-steel powder used in the current project had a density of 6.10 g/cm^3; while the aluminium powder was 2.70 g/cm^3 [64]. Another factor may be the difference between the two powders particle shape. Figure 4.38 shows SEM images of the aluminium and tool-steel powders. Both the images were taken at a magnification of X1110. The aluminium

powder had a more irregular shape and generally large particle shape compared to the tool-steel powder with poorer flow characteristics.
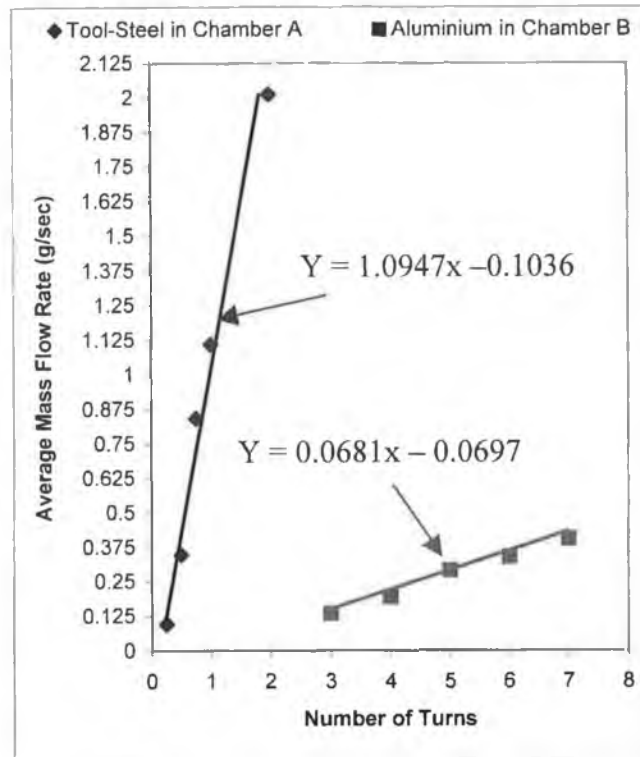
Figure 4.37: Average mass flow rate of the tool-steel and aluminium powder against number of turns of the needle shaped bolt in both chamber A and B.

In order to vary the ratio of the aluminium and tool-steel powder during spraying, the needle shaped bolts inside the powder holders carrying two powders must be given a different number of turns. This can be governed using the fitted equations derived for the flow curves in figure 4.37. The different number of turns of the needle shaped bolts required to obtain different ratios' of the tool-steel and aluminium powder are given in table 4.2

Table 4.2: Different number of turns of the needle shaped bolt required to obtain different ratios' of the tool-steel and aluminium powder.

Ratio of		Number of turns of needle bolt valve inside the powder holder containing	
Aluminium powder	Tool-steel powder	Aluminium powder	Tool-steel powder
4	1	7 and 3/4	1/5
3	1	8	1/4
2	1	6	1/4
1	1	9	1/2
1	2	5	1/2
1	3	4	1/2
1	4	3	1/2
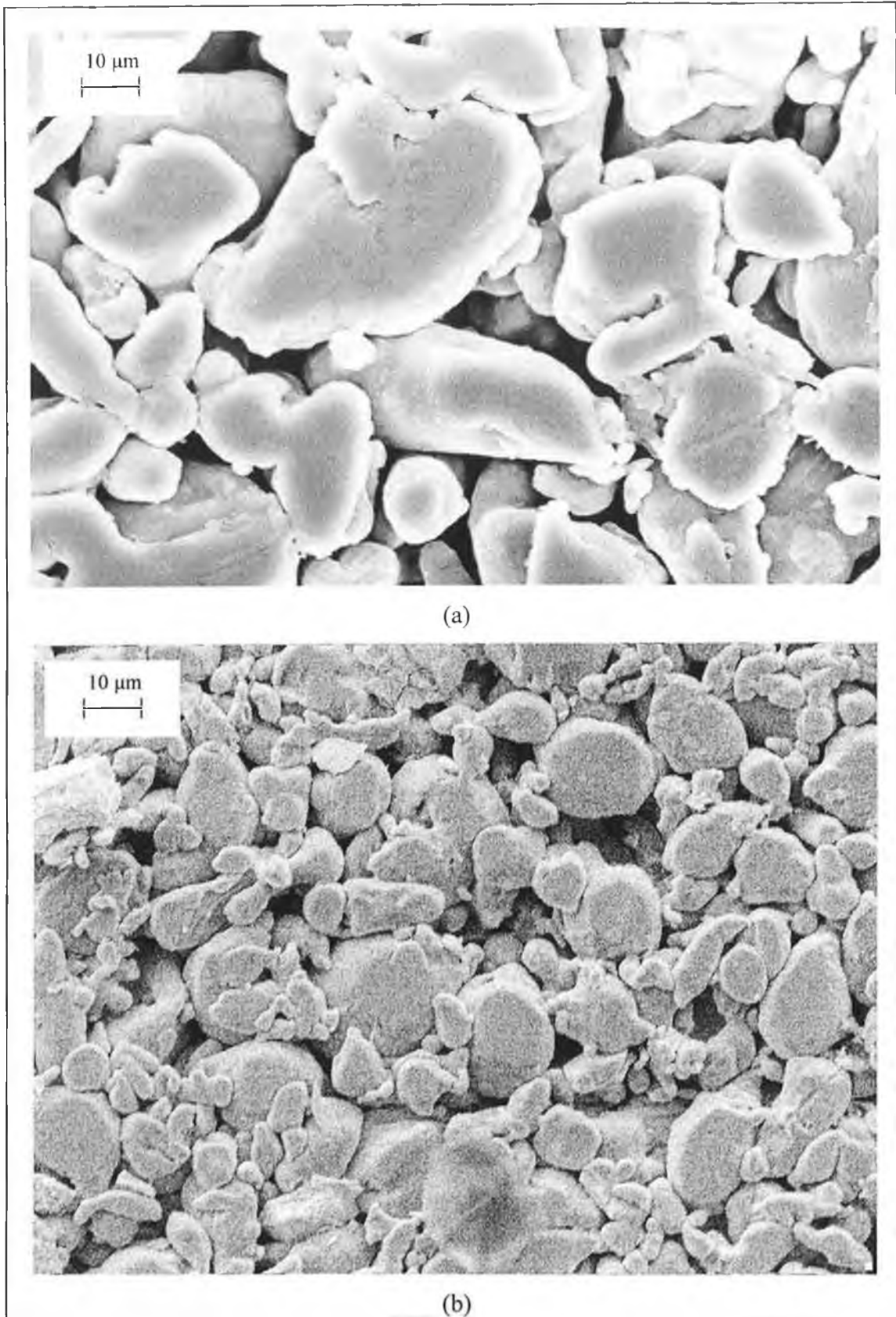
Figure 4.38: SEM images of the (a) aluminium and (b) tool-steel powder.

4.3.2 In-Situ Flow Tests

In-situ flow tests were carried out in to check the functionality of the dual powder feed system inside the hopper unit under pressure. In order to accommodate the needle shaped bolts inside the powder feed hopper, a special top was required. The designed rectangular hopper (figure A11 in Appendix A) cover was used to serve the purpose. The results of the in-situ flow tests are shown in table 4.3 and in figure 4.39. Using table 4.2 (derived from the bench results), the bolts were given different numbers of turns to allow the aluminium and tool-steel powder to flow at ratios' of 1:3, 1:1 and 3:1 into the mixing zone (chapter 3). Experimental (flow) time was 6 minutes for all the tests.

Table 4.3: Results of the magnetic separation technique during obtaining the tool-steel and aluminium powder at ratios' of 1:3, 1:1 and 3:1.

Al = Aluminium, TS = Tool-Steel

Ratio of TS to Al powder Expected	Weight of container (g)	Weight of container + powders used (g)	Weight of powders (Al +TS) (g)	Weight of Al powder left after magnetic separation (g) (a)	Weight of TS powder (g) (b)	Ratio of TS to Al powder Obtained (b/a)
0.33	85	205	120	88	32	0.36
1.00	85	202	117	57	60	1.05
3.00	85	212	127	31	96	3.10
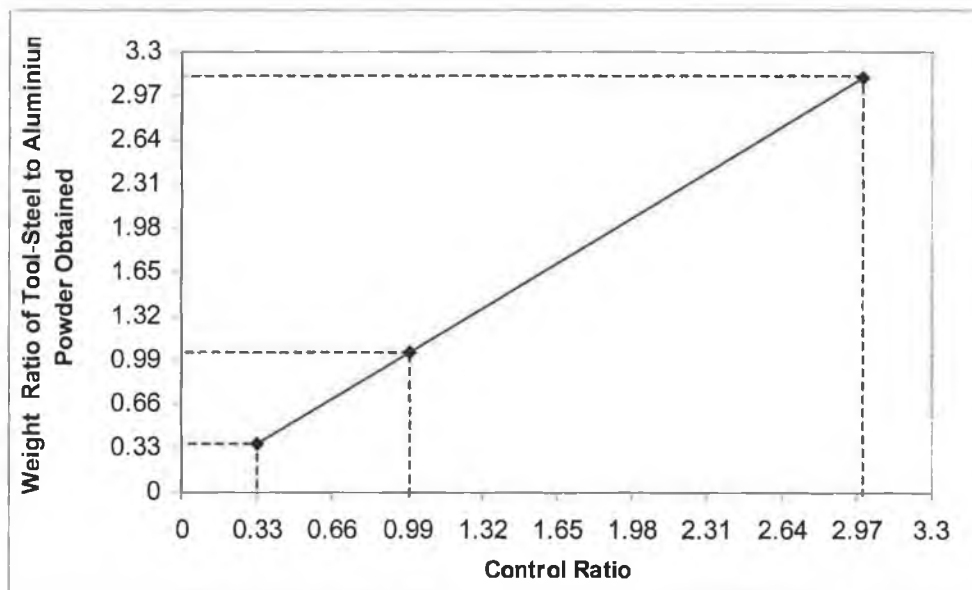
Figure 4.39: Results of the in-situ flow tests.

159

Visual inspection tests showed that the two powders were almost properly (if not totally) mixed when they were taken into the container before the magnetic separation test was conducted. It means that the newly designed dual-powder feed system was successful in mixing two powders before forcing them into the nitrogen gas flow inside the pick-up shaft for every mass fraction ratios' of tool-steel and aluminium powder, as predicted by the ANSYS FLOTRAN CFD simulation. The magnetic separation technique showed that the system was able to control the ratios' of the aluminium and tool-steel powder at required rates. Linearity of the in-situ flow curve proves just that. Maximum difference between the tool-steel to aluminium powder ratio expected and obtained was only 9.09 %. Hence it was decided to use the dual-powder feed system in depositing aluminium/tool-steel functionally graded coatings for the reminder of the project.

4.4 OPTIMISATION OF SPRAY PARAMETERS

As mentioned earlier, 3^3 factorial design of experiments was employed to establish the effects of the spray parameters on residual stress build-up in aluminium/tool-steel functionally graded coatings. The independent variables were set to three levels, which imply that 27 experiments were necessary to explore the variation of all variables at the chosen levels. The Clyne's analytical method was subsequently used to measure residual stress of twenty-seven different sets of coatings. This method uses the deflection, Young's modulus, Poisson's ratio and temperature difference between the substrate and coatings to calculate the residual stress value. While some of the values could be measured in the current project, the relevant temperatures had to be calibrated for specific coating configurations. The calibration test results showed that the designed powder feed system was able to control the ratios' of the aluminium and tool-steel powders at required rate. In order to check whether the ratios' were maintained in the graded coatings, the chemical composition of different layers of a five layer graded coatings was determined using the energy dispersive X-ray spectroscopy (EDS). Microstructure and phases present in the graded coating was also identified. All the results are described in the following sections.

4.4.1 Chemical Composition of Different Layers of a Graded Coating

Results of measurement of chemical composition of a aluminium/tool-steel functionally graded coating using the energy dispersive X-ray spectroscopy (EDS) are shown in figures 4.40 through to 4.42. The aluminium powder used was 99.5 % Al, while the tool-steel powder had a chemical composition of 95.2 % Fe, 3 % Mo and 1.8 % C. So the percentage of Al and Fe present in different layers indicated the percentage of aluminium and tool-steel present in those layers respectively.

Sample /xd1/window1/#1,ts75.spt
Accelerating Voltage: 9.68 keV
Takeoff Angle: 35.00 degrees
Library for system standards:
/imix/spectra/system_standards.dir

Elm Prec.	Rel. K Standard	Z	A	F	ZAF	Norm wt%
Fe 0.00	0.0000 (S)Fe_K	1.154	1.002	1.000	1.1565	0.00
Al 8.24	1.0000 (S)Al_K	1.000	1.000	1.000	1.0000	100.00
Total						100.00

(a)

Sample /xd1/window1/#1,ts25.spt
Accelerating Voltage: 7.56 keV
Takeoff Angle: 35.00 degrees
Library for system standards:
/imix/spectra/system_standards.dir

Elm Prec.	Rel. K Standard	Z	A	F	ZAF	Norm wt%
Fe 7.86	0.2599 (S)Fe_K	1.132	1.000	1.000	1.1320	29.42
Al 5.87	0.6558 (T)Al_K	0.966	1.114	1.000	1.0763	70.58
Total						100.00

(b)

Figure 4.40: Chemical composition of (a) first layer (100 % Al) and (b) second layer (75 % Al, 25 % TS) of a five layer aluminium/tool-steel functionally graded coating.

162

Sample /xd1/window1/#1,ts75.spt
Accelerating Voltage: 7.50 keV
Takeoff Angle: 35.00 degrees
Library for system standards:
/imix/spectra/system_standards.dir

Elm Prec.	Rel. K Standard	Z	A	F	ZAF	Norm wt%
Fe 14.84	0.4828 (S)Fe_K	1.090	1.000	1.000	1.0897	52.61
Al 7.34	0.4213 (T)Al_K	0.938	1.199	1.000	1.1249	47.39
Total						100.00

(a)

Sample /xd1/window1/#1,ts75.spt
Accelerating Voltage: 7.52 keV
Takeoff Angle: 35.00 degrees
Library for system standards:
/imix/spectra/system_standards.dir

Elm Prec.	Rel. K Standard	Z	A	F	ZAF	Norm wt%
Fe 16.54	0.7321 (S)Fe_K	1.045	1.000	1.000	1.0448	76.49
Al 4.87	0.2011 (T)Al_K	0.909	1.287	1.000	1.1693	23.51
Total						100.00

(b)

Figure 4.41: Chemical composition of the (a) third layer (50 % Al, 50 % TS) and (b) fourth layer (25 % Al, 75 % TS) of a five layer aluminium/tool-steel functionally graded coating.

163

```
Sample /xd1/window1/#1,ts75.spt
Accelerating Voltage:              7.48 keV
Takeoff Angle:                     35.00 degrees
Library for system standards:
/imix/spectra/system_standards.dir

Elm   Rel. K      Z     A     F     ZAF    Norm wt%
Prec. Standard

 Fe   1.0000    1.000 1.000 1.000 1.0000   100.00
31.66 (T)Fe_K
 Al   0.0000    0.878 1.367 1.000 1.2000     0.00
0.00 (T)Al_K

Total                                      100.00
```
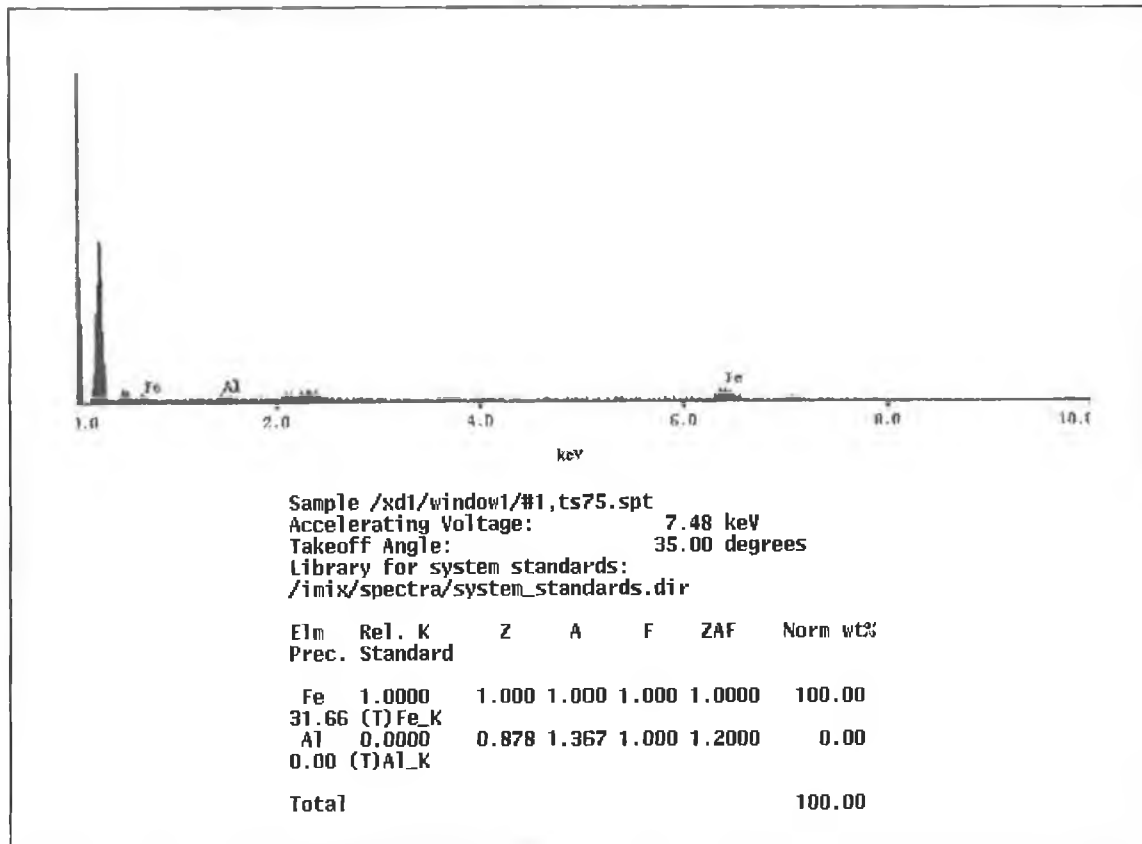
Figure 4.42: Chemical composition of the final layer (100 % TS) of a five layer aluminium/tool-steel functionally graded coating.

The first layer of the five layer aluminium/tool-steel functionally graded coating was of a composition of 100 % aluminium that was expected. The second layer consisted of 70.58 % aluminium and 29.42 % tool-steel (figure 4.40 (b)), which was close to the composition (75 % aluminium, 25 % tool-steel) anticipated. The chemical composition of the third layer was 47.39 % aluminium and 52.61 % tool-steel according to figure 4.41 (a). The expected chemical composition of the third layer was 50 % aluminium and 50 % tool-steel. The fourth layer consisted of 23.51 % aluminium and 76.49 % tool-steel (figure 4.41 (b)), which was again very close to the composition (75 % aluminium, 25 % tool-steel) anticipated. The chemical composition of the final layer was 100 % tool-steel. Table 4.4 shows the chemical composition of the different layers of a five layer graded coating that was anticipated and obtained. Thus the new device was successful in depositing functionally graded coatings with gradual variation in chemical composition from the bond layer to the top layer. Discrepancy may be due to the device and the chemical composition measurement technique.

Table 4.4: Chemical composition of different layers of a five layer aluminium/tool-steel graded coating anticipated and obtained.

Layer Number	Chemical Composition Anticipated	Chemical Composition Obtained
1	100 % Al	100 % Al
2	75 % Al, 25 % TS	70.58 % Al, 29.42 % TS
3	50 % Al, 50 % TS	47.39 % Al, 52.61 % TS
4	25 % Al, 75 % TS	23.51 % Al, 76.49 % TS
5	100 % TS	100 % TS

4.4.2 Microstructure and Phase Identification

Visual inspection (either macro or microscopic) is the primary characterization technique used to gain coating microstructural information such as chemical composition, grain morphology and orientation, defects and so on of thermally sprayed coatings. The grinding and polishing techniques described in the previous chapter was used to prepare graded sample before microstructural observation. Though thickness microstructure of a five layer aluminium/tool-steel functionally graded coating is shown in figure 4.43. Near the aluminium substrate is the aluminium rich region, while the top of figure 4.43 is showing the tool-steel rich region. Mo_2C started to form in iron matrix with increase in amount of tool-steel in the coating. Middle of the coating mainly consisted of dendritic phases of FeAl and Mo_2C. When hot iron (Fe) impinge the presolidified aluminium, Fe softened the aluminium and formed FeAl in the resulted coating. Dendritic FeAl and Mo_2C was found by some researchers in their research [252,253]. Al_2O_3 was also observed in the middle portion of the coating. Top portion of the coating consisted of Mo_2C and Al_2O_3 along with some FeO/Fe_2O_3 in iron matrix.

X-ray diffraction phase analysis and EDS element detection was done subsequently to make sure that the phases and constitute elements are present in the graded coating. The size of the X-ray beam used was 1 mm, so the analysis obtained was from the whole of the coatings. Results are shown in figure 4.44. Besides FeO, Fe_2O_3, Al_2O_3, Mo_2C, Fe and Al, FeAl was also present in the coating according to the XRD results. Dendritic FeAl phase was formed due to the presence of Fe and Al in the starting coating material.
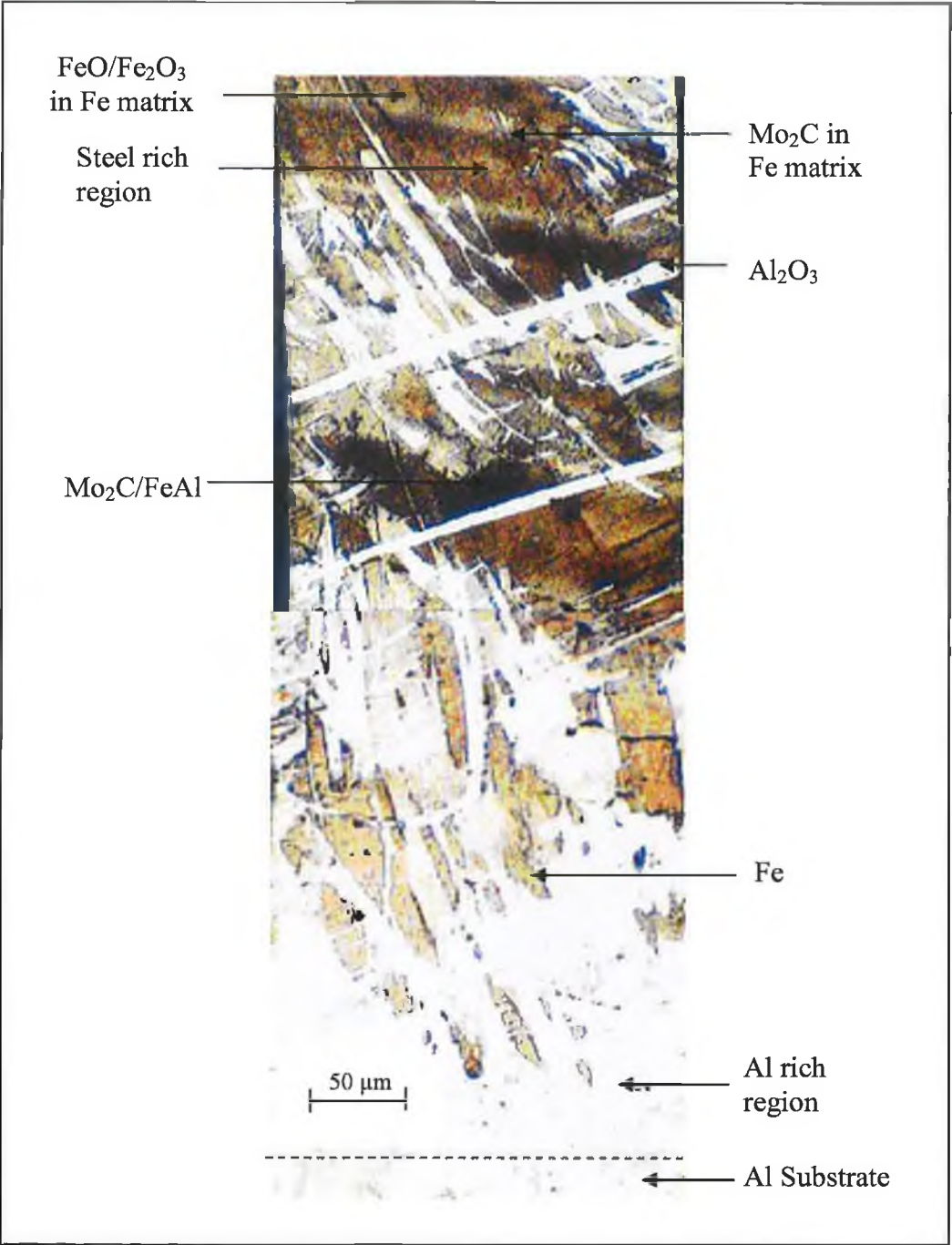
Figure 4.43: Optical micrograph of aluminium/tool-steel graded coating deposited onto an aluminium substrate.
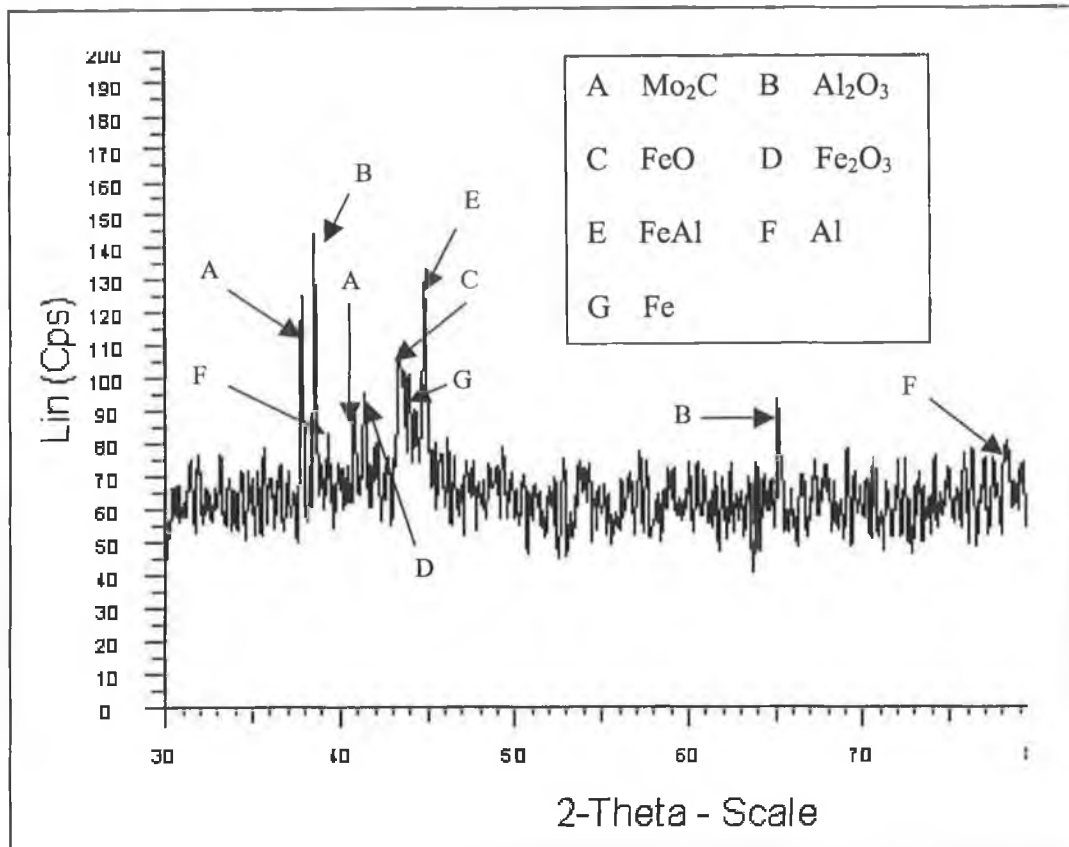
Figure 4.44: Phase analysis of an aluminium/tool-steel graded coating
deposited onto an aluminium substrate.

Figure 4.45 shows the results of chemical analysis of aluminium rich region, middle portion and tool-steel rich region of an aluminium/tool-steel graded coating. Figure 4.45 (a) is showing that aluminium rich region near the aluminium substrate consists mostly of aluminium. In the middle portion of the coating Fe, Al, Mo, C and O were present (figure 4.45 (b)). Al and Fe combined to form FeAl, Mo and C combined to form MoC, while Fe and O combined to form Al_2O_3. Again tool-steel rich region consisted of Fe, Al, Mo, C and O (figure 4.45 (c)). However FeO and Fe_2O_3 were also formed here along with FeAl, MoC and Al_2O_3 due to the present of higher percentage of Fe as indicated by figure 4.42.
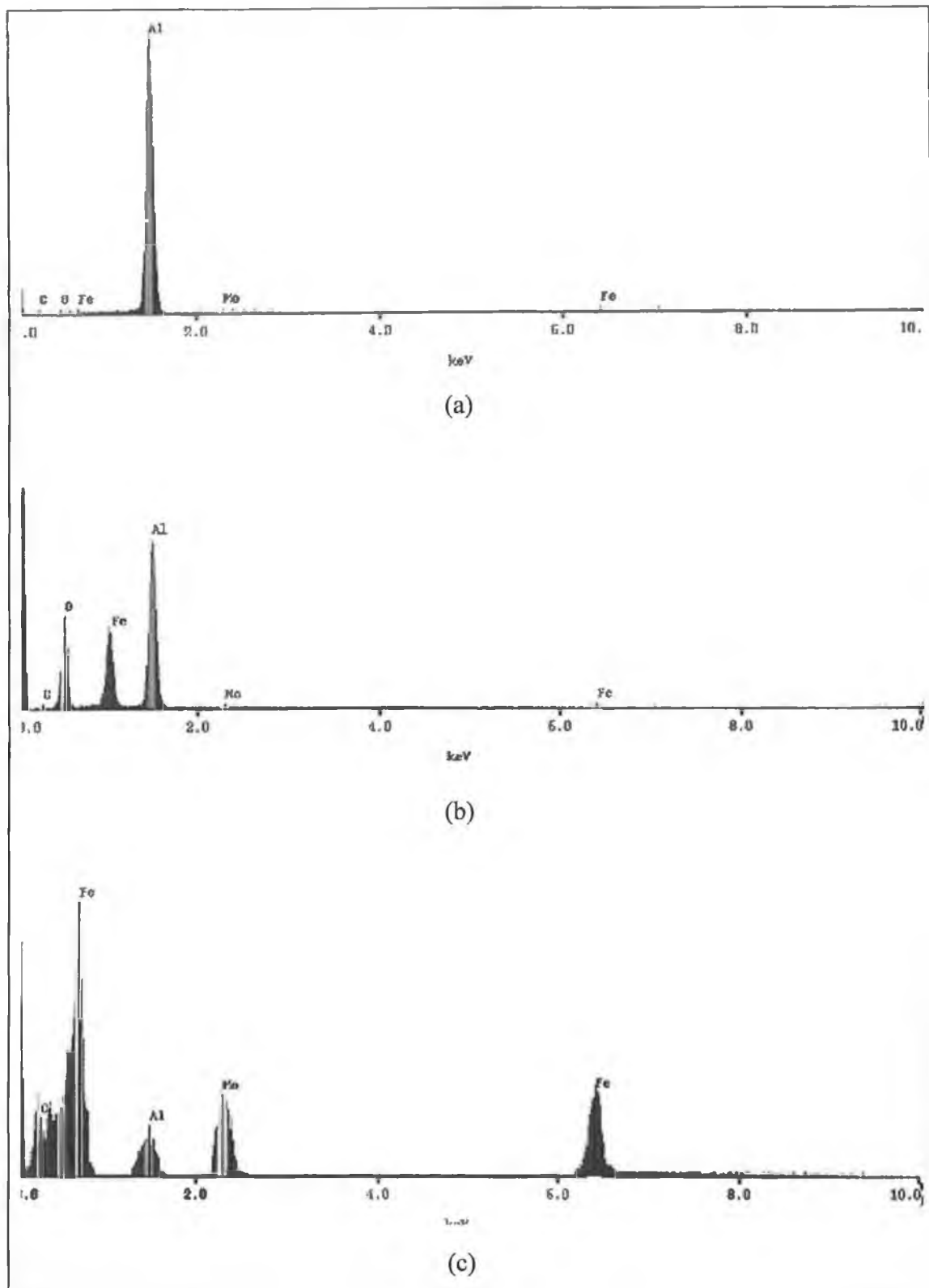
Figure 4.45: Chemical Composition of (a) aluminium rich region, (b) middle portion and (c) tool-steel rich region of an aluminium/tool-steel graded coating.

4.4.3 Measurement of Young's Modulus and Poisson's Ratio

Residual stress distribution through the coating-substrate system is dependent upon the Young's modulus and Poisson's ratio of the coating and the substrate. Therefore it was necessary in the current project to measure the Young's modulus and Poisson's ratio for range of spray parameters. The Cantilever beam method described by Rybicki et al. [224] was used to determine those values. The method is based on a least squares fit of the equilibrium equation (equation 3.25), which was analysed using Microsoft Excel to evaluate the Young's modulus and Poisson's ratio values. The coating deposition matrix used during measurement of the Young's modulus and Poisson's ratio along with the average results is shown in table 4.5. Table 4.5 is also showing the deflection values that were measure using the strain gauge after coating deposition. All the coatings had five graded layers with the composition of 100 % Al, 75 % Al – 25 % TS, 50 % Al – 50 % TS, 25 % Al – 75 % TS and 100 % TS from the bond layer to the top layer respectively. Samples 19, 22 and 25 burnt out as the aluminium substrates could not withstand the temperatures at which the coating particles and combust gases were propelled towards them during coating deposition. Samples 6, 9, 15, 18, 24 and 27 were not considered for the Young's modulus measurement, as the quality of the deposits was very poor in their cases. Thickness was very low and coatings were porous for these six samples.

Table 4.5 shows the dependency of spray parameters on the deposit thickness, Young's modulus and Poisson's ratio. Increase in spray distance resulted in lower particle velocities and lower impact temperatures. This in turn produced coatings having lower density and hardness. With a decrease in the flow rate ratio of oxygen to propylene, the flame temperature increases as shown in figure 4.46 [39]. The flame temperature increased from 3000 to 3070 ^{0}C, with a decrease in the flow rate ratio from 4.50 to 3.75. Increase in flame temperature, in turn increased the coating temperature and produced coatings with different properties. Compressed air is used in the HVOF process to accelerate powder particles onto the substrate and to cool the combustion zone of the gun [34]. Increase in the flow of the compressed air, results in a lower flame and coating temperature, which in turn produced different coating properties. The range of the Young's modulus measured for different spray parameters was between 122 to 153 GPa. The values of the Poisson's ratio measured were between 0.30 to 0.33, again due to the use of different spray parameters during coating deposition.
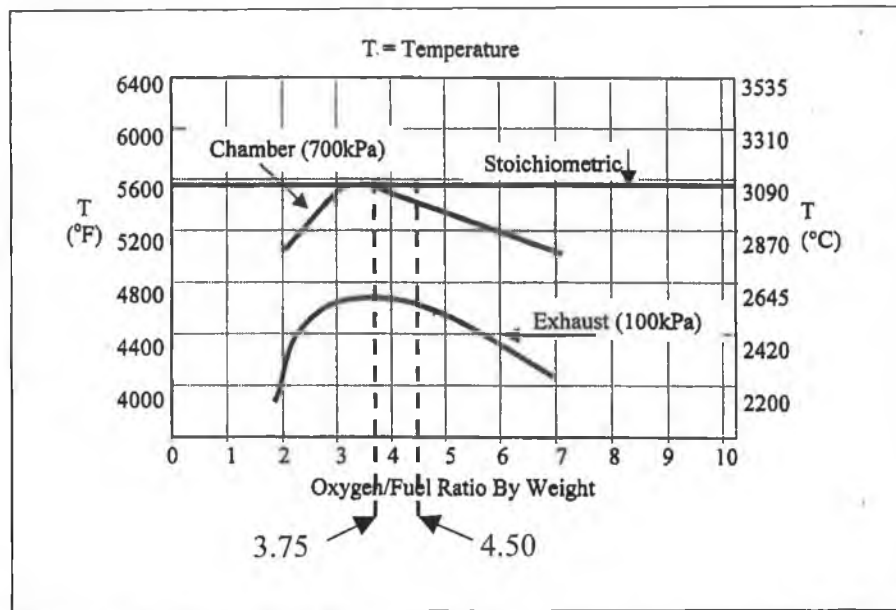
Figure 4.46: Theoretical flame temperature against oxygen/fuel ratio [39].

In order to check the accuracy of the Cantilever beam method, Young's modulus and Poisson's ratio of each sample was measured three times. For an example, the values of Young's modulus found for sample 4 were 146, 148 and 149 GPa respectively, while the Poisson's ratio was found to be the same (0.30). So maximum scatter from average value was 0.90 % only, which proves the suitability of Cantilever beam method in measuring Young's modulus and Poisson's ratio.

Table 4.5: Coating deposition matrix used for the determination of Young's modulus and Poisson's ratio.

Sample No	Flow Rate Ratio of Oxygen to Propylene	Flow Rate of the Compressed Air (SLPM)	Spray Distance (mm)	Coating Thickness (mm)	Young's Modulus (GPa)	Poisson's Ratio	Deflection (mm)
1	4.50	270	225	0.50	153	0.30	1.80
2	4.50	270	250	0.15	133	0.33	1.20
3	4.50	270	275	0.10	127	0.33	1.10
4	4.50	305	225	0.45	148	0.30	1.80
5	4.50	305	250	0.15	133	0.33	1.20
6	4.50	305	275	**			
7	4.50	340	225	0.45	148	0.30	1.75
8	4.50	340	250	0.15	130	0.33	1.20
9	4.50	340	275	**			
10	4.00	270	225	0.40	145	0.30	1.80
11	4.00	270	250	0.10	129	0.33	1.10
12	4.00	270	275	0.05	123	0.33	1.00
13	4.00	305	225	0.40	145	0.30	1.75
14	4.00	305	250	0.10	126	0.33	1.10
15	4.00	305	275	**			
16	4.00	340	225	0.35	144	0.30	1.70
17	4.00	340	250	0.10	125	0.33	1.10
18	4.00	340	275	**			
19	3.75	270	225	*			
20	3.75	270	250	0.05	125	0.33	1.00
21	3.75	270	275	0.05	122	0.33	1.00
22	3.75	305	225	*			
23	3.75	305	250	0.05	124	0.33	1.00
24	3.75	305	275	**			
25	3.75	340	225	*			
26	3.75	340	250	0.05	123	0.33	1.00
27	3.75	340	275	**			

* Substrate Burnt Out

** Poor Deposit

171

4.4.4 Measurement of Residual Stress

The Clyne's analytical method uses temperature difference between the substrate and coatings to calculate the residual stress value. The relevant temperature differences were calibrated for specific coating configurations using thermocouples. One thermocouple was fixed at the back of substrate, where another was fixed at the front of the deposited coating. Temperature gradient was obtained by heating the front of the coating with a heating torch. Five different types of graded coatings were considered, which were deposited by varying the flow rate ratio of oxygen to propylene, flow rate of the compressed air, spray distance and coating thickness. All the coatings had five graded layers with the composition of 100 % Al, 75 % Al – 25 % TS, 50 % Al – 50 % TS, 25 % Al – 75 % TS and 100 % TS from the bond layer to the top layer respectively. The coating deposition matrix used for the temperature measurement is shown in table 4.6.

Back and front temperatures for 0.25 mm graded coating and aluminium substrate are shown in figure 4.47. Figure 4.47 is also showing the Finite Element Analysis results of those uncoated and coated aluminium substrates. Simulation results were in good agreement with the experimental results. For an example, Finite Element temperature distribution through a 0.25 mm graded coating is shown in figure 4.48. Now for aluminium substrate, the experimental and simulation average temperature difference between the front and the back were 0.85 ^{0}C and 0.52 ^{0}C respectively, while the experimental and simulation average temperature difference between the front and the back were 0.91 ^{0}C and 0.64 ^{0}C respectively for 0.25 mm thick graded coating. For the thickest graded coating considered (0.90 mm), the experimental and simulation average temperature difference between the front and the back were 1.67 ^{0}C and 1.56 ^{0}C respectively. Temperature difference for other types (having thickness other than mentioned in table 4.6) of aluminium/tool-steel graded coatings were extrapolated from the temperature difference values found for the aluminium substrate and graded coating (mentioned in table 4.6), which in turn are used to measure residual stress values in those graded coatings using the Clyne's analytical method.

Table 4.6: Coating deposition matrix used for the temperature measurement.

Flow Rate Ratio of Oxygen to Propylene	Flow Rate of the Compressed Air (SLPM)	Spray Distance (mm)	Coating Thickness (mm)	Experimental Temperature Difference (^{0}C)
3.75	340	275	0.10	0.87
4.00	305	250	0.15	0.89
4.50	270	225	0.25	0.91
4.00	305	250	0.80	1.56
4.50	270	225	0.90	1.67
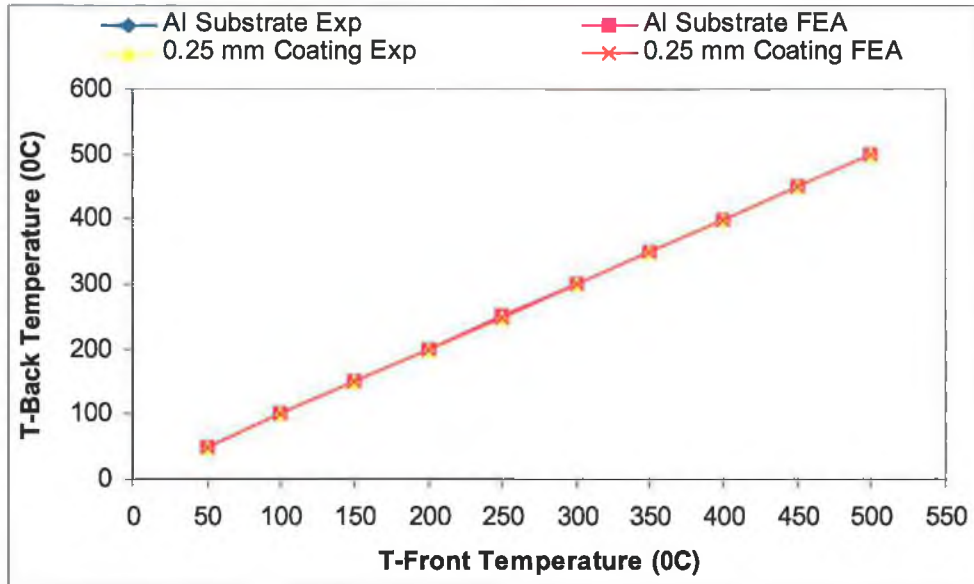
Figure 4.47: Experimental and simulation front and back temperatures for coated and uncoated aluminium substrates.
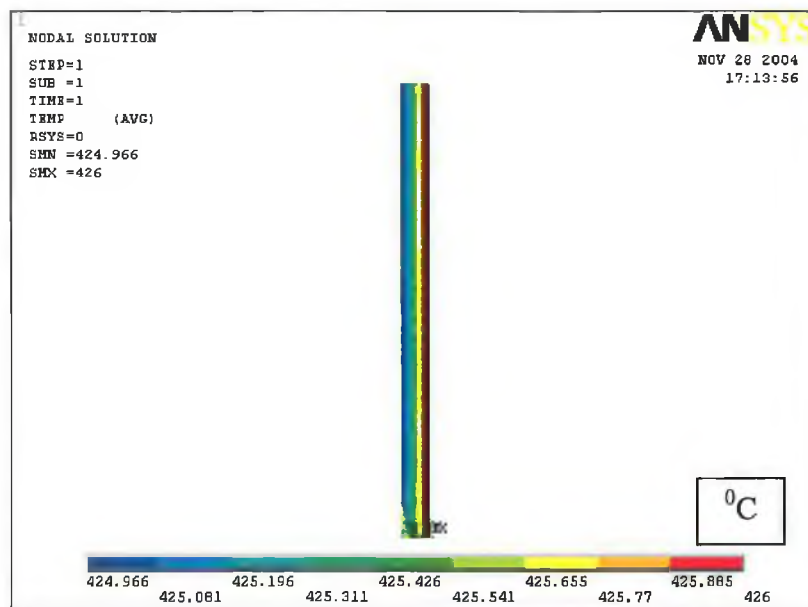
Figure 4.48: Finite Element temperature distribution for 0.25 mm graded coating.

173

As mentioned earlier, the Clyne's Analytical method was used in the current research to measure residual stress in different types of aluminium/tool-steel functionally graded coatings. Equations 3.28 to 3.30 were used to calculate the stress values at the top and the bottom of the substrate, as well as at the mid points of different graded layers. But thickness varied per sample. Among the three spray parameters that were varied during coating deposition, the spray distance showed the greatest effect on the deposited thickness. The results showed that the deposit thickness decreased with an increase in spray distance. For a flow rate ratio of oxygen to propylene of 4.50 and a flow rate of the compressed air of 270 SLPM (Standard Litre per Minute), the deposition thickness were 0.50, 0.15 and 0.10 mm for a spray distance of 225, 250 and 275 mm respectively. Thus deposition thickness increased by 400 % from a spray distance of 225 to 275 mm. With an increase in spray distance, the flight time of the particles from the gun to the substrate is increased, which results in lower impact particle velocities and lower impact temperatures. Some particles may have solidified even before they have impacted with the substrate, while some of them rebounded off the surface due to premature solidification. As a result the deposition thickness decreased. The flow rate ratio of oxygen to propylene and the flow rate of the compressed air had less effect on the deposition thickness compared to spray distance. For a spray distance of 250 mm and a flow rate of the compressed air of 270 SLPM, the deposition thickness was 0.15. 0.10 and 0.05 mm for a flow rate ratio of oxygen to propylene of 4.50, 4.00 and 3.75 respectively. Again for a flow rate ratio of oxygen to propylene of 4.50 and a spray distance of 225 mm, the deposition thickness was 0.50, 0.45 and 0.45 mm for a flow rate of the compressed air of 270, 305 and 340 SLPM respectively.

Figure 4.49 shows the residual stress distribution through a 0.50 mm thick graded deposit sprayed with a oxygen to propylene ratio of 4.50, a flow rate of the compressed air of 270 SLPM and a spray distance of 225 mm. The deposit had a compressive stress of 7 and 59 MPa at the middle of the 5th and 1st layer respectively. So the stress change (difference of stress between the1st and 5th layer) was calculated as −52 MPa. The stress distribution was linear from the middle of the 5th layer to the middle of the 2nd layer, however a sudden drop was found from the middle of the 2nd to the middle of the 1st layer.
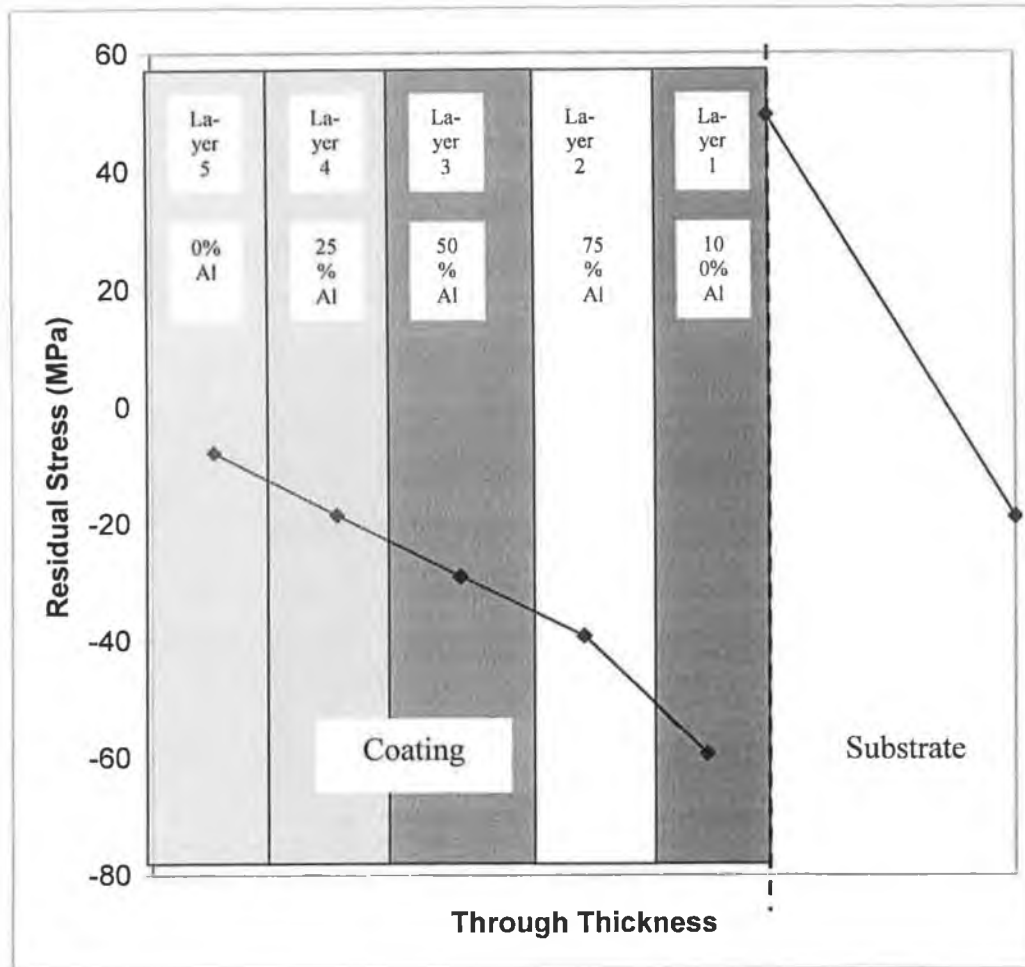
Figure 4.49: Residual stress distribution through a 0.50 mm thick graded
deposit and substrate.

Looking at the equation,

$$\sigma_{cj} = \frac{F_j}{bw} - E_c^{'}\left(k_j - k_{j-1}\right)\left((j-0.5)w - \delta_j\right) \ +$$

$$\sum_{i=j+1}^{n}\left(\frac{-E_c^{'}F_i}{b\left(h_s E_s^{'} + (i-1)w E_c^{'}\right)} - E_c^{'}\left(k_i - k_{i-1}\right)\left((j-0.5)w - \delta_i\right)\right) +$$

$$\frac{F_{CTE}}{bh_c} - E_c^{'}\left(k_c - k_n\right)\left((j-0.5)w - \delta_n\right)$$

used to calculate the stress value at the middle of a particular layer, the $\left(k_j - k_{j-1}\right)$ part,
where the curvature change between the layer (for which the stress was measured) and
the previous layer requires an input value. The thickness of the substrate was much
higher (0.90 mm) than the thickness of each layer (0.10 mm) of coating. So the
curvature change between the first layer and the substrate $\left(k_1 - k_0\right)$ was much higher
than those between the other layers. This in turn gave a higher value of stress

175

(compressive) at the middle of first applied layer compared to other subsequent layers. Deflection for the first layer was measured using a dial gauge and deflections for the other layers were then extrapolated using the thickness of each layer. Curvature values for different layers were then calculated from the deflection values. The stress values found at the top and the bottom of the substrate were 49 and −19 MPa respectively.

In order to find an approximate stress value at the top and the bottom of the deposit, the mid point of the 5th applied layer was linearly extrapolated to the top of the coating, and the mid point of the first applied layer was linearly extrapolated to the bottom of the coating. This extrapolation gave a compressive stress value of 2 and 69 MPa at the top and bottom of the deposit respectively. Figure 4.49 is re-plotted in figure 4.50 with the extrapolated values. It shows that the stress change from the top to the bottom of the deposit was −67 MPa and the stress change from the top to the bottom of the substrate interface was 68 MPa. Again in figure 4.50, the stress from the coating interface to the substrate interface is −119 MPa. For the reminder of the report, the stress distribution through the deposit and substrate will be plotted taking into account the extrapolated values.
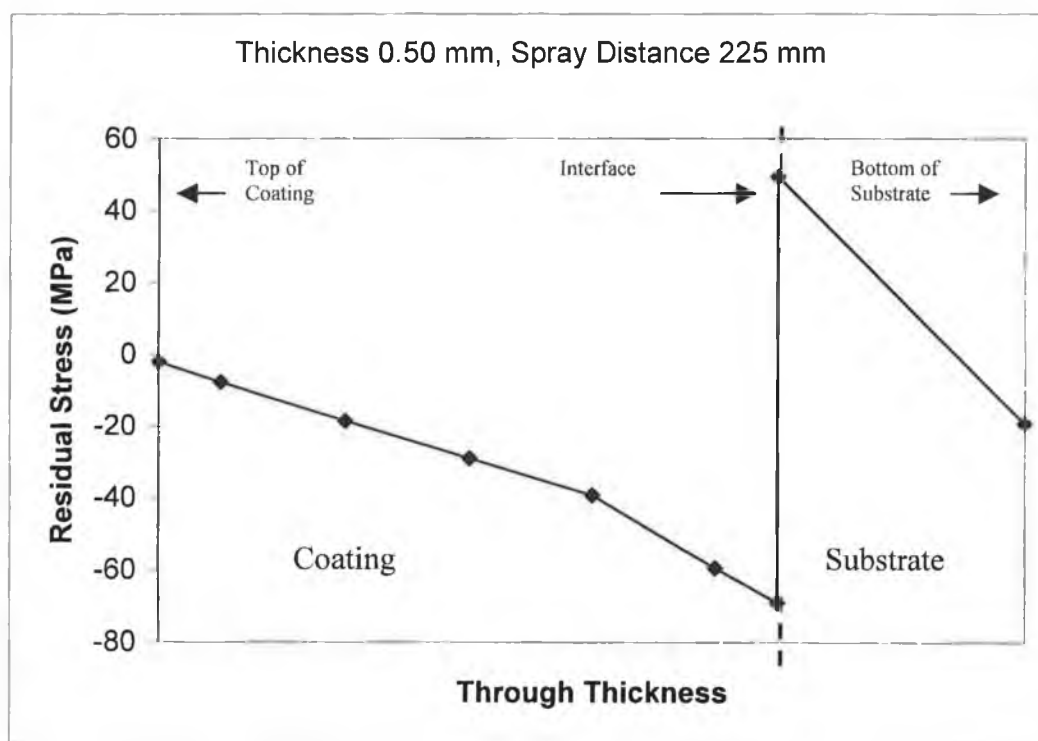
Figure 4.50: Residual stress distribution through a 0.50 mm thick graded deposit and substrate with the extrapolated values.

Results of tensile testing of aluminium/tool-steel graded coating is shown in figure 4.51. The Hounsfield Tensile Tester was used during yield stress determination. The applied force and displacement data was transferred to Excel. The stress-strain curve was obtained from the data and 0.2 % Proof Stress method was used to determine the yield stress of the coated sample. Yield stress of the coated sample was found to be 39 MPa.
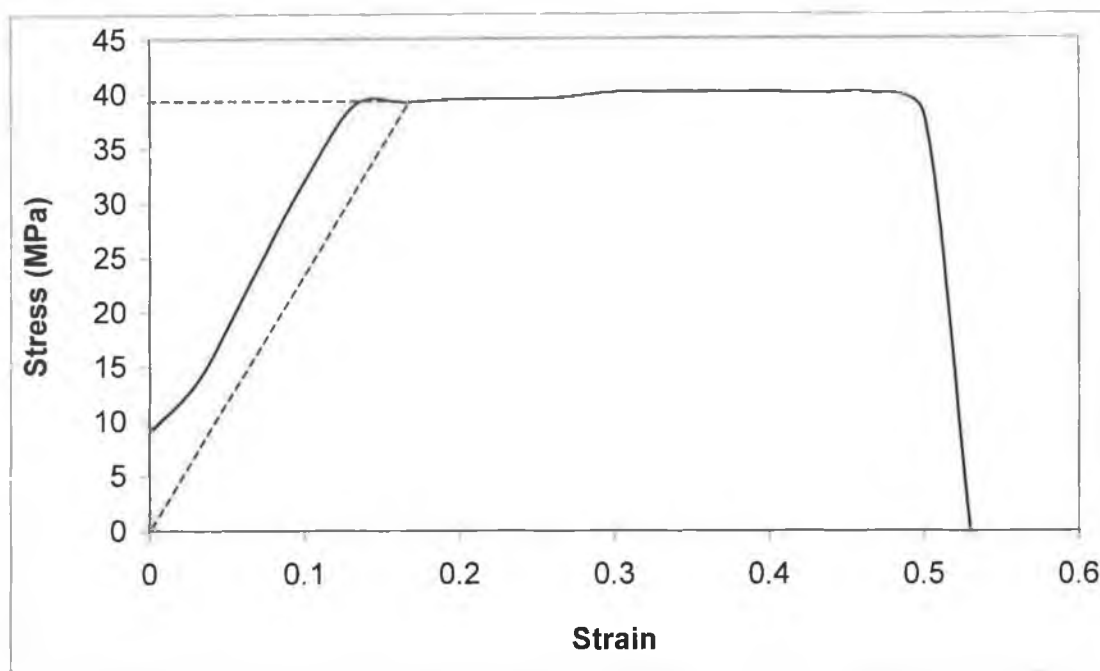
Figure 4.51: Tensile stress-strain curve for the sprayed aluminium/tool-steel graded material.

According to Clyne's results, the stress change from the coating interface to the substrate interface was −119 MPa for 0.50 mm thick sample sprayed with a oxygen to propylene ratio of 4.50, a flow rate of the compressed air of 270 SLPM and a spray distance of 225 mm. Whereas, two times the yield stress value was only 78 (39X2) MPa. As a result, plastic deformation or cracking should have occurred in the coated sample.

During coating deposition, the aluminium substrate was preheated to 50 ^{0}C. However the substrate was heated up to around 500 ^{0}C by gun flame just before deposition. As a result the aluminium substrate was softened a bit. During deposition the coating material impact the substrate and tried to contract, but constrained by each other, and by the substrate. However due to the softening of the aluminium substrate, the degree of contraction was low, and flow occurred at the interface. As a result the coating did not

transfer total strain mismatch into the interface stress, the stress change at the interface might have decreased below the two times the yield stress (78 MPa) and no plastic deformation or crack was observed in the coated sample. The same phenomenon was observed by Taylor et al. [254] in their research. They deposited CoNiCrAlY/YSZ thermal barrier coating using the plasma spray process and measured tensile properties at different temperatures. At around 700 ^{0}C, the yield stress value started to decrease and at around 1000 ^{0}C the yield stress was almost zero. Above 700 ^{0}C, the material started to flow and it did not transfer an apparent strain mismatch into the interface stress.

Effect of Spray Parameters

The deposition matrix used for the Young's modulus measurement was also used for the optimisation of spray parameters, as well as to establish the effects of spray parameters on the deposited thickness and stress distribution through the coating and substrate. Again, some of the samples were not considered due to burnt out and poor quality of deposition. The results of the stress distribution through different types of graded coatings deposited using different spray parameters are shown in table 4.7. The samples were divided into 9 different groups depending on their oxygen to propylene ratio and flow rate of the compressed air as shown in table 4.8. The results of the stress distribution for the relevant samples in each of the different groups are described below.

Group one consisted of samples 1, 2 and 3. They were deposited using a oxygen to propylene ratio of 4.50, a flow rate of the compressed air of 270 SLPM, but with a spray distance of 225, 250 and 270 mm respectively. The results of the stress distribution are shown in figure 4.52. The results showed a negative stress change for the top to the bottom of the coating. Again the stress changed from a compressive to a tensile value from the coating interface to the substrate interface and then from tensile to compressive from the top to the bottom of the substrate for all samples as shown in figure 4.52.
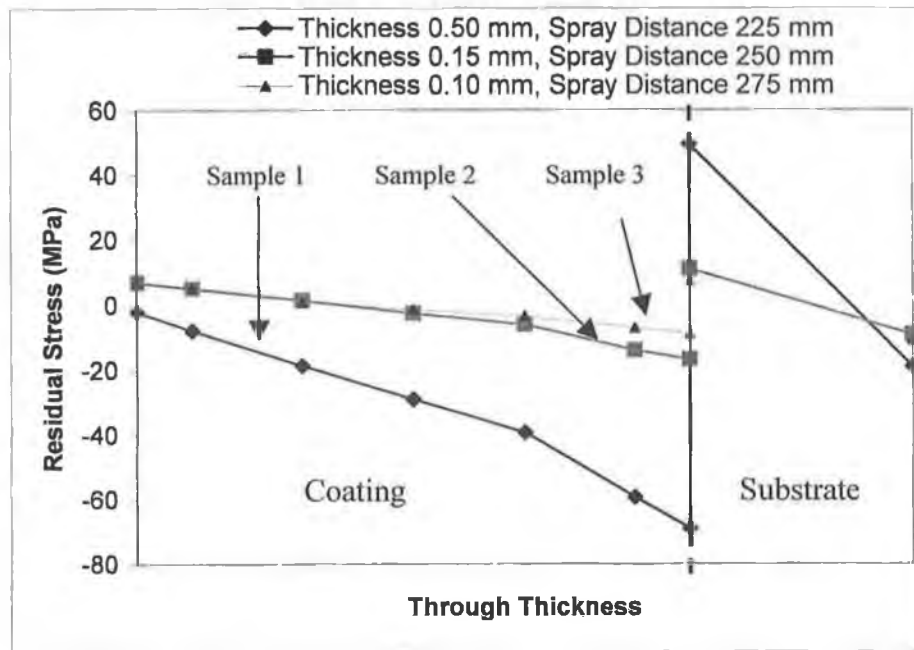
Figure 4.52: Stress distribution through the substrate and coating for samples 1, 2 and 3 in group 1.

All the other groups had same stress distribution profile. Results are tabulated in table 4.7 and are plotted in a series of figures in Appendix E. The experimental matrix of what parameters were kept constant (set) and those varied are shown in table 4.8.

Table 4.7: Stress distribution through different types of graded coatings deposited using different spray parameters.

Sample No	Stress at the Middle of Layer (MPa)					Stress at Substrate (MPa)		σ_s (MPa)	Ratio of σ_s to t_c (MPa/mm)	$\Delta\sigma_{1,5}$ (MPa)	Ratio of $\Delta\sigma_{1,5}$ to t_c (MPa/mm)
	5	4	3	2	1	Top	Bottom				
1	-7	-18	-29	-39	-59	49	-19	-2	-4	-52	-104
2	5	1	-2	-6	-14	11	-9	7	47	-19	-127
3	5	0	-1	-3	-7	7	-11	7	70	-12	-126
4	-4	-15	-23	-32	-57	46	-21	0	0	-53	-118
5	5	1	-2	-6	-14	11	-9	8	53	-19	-127
6**											
7	-4	-15	-24	-32	-56	44	-22	0	0	-52	-116
8	4	0	-2	-6	-15	11	-10	7	47	-19	-127
9**											
10	-2	-11	-19	-27	-54	46	-21	2	5	-52	-130
11	6	0	-3	-3	-10	7	-3	9	90	-16	-160
12	7	6	4	4	1	3	-3	8	160	-6	-120
13	-2	-11	-19	-27	-50	43	-20	3	8	-48	-120
14	5	2	0	-1	-6	8	-7	6	60	-11	-110
15**											
16	-1	-10	-16	-24	-56	35	-20	3	9	-55	-158
17	4	2	0	0	-14	8	-6	5	50	-18	-180
18**											
19*											
20	7	6	5	4	1	3	-4	9	180	-6	-120
21	7	6	5	4	2	3	-3	8	160	-5	-100
22*											
23	7	6	5	4	1	3	-3	8	160	-6	-120
24**											
25*											
26	7	4	4	6	1	3	-3	8	160	-6	-120
27**											

σ_s = Surface stress, $\Delta\sigma_{1,5}$ = Stress change between middle of layers 1 and 5, t_c = Coating thickness
* Substrate burnt out   ** Poor deposit

Table 4.8: Dividation of 27 samples into 9 different groups depending on their oxygen to propylene ratio and flow rate of the compressed air.

Group No	Sample No	Ratio of Oxy/Fuel	Flow Rate of Compressed Air (SLPM)	Spray Distance (mm)
1	1	Set at 4.50	Set at 270	225
	2			250
	3			275
2	4	Set at 4.50	Changed to 305	225
	5			250
	6			275
3	7	Set at 4.50	Changed to 340	225
	8			250
	9			275
4	10	Set at 4.00	Set at 270	225
	11			250
	12			275
5	13	Set at 4.00	Changed to 305	225
	14			250
	15			275
6	16	Set at 4.00	Changed to 340	225
	17			250
	18			275
7	19	Set at 3.75	Set at 270	225
	20			250
	21			275
8	22	Set at 3.75	Changed to 305	225
	23			250
	24			275
9	25	Set at 3.75	Changed to 340	225
	26			250
	27			275

Now the results are reploted as ratio of coating surface stress to thickness (σ_s/t_c) versus spray distance in figures 4.53 through to 4.55 as a means to compare the effects of spray distance, oxygen/fuel ratio and flow rate of the compressed air. The results could have been plotted as surface stress versus spray distance only, however the thickness varied per sample. As the deposition thickness has a huge effect on residual stress build-up in thermally sprayed coatings, measuring σ_s/t_c gives a more accurate method of comparing results. Therefore the results are presented as surface stress to thickness ratio against spray distance rather than stress against distance.

Figure 4.53 shows a non-linear relationship between σ_s/t_c and spray distance for a oxygen to propylene ratio of 4.50. Results show that σ_s/t_c increased with an increase in spray distance. Normally residual stress decreases with an increase in spray distance,

due to decrease of deposition temperature with a decrease in distance [22]. However the deposition thickness decreases with an increase in spray distance. As a result, the σ_s/t_c ratio increased with an increase in spray distance. In the case of spray distance of 225 mm, both residual stress and deposition thickness was higher, than that found at spray distances of 250 mm and 275 mm. However the spray distance of 225 mm gave a lower σ_s/t_c ratio value compared to both 250 mm and 275 mm spray distance. Hence the spray distance of 225 mm gave a better compromise between low residual stress and high deposition thickness compared to 250 mm and 275 mm spray distances.
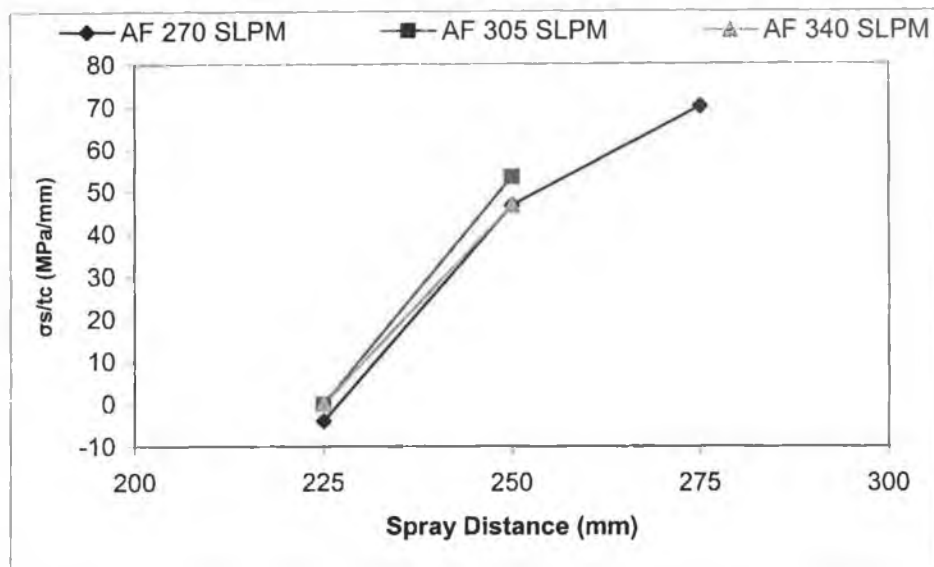
Figure 4.53: Ratio of coating surface stress to thickness (σ_s/t_c) Versus spray distance for a oxygen to fuel ratio of 4.50.

Similar plot for σ_s/t_c versus spray distance for oxygen to propylene ratio of 4.00 is shown in figure 4.54. Again σ_s/t_c increased with an increase in spray distance. However the stress is much higher for higher distances when compared to figure 4.53. Figure 4.54 also shows that the ratio of surface stress to thickness decreased with an increase in the flow rate of compressed air for a spray distance of 250 mm. An increase in flow rate of compressed air decreases the combustion chamber temperature, which in turn decreases the deposition temperature and residual stress. Now comparing figure 4.53 and 4.54, the surface stress to thickness ratio was lower for a spray distance of 225 mm, (flow rate of compressed air of 340 SLPM and oxygen to propylene ratio 4.50) compared to the surface stress to thickness ratio found for same spray distance and flow rate of compressed air but with oxygen to propylene ratio of 4.00. The decrease in oxygen/fuel

ratio from 4.50 to 4.00, increases the combustion temperature (figure 4.46) [39], this in turn increased the residual stress build-up in the coating.
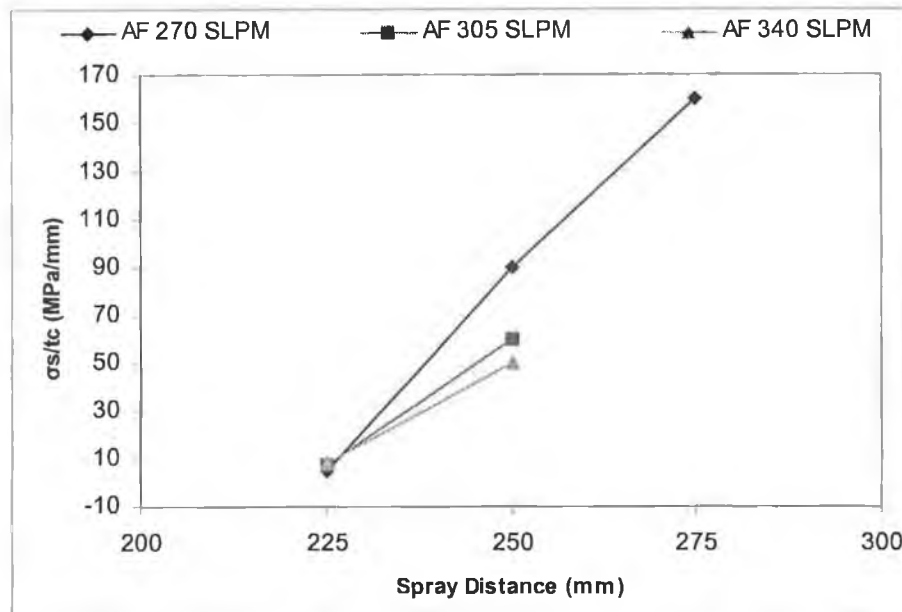
Figure 4.54: Ratio of coating surface stress to thickness (σ_s/t_c) Versus spray distance for a oxygen to fuel ratio of 4.00.

Figure 4.55 shows the plot for σ_s/t_c versus spray distance for oxygen to propylene ratio of 3.75. It shows that σ_s/t_c decreased with an increase in spray distance. However the zoomed out version (figure 4.55 (b), which is set to a similar scale as figure 4.54) showed the difference of σ_s/t_c between the spray distances is not as big a factor as found in figures 4.53 and 4.54. The lower difference might be due to the high chamber temperature for the oxygen to propylene ratio of 3.75.
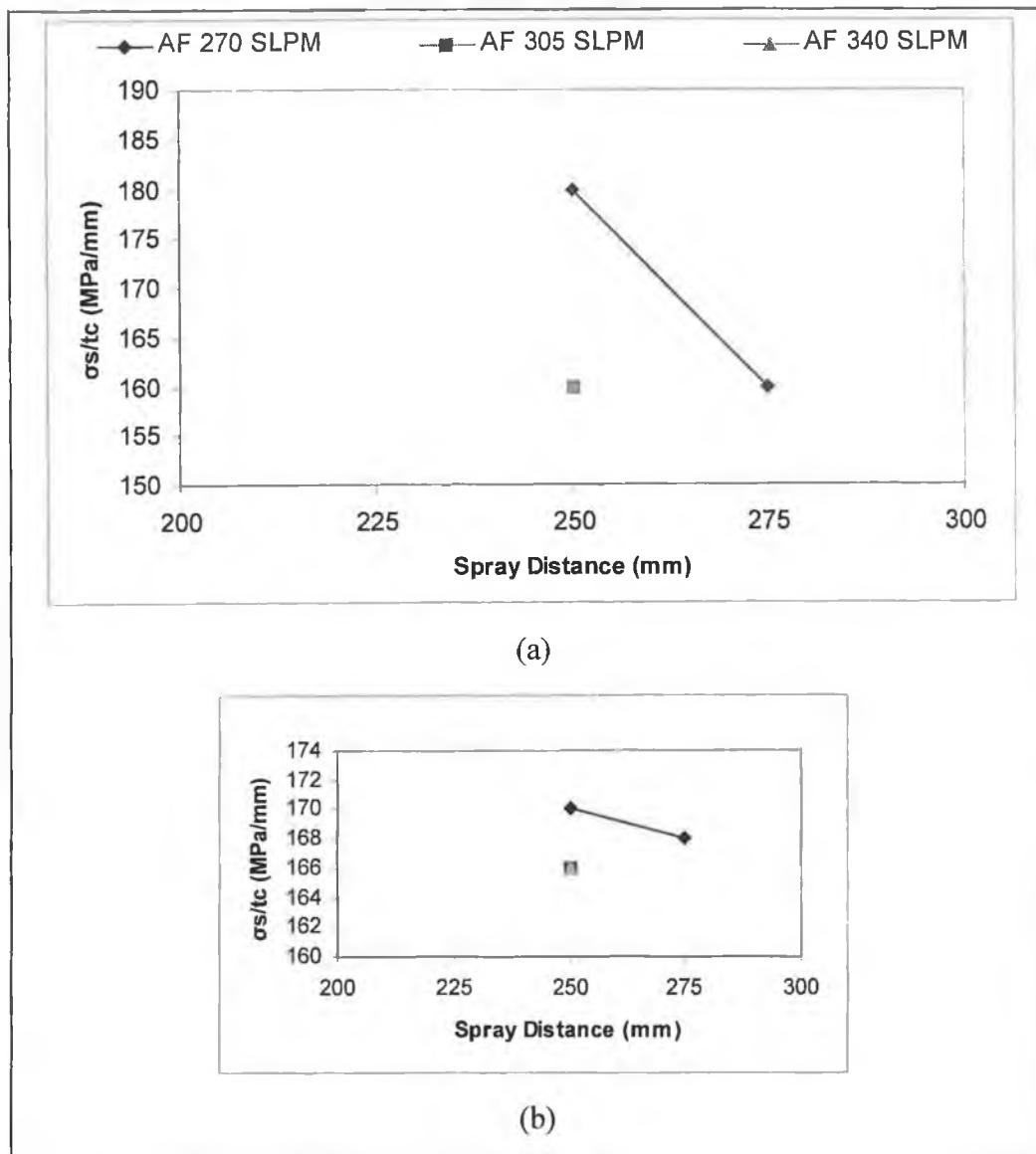
Figure 4.55: (a) Ratio of coating surface stress to thickness (σ_s/t_c) Vs spray distance for a oxygen to fuel ratio of 3.75, (b) zoomed out picture.

In the HVOF thermal spraying process, coating material is melted or semi-melted in the combustion zone depending upon the relative temperature difference between the melting temperature of the material and flame temperature. The flame temperature varies with the ratio of oxygen to fuel and flow rate of compressed air used in the system. In the current work the ratio of oxygen to propylene were varied at 4.50, 4.00 and 3.75. The flame temperature at combustion chamber and chamber exhaust for different oxygen/propylene ratios' can be obtained from figure 4.46 [39]. An explanation for the thermal history of a particle travelling through the combustion chamber has been explained by some authors [34,44]. The physical state of the aluminium and tool-steel coating material as they pass in and out of the combustion

184

chamber is shown in figure 4.56 (with varying oxygen to propylene ratio, but constant air flow) and described below.
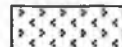
Figure 4.56 (a) shows the case for oxy/fuel ratio of 4.50 (figure 4.53 results), the flame temperature in the chamber and exhaust is 3000 ^{0}C and 2540 ^{0}C respectively (taken from figure 4.46). When the aluminium particle travels inside the combustion zone, the outer surface of the particle evaporates, because the chamber temperature is higher than the boiling point of aluminium. The particle contains a solid with a liquid layer between the solid and vapour at this point in the chamber. The particle exits the chamber into the exhaust and is then cooled (particle raised to 3000 ^{0}C but the exhaust at 2540 ^{0}C) by the flame to produce a solid with liquid inside, this leads to a particle smaller than the initial one when the particle impacts the substrate [34,44]. In case of the tool-steel powder, its boiling temperature is higher than the chamber temperature. Hence no evaporation occurs. The tool-steel contains a liquid layer with a solid core while inside the combustion chamber. On exiting the chamber it has a liquid layer, sandwiched between two solid layers. On impact the tool-steel powder material is a solid having a diameter larger than that of the aluminium.

In figure 4.56 (b), the flame temperature in the chamber and exhaust is increased to 3050 ^{0}C and 2580 ^{0}C respectively for oxy/fuel ratio of 4.00 (figure 4.54 results). Due to increase in combustion flame temperature, higher portion of the aluminium powder is evaporated. So when it exits the chamber it has lower solid and higher liquid content than, that of the previous ratio, which results in a smaller aluminium particle than before. The outside portion of the tool-steel is evaporated slightly in the combustion chamber for the ratio of 4.00 with a liquid a solid layer next to it. So when it leaves the chamber it has solid surface with a liquid core. The resulting particle on impact is solid, with a diameter bigger than the aluminium one for this ratio, but smaller than the tool-steel particle diameter for the previous ratio of 4.50.

Finally for the oxy/fuel ratio of 3.75 (figure 4.56 (c)), the flame temperature in the chamber and exhaust is 3070 ^{0}C and 2600 ^{0}C respectively. This is the situation for the results presented in figure 4.50. Almost the whole of the aluminium particle is evaporated in combustion chamber, which results in a small solid aluminium particle on impact. In the case of the tool-steel particle, the rate of evaporation is higher than the

previous ratios'. This results in a tool-steel particle having the lowest diameter produced between the three different oxy/fuel ratios'.

(a)	O/F	AF	T (Chamber)	T (Exhaust)	Impact
	4.50	270	3000 ^{0}C	2540 ^{0}C	
Al (BP) = 2519 ^{0}C [255]					
TS (BP) = 3028 ^{0}C [256]					

(b)	O/F	AF	T (Chamber)	T (Exhaust)	Impact
	4.00	270	3050 ^{0}C	2580 ^{0}C	
Al (BP) = 2519 ^{0}C					
TS (BP) = 3028 ^{0}C					

(c)	O/F	AF	T (Chamber)	T (Exhaust)	Impact
	3.75	270	3070 ^{0}C	2600 ^{0}C	
Al (BP) = 2519 ^{0}C					
TS (BP) = 3028 ^{0}C					

Solid   Liquid   Vapour

BP = Boiling point, AF = Air flow, O/F = Oxygen/Fuel, T = Temperature

Figure 4.56: Physical state of the aluminium and tool-steel coating material as they pass in and out of the combustion chamber.

While processing functionally graded coatings, absence of the aluminium powder is not desirable, hence the parameters given in figure 4.55 are not worthy of using.

Figure 4.54 shows high stress results, however when the air flow rate was increased from 270 SLPM to 340 SLPM, it reduced the chamber temperature. This gave stress results similar to that found in figure 4.53 for an air flow of 270 SLPM. This suggests that increasing the air flow for figure 4.54 for oxygen to propylene ratio of 4.00, reduces the temperature and brings the temperature to that similar for oxy/propylene ratio of 4.50.

An oxygen to propylene ratio of 4.50 yields the lowest stress results of a spray distance of 225 mm. Any air flow value may be used as they all produce low stress values. The author feels that an increase in air flow does not effect the results in figure 4.53 as evaporation of the aluminium particle reduces with lower chamber temperature (as the chamber temperature tends towards the boiling point of the aluminium particle). Hence little of the aluminium is lost at this condition (thus maximising the quantity of aluminium powder on impact). However air flow of 270 SLPM along with oxygen to propylene ratio of 4.50 and spray distance of 225 mm was chosen here considering the economy of the system. Thus the set of spray parameters having a spray distance of 225 mm, an oxygen to fuel ratio of 4.50 and a flow rate of compressed air of 270 SLPM provided the best compromise between low surface residual stress and high deposition thickness. However the stress change through the deposit is also a big factor for thermal spray coatings. According to table 4.7, samples 1 and 21 had the lowest ratio of stress change between layers 1 and 5 to coating thickness (-104 MPa/mm and –100 MPa/mm respectively). Deposition thickness of samples 1 and 21 were 0.50 and 0.05 mm respectively. Due to very low deposition thickness of sample 21, sample 1 was considered to give best compromise between low stress change through the deposit and high deposition thickness. Again, sample 1 was associated with the same set of spray parameters that gave the best compromise between low surface stress and high deposition thickness.

The conclusion here is that the parameters required to deposit aluminium/tool-steel functionally graded coating is dependent on the lower boiling point powder material (in this case aluminium) of the two powders been investigated, when they are compared with the compromised parameters found in this research. When the parameters found in

this research for spraying aluminium/tool-steel functionally graded coatings are compared to the METCO [67,147] parameters for spraying of individual aluminium and tool-steel coating powders, they resemble the aluminium parameters as shown in table 4.9. This supports the statement that the parameters depend on the lowest boiling point powder material.

Table 4.9: Spray parameters recommended for the aluminium and tool-steel along with compromised parameters found in this research [67,147].

	Tool-Steel (METCO)	Aluminium (METCO)	Compromised (Current research)
Flow Rate of Oxygen (SLPM)	278.1	196	198
Flow Rate of Propylene (SLPM)	74.9	44	44
Oxygen/Fuel Ratio	3.71	4.45	4.50
Flow Rate of Air (SLPM)	338.6	269	270
Spray Distance (mm)	220-275	200-300	225

4.5 VARIATION OF RESIDUAL STRESS

Having established the above spray parameters, different types of graded coatings were then deposited to establish the variation of stress distribution with deposit thickness and number of graded layers. Results are described in the following sections.

4.5.1 Variation of Residual Stress with Deposit Thickness

The coating deposition matrix used to investigate the effect of the deposit thickness and number of graded layers on residual stress is shown in table 4.10. Figure 4.57 shows the distribution of residual stress through the coating and substrate for different deposit thickness. The residual stress found at the top of the coatings (extrapolated values) was –2, 5, 4 and 6 MPa for samples A1, A2, A3 and A4 respectively. Thus there is a transition of surface stress from compressive to tensile with decrease in deposition thickness. A similar result was found by Stokes [86] in his research. Stokes [86] reported that at a certain thickness the stress at the top of the deposit changed from a tensile state to a compressive state (figure 4.58 (c)). In the current research, graded coatings of thickness of 0.50 mm had compressive stress at the surface. They followed pattern (a) stress distribution shown in figure 4.58, where the residual stress was compressive at the top of the deposit. However graded coatings of thickness of 0.40 mm or less followed the 4.58 (b) pattern, where the residual stress was tensile at the top of the substrate. In both cases the shape of the final coated sample was convex as shown in figure 4.59. Again figure 4.57 is showing a negative stress change between layers 1 and 5 for each deposit, the size of which reduced as the deposit thickness decreased. The stress change between layers 1 and 5 (difference of stress between those layers) for sample A1 was –52 MPa, which was greatly higher than that of –9 MPa for sample A4. The decrease of residual stress with a decrease in the coating thickness was found by some other researchers including [257-259]. Looking at the equation,

$$\sigma_{cj} = \frac{F_j}{bw} - E_c'\left(k_j - k_{j-1}\right)\left((j-0.5)w - \delta_j\right) \ +$$

$$\sum_{i=j+1}^{n}\left(\frac{-E_c'F_i}{b\left(h_sE_s' + (i-1)wE_c'\right)} - E_c'\left(k_i - k_{i-1}\right)\left((j-0.5)w - \delta_i\right)\right) +$$

$$\frac{F_{CTE}}{bh_c} - E_c'\left(k_c - k_n\right)\left((j-0.5)w - \delta_n\right)$$

used to calculate the stress value at the middle of a particular layer, the difference of δ (distance from the interface to neutral axis) between first layer and final layer increases with an increase in coating thickness. This in turns increases the stress change from the first layer to final layer with an increase in coating thickness. The results showed the stress at the interface changed from a compressive to a tensile value from the deposit interface to the substrate interface (due to what is known as misfit strain [246]), while the stress changed from tensile to compressive from the top to the bottom of the substrate in each case.

Table 4.10: Coating deposition matrix used to figure out the effect of deposit thickness and number of graded layers on residual stress.

Sample No	Flow Rate Ratio O_2/C_3H_6	Flow Rate of Compressed Air (SLPM)	Spray Distance (mm)	No of Layers	Coating Thickness (mm)
A1				5	0.50
A2				5	0.30
A3				5	0.20
A4	4.50	270	225	5	0.10
A5				3	0.50
A6				2	0.50
A7				1 (Tool-Steel)	0.50
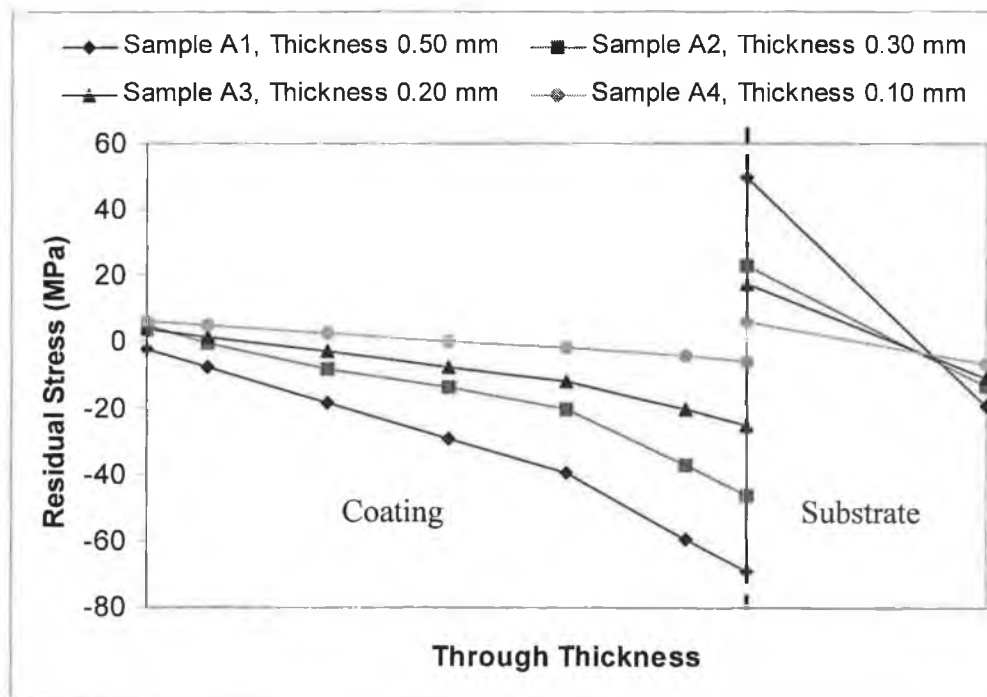
Figure 4.57: Distribution of residual stress through the coating and substrate for different deposit thickness.
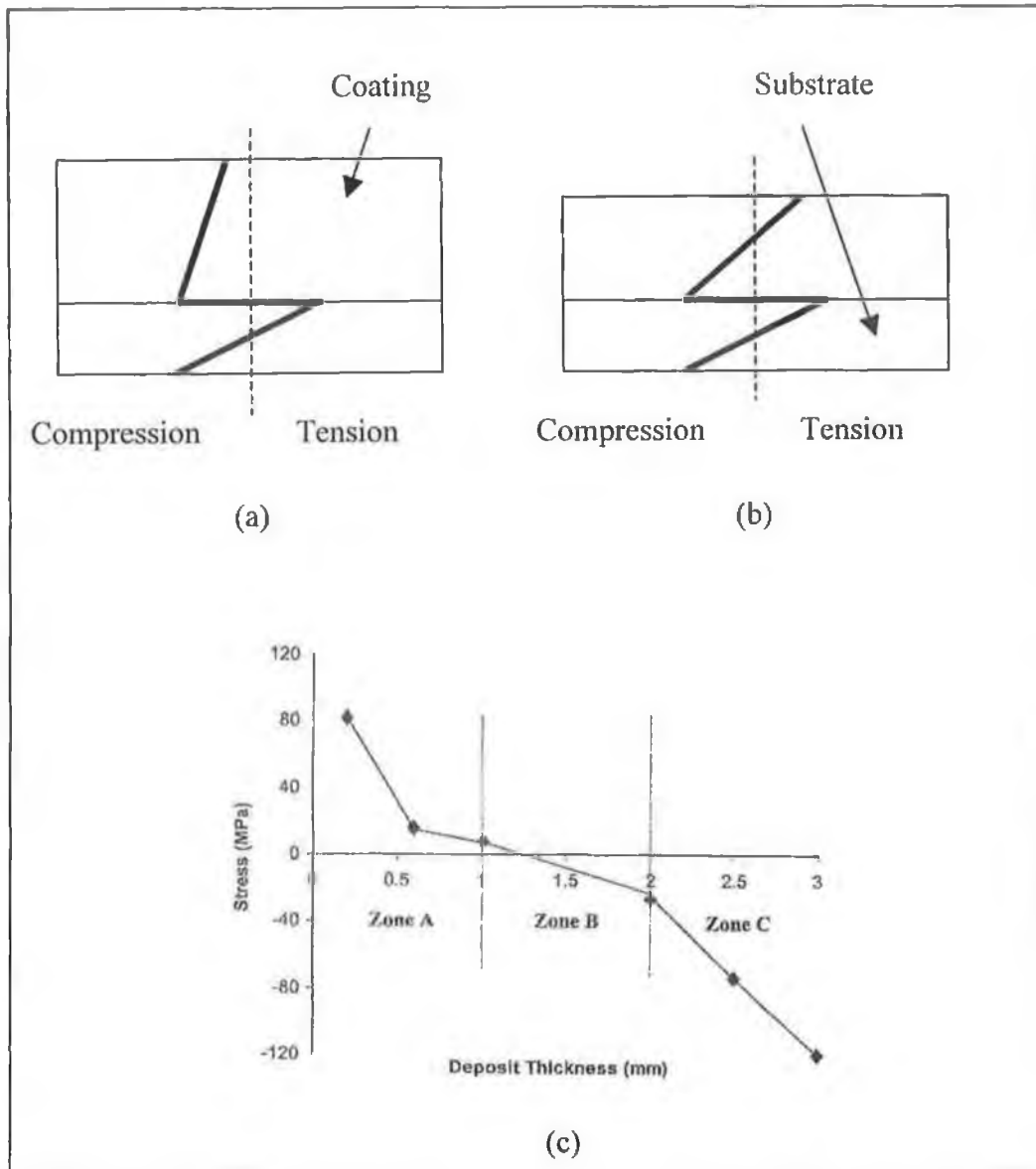
Figure 4.58: Final stress distribution through (a) thick (b) thin aluminium/tool-steel functionally graded coating-aluminium substrate system, (c) surface stress as a function of thickness found by Stokes [86].
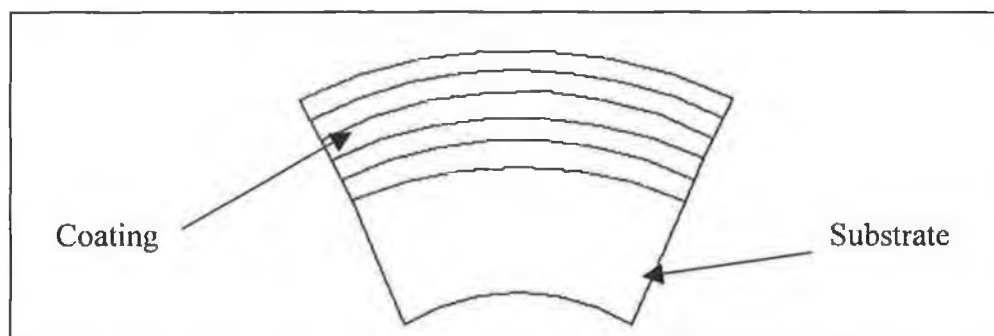
Figure 4.59: Final shape of aluminium/tool-steel coated aluminium substrate after stress development.

191

4.5.2 Variation of Residual Stress with Number of Layers

Figure 4.60 shows the distribution of residual stress through the coating and substrate for different number of layers. The residual stress decreased with an increase in number of layers, as found by Khor et al. for graded coatings [91,103]. The residual stress at the top of the coatings (extrapolated values) was –2, -3, -7 and –19 MPa for samples A1, A5, A6 and A7 respectively. Sample A7 was not a functionally graded coating, rather a traditionally coated substrate, in this case an aluminium substrate coated with tool-steel to a height of 0.50 mm. Tool-steel coating was deposited by several passes of the gun. The reason for producing a traditional deposit is to compare the results of the "normal" method to the functionally graded material types. The results showed a negative stress change from top to the bottom of the coating, the size of which reduced as the number of graded layers increased as shown in figure 4.61. The single layer's (A7, traditionally coated substrate) stress distribution is much higher than that of the FGM layers (A1, A5 and A6). It can be observed that an increase in number of graded layers causes a decrease in residual stress build-up in the deposits. The results indicate that increasing the number of layers to 2, 3, 5 or more has more on an effect on the stress change across the deposit rather than the stress at the top of the deposit, which can be attributed to the mismatch of properties specially the Young's modulus and co-efficient of thermal expansion (CTE) between the layers decreased [24,109,113,155-157], thus increasing the number of layer is a useful way of reducing the residual stress in graded coatings. The stress at the interface changed from a compressive to a tensile value from the deposit interface to the substrate interface, while the stress changed from tensile to compressive from the top to the bottom of the substrate in each case.
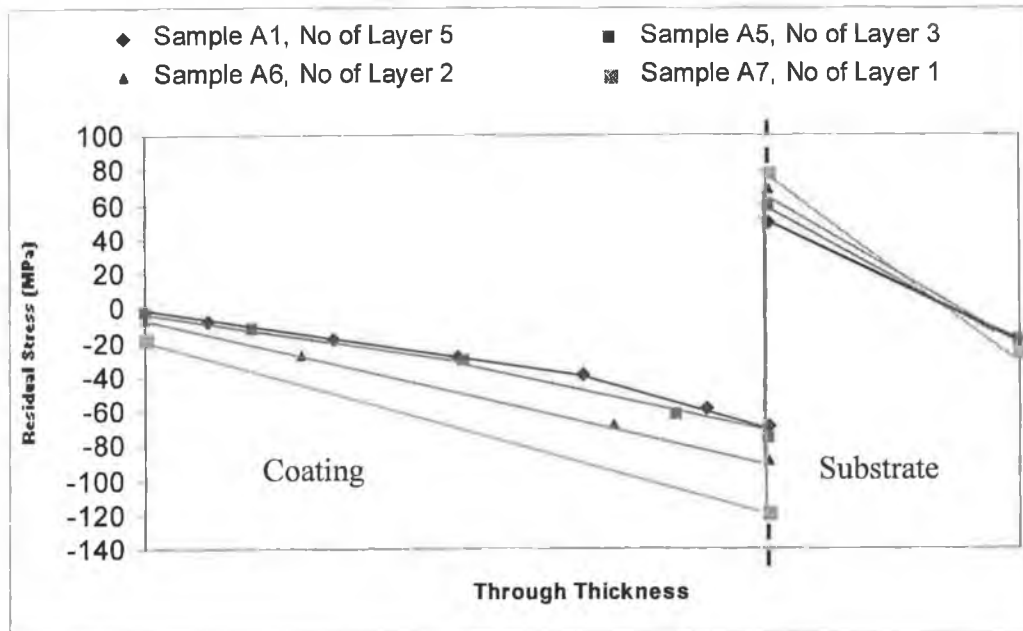
Figure 4.60: Distribution of residual stress through the coating and substrate for different number of layers.
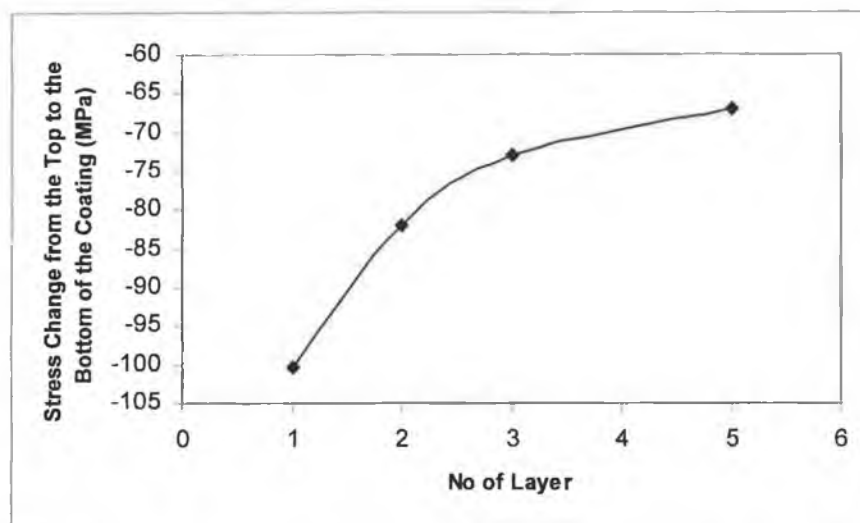
Figure 4.61: Stress change against number of layer.

4.5.3 Effect on Hardness

Coatings are generally produced to improve the wear resistance of the base material, hence hardness is an important quality. Therefore it is important to this stage of the research to quantify if producing functionally graded deposits as compared to the traditional method has any effect on hardness and if so to what effect. The results of previous two sections showed that, residual stress build-up in the graded coatings is dependent upon deposition thickness and number of layers. In order to investigate the

193

effects of thickness and number of layers, the hardness of the aluminium/tool-steel functionally graded deposits was measured by the Vickers test method using the Leitz Miniload hardness tester. A 500 gm load was applied to the surface of different samples and the indentation was observed using a microscope at a magnitude of 50X. The samples were sectioned and prepared before measurement. The hardness was measured for graded coatings having different deposit thickness and number of layers (including 1 layer). Variation of hardness with deposit thickness and number of layers are described below.

Variation of hardness with deposit thickness (all having 5 layers) is shown in figure 4.62. For each deposit thickness five readings were taken, with the minimum, average and maximum values are shown in the figure. The line is drawn using the average hardness values. The maximum difference found between the minimum or maximum to average hardness values for a particular deposit thickness was 4.7 %. Thermally sprayed coatings produced in air are a heterogeneous mixture of sprayed materials, oxide inclusion and porosity [11]. Therefore the microhardness values are not constant throughout the coating, which resulted in scattering in results. Figure 4.60 shows that the hardness increased with an increase in the deposit thickness, as found by some other researchers [260-263]. The reason may be the increase of the residual stress with an increase in the deposition thickness, which in turn increased the hardness [264-268]. The average hardness value of a 0.50 mm deposit was 419 HV, which was 35 % higher than that of 310 HV found for a deposit of 0.10 mm thickness.
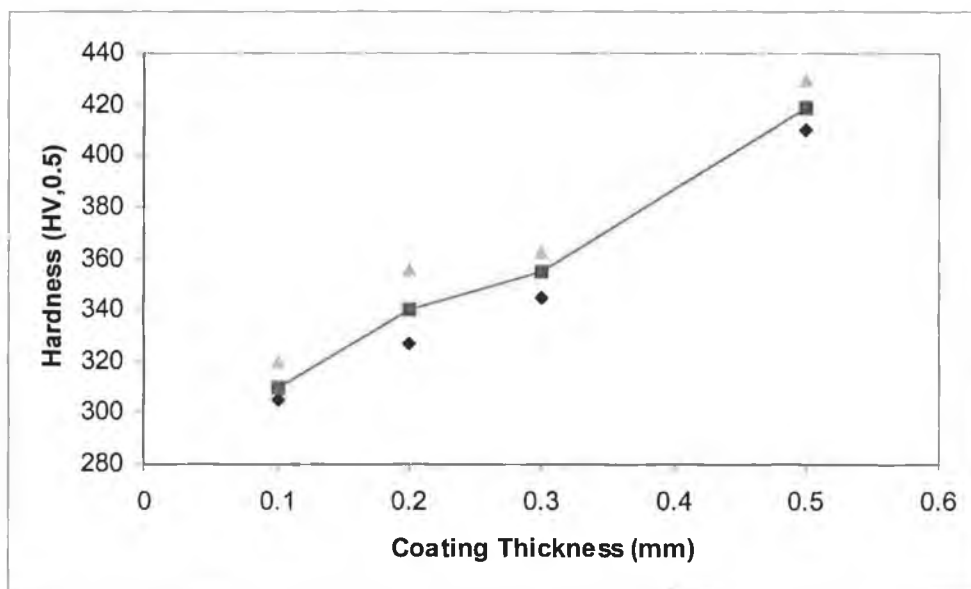
Figure 4.62: Variation of hardness with deposit thickness.

Figure 4.63 shows the variation of hardness with number of layers. Again the figure shows only three readings (minimum, maximum, and average) out of the five taken. The line is drawn using the average hardness values. The maximum difference found between the minimum or maximum to average hardness values for a particular no of layer was 4.72 %, which again might have caused due to the inohomogenity of the thermally sprayed coating. The hardness increased with a decrease in number of layers, possibly due to the increase of residual stress with a decrease in number of layers. The average hardness value of a single layer deposit was 488 HV, which was 17 % higher than that of 419 HV for a five layer deposit of same thickness. Again hardness values increased linearly from a 5 layer graded coating to a 2 layer one. However there was higher increase from the 2 layer coating to the single layer coating. The single layer coating was not a functionally graded coating, rather an aluminium substrate coated with the tool-steel of a height of 0.50 mm. As a result it gave a much higher hardness values compared to the graded coatings.
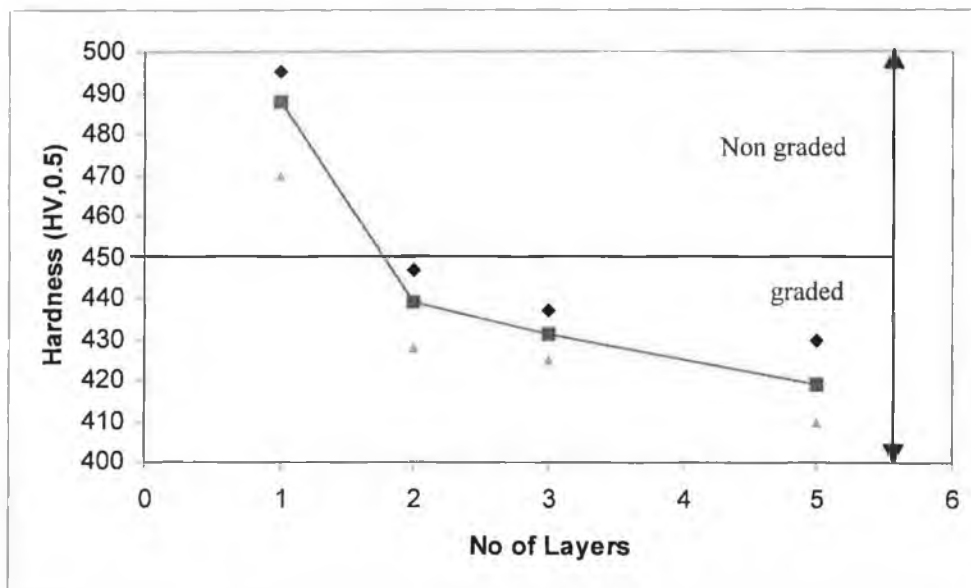
Figure 4.63: Variation of hardness with number of layers.

Results of previous section showed that the residual stress decreases with an increase in number of layers. However the hardness decreases with an increase in number of layers. Therefore an engineer must compromise between the hardness and stress values when designing a functionally graded coating-substrate system.

4.6 COMPARISON BETWEEN STRESS MEASUREMENTS

Some of the samples used in the Clyne's analytical method were also used to measure residual stress using the Hole drilling method to compare between the two techniques of stress measurement. In the Hole drilling method, stress in the sample is relieved using a semi-destructive method, where a hole is drilled through the sample. The relief is nearly complete within the close vicinity of the hole, when the depth of the drilled hole approaches 0.4D (the mean diameter of the strain gage circle) or in the case of a material whose total thickness is less than 1.2D, a hole passing through the entire thickness. A photograph of Hole drill coated sample is shown in figure 4.64.
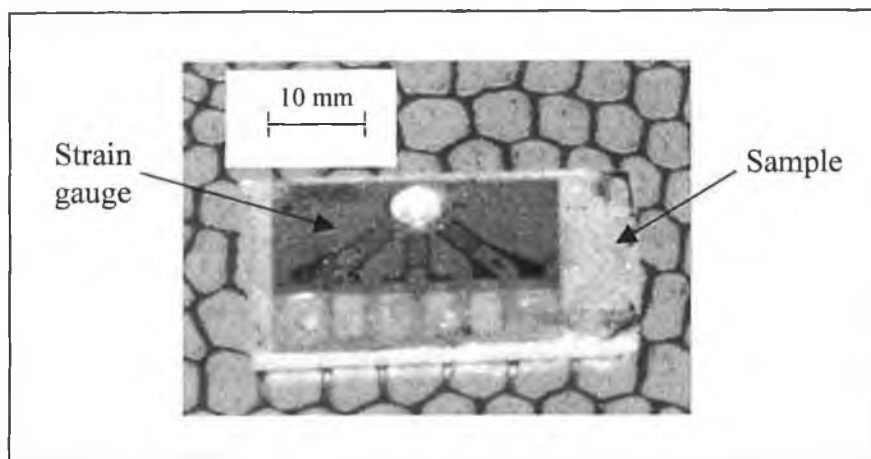
Figure 4.64: Photograph of Hole drilled coated sample.

Table 4.11 shows the relationship between the residual stress measured using the Clyne's method and the results found using the Hole drilling method. While there were differences between the two measurement methods, correlation between them was reasonable. Results found using the Clyne's method show that the surface stress of graded coatings of thickness of less than 0.40 mm or less was tensile, while the stress was compressive for the coatings having thickness of more than 0.40 mm. The results of the Hole drilling method also show the same trend. The range of difference of the surface stress found between the two methods was 10 to 12 MPa, which was closer to the range (16 to 22 MPa) found by Stokes [22] for various WC-Co coatings of thickness of 0.20 to 0.60 mm.

Table 4.11: Comparison of Clyne's and Hole drilling residual stress measurement techniques.

Sample No	Deposition Thickness (mm)	No of Layers	Clyne's Method Surface Stress (MPa)	Hole Drilling Method Surface Stress (MPa)
A1	0.50	5	-2	-14
A2	0.30	5	5	16
A3	0.20	5	4	14

CHAPTER 5

CONCLUSIONS & RECOMMENDATIONS

5.1 CONCLUSION

In this study, innovative modification to a HVOF thermal spray process was investigated to produce functionally graded thick coatings. The modified parts were then used to deposit aluminium/tool-steel graded coatings on aluminium substrates. The conclusions resulting from the investigation are summarised below:

• Co-injection method of two powders was chosen to deposit functionally graded coatings. In order to co-inject two powders, significant modification to a commercial powder feed hopper was required. Various concepts were examined for potential feasibility. Advantages and disadvantages of each concept were examined and a rating chart was obtained. Finally the concept with the highest rating was chosen to produce functionally graded coatings. The chosen concept consisted of addition of some parts inside the existing cylindrical powder feed hopper. There were two separate holders for two different powders inside the modified feed system.

• A process model was developed using the FLOTRAN CFD ANSYS Finite Element Analysis to simulate the nitrogen gas-powder flow through the chosen design. Simulation results predicted that the design was able to carry both aluminium and tool-steel powder from the powder container to the mixing zone, mix them and then force the powder mixture through the pick-up shaft hole into the nitrogen gas line.

• The designed device was manufactured, commissioned with the existing powder feed system and calibrated. Calibration tests included powder flow bench tests and in-situ flow tests. Powder flow bench tests were carried out in order to relate the effect of turning the needle shaped bolts had on powder flow. The in-situ flow tests showed that the modified parts was able to control the ratio of aluminium and tool-steel powders at required rate to produce different layers of graded coatings. Results also showed that the designed parts was successful in carrying, mixing and forcing the powder mixture experimentally through the pick-up shaft hole into the nitrogen gas flow inside the pick-up shaft.

• The chemical composition of different layers of a five layer aluminium/tool-steel functionally graded coating was determined using the energy dispersive X-ray spectroscopy (EDS) in order to check whether the ratios' of the two powders obtained

in the calibration tests was maintained in the resulting coatings. Results showed that the chemical composition of different layers was very close to that anticipated.

- The elastic properties of different types of graded coatings having deposited with different spray parameters were measured using the Cantilever test. The Young's modulus and Poisson's ratio were found to be in the range of 122 to 153 GPa and 0.30 to 0.33 respectively. Variation in spray parameters resulted in various deposition temperature, which in turn produced coatings having different Young's modulus and Poisson's ratio values.

- Thermocouples were used to measure the temperature difference between the substrate and the coating by fixing one thermocouple at the back of substrate and another at the front of the deposited coating. The temperature difference found was between 1 to $1.3\,^{0}C$ for graded coatings over a thickness range of 0.10 to 0.50 mm.

- 3^3 Factorial design of experiments was employed to optimise the spray parameters and establish the effects of spray parameters on residual stress build-up in the aluminium/tool-steel functionally graded coatings. The flow rate ratio of oxygen to propylene, flow rate of the compressed air and spray distance were the three spray parameters varied. Clyne's analytical method was used to measure residual stress of different types of graded coatings. Among the three spray parameters, the spray distance had the greatest effect on the ratio of surface stress to deposit thickness compared to the oxygen to propylene ratio and flow rate of the compressed air.

- The best performing set of spray parameters that produced the best deposit was based on having the lowest ratio of surface stress to coating thickness. Results showed that the optimised set of spray parameters, that is an oxygen to propylene ratio of 4.50, a spray distance of 225 mm and a flow rate of the compressed air of 270 Standard Litre per Minute (SLPM), resembles the parameters recommended by METCO for the aluminium alone. Thus suggesting that the parameters required to deposit functionally graded coatings depends upon the lower boiling point powder coating material of the two powders being investigated.

- Variation of residual stress with deposit thickness and number of graded layers was investigated. Surface residual stress changed from tensile to compressive with an

increase in deposition thickness. The residual stress change from the top layer to the bottom layer of coating increased from –9 MPa to –52 MPa with an increase in coating thickness from 0.10 mm to 0.50 mm, while decrease in number of layers from 5 to 1 increased the stress change from –52 MPa to –100 MPa.

● Vickers hardness values of graded coatings was measured with varying deposit thickness and number of graded layers in order to investigate the effect of gradation on hardness. Average hardness increased from 310 HV to 419 HV (35.16 %) with an increase in deposition thickness from 0.10 mm to 0.50 mm. Again decrease in number of layers from 5 to 1 increases the average hardness from 419 HV to 488 HV (16.47 %). As residual stress also increased with an increase in deposition thickness and decrease in number of layers, therefore an engineer must compromise between the hardness and stress values while designing a functionally graded coating-substrate system. Hardness values also showed a greater increase from a 2 layer coating to a single layer coating compared to hardness increase between other graded coatings. The single layer coating was not a functionally graded coating, rather than an aluminium substrate coated with a 0.50 mm thick tool-steel, while gave higher hardness change.

5.2 RECOMMENDATIONS FOR FUTURE WORK

The results documented in the current research are significant, however recommendations for further investigation are as follows:

- The current system should be further developed to improve the range of its capabilities and repeatability of process. Specifically, flow control of powder from the dual feeder should be automated, the possible flow rates of powder should be increased, and the system could be improved to allow for an increased number of mixed powders. This would facilitate investigation of more complex 'designer' composite coatings.

- It is desirable to validate the relationship proposed in this thesis between powder thermal properties and optimum composite coating spray parameters. This could be done through the systematic study of a range of material combinations.

- A benefit/loss effect of grading coatings has been identified in the current work in relation to stress and hardness. This balance should be investigated for other materials, and for a wider range of properties important to relevant applications.

PUBLICATIONS ARISING FROM THIS WORK

Current Publications:

- M. Hasan, J. Stokes, L. Looney and M. S. J. Hashmi, "Residual Stress Determination in HVOF Thermal Sprayed Aluminium/Tool-Steel Functionally Graded Coatings", Proceedings of the 21st International Manufacturing Conference, Limerick, Ireland. 2004, pp. 299-304.

Journal Publications in Preparation:

- M. Hasan, J. Stokes, L. Looney and M. S. J. Hashmi, "Design and Calibration of a Multi-Powder HVOF Deposition Process".

- M. Hasan, J. Stokes, L. Looney and M. S. J. Hashmi, "Effect of Spray Parameters on Residual Stress Build-Up of HVOF Sprayed Aluminium/Tool-Steel Functionally Graded Coatings".

REFERENCES

[1] Couch, K. W., et al., "Studies of the Flame Spraying of Polymers", Proceedings of the 9th National Thermal Spray Conference, Ohio, USA, 1996, pp. 251-255.

[2] Nakano, A., et al., "Production of Heat and Corrosion-Resistant Plastic Coatings", Proceedings of the 9th National Thermal Spray Conference, Ohio, USA, 1996, pp. 257-262.

[3] Mareceau, J. A., & Adjorlolo, A. A., "Commercial Aircraft" in ASTM, Corrosion Tests and Standards: Application and Interpretation", American Society for Testing and Materials Society, 1995, pp. 574-578.

[4] Groshart, E. C., "Military Aircraft and Aerospace", in ASTM, Corrosion Tests and Standards Manual: Application and Interpretation", American Society for Testing and Materials Society, 1995, pp. 579-581.

[5] Seki, M., et al., "Application of Thermal Spray Coatings to Prevent Corrosion of Construction in Japan", Proceedings of the 5th National Thermal Spray Conference, California, USA, 1993, pp. 679-684.

[6] Zhao, L., et al., "Influence of the Spraying Processes on the Properties of 316L Stainless Steel Coatings", Surface and Coatings Technology, Vol. 162, 2002, pp. 6-10.

[7] Ohmori, A., "Thermal Spraying: Current Status and Future Trends", Proceedings of the 14th International Thermal Spray Conference, Kobe, Japan, 1995, 1241-3047.

[8] Nakagawa, P. M., et al., "Trends in Automotive Applications of Thermal Spray Technology in Japan", Proceedings of the 7th National Thermal Spray Conference, Boston, USA, 1994, pp. 1-6.

[9] Nicoll, A. R., "Production Plasma Spraying in the Automotive Industry: A European Viewpoint", Proceedings of the 7th National Thermal Spray Conference, Boston, USA, 1994, pp. 7-17.

[10] Bowen, K. T., et al., "Metallurgical Evaluation of Plasma Sprayed Structural Materials for Rocket Engines", Proceedings of the 13th International Thermal Spray Conference, Florida, USA, 1992, pp. 321-326.

[11] Parker, D. W., & Kutner, G., L., "HVOF-Spray Technology-Poised for Growth", Journal of Advanced Materials and Processes, Vol. 4, 1991, pp. 68-74.

[12] Parker, D. W., "HVOF Moves into the Industrial Mainstream", Journal of Advanced Materials and Processes, Vol. 146, Issue 1, 1994, pp. 31-35.

[13] Moore, D., "Protective Finishing Systems for Navy Aircraft", Journal of Advanced Materials and Processes, Vol. 155, Issue 4, 1999.

[14] Moskowitz, L. N., "Application of HVOF Thermal Spraying to Solve Corrosion Problems in the Petroleum Industry", Proceedings of the 13th International Thermal Spray Conference, Florida, USA, 1992, pp. 611-618.

[15] Rossi, A., et al., "A Contribution to the Surface Analysis and Characterisation of HVOF Coatings for Petrochemical Application", Wear, Vol. 250, 2001, pp. 107-113.

[16] Byrnes, L., et al., "Method and Apparatus for the Application of Thermal Spray Coatings onto Aluminium Engine Cylinder Bores", Proceedings of the 7th National Thermal Spray Conference, Boston, USA, 1994, pp. 39-48.

[17] Fukutome, H., et al., "The Application of Cermet Coating on Piston Ring by HVOF", Proceedings of the 14th International Thermal Spray Conference, Kobe, Japan, 1995, pp. 21-26.

[18] Matsubara, Y., et al., "Surface Texture and Adhesive Strength of High Velocity Oxy-Fuel Sprayed Coatings for Rolls of Steel Mills", Proceedings of the 13th International Thermal Spray Conference, Florida, USA, 1992, pp. 637-645.

[19] METCO/ Perkin Elmer, "Diamond Jet Process Manual", USA, 1989.

[20] Helali, M. D., "Spray Forming of Thin Walled Net-Shaped Components of Hard Material by the HVOF Thermal Spraying Process". Ph.D. Thesis, Dublin City University, Ireland, 1994.

[21] Tan, J. C., "Optimisation of the HVOF Thermal Spray Process for Coating, Forming and Repair of Components", Ph.D. Thesis, Dublin City University, Ireland, 1997.

[22] Stokes, J., "Production of Free Standing Engineering Components using the HVOF (High Velocity Oxy-Fuel) Process", Ph.D. Thesis, Dublin City University, Ireland, 2003.

[23] Kesler, O., et al., "Measurement of Residual Stress in Plasma-Sprayed Metallic, Ceramic and Composite Coatings", Materials Science and Engineering A, Vol. 257, 1998, pp. 215-224.

[24] Khor, A., et al., "Plasma Sprayed Functionally Graded Thermal Barrier Coatings", Material Letters, Vol. 38, Issue 6, 1999, pp. 437-444.

[25] Halling, J., "Recent Developments in Surface Coating and Modification Processes", Waveney Print Services Ltd, Suffolk, UK, ISBN No 0852985827, 1985.

[26] Chapman, B. N., & Anderson, T. C., "Science and Technology of Surface Coating", Academic Press, UK, ISBN No 0121683508, 1974.

[27] Hillery, R. V., "Coatings for High-Temperature Structural Materials, Trends and Opportunities", National Academy Press, Washington, ISBN No 0309053811, 1996.

[28] Holmberg, K., & Matthews, A., "Coatings Tribology: Properties, Techniques and Applications in Surface Engineering", Elsevier Science, The Netherlands, ISBN No 0444888705, 1994.

[29] Bhushan, B., & Gupta, B. K., "Handbook of Tribology: Material Coating and Surface Treatments", McGraw-Hill, New York, ISBN No 007052492, 1991.

[30] Sulzer METCO, "Product Information", 2001, www.sulzermetco.com. Date of access 08/06/02.

[31] Heimann, R. B., "Plasma-Spray Coating, Principles and Applications", VCH Publishers, New York, USA, ISBN No 3527294309, 1996.

[32] Online Sulzer METCO document, www.sulzermetco.com/tech/pr-ts.html. Date of access 20/12/01.

[33] Online EWI Weldnet Company Document, http://www.ewi.org/technologies/ arcwelding/thermalspray.asp, Date of access 09/09/04.

[34] Stokes, J., "The Theory and Application of the HVOF Thermal Spray Process", School of Mechanical and Manufacturing Engineering, Dublin City University, Ireland, 2003.

[35] Knight, R., & Smith, R. W., "HVOF Sprayed 80/20 NiCr Coatings: Process Influence Trends", Proceedings of the 13th International Thermal Spray Conference, Florida, USA, 1992, pp. 159-164.

[36] TAFA, "Model TJ-4000: The Most Affordable HVOF in the World-Product Brochure", TAFA Incorporated, 1998.

[37] PRAXAIR Surface Technologies and TAFA, "Thermal Spray Solutions-Product Brochure", PRAXAIR Surface Technologies and TAFA Incorporated, 2000.

[38] AEROSTAR Coatings, "HFPD: The New Alternative for the Thermal Spray Industry", AEROSTAR Coatings, 2000.

[39] Thorpe, M. L., & Richter, H. J., "A Pragmatic Analysis and Comparison of HVOF Processes", Proceedings of the 13th International Thermal Spray Conference, Florida, USA, 1992, pp. 137-147.

[40] Gartner, "Professional Thermal Spray Equipment", Gartner Thermal Spraying Company, 1999.

[41] Helali, M., & Hashmi, M. S. J., "A Comparative Study of Plasma Spraying and HVOF Thermal Spraying", Proceedings of the 10th Irish Manufacturing Committee (IMC-10) Conference, Galway, 1993, pp. 376-387.

[42] Vuoristo, P., et al., "Abrasion and Erosion Wear Resistance of Cr3C2-NiCr Coatings Prepared by Plasma, Detonation and High Velocity Oxyfuel Spraying", Proceedings of the 7th National Thermal Spray Conference, Boston, USA, 1994, pp. 121-126.

[43] Makela. A., et al., "Rolling Contact Fatigue Testing of Thermally Sprayed Coatings", Proceedings of the 7th National Thermal Spray Conference, Boston, USA, 1994, pp. 759-764.

[44] Pawlowski, L., "The Science and Engineering of Thermal Spray Coatings", Wiley and Sons, UK, ISBN No 0471952532, 1995.

[45] METCO/ Perkin Elmer, "Diamond Jet System and Gun Manual", USA, 1989.

[46] Thorpe, R., et al., "HVOF Thermal Spray Technology", Journal of Advanced Materials and Processes, Vol. 157, Issue 4, 2000, pp. 27-29.

[47] Bolles, C. D., "HVOF Thermal Spraying: An Alternative to Hard Chromes Plating", Welding Journal, Vol. 74, Issue 10, 1995, pp. 31-34.

[48] Online Concurrent Technologies Corporation Document, http://www.dppr.ctc.com/ plating/rhvofspr.htm, Date of access 06/01/02.

[49] Browing, J. A., et al., "A New HVOF Thermal Spray Concept", Proceedings of the 8th National Thermal Spray Conference, Texas, USA, 1995, pp. 7-10.

[50] Hackett, C. M., et al., "Independent Control of HVOF Particle Velocity and Temperature" Proceedings of the 9th National Thermal Spray Conference, Ohio, USA, 1996, pp. 665-673.

[51] Hacket, C. M., et al., "The Influence of Nozzle Design on HVOF spray Particle Velocity and Temperature", Proceedings of the 8th National Thermal Spray Conference, Texas, USA, 1995, pp. 135-140.

[52] Online Sulzer METCO Company Document, www.sulzermetco.com/tech/pr-comp.html, Date of access 20/12/2001.

[53] Hackett, C. M., et al., "On the Gas Dynamics of HVOF Thermal Sprays", Proceedings of the 5th National Thermal Spray Conference, California, USA, 1993, pp. 167-172.

[54] Thorpe, R. J., & Thorpe, M. L., "High Pressure HVOF: An Update", Proceedings of the 5th National Thermal Spray Conference, California, USA, 1993, pp. 199-204.

[55] Key, J. F., et al., "Use of De Laval Nozzles in Spray Forming", Proceedings of the 5th National Thermal Spray Conference, California, USA, 1993, pp. 75-80.

[56] Kowalsky, K. A., et al., "HVOF: Particles, Flame Diagnostics and Coating Characteristics", Proceedings of the 3rd National Thermal Spray Conference, California, USA, 1990, pp. 587-596.

[57] Online Sulzer METCO Company Document, http://www.sulzermetco.com/ news/nd13.html, Date of access 21/12/01.

[58] Stokes, J., & Looney, L., "Properties of WC-Co Components Produced using the HVOF Thermal Spray Process", Proceedings of the 1st International Thermal Spray Conference, Montreal, Canada, 2000, pp. 263-270.

[59] Young, P. M., et al., "Parameter Study of HP/HVOF Deposited WC-Co Coatings", Journal of Thermal Spray Technology, Vol. 7, Issue 1, 1998, pp. 97-107.

[60] Jacobs, L., et al., "Comparative Study of WC-Cermet Coatings Sprayed Via the HVOF and HVAF Coatings", Journal of Thermal Spray Technology, Vol. 7, Issue 2, 1998, pp. 213-218.

[61] Li. C. J., et al., "Effect of Types of Ceramic Materials in Aggregated Powder on the Adhesive Strength of High Velocity Oxy-Fuel Sprayed Cermet Coatings", Surface and Coatings Technology, Vol. 145, 2001, pp. 113-120.

[62] Cole, M. A., et al., "Process Gasses for High Velocity Oxy- Fuel Thermal Spraying", Proceedings of the 7th National Thermal Spray Conference, Boston, USA, 1994, pp. 233-238.

[63] Cole, M. A., et al., "High Temperature Erosion Properties Thermal Barrier Coatings Produced by Acetylene Sprayed High Velocity Oxygen Fuel Process", Proceedings of the 1st International Thermal Spray Conference, Canada, 2000, pp. 1191-1200.

[64] Metals Handbook, "Powder Metallurgy", Vol. 7, American Society for Metals, Metals Park, Ohio, ISBN No 0871700131, 1984.

[65] Online Flexographic Technical Association Document, http://www.cellramic. storkgroup.com/thermal.htm, Date of access 04/01/02.

[66] Online Goodfellow Company Document, www.goodfellow.com, Date of access 09/09/04.

[67] Technical Bulletin, #10-442, Sulzer METCO, October 2000.

[68] German, M. R., "Sintering Theory and Practice", John Willey and Sons, USA, ISBN No 047105786X, 1996.

[69] Kadyrov, E., et al., "Interaction of Particles with Carrier Gas in HVOF Spraying Systems", Journal of Thermal Spray Technology, Vol. 3, Issue 4, 1994, pp. 389-397.

[70] Rangel, R. H., et al., "Numerical Investigation of Micro-Pore Formation During Substrate Impact of Molten Droplets in Spraying Processes", Proceedings of the 7th National Thermal Spray Conference, Boston, USA, 1994, pp. 375-380.

[71] Mostaghimi, J., et al., "Deformation and Solidification of Molten Particles on a Substrate in Thermal Plasma Spraying", Proceedings of the 7th National Thermal Spray Conference, Boston, USA, 1994, pp. 405-414.

[72] Ohmori, A., et al., "Behaviour of Molten Droplets Impinging on Flat Surfaces", Proceedings of the 7th National Thermal Spray Conference, Boston, USA, 1994, pp. 563-568.

[73] Smith, M. F., et al., "An Investigation of the Effects of Droplet Impact Angle in Thermal Spray Deposition", Proceedings of the 7th National Thermal Spray Conference, Boston, USA, 1994, pp. 603-608.

[74] Mostaghimi, J., et al., "Droplet Impact and Solidification in a Thermal Spray Process: Droplet-Substrate Interactions", Proceedings of the 9th National Thermal Spray Conference, Ohio, USA, 1996, pp. 637-646.

[75] Bhol, R., et al., "Splat Solidification of Tin Droplets", Proceedings of the 9th National Thermal Spray Conference, Ohio, USA, 1996, pp. 657-663.

[76] Jiang, X. L., et al., "Induction Plasma Spraying of Refractory Materials", Proceedings of the 13th International Thermal Spray Conference, Florida, USA, 1992, pp. 39-44.

[77] Gawne, D. T., et al., "Splat Morphology and Adhesion of Thermally Sprayed Coatings", Proceedings of the 8th International Thermal Spray Conference, Japan, 1995, pp. 779-784.

[78] Roemer, T. J., et al., "Surface Roughness of Thermal Spray Coatings Made with Off-Normal Spray Angles", Journal of Thermal Spray Technology, Vol. 7, Issue 2, 1998, pp. 219-228.

[79] Greving, J. D., et al., "The Effect of Residual Stress in HVOF Tungsten Carbide Coatings on the Fatigue Life in Bending of Thermal Coatings", Journal of Thermal Spray Technology, Vol. 7, Issue 4, 1998, pp. 546-552.

[80] Kroupa, F., et al., "Residual Stresses in Graded Thick Coatings", Report from Institute of Electrical Engineering of Academy of Science, Czech Republic, Vol. 39, 1993, pp. 29-74.

[81] Kroupa, F., "Stresses in Coatings on Cylindrical Surfaces", Report from Institute of Electrical Engineering of Academy of Science, Czech Republic, Vol. 39, 1994, pp. 243-274.

[82] ASM Handbook, "Properties and selection: Nonferrous Alloys and Special Purpose Materials, Vol. 2, 10th Edition, The Materials Society, ISBN No 0871703785, 1990.

[83] ASM Handbook, "Properties and selection: irons, steels, and high-performance alloys, Vol. 1, 10th Edition, The Materials Society, ISBN No 0871703777, 1990.

[84] Online MatWeb Document, http://www.matweb.com/search/ SpecificMaterial.asp?bassnum=NCARN01, Date of access: 20/09/04.

[85] Rahman, M., et al., "Finite Element Modelling of Thermal Stresses in Sputter Deposited Graded Coating System", Proceedings on the 21st International Manufacturing Conference, Ireland, 2004, pp. 175-182.

[86] Stokes, J., & Looney, L., "Residual Stress in HVOF Thermally Sprayed Thick Deposits", Surface and Coatings Technology, Vol. 177-178, 2004, pp. 18-23.

[87] Itoh, A., & Clyne. T. W., "Initiation and Propagation of Interfacial Cracks During Spontaneous Debonding of Thermally Sprayed Coatings", Proceedings of the 8th National Thermal Spray Conference, Texas, USA, 1995, pp. 425-432.

[88] Vijgen, R. O. E., et al., "Mechanical Measurement of the Residual Stress in Thin PVD Films" Journal of Thin Solid Films, Vol. 270, 1995, pp. 264-269.

[89] Senderoff, S., et al., Journal of Research, National Bureau of Standards, Vol. 42, Issue 2, 1949, pp. 105-123.

[90] Tipton, A. A., "The Effect of HVOF Sprayed Coatings on the Elevated Temperature High Cycle Fatigue Behaviour of a Martensitic Stainless Steel", Proceedings of the 8th National Thermal Spray Conference, Texas, USA, 1995, pp. 463-468.

[91] Shadley, J. R., et al., "Effects of Coating Thickness and Residual Stress on Bond Strength of C633-79 Thermal Spray Coating Test Specimens", Proceedings of the 7th National Thermal Spray Conference, Boston, USA, 1994, pp. 639-645.

[92] Sobolev, V. V., et al., "Development of Coating Structure and Adhesion During High Velocity Oxygen-Fuel Spraying of WC-Co Powder on a Copper Substrate", Journal of Thermal Spray Technology, Vol. 9, Issue 1, 2000, pp. 100-106.

[93] Suresh, A., & Mortensen, A., "Fundamentals of Functionally Graded Materials: Processing and Thermomechanical Behaviour of Graded Metals and Metal-Ceramic Composites", The University Press, Cambridge, ISBN No 1861250630, 1998.

[94] Mortensen, A., "Kinetics of Densification by Sloution-Reprecipitation", Acta Materiala, Vol. 45, Issue 2, 1997, pp. 749-758.

[95] Merzhanov, A. G., "Self-Propagating High-Temperature Synthesis. Twenty Years of Search and Findings", Proceedings of the International Symposium on Combustion and Plasma Synthesis of High-Temperature Materials, California, USA, 1990, pp. 1-53.

[96] Holt, J. B., et al., "Self-Heating Synthesis of Materials", Annual Review of Materials Science, Vol. 21, 1991, pp. 305-334.

[97] Varma, A., et al., "Combustion Synthesis of Advanced Materials", Chemical Engineering Science, Vol. 47, Issue 9-11, 1992, pp. 2179-2194.

[98] Cline, C. F., "Preparation and Properties of Gradient TiC Cermet Cutting Tool" Lawrence Livermore National Laboratory, USA, 1973.

[99] Urai, S., et al., "Fabrication and Mechanical Properties of Cu/N and Ag/Ni Super-Laminates", Faculty of Medicine, Kyoto University, Japan, 1994, pp. 343-348.

[100] Watanabe, Y., et al., "Fabrication of Magnetic Functionally Graded Material by Martensitic Transformation Technique", Functionally Graded Materials, 1996, pp. 713-718.

[101] Smith, S. C., "A History of Metallography-The Development of Ideas on the Structure of Metals Before 1890", 2nd Edition, The MIT Press, Cambridge, Mass, USA, 1988.

[102] Dussoubs, B., et al., "Modelling of Plasma Spraying of Two Powders", Journal of Thermal Spray Technology, Vol. 10, Issue 1, 2001, pp. 105-110.

[103] Khor, K.A., & Gu, W.Y., "Effects of Residual Stress on the Performance of Plasma Sprayed Functionally Graded ZrO_2/NiCoCrAlY Coatings", Journal of Material Science and Engineering A, Vol. 277, Issue 1-2, 2000, pp. 64-76.

[104] Celik, E., et al., "Oxidation Behaviour of Functionally Gradient Coatings Including Different Composition of Cermets", Surface and Coatings Technology, Vol. 142-144, 2001, pp. 551-556.

[105] Smith, W., et al, "Plasma Processing of Functionally Graded Materials: Diagnostics and Characterization", Proceedings of the 9th National Thermal Spray Conference, Ohio, USA, 1996, pp. 317-324.

[106] Musil, J., et al., "Plasma Spraying Deposition of Graded Thermal Barrier Coatings", Proceedings of the 13th International Thermal Spray Conference, Florida, USA, 1992, pp. 525-530.

[107] Usmani, S., & Sampath, S., "Erosion Studies on Duplex and Graded Ceramic Overlay Coatings", JOM, Vol. 48, Issue 11, 1996, pp. 51-54.

[108] Sampath, S., et al., "Thermal Spray Processing of FGM", MRS Bulletin, Vol. 20, Issue 1, 1995, pp. 27-31.

[109] Sampath, S., et al., "Friction and Wear Properties of WC-Co and $Mo-Mo_2C$ Based Functionally Graded Materials", Wear, Vol. 249, 2001, pp. 1103-1115.

[110] Kim, M. R., et al., "Vacuum Plasma Spraying of Tungsten Base Functionally Gradient Composites", Proceedings of the 9th National Thermal Spray Conference, Ohio, USA, 1996, pp. 7-11.

[111] Mateus, C., et al., "Fluoroplymer-Ceramic Composite Coatings by Plasma Spraying", To be published in Journal of Materials Processing Technology.

[112] Khor, K. A., et al., "Non-Destructive Evaluation of Plasma Sprayed Functionally Graded Thermal Barrier Coatings", Surface and Coatings Technology, Vol. 130, Issue. 2-3, 2000, pp. 233-239.

[113] Khor, K. A., et al., "Influence of Oxide Mixtures on Mechanical Properties of Plasma Sprayed Functionally Graded Coatings", Thin Solid Films, Vol. 368, Issue. 1, 2000, pp. 86-92.

[114] Khor, K. A., et al., "Microstructure Formation in Plasma-Sprayed Functionally Graded NiCoCrAlY/Yttria - Stabilized Zirconia Coatings", Surface and Coatings Technology, Vol. 114, Issue 2-3, 1999, pp. 181-186.

[115] Hu, W., et al., "Graded Coatings Prepared by Plasma Spraying With Ni-Coated ZrO_2 Powders", Surface and Coatings Technology, Vol. 105, Issue 1-2, 1998, pp. 102-108.

[116] Lima, C. R. C., & Trevisan, R. E., "Graded Plasma Spraying of Premixed Metal-Ceramic Powders on Metallic Substrates", Journal of Thermal Spray Technology, Vol. 6, Issue 2, 1997, pp. 199-204.

[117] Cetinel, H., et al., "Wear Properties of Functionally Gradient Layers on Stainless Technology, Steel Substrates for High Temperature Applications", Surface and Coatings, Vol. 174-175, 2003, pp. 1089-1094.

[118] Yin, Y. S., et al., "Mechanical Properties of Fe_3Al/Al_2O_3 Composite Graded Coatings", Surface and Coatings Technology, Vol. 221, Issue 1-4, 2003, pp. 384-391.

[119] Hamatani, H., et al., "Effect of Composition Profile and Density of LPPS Sprayed Functionally Graded Coating on the Thermal Shock Resistance", Surface and Coating Technology, Vol. 4, Issue 2, 2003, pp. 197-203.

[120] Bunshah, R. F., "Handbook of Deposition Technologies for Films and Coatings", Noyes Publications, USA, ISBN No 0815513372, 1994.

[121] Koch, F., et al., "Experiments and Modelling of Combined PVD and CVD Processes Using a Hollow Cathode Arc Discharge Plasma", Surface and Coatings Technology, Vol. 108-109, 1998, pp. 520-525.

[122] Pinkas, M., et al., "Structural Analysis of $(Ti_{1-x}Al_x)N$ Graded Coatings Deposited by Reactive Magnetron Sputtering", Thin Solid Films, Vol. 355-356, 1999, pp. 380-384.

[123] Harry, E., et al., "Failure and Adhesion Characterization of Tungsten-Carbon Single Layers, Multilayered and Graded Coatings", Surface and Coatings Technology, Vol. 116-119, 1999, pp. 172-175.

[124] He, K., et al., "Oxidation Behaviour of Stainless Steel-Al Coatings Produced by Co-Sputtering and Reactive Sputtering", Material Letters, Vol. 46, 2000, pp. 53-59.

[125] Choy, K. L., "Functionally Graded Coatings on SiC Fibres for Protection in Ti-Based Metal Matrix Composites", Scripta Materiala, Vol. 34, Issue 11, 1996, pp. 1753-1758.

[126] Movchan, B. A., "Functionally Graded EB PVD Coatings", Surface and Coatings Technology, Vol. 149, 2002, pp. 252-262.

[127] Hongbo, G., et al., "Evaluation of Hot-Fatigue Behaviors of EB-PVD Gradient Thermal Barrier Coatings", Materials Science and Engineering A, Vol. 325, 2002, pp. 261-269.

[128] Marinski, G. S., et al., "Gradient Protective Coatings of Different Application Produced by EB-PVD", Surface and Coatings Technology, Vol. 100-101, 1998, pp. 309-315.

[129] Gong, S., et al., "Oxidation Behavior of TiAl/TiAl-SiC Gradient Coatings on Gamma Titanium Aluminides", Surface and Coatings Technology, Vol. 130, 2000, pp. 128-132.

[130] Gust, W., et al., "Vacuum Arc Deposition of Ni-Ti Gradient Coatings", Surface and Coatings Technology, Vol. 100-101, 1998, pp. 316-319.

[131] Guo, H., et al., "Preparation of Al_2O_3-YSZ Composite Coating by EB-PVD", Materials Science and Engineering A, Vol. 325, 2003, pp. 389-393.

[132] Nothe, M., et al., "Investigation of the Structure and Properties of a –C:H Coatings with Metal and Silicon Containing Interlayers", Applied Surface Science, Vol. 179, 2001, pp. 123-129.

[133] Donnet, C., et al., "Diamond-Like Carbon-Based Functionally Gradient Coatings for Space Tribology", Surface and Coatings Technology, Vol. 120-121, 1999, pp. 548-554.

[134] West, D. R. F., et al., "Functionally Graded Nickel-Aluminide and Iron-Aluminide Coatings Produced via Laser Cladding", Journal of Materials Science", Vol. 30, 1995, pp. 5931-5938.

[135] Levin, P., et al., "Laser Produced Functionally Graded Tungsten Carbide Coatings on M2 High-Speed Tool Steel", Materials Science and Engineering A, Vol. 302, 2001, pp. 106-114.

[136] Pei, Y. T., "Functionally Graded Materials Produced by Laser Cladding", Acta Materialia, Vol. 48, 2000, pp. 2617-1624.

[137] Tomota, Y., et al., "Functionally Graded Coating for Steels by Reaction Diffusion Using $FeAl_3$ Powder", ISIJ International, Vol. 40, Issue 10, 2000, pp. 1029-1034.

[138] Watanabe, R., et al., "Evaluation of Thermomechanical Performance for Thermal Barrier Type of Sintered Functionally Graded Materials", Composites B, Vol. 28, 1996, pp. 29-35.

[139] Kumar, R. R., et al., "Functionally Graded Coatings of HA-G-Ti Composites and their in Vivo Studies", Materials Science and Engineering A, Vol. 334, 2002, pp. 156-162.

[140] Jun, L., et al., "Electroforming of Nickel and partially Stabilized Zirconia (Ni + PSZ) Gradient Coating", Surface and Coatings Technology, Vol. 91, 1997, pp. 131-135.

[141] Watanabe, R., et al., "Thermal Fracture Behaviour of Metal/Ceramic Functionally Graded Materials", Engineering Fracture Mechanics, Vol. 69, 2002, pp. 1713-1728.

[142] Peters, M., et al., "Graded Coatings for Thermal, Wear and Corrosion Barriers", Materials Science and Engineering A, Vol. 362, 2003, pp. 61-80.

[143] Kim, J. H., et al., "Evaluation of Functionally Graded Thermal Barrier Coatings Fabricated by Detonation Gun Spray Technique", Surface and Coatings Technology, Vol. 168, 2003, pp. 275-280.

[144] Khor, K. A., et al., "Functionally Graded ZrO_2-NiCrAlY Coatings Prepared by Plasma Spraying Using Premixed, Spheroidized Powders", Surface and Coatings Technology", Vol. 96, 1997, pp. 305-312.

[145] Khor, K. A., & Gu, W.Y., "Thermal Properties of Plasma-Sprayed Functionally Graded Thermal Barrier Coatings", Thin Solid Films, Vol. 372, Issue 1-2, 2000, pp. 104-113.

[146] Khor, K. A., et al., "Mechanical Behaviour of Plasma-sprayed Functionally Graded YSZ/NiCoCrAlY Composite Coatings", Surface and Coatings Technology", Vol. 139, Issue 2-3, 2001, pp. 200-206.

[147] Walter, L., et al., "Functionally Graded Hardmetals", Journal of Alloys and Compounds", Vol. 338, Issue 1-2, 2002, pp. 194-212.

[148] Avci, E., et al., "Evaluation of Functionally Graded Coatings Produced by Plasma-Spray Technique", Surface and Coatings Technology, Vol. 116-119, 1999, pp. 292-295.

[149] Pan, C., et al., "Microstructural Characteristics in Plasma Sprayed Functionally Graded ZrO_2/NiCrAl Coatings", Surface and Coatings Technology, Vol. 162, 2003, pp. 194-201.

[150] Voevodin, A. A., et al., "Investigation into Three-Dimensional Laser Processing of Tribological Coatings", Surface and Coatings Technology, Vol. 107, 1998, pp. 12-19.

[151] ASM Handbook, "Mechanical Testing", Vol. 8 The Materials Information Society, ISBN No 0871700077, 1985.

[152] METCO/ Perkin Elmer, "Diamond Jet Application Data Charts", USA, 1989.

[153] Evans, H. E., et al., "Smart Overlay Coatings-Concept and Practice", Surface and Coatings Technology, Vol. 149, 2002, pp. 236-244.

[154] Khor, K. A., et al., "Plasma Spraying of Functionally Graded Hydroxyapatite/Ti-6Al-4V Coatings", Surface and Coatings Technology, Vol. 168, 2003, pp. 195-201.

[155] Shaw, L. L., "Thermal Residual Stresses in Plates and Coatings of Multilayered and Functionally Graded Materials", Composites B, Vol. 29, 1998, pp. 199-210.

[156] Teixiera, V., "Numerical Analysis of the Influence of Coating Porosity and Substrate Elastic Properties on the Residual Stresses in High Temperature Graded Coatings", Surface and Coatings Technology, Vol. 146-147, 2001, pp. 79-84.

[157] Ma, F., et al., "Diamond-Like Carbon Gradient Film Prepared by Unbalanced Sputtering and Plasma Immersion Ion Implantation Hybrid Technique", Materials Letters, Vol. 57, 2002, pp. 82-86.

[158] Parks, W. P., et al., "Thermal Barrier Coatings Issues in Advanced Land-Based Gas Turbines", Journal of Thermal Spray Technology, Vol. 6, Issue 2, 1997, pp. 187-192.

[159] Mutasim, Z., et al., "Thermal Barrier Coatings for Industrial Gas Turbine Applications: An Industrial Note", Journal of Thermal Spray Technology, Vol. 6, Issue 1, 1997, pp. 105-108.

[160] Yonushonis, T. M., "Overview of Thermal Barrier Coatings in Diesel Engines", Journal of Thermal Spray Technology, Vol. 6, Issue 1, 1997, pp. 50-56.

[161] Miller, R. A., "Thermal Barrier Coatings for Aircraft Engines: History and Directions", Journal of Thermal Spray Technology, Vol. 6, Issue 1, 1997, pp. 35-42.

[162] Beele, W., et al., "The Evaluation of Thermal Barrier Coatings-Status and Upcoming Solutions for Today's Key Issues", Surface and Coatings Technology, Vol. 120-121, 1999, pp. 61-67.

[163] Stover, D., "Effects of Deposition Temperature and Thermal Cycling on Residual Stress State in Zirconia-Based Thermal Barrier Coatings", Surface and Coatings Technology, Vol. 120-121, 1999, pp. 103-111.

[164] Hongbo, H., et al., "Effect of Thermal Exposure on the Microstructure and Properties of EB-PVD Gradient Thermal Barrier Coatings", Surface and Coatings Technology, Vol. 168, 2003, pp. 23-29.

[165] Rangraj, S., et al., "Estimating the Fracture Resistance of Functionally Graded Thermal Barrier Coatings from Thermal Shock tests", Surface and Coatings Technology, Vol. 173, 2003, pp. 201-212.

[166] Kon, M., et al., "Development of Calcium Phosphate Based Functional Gradient Bioceramics", Biomaterials, Vol. 16, Issue 9 1995, pp. 709-714.

[167] Kumar, R. R., et al., "Functionally Graded Bioactive Coatings of Hydroxypatite/Titanium Oxide Composite System", Materials Letters, Vol. 55, 2002, pp. 133-137.

[168] Wang, C. X., "Functionally Graded Calcium Phosphate Coatings Produced by Ion Beam Sputtering/Mixing Deposition", Biomaterials, Vol. 22, Issue 12, 2001, pp. 1619-1626.

[169] Remer, P., et al., "Realisation of Graded Coatings for Biomedical Use", Materials Science Forum, Vol. 308-311, 1999, pp. 368-373.

[170] Liu, G., et al., "Graded Ni-P-PTFE Coatings and Their Potential Applications", Surface and Coatings Technology, Vol. 155, 2002, pp. 279-284.

[171] Verne, E., et al., "Graded Coatings on Ceramic Substrates for Biomedical Applications", Journal of European Ceramic Society, Vol. 21, 2001, pp. 2855-2862.

[172] Park, E., et al., "Graded Coatings of Hydroxyapatite and Titanium by Atmospheric Plasma Spraying", Material Letters, Vol. 40, 1999, pp. 228-234.

[173] Ding, S. J., "Properties and Immersion Behavior of Magnetron-Sputtered Multi-Layered Hydroxyapatite/Titanium Composite Coatings", Biomaterials, Vol. 24, Issue 23, 2003, pp. 4233-4238.

[174] Kumar, R. R., et al., "Functionally Graded Coatings of HA-G-Ti Composites and their in Vivo Studies", Materials Science and Engineering A, Vol. 334, 2002, pp. 156-162.

[175] Khor, K. A., et al., "Significance of Melt-Fraction in HVOF Sprayed Hydroxyapatite Particles, Splats and Coatings", Biomaterials, Vol. 25, 2004, pp. 1177-1186.

[176] Miller, W. S., et al., "Recent Development in Aluminium Alloys for the Automotive Industry", Material Science and Engineering A, Vol. 280, 2000, pp. 37-49.

[177] European Commission White Book, "European Transport Policy for 2010: Time to Decide".

[178] Schumann, S., et al., "Research for a - New Age of Magnesium - in the Automotive Industry", Journal of Materials Processing Technology, Vol. 117, 2001, pp. 276-281.

[179] Gray, J. E., et al., "Protective Coatings on Magnesium and its alloys-A Critical Review", Journal of Alloys and Compounds, Vol. 336, 2002, pp. 88-113.

[180] Nie, X., et al., "Thickness Effects on the Mechanical Properties of Micro-Arc Discharge Oxide Coatings on Aluminium Alloys", Surface and Coatings Technology, Vol. 116-119, 1999, pp. 1055-1060.

[181] Funatani, K., "Emerging Technology in Surface Modification of Light Metals", Surface and Coatings Technology, Vol. 133-134, 2000, pp. 264-272.

[182] Edrisy, A., et al., "Wear of Thermal Spray Deposited Low Carbon Steel Coatings on Aluminium Alloys", Wear, Vol. 251, 2001, pp. 1023-1033.

[183] Merlo, A. M., "The Contribution of Surface Engineering to the Product Performance in the Automotive Industry", Surface and Coatings Technology, Vol. 174-175, 2003, pp. 21-26.

[184] Wenzelburger, M., et al., "Modeling of Thermally Sprayed Coatings on Light Metal Substrates: - Layer Growth and Residual Stress Formation", Surface and Coatings Technology, Vol. 180-181, 2004, pp. 429-435.

[185] Hunt, W. H., et al., "Metallurgical Considerations in the Design and Processing of Aluminium Powder-Metallurgy Alloys", Powder Metallurgy Aluminium and Light Alloys for Automotive Applications Conference, Michigan, USA, 1998, pp. 1-9.

[186] Billi, F., et al., "Micromechanical Modification Induced by Cyclic Thermal Stress on Metal Matrix Composites for Automotive Applications", Composites B, Vol. 32, 2001, pp. 529-533.

[187] Heath, P. J., "Developments in Application of PCD Tooling", Journal of Materials Processing Technology, Vol. 116, 2001, pp. 31-38.

[188] Mumm, D. R., et al., "Microstructure, Deformation and Cracking Characteristics of Thermal Spray Ferrous Coatings", Materials Science and Engineering A, Vol. 269, Issue 1-2, 1999, pp. 152-165.

[189] Carle, D., et al., "The Suitability of Aluminium as an Alternative Material for Car Bodies", Materials and Design, Vol. 20, 1999, pp. 267-272.

[190] Barnes, T. A., et al., "Joining Techniques for Aluminium Spaceframe Used in Automobiles Part I – Solid and Liquid Phase Welding", Journal of Materials Processing Technology, Vol. 99, Issue 1-3, 2000, pp. 62-71.

[191] Barnes, T. A., et al., "Joining Techniques for Aluminium Spaceframes Used in Automobiles Part II – Solid and Liquid Phase Welding", Journal of Materials Processing Technology, Vol. 99, Issue 1-3, 2000, pp. 72-79.

[192] Stoloff, N. S., "Iron Aluminide: Present Status and Future Prospects", Materials Science and Engineering A, Vol. 258, Issue 1-2, 1998, pp. 1-14.

[193] Schubert, E., et al., "Light-Weight Structures Produced by Laser Beam Joining for Future Applications in Automobile and Aerospace Industry", Journal of Materials Processing Technology, Vol. 115, Issue 1, 2001, pp. 2-8.

[194] Heinz, A., et al., "Recent Development in Aluminium Alloys for Aerospace Applications", Materials Science and Engineering A, Vol. 280, 2000, pp. 102-107.

[195] Piegari, A., et al., "Ultraviolet-Graded Coatings for Lasers: Surface Optical Performance", Thin Solid Films, Vol. 373, 2000, pp. 155-158.

[196] METCO/Perkin Elmer, "Powder Feed Unit Manual", USA, 1988.

[197] METCO/Perkin Elmer, "METCO Thermal Spraying: General Overview", 1989.

[198] Stokes, M., "Design and Development of an Erosion Testing Device", Final Year Project, Dublin City University, Ireland, 2002.

[199] Vardelle, M., et al., "Dynamic of Splat Formation and Solidification in Thermal Spraying Processes", Proceedings of the 7th National Thermal Spray Conference, Boston, USA, 1994, pp. 555-562.

[200] Stokes, J., & Looney, L., "HVOF System Definition to Maximise the Coating Thickness of Formed Components", Proceedings of Advances in Materials and Processing Technologies, Dublin, Ireland, 1999, pp. 775-784.

[201] Sulzer METCO, "Product Information", www.sulzermetco.com, 2002.

[202] ANSYS Version 6.1 Help menu, 2004.

[203] James, E. A. J., & William, L. H., "Introduction to Fluid Mechanics", Prentice-Hall, Englewood Cliffs, New Jersey, ISBN No 0134839412, 1980.

[204] Online Aquamim Technology Document, http://www.planetpolymer.com/ AQUAMIM%20m4.htm, Date of Access 05/03/04.

[205] Anderson, J. D., "Computational Fluid Dynamics", McGraw-Hill International Edition, ISBN No 0071132104, 1995.

[206] Massey, B. S., "Mechanics of Fluid", 6th Edition, Chapman and Hall, London, ISBN No 0412342804, 1989.

[207] Douglas, J. F., et al., "Fluids Mechanics", 3rd Edition, Singapore Publisher Limited, Singapore, ISBN No 0582234085, 1998.

[208] ANSYS 5.7 Documentation online, ANSYS Corporate, Date of access 21/03/02.

[209] METCO/Perkin-Elmer, "Hand Note", 1989.

[210] Smith, M. F., et al., "A Comparison of Techniques for the Metallographic Preparation of Thermal Sprayed Samples", Proceedings of the 4th National Thermal Spray Conference, Pennsylvania, USA, 1991, pp. 97-104.

[211] Glancy, S. D., "How Metallographic Preparation Affects the Microstructure of WC/Co Thermal Spray Coatings", Proceedings of the 7th National Thermal Spray Conference, Boston, USA, 1994, pp. 771-777.

[212] Glancy, S. D., "Preserving the Microstructure of Thermal Spray Coatings", Journal of Advanced Materials and Processes, Vol. 148, Issue 1, 1995, pp. 37-40.

[213] Sampath, S., et al., "Effects of Grinding Mechanisms on Surface Finish and Hardness of Thermally Sprayed WC-Co", Proceedings of the 9th National Thermal Spray Conference, Ohio, USA, 1996, pp. 493-500.

[214] BUEHLER, "Metallography Europe Reference Manual: 3 Day Certified Vocational Training Course", 1994.

[215] Glancy, S. D., "Pursuit of a Universal Metallographic Procedure for Thermally Sprayed Coatings", Proceedings of the 8th National Thermal Spray Conference, Texas, USA, 1995, pp. 493-498.

[216] Whichard, G. C., et al., "Evaluation of the Phase Content and Properties of a Detonation Gun Coatings", Proceedings of the 7th National Thermal Spray Conference, Boston, USA, 1994, pp. 727-731.

[217] Blann, G. A., "The Important Role of Microstructural Evaluation in Each Phase of Thermally Sprayed Coatings Application", Proceedings of the 13th International Thermal Spray Conference, Florida, USA, 1992, pp. 959-966.

[218] Carle, V., et al., "Metallographic Etching", ASM International, The Materials Information Society, 2nd Edition, ISBN No 0871706334, 1999.

[219] Brundle, C. R., et al., "Encyclopaedia of Materials Characterization", Manning Publications Company, Greenwich, ISBN No 0750691689, 1992.

[220] ASM Handbook, "Materials Characterization", Vol. 10, The Materials Information Society, ISBN No 0871700077, 1986.

[221] Cullity, B., D., "Elements of X-Ray Diffraction", Addison-Wesley, USA, ISBN No 0201610914, 1978.

[222] ASTM E367-69, "Standard Practice for Measuring Coating Thickness by Magnetic Field Eddy Current (Electromagnetic) Test Method", 1985.

[223] ISO 1463, "Metallic and Oxide Coatings – Measurement of Coating Thickness – Microscopical Method", International Standard, 1983.

[224] Rybicki, J. R., et al., "A Cantilever Beam Method for Evaluation of Young's Modulus and Poison's Ratio of Thermal Spray Coatings", Journal of Thermal Spray Technology, Vol. 4, Issue 4, 1995, pp. 377-383.

[225] Sampath, S., et al., "Intrinsic Residual Stresses in Single Splats Produced by Thermal Spray Processes", Acta Materiala, Vol. 49, 2001, pp. 1993-1999.

[226] Yang, Y. C., et al., "Influence of Residual Stress on Bonding Strength and Fracture of Plasma-Sprayed Hydroxyapatite Coatings on Ti-6Al-4V Substrate", Biomaterials, Vol. 22, Issue 13, 2001, pp. 1827-1836.

[227] Kolman, B., et al., "Structure and Residual Stresses in Thermally Sprayed Steel Coatings", Materials Science Forum, Vol. 308-311, 1999, pp. 232-237.

[228] Hashmi, M. S. J., et al., "Residual Stresses in Structures Coated by a High Velocity Oxy-Fuel Technique", Journal of Materials Processing Technology, Vol. 75, Issue 1-3, 1998, pp. 81-86.

[229] Perry, J. A., et al., "Practical Measurement of the Residual Stress in Coatings", Surface and Coatings Technology, Vol. 81, 1996, pp. 17-28.

[230] Musil, J., et al., "Stress Analysis of Thermal Sprayed Coatings Using a Semi-Destructive Hole-Drilling Strain Gauge Method", Proceedings of the 8th National Thermal Spray Conference, Texas, USA, 1995, pp. 445-449.

[231] Montay, G., et al., "Development of the High-Precision incremental-Step Hole-Drilling Method for the Study of Residual Stress in Multi-Layer Materials: Influence of Temperature and Substrate on ZrO_2-Y_2O_3 8 wt.% Coatings", Surface and Coatings Technology, Vol. 155, Issue 2-3, 2002, pp. 152-160.

[232] Richard, C. S., et al., "The Influence of Heat Treatment and Interdiffusion on the Adhesion of Plasma-Sprayed NiCrAlY Coatings", Surface and Coatings Technology, Vol. 82, 1996, pp. 99-109.

[233] Gadow, R., et al., "Experimental and Numerical Residual Stress Analysis of Layer Coated Composites", Materials Science and Engineering A, Vol. 288, 2000, pp. 154-159.

[234] Rendler, N. J., et al, "Hole-Drilling Strain Gauge Method of Measuring Residual Stresses", Experimental Mechanics, Vol. 6, 1966, pp. 577-586.

[235] ASTM E837-95, "Determining Residual Stresses by the Hole-Drilling Strain Gauge Method", American Society for Testing Materials Standards, Philadelphia, 1995.

[236] Kim, J. G., et al., "Comparative Study of Residual Stresses Measurement Methods on CVD Diamond Films", Scripta Materiala, Vol. 39, Issue 6, 1998, pp. 807-814.

[237] Teixeira, V., et al., "Analysis of Residual Stresses in Thermal Barrier Coatings", Journal of Materials Processing Technology, 1999, Vol. 92-93, pp. 209-216.

[238] Greving, D. J., et al., "The Effect of Coating Residual Stress on the Fatigue Life of Thermal Spray-Coated Steel and Aluminium", Surface and Coatings Technology, Vol. 108-109, Issue 1-3, 1998, pp. 59-64.

[239] Persson, C., et al., "Analysis of the Stress State in Thermal Barrier Coatings during a Thermal Cycle", Proceedings of the 9th National Thermal Spray Conference, Ohio, USA, 1996, pp. 897-902.

[240] Greving, D. J., et al., "Residual Stress Evaluations of Thermal Spray Coatings by a Modified Layer Removal Method", Proceedings of the 7th National Thermal Spray Conference, Boston, USA, 1994, pp. 647-653.

[241] SAE J443, "Procedures for Using Standard Shot Peening Test Strip", Surface Vehicle Recommended Practice, 1990.

[242] Brandt, O. C., "Measuring of Residual Stresses in Thermal Sprayed Coatings", Proceedings of the 8th National Thermal Spray Conference, Texas, USA, 1995, pp. 451-455.

[243] Knight, R., & Smith, R. W., "Residual Stress in Thermally Sprayed Coatings", Proceedings of the 5th National Thermal Spray Conference, California, USA, 1993, pp. 607-612.

[244] Pron, H., et al., "Estimation of Residual Stresses Induced by Shot-Peening. Measurement of the Thermal Dissipation with an Infrared Camera", International Journal of Thermal Sciences, Vol. 41, 2002, pp. 369-375.

[245] Dong, Z., et al., "Residual Stress Evaluations of Thermally Sprayed Coatings by a Modified Almen Test Method", China Welding, Vol. 7, Issue 2, 1998, pp. 130-138.

[246] Tsui, Y. C., & Clyne, T. W., "An Analytical Model for Predicting Residual Stresses in Progressively Deposited Coatings", Thin Solid Films, Vol. 306, 1997, pp. 23-33.

[247] Hunt, M. W., "Guide to Engineering Materials 2001", Journal of Advanced Materials and Processes, Vol. 158, Issue 6, 1991.

[248] Holman, J. P., "Heat Transfer", McGraw-Hill, New York, 5th Edition, ISBN No 0070296189, 1981.

[249] Benedict, R. P., "Fundamentals of Fluid Flow", John Wiley & Sons, USA, ISBN No 0471033758, 1980.

[250] Corcoran, B. G., "Pharmaceutical Water System and the 6D Rule, A Computational Fluid Dynamics Analysis", Ph.D. Thesis, Dublin City University, Ireland, 2003.

[251] O'Rouke, M., "Content of Fluid Dynamics & Heat Transfer Module" University College Dublin, Ireland, 2001.

[252] Chen, Y., & Wang, H. M., "Growth Morphology and Mechanism of Primary TiC Carbide in Laser Clad TiC/FeAl Composite Coating", Material Letters, Vol. 57, 2003, pp. 1233-1238.

[253] Lu, J., & Jansson, U., "Chemical Vapour Deposition of Molybdenum Carbides: Aspects of Nanocrystallinity", Thin Solid Films, Vol. 396, 2001, pp. 53-61.

[254] Taylor, T. A., & Walsh, P. N., "Thermal Expansion of MCrAlY Alloys", Surface and Coatings Technology, Vol. 177-178, 2004, pp. 24-31.

[255] Lide, D. R., "Handbook of Chemistry and Physics", 84th Edition, CRC Press, USA, ISBN No 0849304849, 2003.

[256] Online Document, http://ej.iop.org/links/q34/t3CutnvbhbY3O6EWRr 9g8w/e60417.pdf, Date of access 20/09/04.

[257] Celik, E., et al., "Thermal Analysis of High Temperature ZrO_2 Insulation Ceramic Coatings on Ag Tapes used as Sheath of Bi-2212 Superconducting Materials using Finite element Method", Materials and Design, Vol. 24, 2003, pp. 543-546.

[258] Sarikaya, O., et al., "Effects of Residual Stress on Thickness and Interlayer of Thermal Barrier Ceramic MgO- ZrO_2 Coatings on Ni and AlSi Substrates using Finite Element Method", Materials and Design, Vol. 23, 2002, pp. 645-650.

[259] Totemeier, T. C., et al., "Microstructure and Stresses in HVOF Sprayed iron Aluminide Coatings", Journal of Thermal Spray Technology, Vol. 11, Issue 3, 2002, pp. 400-408.

[260] Huang, L. Y., et al., "Investigation of the Relation Between Structure and Mechanical Properties of Hydrogenated Diamond-Like Carbon Coatings Prepared by PECVD", Materials Science and Engineering A, Vol. 373, 2004, pp. 45-53.

[261] Madar, K. Z., et al., "The Effect of Thermochemical Treatment on the Structure and Hardness of Electroless Ni-P Coated Low Alloy Steel", Surface and Coatings Technology, Vol. 182, 2004, pp. 65-71.

[262] Kim, K. R., et al., "Effect of Intrinsic Properties of Ceramic Coatings on Fatigue Behavior of Cr-Mo-V Steels", Surface and Coatings Technology, Vol. 171, 2003, pp. 15-23.

[263] Ishii, Y., et al., "Mechanical Properties of Arc-Evaporated CrN Coatings. Part II: Intrinsic Film Hardness and Composite Hardness", Surface and Coatings Technology, Vol. 145, 2001, pp. 94-100.

[264] Karlsson, l., et al., "Influence of Residual Stresses on the Mechanical Properties of TiC_xN_{1-x} (x = 0, 0.15, 0.45) thin Films Deposited by arc Evaporation", Thin Solid Films, Vol. 371, 2000, pp. 167-177.

[265] Vaz, F., et al., "Influence of Nitrogen Content on the Structural, Mechanical and Electrical Properties of TiN Thin films", To be Published in the Journal of Surface and Coatings Technology.

[266] Oettel, H., et al., "Mechanical Behaviour of TiN Coatings", Surface and Coatings Technology, Vol. 97, 1997, pp. 785-789.

[267] Vaz, F., et al., "Mechanical Characterization of Reactively Magnetron-Sputtered TiN Films", Surface and Coatings Technology, Vol. 174-175, 2003, pp. 375-382.

[268] Peters, A. M., et al., "Effect of Carrier Gas on the Deposition of Titanium Carbon-Nitride Coatings by a Novel Organo-Metallic Plasma Immersion Ion Processing Technique", Vacuum, Vol. 67, 2002, pp. 169-175.

APPENDICES

APPENDIX A

Different Parts Involving Concept Four

All dimension are in mm

—M10

M10

62

22

116

9

60°

THIRD ANGLE PROJECT	˙MEng, School of MME		
	NEEDLE SHAPED BOLT		
Mahbub Hasan	QTY: 2	MATERIAL: STAINLESS STEEL	
DATE: 02/21/01	SCALE: NONE	PROJECT: MY07	SHEET: 2 OF 5
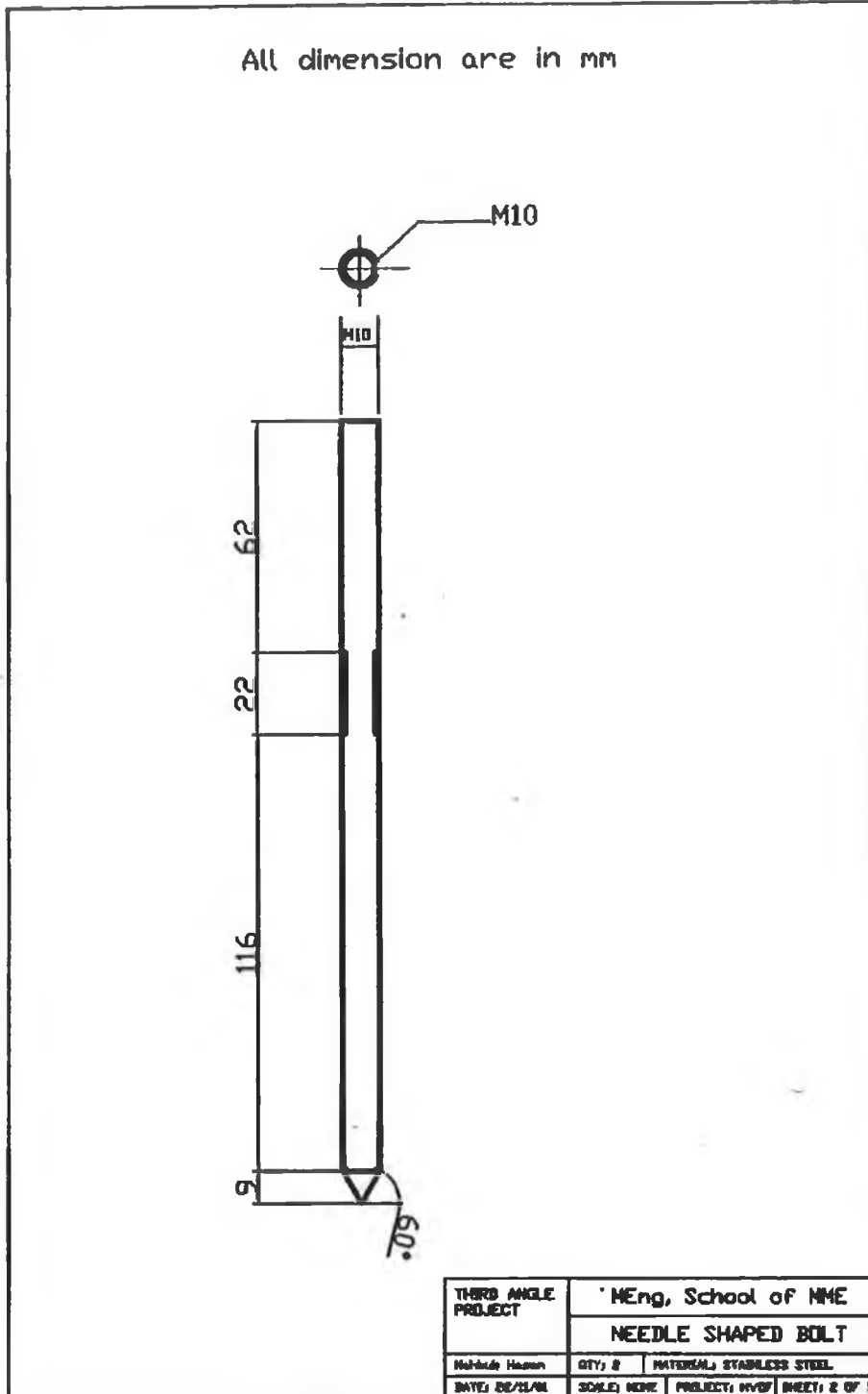
Figure A1: Needle shaped bolt.

All dimension are in mm

2 off
M10
equally
spaced
holes

M10

A

A

Section A-A

THIRD ANGLE PROJECTION	MEng, School of MME		
	TOP PLATE		
Mahbub Hasan	QTY: 1	MATERIAL: STAINLESS STEEL	
DATE: 22/11/01	SCALE: NONE	PROJECT: HVOF	SHEET: 4 of 9
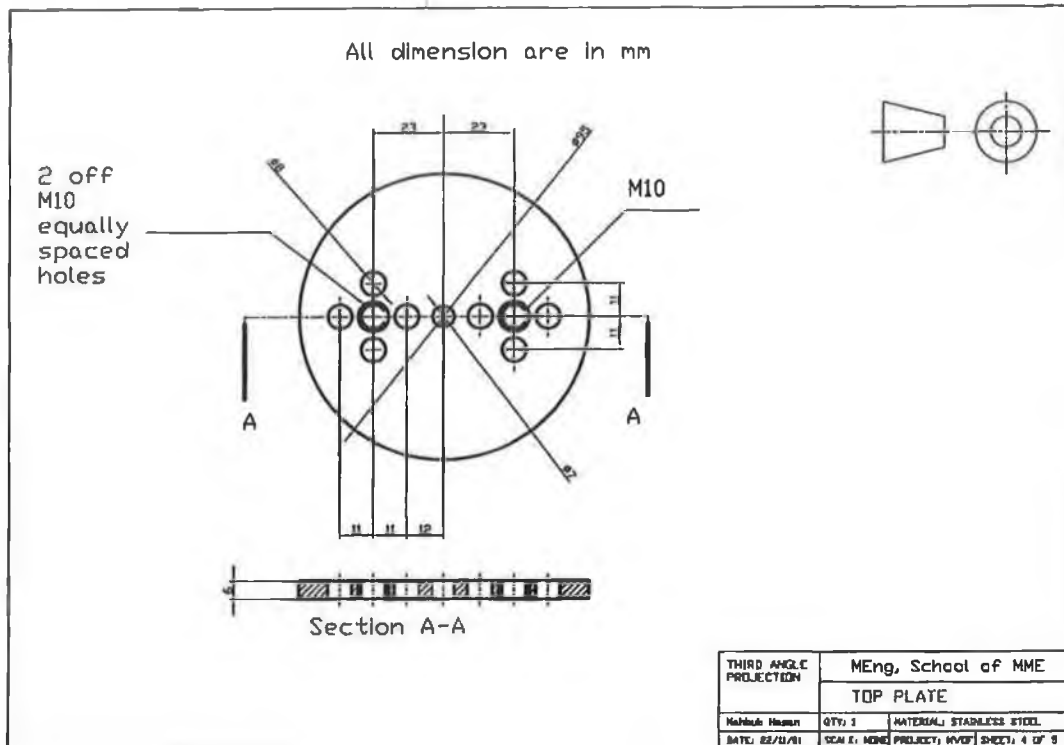
Figure A2: Top plate.

All dimension are in mm

Ø38

Ø34

Ø6,4

A   A

104

24

2

6,4

60°
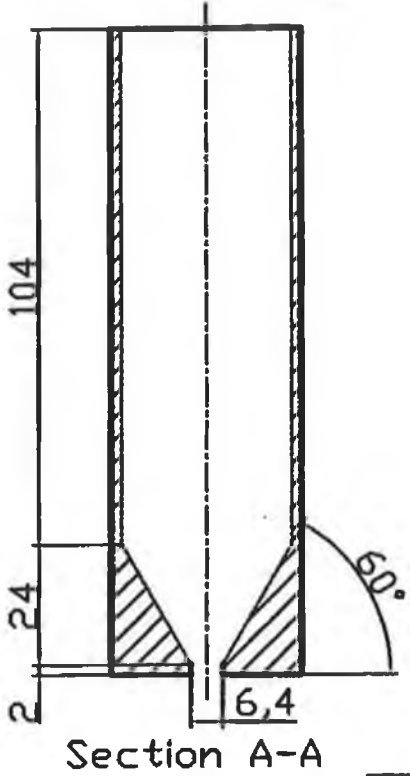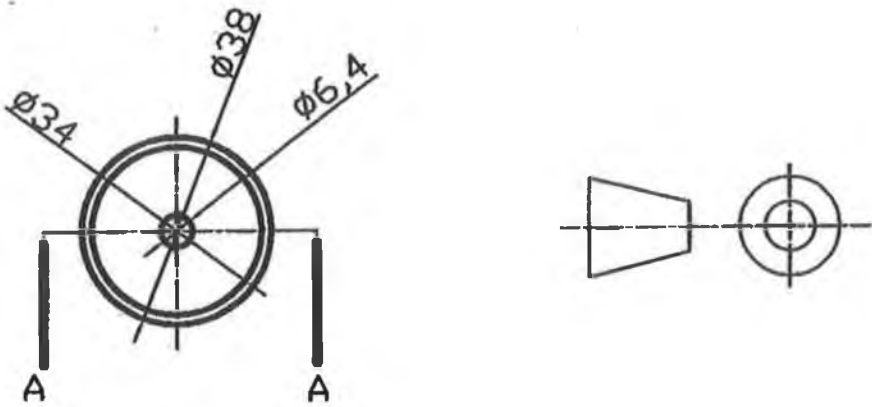
Section A-A

THIRD ANGLE PROJECTION		MEng, School of MME	
		POWDER HOLDER	
Mahbub Hasan	QTY; 2	MATERIAL; STAINLESS STEEL	
DATE; 22/11/01	SCALE; NONE	PROJECT; HVOF	SHEET; 3 OF 5

Figure A3: Individual powder holder.

A3

All dimension are in mm

23 23

Ø95

Ø7

A   A

Section A-A

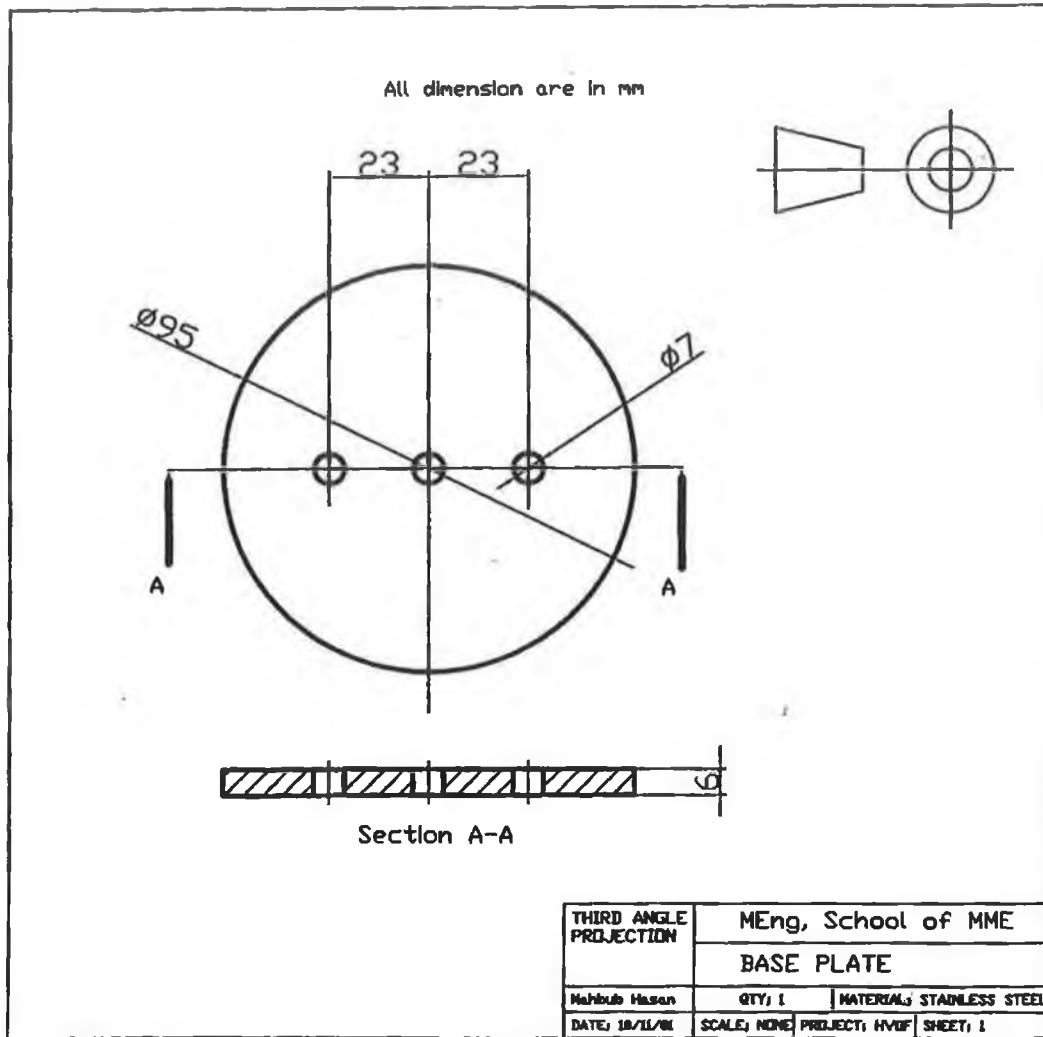| THIRD ANGLE PROJECTION	MEng, School of MME	
	BASE PLATE	
Mahbub Hasan	QTY: 1	MATERIAL: STAINLESS STEEL
DATE: 18/11/01	SCALE: NONE	PROJECT: HVOF	SHEET: 1

Figure A4: Base plate.
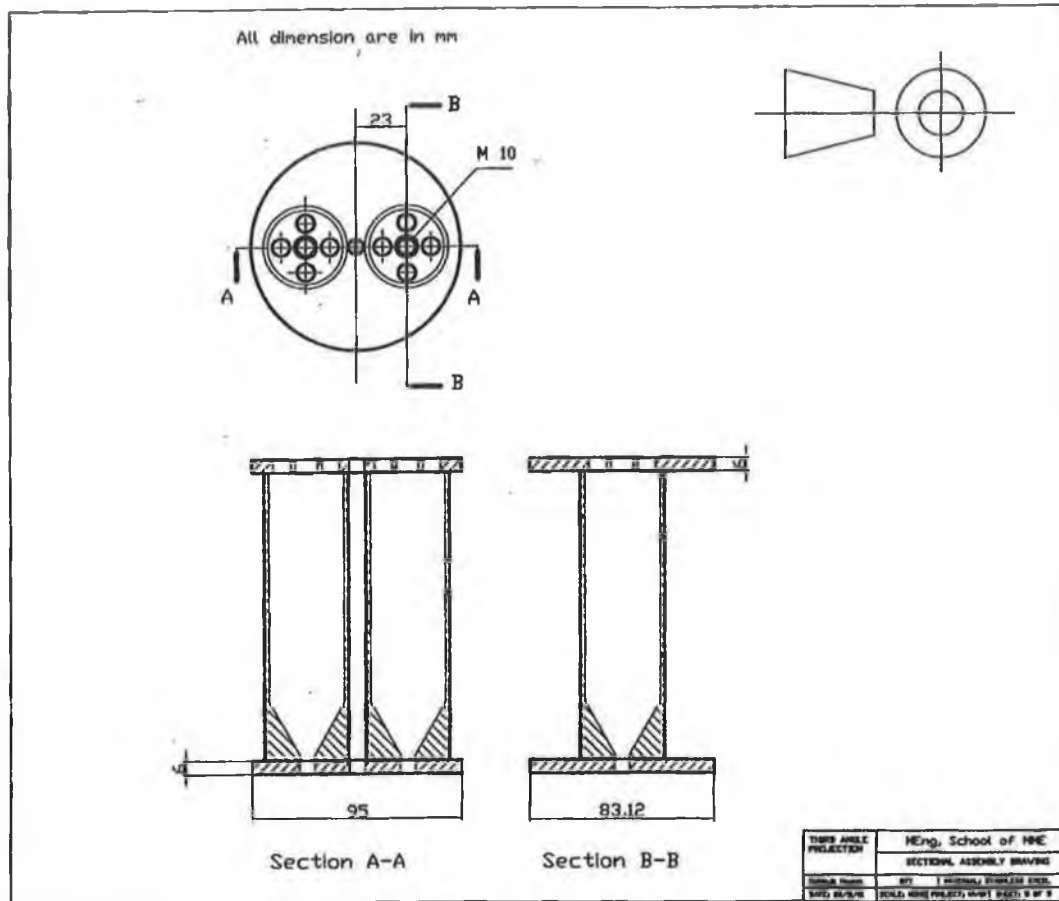
Figure A5: Sectional assembly drawing of the base plate, the top plate and the individual powder holders.

All dimension are in mm

7

22

55

72°

45

Ø7

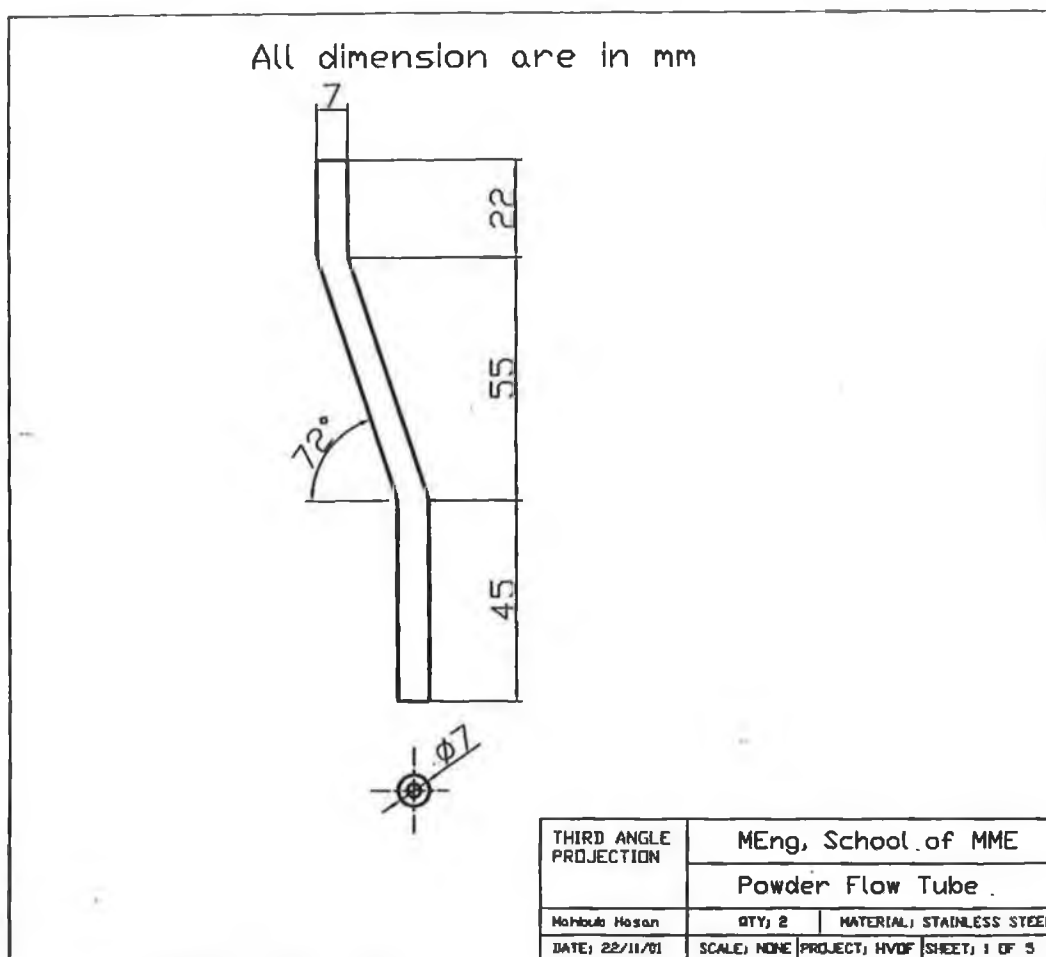| THIRD ANGLE PROJECTION	MEng, School of MME	
	Powder Flow Tube	
Mahbub Hasan	QTY: 2	MATERIAL: STAINLESS STEEL
DATE: 22/11/01	SCALE: NONE PROJECT: HVOF	SHEET: 1 OF 3

Figure A6: Powder flow tube.
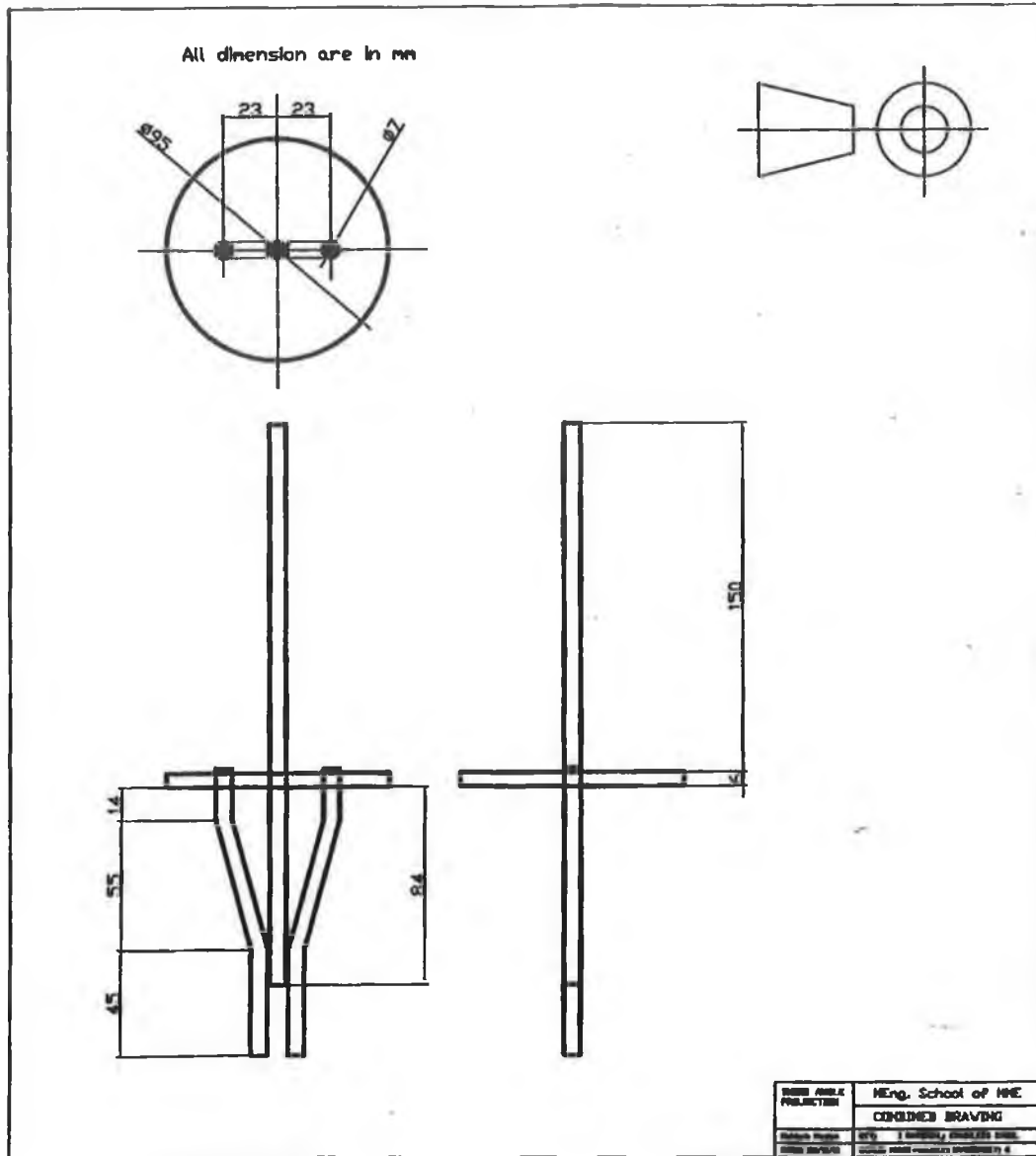
Figure A7: Combined drawing of the base plate, the inlet pressure tube and
the powder flow tubes.

All dimension are in mm

THIRD ANGLE PROJECTION | MEng, School of MME
| POWDER MIXING HOLDER
Mahbub Hasan | QTY, 1 | MATERIAL, ALUMINIUM
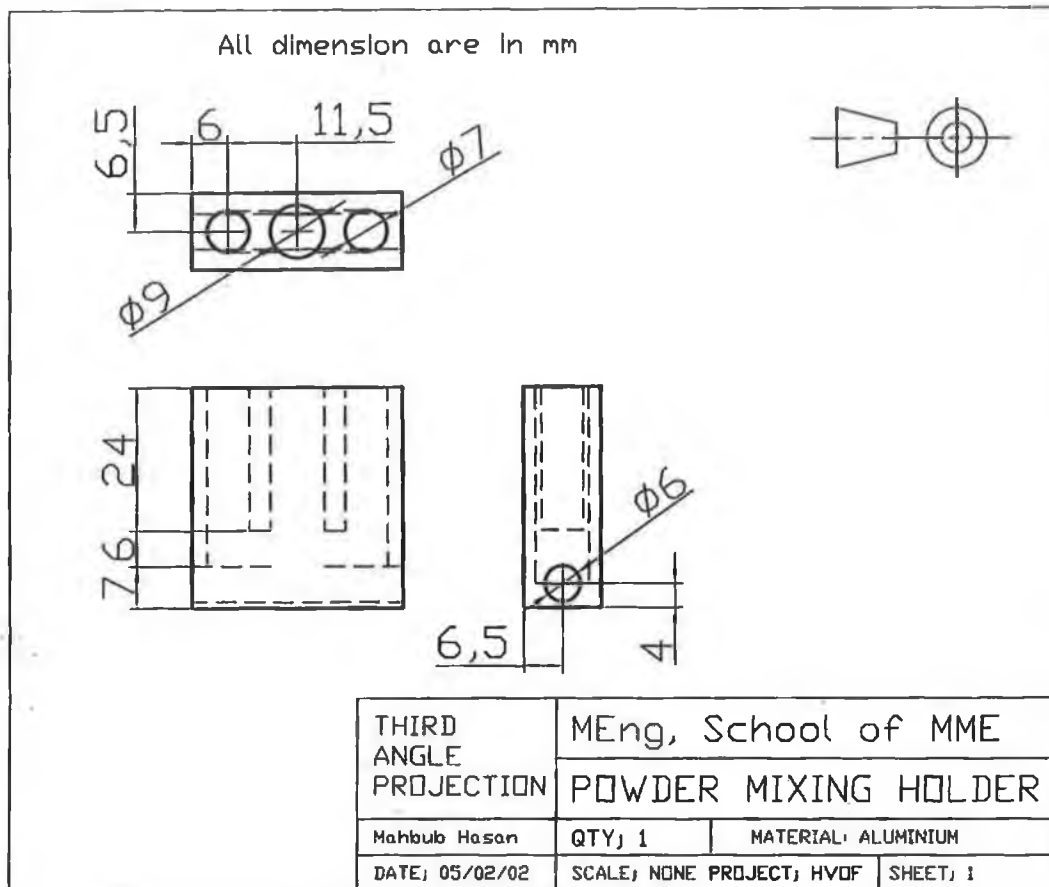DATE, 05/02/02 | SCALE, NONE PROJECT, HVOF | SHEET, 1
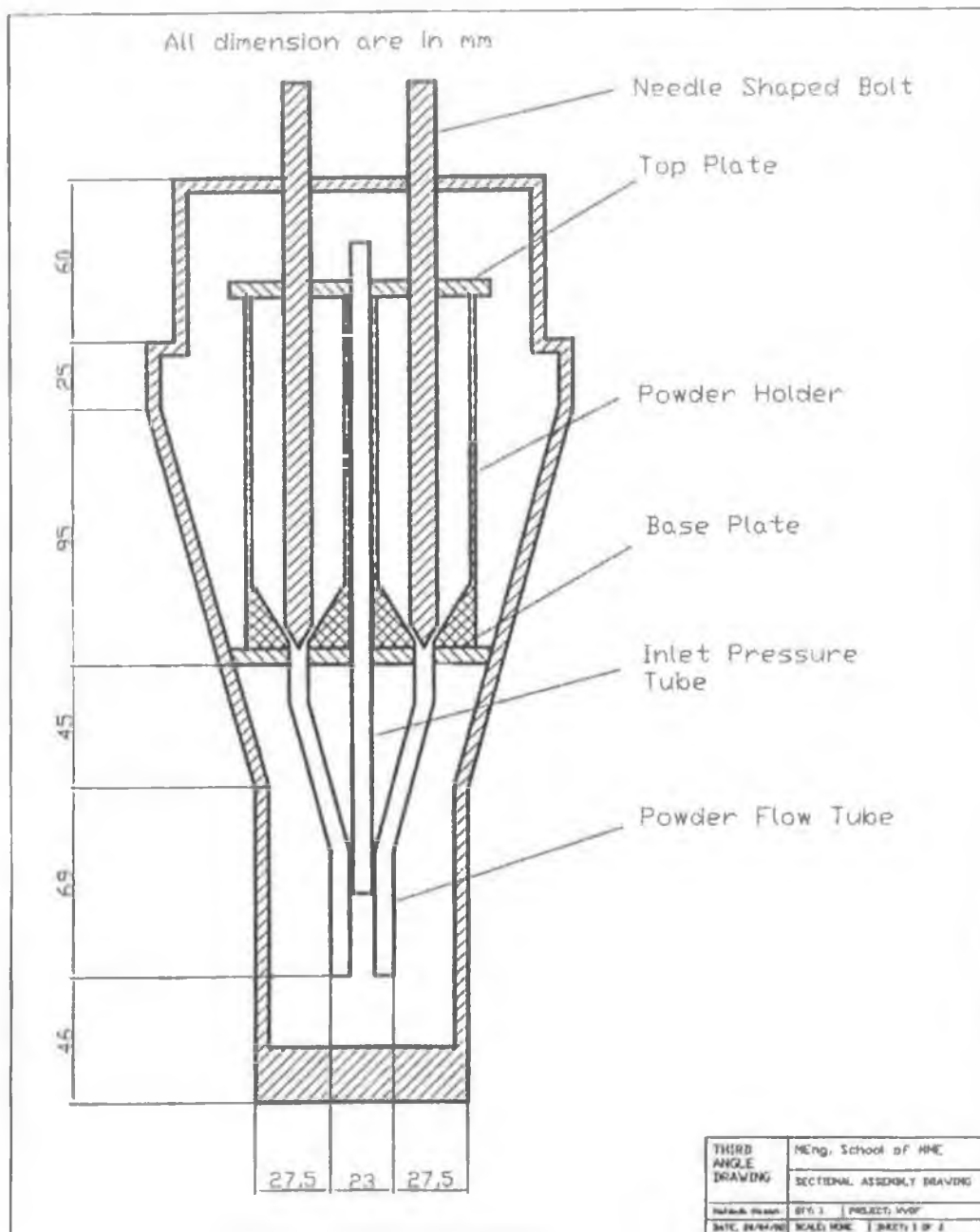
Figure A8: Powder mixing holder.

Figure A9: Sectional assembly drawing of the needle shaped bolt, the top plate, the individual powder holders, the base plate, the inlet pressure tube, the powder flow tubes and the powder feed hopper.

All dimension are in mm

Inlet Pressure Tube

Powder Flow Tube

Powder Mixing Holder

Pick-Up Shaft

30

46

21,5   35   21,5

THIRD ANGLE PROJECTION	MEng, School of MME
	SECTIONAL ASSEMBLY DRAWING

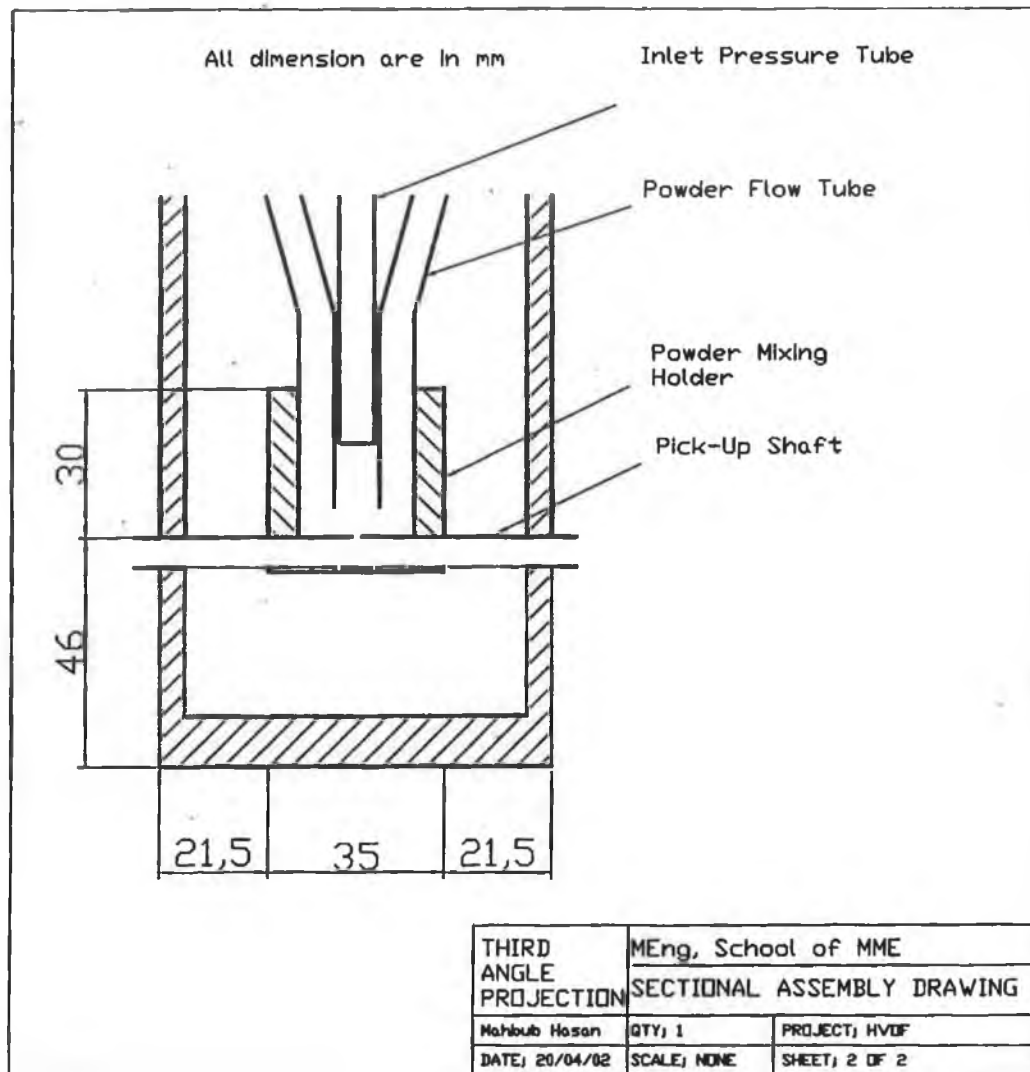| Mahbub Hasan	QTY; 1	PROJECT; HVOF
DATE; 20/04/02	SCALE; NONE	SHEET; 2 OF 2

Figure A10: Sectional assembly drawing of the lower portion of powder feed hopper, the inlet pressure tube, the powder flow tubes, the powder mixing holder and the pick-up shaft.
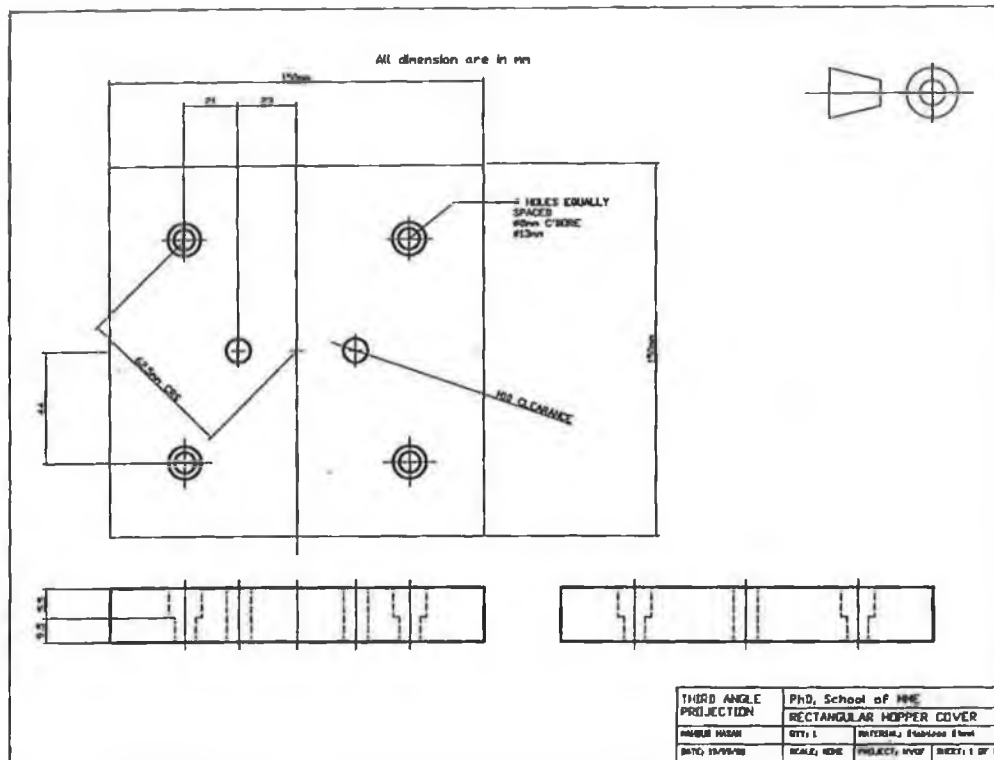
A10

Figure A11: Rectangular hopper cover.

APPENDIX B

ANSYS Results

(a)

(b)

Figure A12: The velocity profile of the fluids through the (a) gas-powder flow tubes and (b) pick-up shaft with powders at a ratio of 3:1 and a nitrogen gas pressure ratio of 9:1 on the inlet pressure tube to the pick-up shaft.

Figure A13: The velocity profile of the fluids through the (a) gas-powder flow tubes and (b) pick-up shaft with powders at a ratio of 3:1 and a nitrogen gas pressure ratio of 10:1 on the inlet pressure tube to the pick-up shaft.
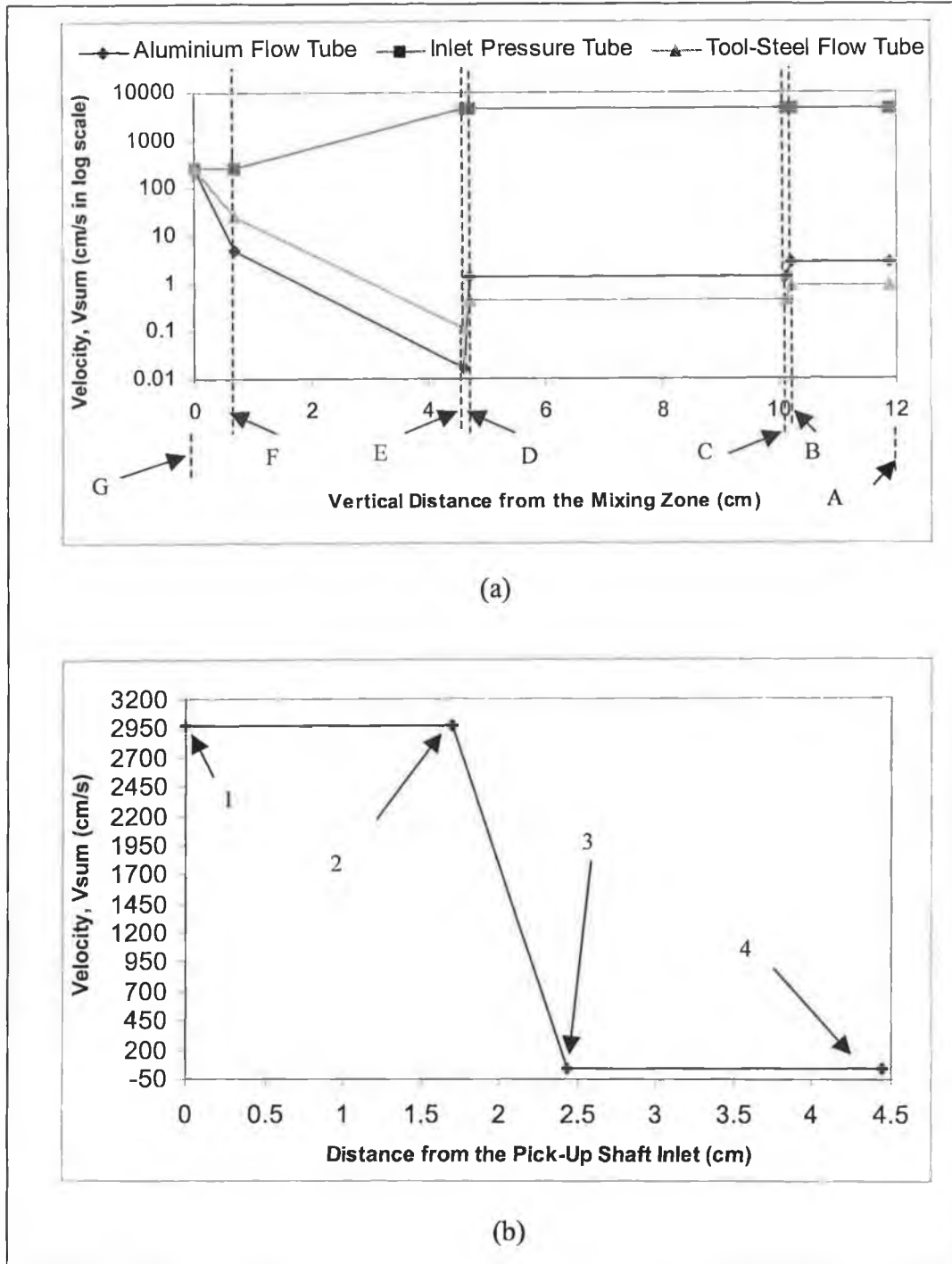
(a)

(b)

Figure A14: The velocity profile of the fluids through the (a) gas-powder flow tubes and (b) pick-up shaft with powders at a ratio of 1:1 and a nitrogen gas pressure ratio of 8:1 on the inlet pressure tube to the pick-up shaft.

(a)

(b)

Figure A15: The velocity profile of the fluids through the (a) gas-powder flow tubes and (b) pick-up shaft with powders at a ratio of 1:1 and a nitrogen gas pressure ratio of 9:1 on the inlet pressure tube to the pick-up shaft.
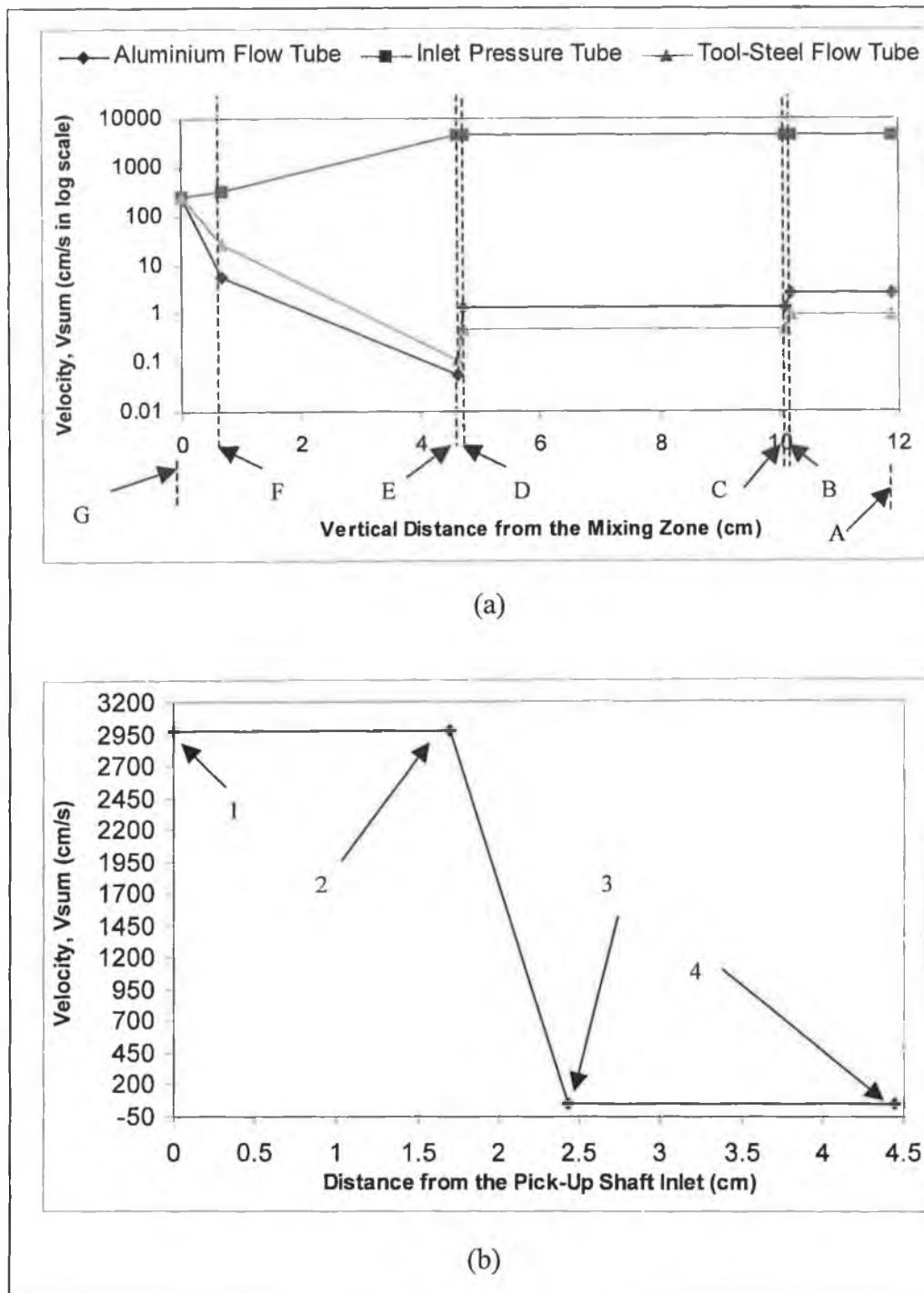
Figure A16: The velocity profile of the fluids through the (a) gas-powder flow tubes and (b) pick-up shaft with powders at a ratio of 1:1 and a nitrogen gas pressure ratio of 10:1 on the inlet pressure tube to the pick-up.
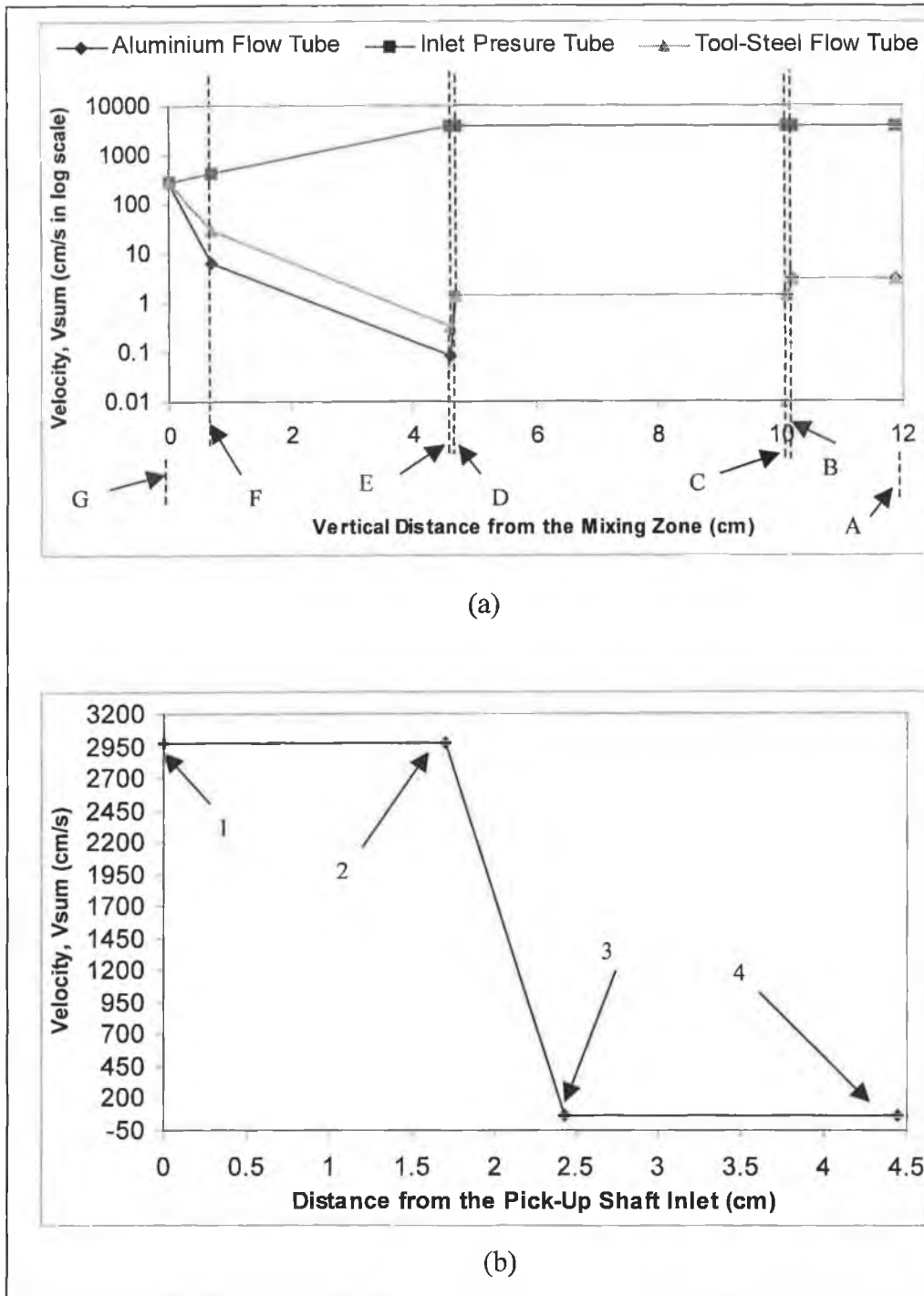
Figure A17: The velocity profile of the fluids through the (a) gas-powder flow tubes and (b) pick-up shaft with powders at a ratio of 1:3 and a nitrogen gas pressure ratio of 8:1 on the inlet pressure tube to the pick-up.

(a)

(b)

Figure A18: The velocity profile of the fluids through the (a) gas-powder flow tubes and (b) pick-up shaft with powders at a ratio of 1:3 and a nitrogen gas pressure ratio of 9:1 on the inlet pressure tube to the pick-up.
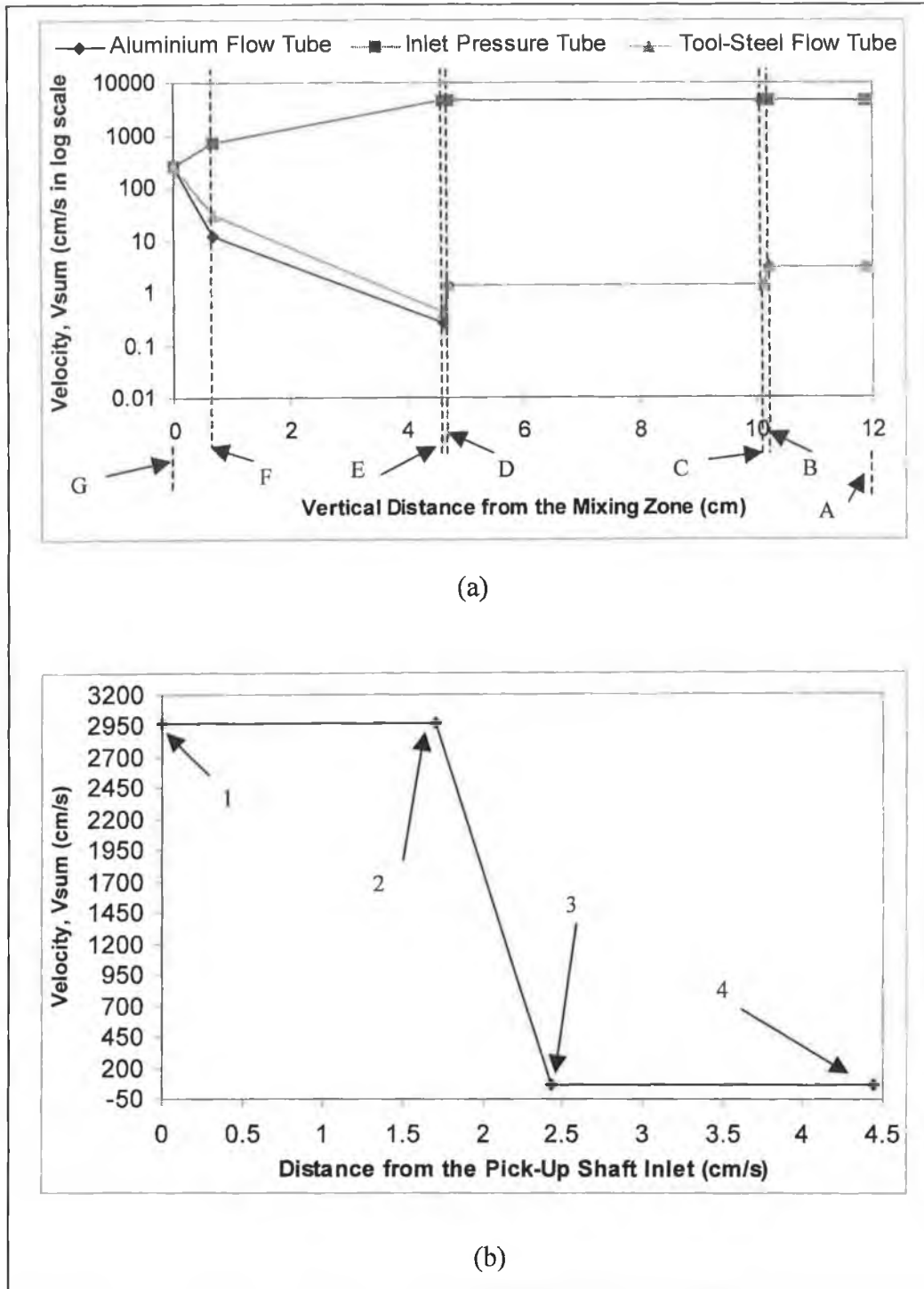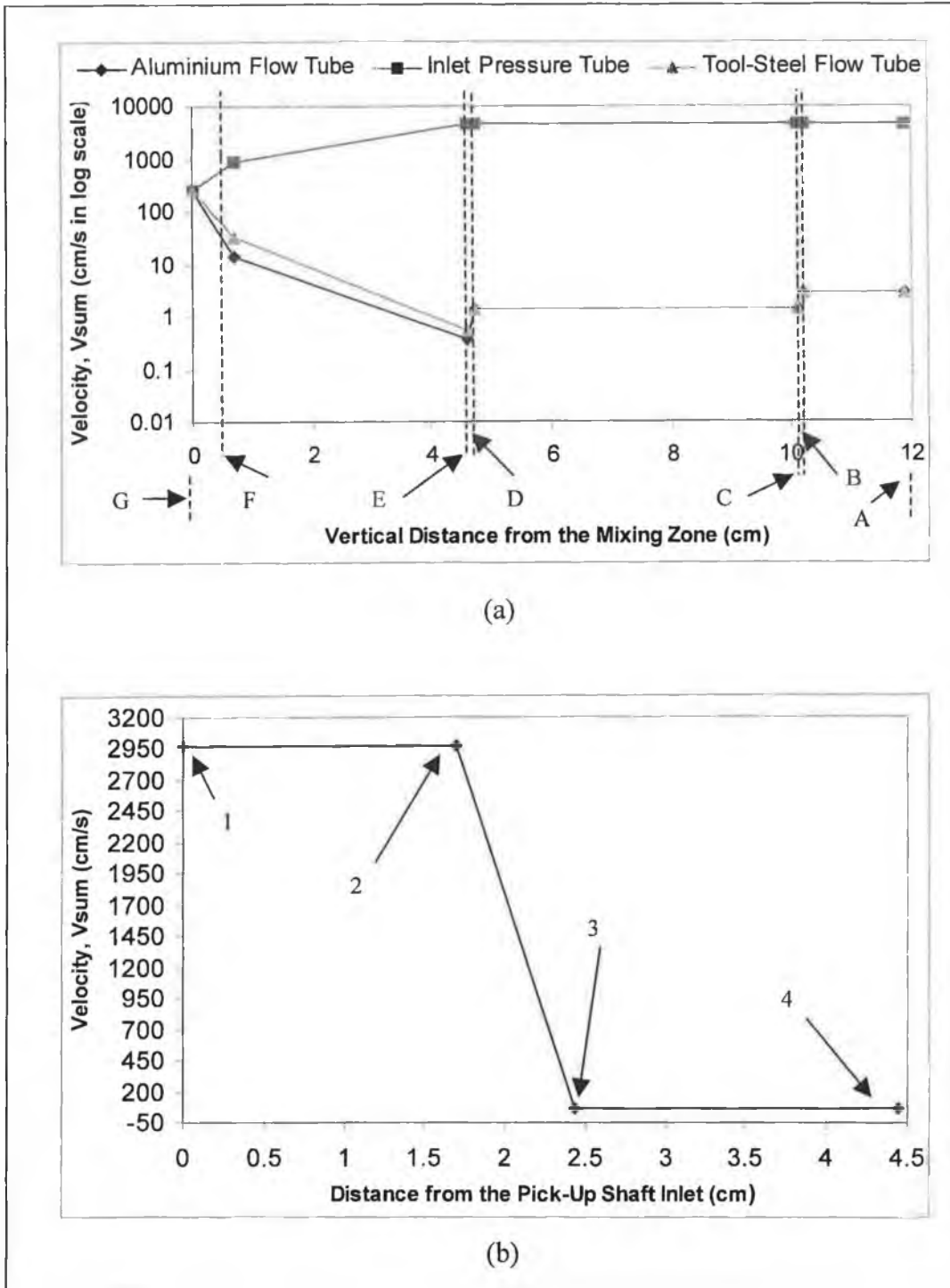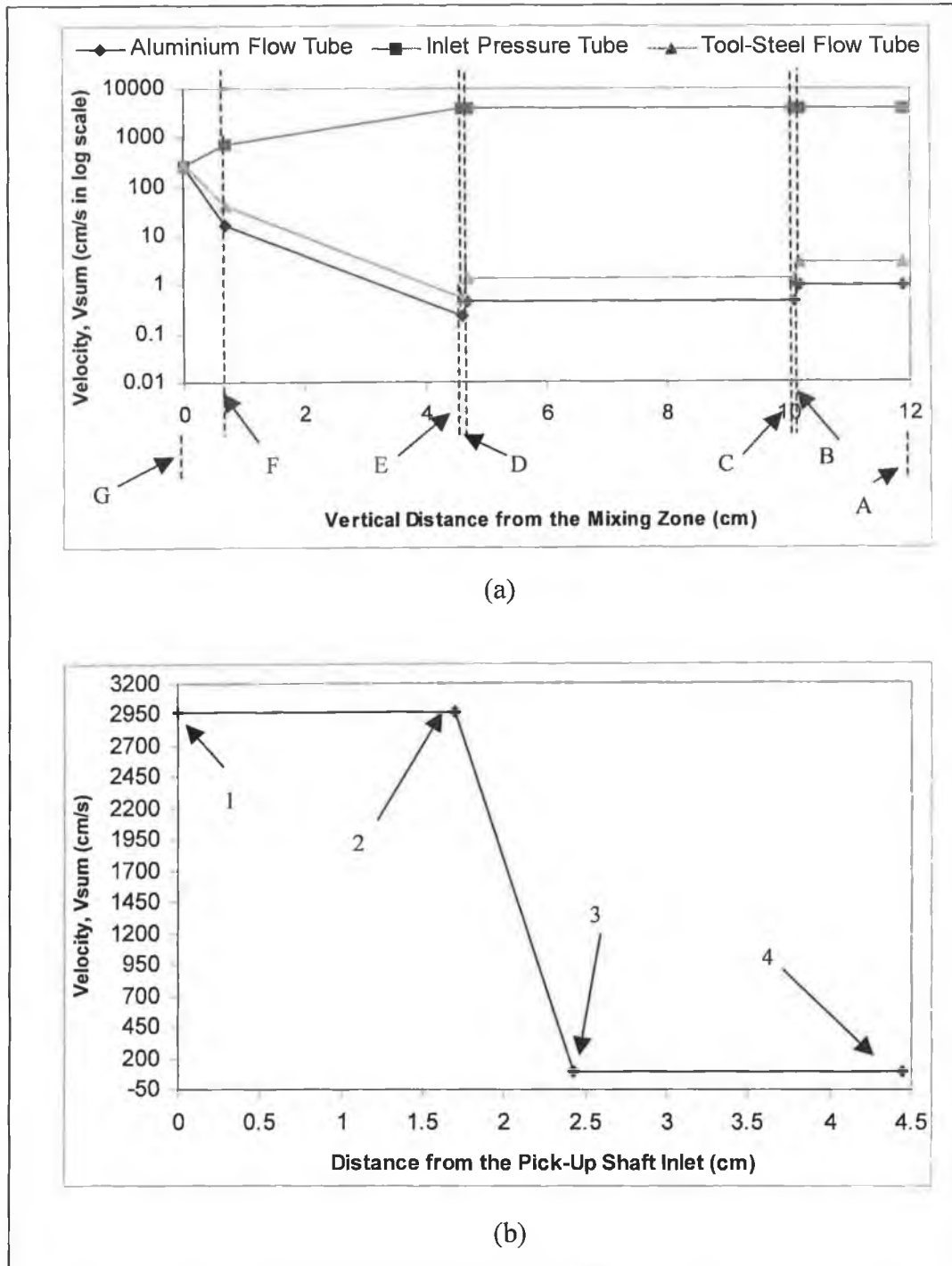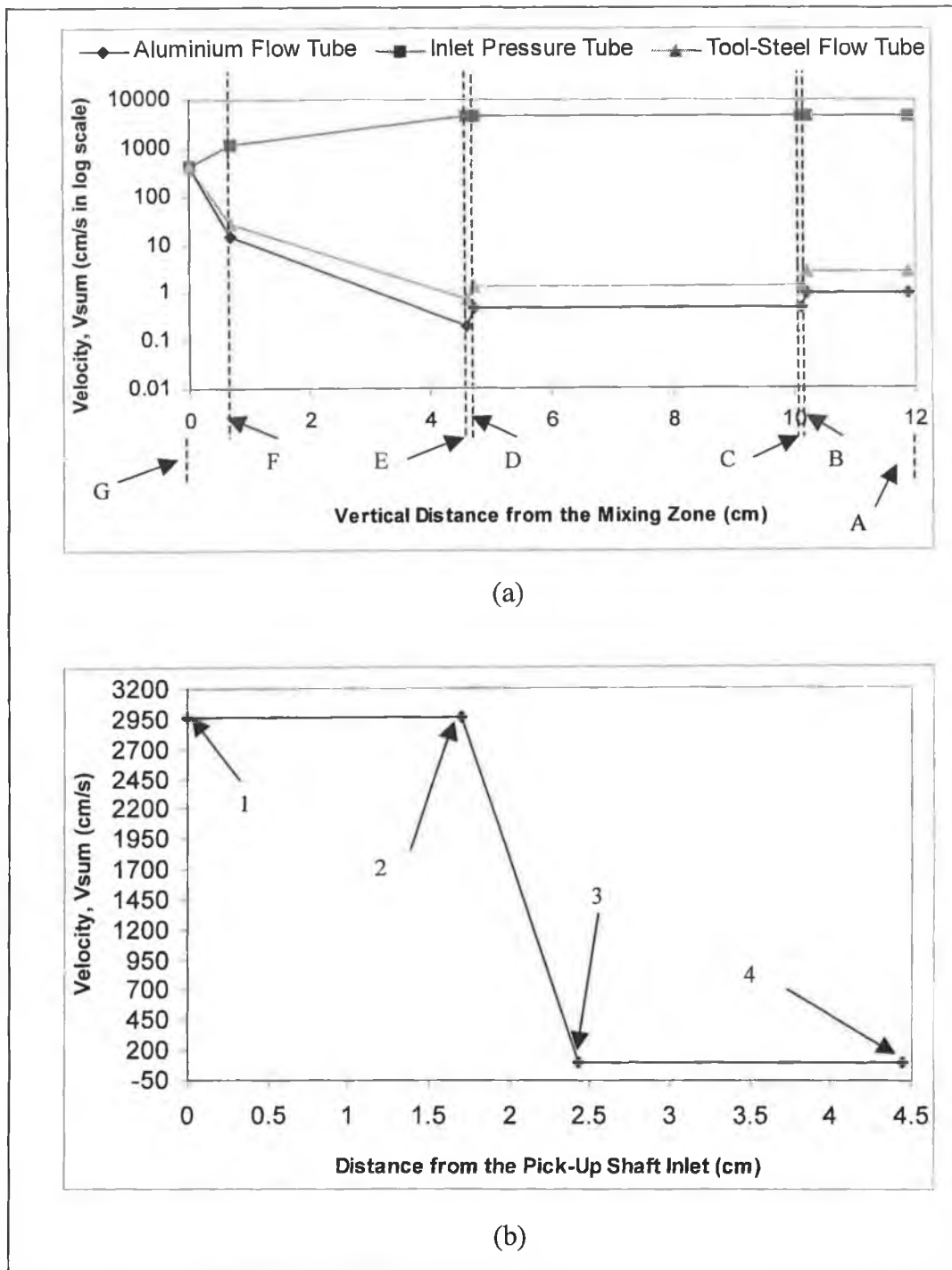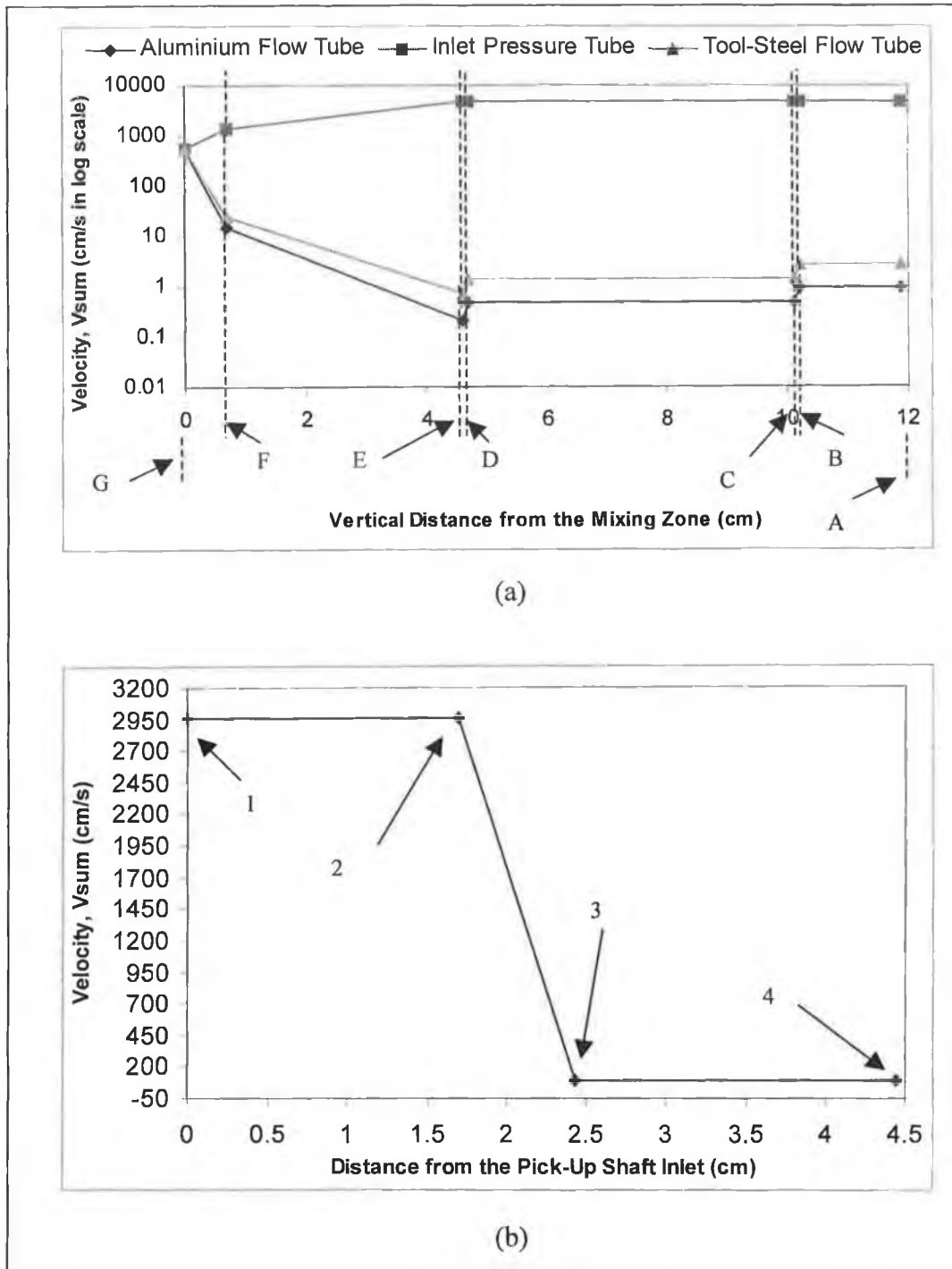
(a)

(b)

Figure A19: The velocity profile of the fluids through the (a) gas-powder flow tubes and (b) pick-up shaft with powders at a ratio of 1:3 and a nitrogen gas pressure ratio of 10:1 on the inlet pressure tube to the pick-up.

APPENDIX C

Results of Aluminium Powder Flow Bench Tests

Table A1: Amount of flow of the aluminium powder for 3 turns of the needle in chamber A*.

Test Number	Number of turns	Weight of container + powder (g)	Weight of container (g)	Weight of powder (g)	Average weight of powder (g)
1	3	45.68	42.95	2.73	
2	3	45.49	42.90	2.59	
3	3	45.64	42.99	2.65	2.64
4	3	45.59	42.93	2.66	
5	3	45.44	42.87	2.57	

Table A2: Amount of flow of the aluminium powder for 4 turns of the needle in chamber A *.

Test Number	Number of turns	Weight of container + powder (g)	Weight of container (g)	Weight of powder (g)	Average weight of powder (g)
1	4	46.85	43.02	3.83	
2	4	46.70	42.95	3.75	
3	4	46.75	42.90	3.85	3.83
4	4	46.88	42.97	3.91	
5	4	46.74	42.93	3.81	

Table A3: Amount of flow of the aluminium powder for 5 turns of the needle in chamber A*.

Test Number	Number of turns	Weight of container + powder (g)	Weight of container (g)	Weight of powder (g)	Average weight of powder (g)
1	5	48.54	42.94	5.60	
2	5	48.61	42.91	5.70	
3	5	48.59	42.87	5.72	5.73
4	5	48.40	42.90	5.90	
5	5	48.66	42.93	5.73	

Table A4: Amount of flow of the aluminium powder for 6 turns of the needle in chamber A*.

Test Number	Number of turns	Weight of container + powder (g)	Weight of container (g)	Weight of powder (g)	Average weight of powder (g)
1	6	49.62	42.88	6.74	
2	6	49.53	42.80	6.63	
3	6	49.57	42.82	6.75	6.72
4	6	49.47	42.79	6.68	
5	6	49.65	42.83	6.82	

Table A5: Amount of flow of the aluminium powder for 7 turns of the needle in chamber A*.

Test Number	Number of turns	Weight of container + powder (g)	Weight of container (g)	Weight of powder (g)	Average weight of powder (g)
1	7	51.26	42.86	8.40	
2	7	50.73	42.81	7.92	
3	7	50.98	42.83	8.15	7.97
4	7	50.77	42.79	7.98	
5	7	50.70	42.80	7.90	

Table A6: Amount of flow of the aluminium powder for 3 turns of the needle in chamber B**.

Test Number	Number of turns	Weight of powder + container (g)	Weight of container (g)	Weight of powder (g)	Average weight of powder (g)
1	3	45.75	43.04	2.71	
2	3	45.58	42.98	2.66	2.69
3	3	45.70	43.01	2.69	

Table A7: Amount of flow of the aluminium powder for 4 turns of the needle in chamber B**.

Test Number	Number of turns	Weight of powder + container (g)	Weight of container (g)	Weight of powder (g)	Average weight of powder (g)
1	4	46.93	43.04	2.71	
2	4	45.58	42.98	2.60	3.86
3	4	46.81	42.98	3.83	

Table A8: Amount of flow of the aluminium powder for 5 turns of the needle in chamber B**.

Test Number	Number of turns	Weight of powder + container (g)	Weight of container (g)	Weight of powder (g)	Average weight of powder (g)
1	5	48.94	43.03	5.91	
2	5	48.68	42.98	5.70	5.78
3	5	48.70	42.95	5.75	

Table A9: Amount of flow of the aluminium powder for 6 turns of the needle in chamber B**.

Test Number	Number of turns	Weight of powder + container (g)	Weight of container (g)	Weight of powder (g)	Average weight of powder (g)
1	6	49.77	43.01	6.76	
2	6	49.69	42.95	6.74	6.73
3	6	49.72	43.03	6.69	

Table A10: Amount of flow of the aluminium powder for 7 turns of the needle in chamber B**.

Test Number	Number of turns	Weight of powder + container (g)	Weight of container (g)	Weight of powder (g)	Average weight of powder (g)
1	7	50.93	43.08	7.85	
2	7	51.15	42.95	8.20	8.04
3	7	51.07	43.01	8.06	

* Chamber B was closed.

** Chamber A was closed.

Results of Tool-Steel Powder Flow Bench Tests

Table A11: Amount of flow of the tool-steel powder for ¼ a turn of the
needle in chamber B**.

Test Number	Number of turns	Weight of container + powder (g)	Weight of container (g)	Weight of powder (g)	Average weight of powder (g)
1	¼	45.80	43.72	2.08	
2	¼	45.64	43.79	1.65	
3	¼	45.77	43.75	2.02	2.05
4	¼	45.80	43.77	2.03	
5	¼	46.10	43.83	2.27	

Table A12: Amount of flow of the tool-steel powder for ½ a turn of the
needle in chamber B**.

Test Number	Number of turns	Weight of container + powder (g)	Weight of container (g)	Weight of powder (g)	Average weight of powder (g)
1	½	51.37	43.69	7.68	
2	½	51.43	43.72	7.71	
3	½	50.09	43.73	6.36	6.98
4	½	50.45	43.70	6.75	
5	½	51.10	43.70	6.40	

Table A13: Amount of flow of the tool-steel powder for ¾ a turn of the
needle in chamber B**.

Test Number	Number of turns	Weight of container + powder (g)	Weight of container (g)	Weight of powder (g)	Average weight of powder (g)
1	3/4	60.61	43.70	16.91	
2	3/4	60.60	43.78	17.02	
3	3/4	60.54	43.73	16.81	16.93
4	3/4	60.64	43.72	16.92	
5	3/4	60.72	43.75	16.97	

Table A14: Amount of flow of the tool-steel powder for1 turn of the
needle in chamber B**.

Test Number	Number of turns	Weight of container + powder (g)	Weight of container (g)	Weight of powder (g)	Average weight of powder (g)
1	1	65.80	43.60	22.20	
2	1	68.74	43.57	25.17	
3	1	67.08	43.58	23.5	22.87
4	1	65.17	43.60	21.57	
5	1	65.48	43.56	21.92	

Table A15: Amount of flow of the tool-steel powder for 2 turns of the
needle in chamber B**.

Test Number	Number of turns	Weight of container + powder (g)	Weight of container (g)	Weight of powder (g)	Average weight of powder (g)
1	2	83.88	43.78	40.10	
2	2	83.34	43.63	39.71	
3	2	83.43	43.58	39.85	41.08
4	2	86.40	43.74	42.66	
5	2	86.75	43.67	43.08	

Table A16: Amount of flow of the tool-steel powder for ¼ a turn of the
needle in chamber A*.

Test Number	Number of turns	Weight of container + powder (g)	Weight of container (g)	Weight of powder (g)	Average weight of powder (g)
1	1/4	44.97	42.98	1.99	
2	1/4	44.90	43.02	1.92	1.92
3	1/4	44.95	43.05	1.90	

Table A17: Amount of flow of the the tool-steel powder for ½ a turn of the
needle in chamber A*.

Test Number	Number of turns	Weight of container + powder (g)	Weight of container (g)	Weight of powder (g)	Average weight of powder (g)
1	1/2	49.89	42.99	6.90	
2	1/2	50.01	43.01	7.00	6.94
3	1/2	49.95	43.03	6.92	

Table A18: Amount of flow of the tool-steel powder for ¾ a turn of the needle in chamber A*.

Test Number	Number of turns	Weight of powder + container (g)	Weight of container (g)	Weight of powder (g)	Average weight of powder (g)
1	3/4	59.92	43.02	16.90	
2	3/4	59.80	42.97	16.84	16.84
3	3/4	59.79	43.00	16.79	

Table A19: Amount of flow of the tool-steel powder for 1 turn of the needle in chamber A*.

Test Number	Number of turns	Weight of container + powder (g)	Weight of container (g)	Weight of powder (g)	Average weight of powder (g)
1	1	65.27	42.99	22.28	
2	1	65.25	43.05	22.20	22.21
3	1	65.06	42.90	22.16	

Table A20: Amount of flow of the tool-steel powder for 2 turns of the needle in chamber A*.

Test Number	Number of turns	Weight of container + powder (g)	Weight of container (g)	Weight of powder (g)	Average weight of powder (g)
1	2	84.04	43.02	41.02	
2	2	82.80	42.98	39.82	40.25
3	2	82.85	42.95	39.90	

** Chamber A was closed

* Chamber B was closed

APPENDIX E

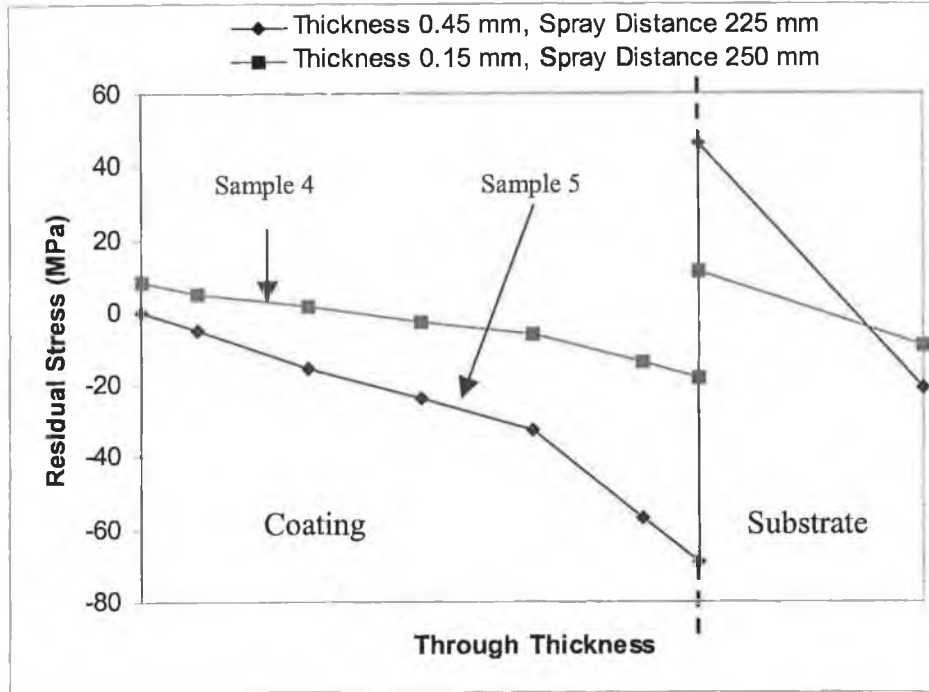## Stress Distribution Profile

Figure A20: Stress distribution through the substrate and coating for samples 4 and 5 in group 2.
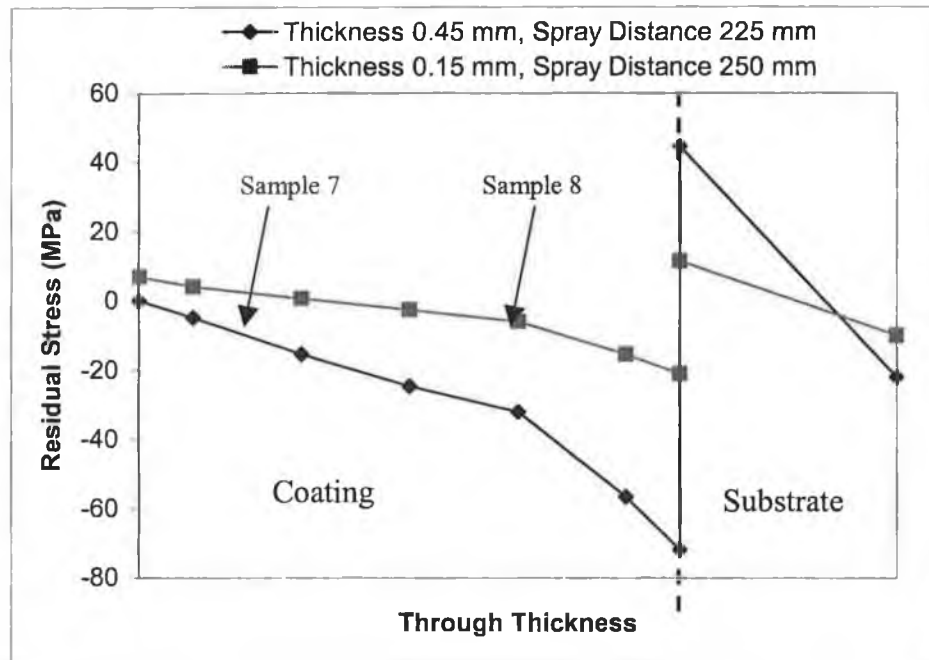

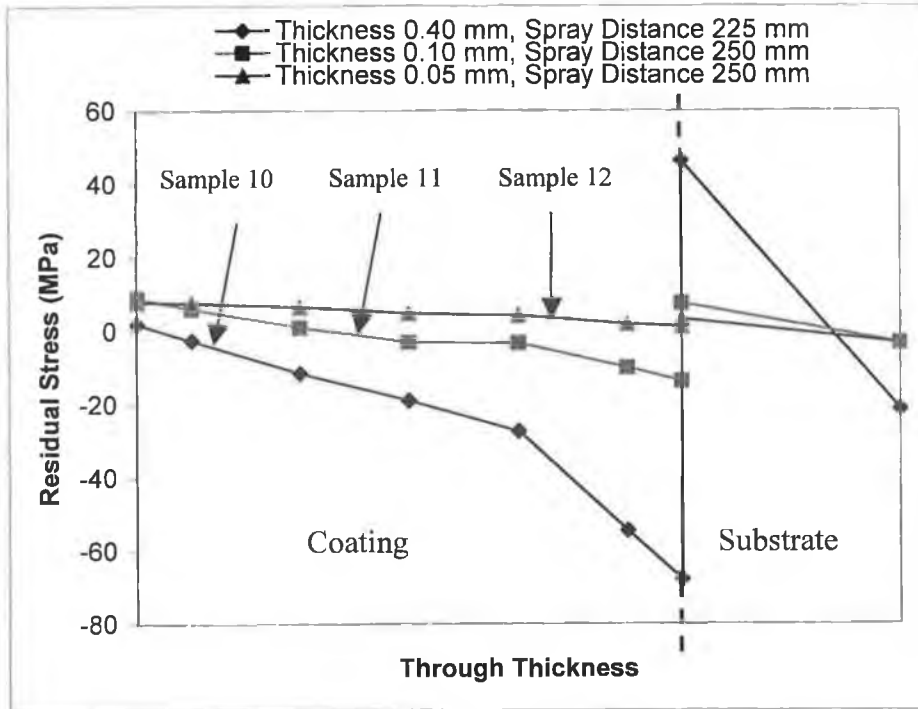Figure A21: Stress distribution through the substrate and coating for samples 7 and 8 in group 3.

Figure A22: Stress distribution through the substrate and coating for samples 10, 11 and 12 in group 4.
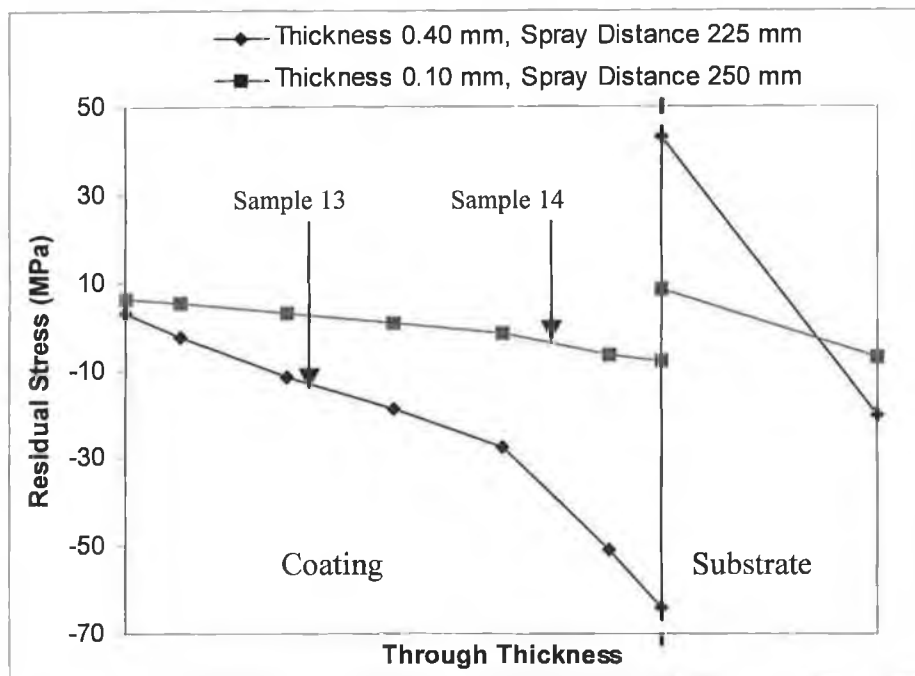

Figure A23: Stress distribution through the substrate and coating for samples 13 and 14 in group 5.
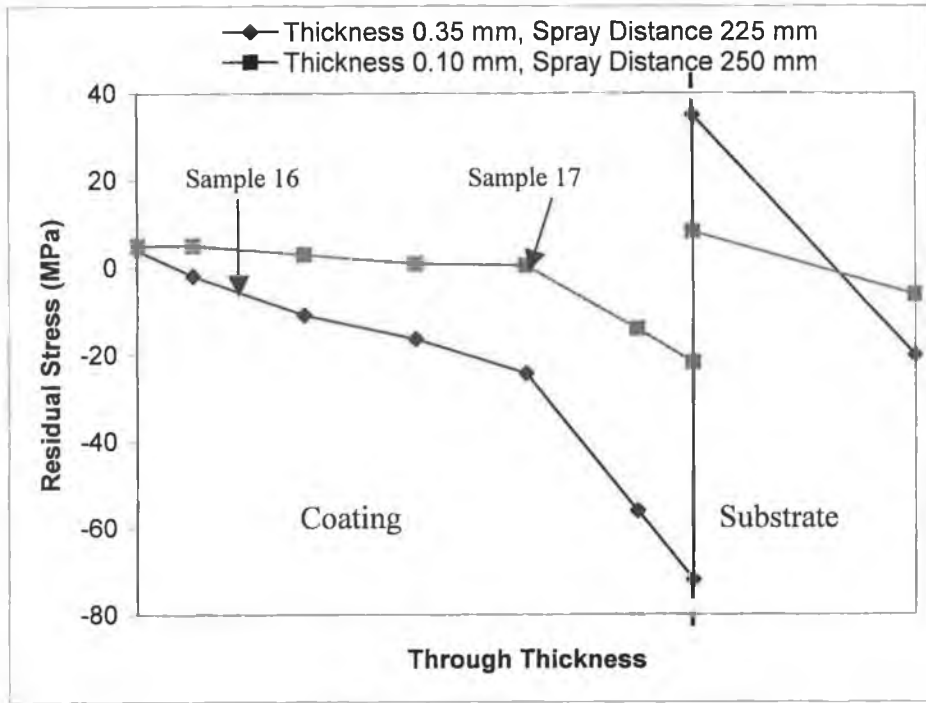
Figure A24: Stress distribution through the substrate and coating for samples 16 and 17 in group 6.
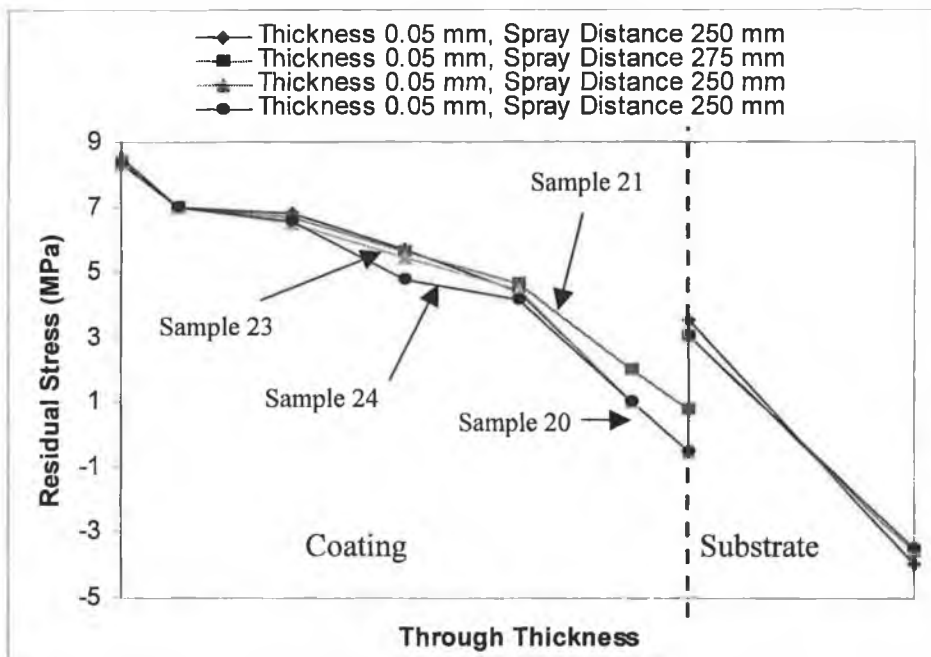

Figure A25: Stress distribution through the substrate and coating for samples 20, 21, 23 and 26 in group 7.